Digital X-ray Analysis for Monitoring Fracture Healing

Sarah P. Dawson

Doctor of Philosophy

The University of Edinburgh

August 2009

Declaration

I, Sarah Penelope Dawson, hereby declare that this thesis has been composed by myself, that the work in the thesis is my own original work (except where acknowledgements indicate otherwise) and that neither the whole, nor any part of it, has been, is being or is to be submitted for any other degree in this or any other University.

S.P. Dawson

4 August 2009

Abstract

X-ray based evaluation of different stages of fracture healing is a well established clinical standard. However, several studies have shown plain radiography alone to be an unreliable method to assess healing. The advent of digital X-ray systems provides the potential to perform quantitative analysis on X-ray images without disrupting normal clinical practice. Two aspects were explored in this study. The first was the measurement of mechanical fracture stiffness under four point bending and axial loading. The second was the inclusion of an Aluminium step wedge to provide Aluminium-equivalent thickness calibration information.

Mechanical stiffness studies involved the development of equipment to perform four point bending on intra-medullary (IM) nailed tibial fractures, equipment to perform axial loading on conservatively treated humeral fractures, and fracture models to examine the developed systems. Computational procedures to automatically measure the angle and offset occurring at the fracture site by comparing loaded and unloaded X-ray images were developed utilising cross-correlation. The apparatus and procedures were tested using the fracture models both in X-ray and using the Zwick materials testing machine. The four point bending system was applied clinically to a series of IM nailed tibial fracture patients and the axial loading system to two conservatively treated humeral fracture patients.

Mechanical stiffness results showed that the apparatus worked well in the clinical radiography environment and was unobtrusive to normal practice. The developed X-ray analysis procedure provided reliable measurements. However, in the case of IM nailed tibial fractures, both angular and displacement movements were too small to be accurately assessed or to provide reliable stiffness measurements. This indicated that this patient group was possibly unsuitable for mechanical stiffness measurements or that higher loads needed to be applied to the fracture site. The case studies of conservatively treated humeral fractures showed potential in detecting movement between loaded and unloaded X-rays and using this to provide stiffness information.

Further investigation is required to show that this technique has the potential to aid fracture healing monitoring.

Investigation into Aluminium step wedge calibration began with the design of different step wedges and X-ray phantoms. Initial image analysis involved studying the automatic processing applied by a digital Computed Radiography (CR) Fuji system and modelling of the inhomogeneities in X-ray images as well as investigation into the effect of and correction for scatter, overlying soft tissue and bone thickness. Computational procedures were developed to semi-automatically detect the steps of the step wedge, form an exponential Aluminium step thickness to grey level calibration graph, measure soft tissue and bone thickness, and correct for the heel effect and scatter contributions. Tests were carried out on pre-clinical models and results compared to ash weight and peripheral quantitative computed tomography (pQCT). A clinical study of radial fractures was used to investigate the effectiveness of the step wedge calibration system in monitoring fracture healing changes.

Results using the step wedge indicated that the calibration technique was effective in detecting and correcting for aspects influencing Aluminium-equivalent thickness measures. With careful processing, useful information was obtained from digital X-rays that included the Aluminium step wedge and these correlated well with existing density measures. The use of the wedge in patient images showed that small increases in Aluminium-equivalent thickness of the fracture site could be detected. This was most useful for intra-patient comparisons throughout the course of healing rather than providing quantitative measurements which were comparable to other density measures.

In conclusion, this thesis shows the potential for accurate analysis of digital X-rays to aid the monitoring of healing changes in fracture patients, particularly with application of axial loading and the use of step wedge calibration.

Acknowledgements

I would like to thank the following people for their help during this project:

1. Prof. Hamish Simpson for his clinical insight and research experience.
2. Dr. Tom MacGillivray for his advice on image processing and thorough proof-reading.
3. Andrew Muir for his guidance and encouragement.
4. Andrew Downie for his help with and ideas for the manufacture of the experimental apparatus.
5. Kathryn Stewart and the staff of OPD 6 for assisting with X-ray testing and clinical trials.
6. Nicola Bate for her untiring help taking the test images on the Fuji CR system.
7. Jerry Williams for his advice and guidance with the Medical Physics aspects of the study.
8. Pankaj for his time in reviewing the mechanical engineering sections of the project.
9. Erin Ross and Rob Wallace for their help with the pre-clinical tests.
10. Deborah MacDonald for her assistance with ethics applications.
11. Andrew Whiley for his support and encouragement during the entire project.

Contents

List of Figures

List of Tables

List of Abbreviations

1D	One Dimensional
2D	Two Dimensional
3D	Three Dimensional
ADA	American Dental Association
AGC	Automatic Gain Control
AlEq	Aluminium Equivalent thickness
AP	Antero-Posterior
BMC	Bone Mineral Content
BMD	Bone Mineral Density
CE	Conversion Efficiency
CI	Confidence Interval
CR	Computed Radiography
CT	Computer Tomography
DEXA	Dual Energy X-ray Absorptiometry
DICOM	Digital Imaging in Communications and Medicine
DNA	Did Not Attend
DQE	Detective Quantum Efficiency
DR	Digital Radiography
EDR	Exposure Data Recogniser
EDTA	Ethylene Diaminatetra Acid
FE	Finite Element
GL	Grey Level
HU	Hounsfield Units
ID	Identification
IM	Intramedullary
IP	Imaging Plate
ISO	International Organisation for Standardisation

L	Latitude
LUT	Look Up Table
ML	Medio-Lateral
PACS	Picture Archiving and Communication System
PET	Positron Emission Tomography
PI	Prediction Interval
pQCT	Peripheral Quantitative Computer Tomography
PSF	Point Spread Function
PSL	Photostimulated Luminescence
PSP	Photostimulable Phosphor
PVC	Polyvinyl Chloride
QCT	Quantitative Computer Tomography
QDE	Quantum Detection Efficiency
QMRI	Quantitative Magentic Resonance Imaging
RGB	Red Green Blue
RIE	Royal Infirmary of Edinburgh
ROI	Region of Interest
RSA	Radiostereometric Analysis
S	Sensitivity
SD	Standard Deviation
SXA	Single X-ray Absorptiometry

Part I

Introduction and Literature Review

Chapter 1

Introduction

1.1 SUBJECT

This study investigates the use of digital X-ray images to aid the evaluation of fracture healing. Two methods are assessed: monitoring fracture stiffness and monitoring fracture density. In the first, digital X-rays are used to measure movement at the fracture site due to bending and tensile stiffness tests. The second method is based on including an Aluminium step wedge in digital X-rays of fracture patients. This provides a calibration tool for calculating Aluminium-equivalent thickness measurements of the fracture from the grey scales in the X-ray image.

1.2 BACKGROUND

A well defined and consistently quantifiable method to monitor fracture healing is not presently available in the standard clinical setting. Evaluation of the stage and rate of healing is important for predicting ability to bear weight fully as well as to identify fractures which may be affected by delayed or non-union. Techniques currently used clinically, especially those using conventional radiography, do not offer quantifiable measurements. Both fracture stiffness and fracture density measurement have been suggested as potential solutions to this problem.

Digital X-ray systems are relatively new to the clinical radiography environment. They offer potential in enhancing existing X-ray techniques due to their high quality digital output in which post-processing can be controlled. The potential of combining digital X-ray with the proposed methods of assessing fracture healing has not previously been studied. If digital X-ray can be used to provide quantitative measurements of fracture healing it could offer benefits in the clinical setting and improve development, testing and evaluation in the orthopaedic research environment.

1.3 CONTEXT

The problems encountered in using digital X-ray to monitor fracture stiffness and fracture density fall into two categories. The first concerns the modifications necessary to the radiography environment and the second involves the image processing techniques necessary to analyse the digital X-rays. In the first, the development of tools to apply stiffness tests during X-ray imaging without exposing staff or patients to extra radiation is needed, as well as the testing of the most suitable type of step wedge to be included for density analysis. In the second area, X-ray images need to be aligned for measurement of displacement occurring due to loading. For step wedge calibration, approaches developed for conventional X-ray must be updated. Investigation of the effects of image inhomogeneities and other influences of measured density are also necessary.

1.4 RESEARCH OBJECTIVES

1.4.1 Hypothesis

Two elements of the clinical monitoring of fracture healing have been identified. The first is that the method of monitoring fractures which is preferable to clinicians and hospitals is X-ray imaging. The second is that current techniques do not offer the accuracy required to monitor fractures with an acceptable degree of precision. The advent of digital radiography offers potential in terms of improving current fracture imaging techniques to provide more information on fracture healing.

Based on this, the hypothesis that this thesis sets out to prove is that

"Image processing of digital X-ray images can be optimised to aid the management of fracture patients."

1.4.2 Research Questions

Investigation into the two areas of monitoring fracture healing forms the basis for the two major research questions to be answered by this thesis:

1. Can the stiffness of a fracture be monitored using analysis of digital X-rays of loaded and unloaded fractures?
2. Can an Aluminium step wedge included in digital X-rays be used to assess the bone and callus density in fracture patients?

In answering these questions, several secondary questions will be addressed:

1. Concerned with fracture stiffness measurement:
   (a) Can a suitable method of applying bending and axial load during X-ray be developed?
   (b) Can an image processing technique to measure the difference between loaded and unloaded X-rays be developed?
   (c) What magnitude of movement can be measured at the fracture site?
   (d) Can meaningful stiffness measurements be made from the displacement measurements?
   (e) Can stiffness measurements be related to the stage of healing of the fracture?
2. Concerned with fracture density measurement:
   (a) What is the best wedge design for calibration of patient X-ray images?
   (b) What is the best calibration technique to use for an Aluminium step wedge in digital X-ray images?
   (c) Can background inhomogeneities in the X-ray image be corrected in a simple manner?
   (d) Can corrections be made for the contributions of bone and soft tissue thickness and scatter?
   (e) Can the measurement from digital X-ray images be related to validated methods of measuring density?
   (f) Can Aluminium-equivalent thickness readings from digital X-rays of a fracture be related to the stage of healing of the fracture?

1.5 SCOPE

This project aims to evaluate the potential of digital X-ray when used as a tool to aid the assessment of fracture healing, and to identify problems associated with this. As such it involves the testing and development of two methods of using digital X-ray – fracture stiffness monitoring and fracture density monitoring. The scope of the project is limited to an initial evaluation of the potential of these methods, rather than the development of final products ready for use clinically or in research.

1.6 INVESTIGATIVE PROCESS

This study consists of two main areas – fracture stiffness monitoring and fracture density monitoring. To clarify the development of these two ideas, the thesis is arranged in several parts.

The thesis begins with a review of the literature in Part I. This covers the conventions and problems in monitoring fracture healing, the use of stiffness to evaluate fractures and the role of X-ray analysis in fracture monitoring.

Part II deals with the question of using stiffness to monitor fracture healing. It begins with a description of the apparatus and image analysis techniques developed. This is followed by the results of pre-clinical tests. Feasibility studies on patients are then described.

Part III involves the possibility of using an Aluminium step wedge to provide density information from digital X-ray images. The equipment developed for evaluating this is described, followed by a discussion of the investigations into effects on image quality and the processing methods used to analyse the X-ray images. Pre-clinical tests on different density models are then presented, followed by a feasibility study on radial fracture patients.

In Part IV, conclusions from the results and discussions in the previous sections are drawn. Recommendations for extension of the work and future developments are made.

Chapter 2

Monitoring Fracture Healing

2.1 INTRODUCTION

An estimated one million fractures occur every year in the United Kingdom due to high energy traumas, sporting injuries or fragility due to osteoporosis [1]. Early mobilisation and weight bearing have been shown to be beneficial to the healing process [2], and, for patients treated with external fixation, accurate knowledge of the stage of bone healing would reduce unnecessary time in a fixator, thus being beneficial for both the patient's comfort and well being as well as in terms of costs to health services. An additional benefit would be the possibility of early detection of potential non-unions, infections and other delays to healing so that interventions could be made as soon as possible to avoid unnecessary complications [2, 3]. In this chapter, an overview of fractures, the healing process and the current treatment methods is given. The methods used clinically to assess fracture healing are also discussed and the lack of accuracy in these illustrated the difficulty and importance in defining and measuring the end point of fracture healing. Finally, alternative methods of monitoring fracture healing are explored.

2.2 FRACTURES

A fracture is defined as a "loss of continuity in the substance of the bone" [4, p4]. There are four different kinds of fracture, grouped according to how they are caused. The less common types include fatigue fractures which occur due to repeated stress on the bone causing microdamage that develops into a full fracture, and pathological fractures which occur in bone weakened by disease. Fragility fractures are an increasingly common occurrence and happen in bone weakened by osteoporosis. The main type of fracture which is commonly

seen by clinicians is the traumatic fracture, which is caused by sudden injury. There are various kinds of traumatic fractures including closed (simple), where the bone does not break through the skin; open (compound), where there is an opening in the skin; partial; complete and comminuted, where the bone has split into several fragments. There are as many different ways for a bone to fracture as there are ways to apply force to it resulting in spiral, impacted, compression, avulsion, transverse and oblique fractures. Parts of the bone can be torn off or moved out of anatomical alignment. The type and pattern of fracture indicates both the likely cause of fracture and the most appropriate treatment method.

2.2.1 Healing

There are five major physiological steps involved in the healing of fractures with callus [4, 5, 6, 7]. Firstly, a fracture haematoma (blood clot) forms throughout the damaged area resulting in cellular death at the fracture site, followed by swelling and inflammation. The second stage is of cellular proliferation in the periosteum close to the fracture. Cells also proliferate in the medullary canal and debris and dead bone is cleared away by phagocytic cells. In the third stage, this cellular tissue gives rise to osteoblasts and chondroblasts which lay down an intercellular matrix of collagen and polysaccharide which fills the gap between the fragmented bone. Calcium salts impregnate this matrix and it forms immature or woven bone. This woven bone gives the fracture some rigidity and is the first sign of healing detectable on radiographs. It is also the precursor to bone formation. During the fourth stage, the woven bone is gradually changed into more mature bone. Progressive mineralisation and remodelling of the fracture callus, which occurs by breaking down the callus and re-establishing a blood supply, results in a repair tissue that is indistinguishable from the adjacent normal compact bone. Finally, in the stage of remodelling, the bulbous collar of bone reinforcing the fracture is gradually strengthened where stress occurs and removed where it is unnecessary. The time required for a fracture to unite is variable. It differs due to age, type of fracture, location of fracture and method of treatment.

2.2.2 Treatment

The main aims of fracture treatment are to attain sound bony union without deformity and to restore function [4, 5, 7]. There are many different ways to aid the healing of fractures. The general treatment involves re-aligning the broken parts of bone and then immobilising them whilst maintaining function. In the first stage, reduction, the aim is to reduce the malalignment of the bone fragments. This can be by closed manipulation performed manually under anaesthetic, mechanical traction either in the short term or over a more gradual time, and operative reduction which is only undertaken if the other

methods are unsuitable. The next treatment step is immobilisation. This is performed to prevent displacement of the fracture fragments, prevent movement that might slow down the process of union and relieve pain.

Either of these steps may be unnecessary depending on the type of fracture. However, all fractures require rehabilitation in order to preserve function whilst the fracture is healing and to restore it fully once the fracture has healed completely. Rehabilitation can form a combination of active use, active exercises and passive motion. Once new bone tissue forms to the extent that the patient can bear weight with no pain, the fracture can be considered to be healed. However, there is debate as to whether this end point of healing is valid and how best to measure it.

In order to achieve the three steps of fracture healing, particularly immobilisation, various fracture treatment devices are available, each being suited to different fracture types and locations. Some of the more commonly used types are discussed briefly below.

2.2.3 Conservative Treatment

Non-surgical treatment usually involves the use of a plaster cast to stabilise the fracture. The clinician aims to reduce and align the fracture fragments and maintain this in a mainly rigid way. However, perfect alignment and motionless fixation are not judged to be necessary and fracture healing thus occurs through the movement of bone fragments inducing callus formation [8]. Other external splints made from malleable materials are also used, especially in the leg, thigh and fingers. Cast or (functional) bracing is the use of a cast to stabilise a long bone fracture whilst maintaining function in adjacent joints and is usually only employed several weeks after injury. In certain fractures, where alignment using plaster or splints is not possible, sustained mechanical traction can be employed to balance the pull of the muscles and maintain alignment.

2.2.4 External Fixation

External fixation refers to anchorage of the bone fragments to an external bar through pins inserted into the proximal and distal fragments of the fracture. A frame or fixator is used to achieve this and allows for adjustment in position or compression of the fracture. External fixation is usually used in open fractures and aims for indirect healing with external callus formation.

2.2.5 Internal Fixation

Internal fixation is used to provide early mobility in patients and situations where operative reduction is necessary or where splintage will not maintain reduction. Methods of internal fixation that are commonly used include a metal plate held by screws, the intramedullary (IM) nail, the dynamic compression screw-plate, the condylar screw-plate, tension band wiring and transfixion screws. The choice depends on the site and pattern of fracture. Internal fixation aims for accurate fracture reduction and rigid stabilisation of the fragments to allow immediate mobilisation with no external splints. The result is ideally direct healing with little external callus formation [8, 9].

2.2.6 Complications

Most fractures are treated successfully and go on to full union. However, several factors may result in a delayed healing response, such as if blood supply to the fracture is impaired or if excessive and damaging movement between bone fragments occurs. Infection or the involvement of a tumour also hinder healing. The types of complications are grouped according to whether they involve the fracture itself or an associated injury in other tissues. Infection most often occurs in open fractures and can result in osteomyelitis. Prevention and early detection is key and treatment includes drainage of the infected site and antibiotic medication.

Although there is no strict time limit for a fracture to heal, delayed union is said to occur when the fracture remains freely mobile several months after injury. This can persist to non-union when it becomes clear that no healing will occur without intervention. The factors causing these states can be infection, poor mechanical environment, damage to the fracture haematoma or damage to the bone ends. Treatment can be surgical and sometimes involves bone grafting. Avascular necrosis (death of bone due to a deficient blood supply), mal-union (union in an imperfect position) and shortening of the bone after fracture are further complications.

Complications involving associated tissues include injury to major blood vessels, compartment syndrome where swelling in the compartment of injury reduces blood supply, and injury to various tissues such as nerves, viscera and tendons. Injuries to joints and joint stiffness due to adhesions are also fairly common complications of fractures which are treated by manipulation or in serious cases, surgery [4, 7].

2.3 ASSESSING FRACTURE HEALING

Despite the volume of people who require treatment for a fractured bone, methods of healing assessment are vague at best [2]. The current procedure which clinicians use to monitor the union of a fractured bone is a combination of patient feedback, manual strength testing and radiography. There are problems with accuracy for each of these methods. Clearly, patient feedback is subjective, and thus prone to psychological and mood differences between patients, and between the same patient at different times [10, 11].

Surgeons perform manual assessment of the strength of a healing bone by taking hold of the bone on either side of the fracture and putting opposing forces on the bones. The movement they feel supposedly gives an indication of how well healed the bone is. However, this is considered a highly inaccurate and subjective method of testing healing strength [10, 12]. Webb *et al.* compared the ability of 20 orthopaedic clinicians and 20 untrained controls to rank fracture models according to healing [11]. Their results show that neither training nor experience aids diagnosis in this fashion, and that overestimation of fracture stiffness occurred 83% of the time whilst underestimation occurred 13% of the time.

In a standard situation, medio-lateral (ML or lateral) and antero-posterior (AP) X-ray images of the broken limb are obtained at various stages during healing. The callus formation and clarity of the fracture line seen in these X-rays supposedly gives an indication of how well the bone is healing. However, studies have shown that plain radiographs correlate poorly with bone strength and are unreliable for assessing the stage of fracture healing or the likelihood of complications [2, 12, 13, 14, 15]. Despite knowledge about the unreliability of radiographic assessment it is still the primary test used by most surgeons.

For instance, Nicholls *et al.* allowed 27 clinicians (surgeons and radiologists) to rank the strength of fractured rabbit tibiae in various stages of healing according to their radiographs [16]. Their accuracy was found to be not statistically significant, in other words, that a random categorisation would have been as reliable. Panjabi *et al.* explained these findings in a well designed trial comparing many radiographic parameters of rabbit tibial fractures at various stages of healing to mechanically tested bone strength [17]. In a statistical analysis of the results, they found that there was insufficient information in plain radiographs to predict the strength of a healing fracture. Hammer *et al.* supported these results reporting the probability of correct radiographic evaluation to be as low as 0.5 [18]. In a more recent investigation of the accuracy of radiographs, Blokhuis *et al.* compared the results of two experienced clinicians examining X-ray images to mechanical and histological tests of fractures in the tibiae of goats [13]. They found that, although the clinician's results correlated reasonably well with estimated stage of fracture healing and broad mechanical strength, they correlated poorly or not at all with more discrete mechanical and histological

parameters. They concluded that radiographs may be useful in a clinical setting when visualising major changes in fracture healing or obvious problems in the healing process but that they were not sensitive enough to measure small changes.

2.4 NEED FOR AN ACCURATE OUTCOME MEASURE

As far back as 1942, clinicians were calling for objective outcome measures in fracture studies, saying that no unanimity on the factors which determine bone union had been reached and that there was no scientific standard with which to compare results [19]. These comments were made when traction and plaster were almost exclusively the methods of treatment used. Today there is still no answer to outcome measure in fracture healing and the question is complicated by several issues. Firstly, the end point of fracture healing is only vaguely known using current methods. It is often defined as the point when full weight bearing can be achieved without re-fracture but the only way to test this is to risk re-fracture of the patient. Marsh *et al.* point out that fracture union is, in fact, a continuous process and to define an end point requires the application of a somewhat arbitrary threshold [20]. Furthermore, the definition of this threshold depends on the validity of the aspects of the fracture healing process that can be measured. There is also confusion as to the definitions of delayed and non-union. Both of these situations mean that to reliably classify a fracture as being healed or being un-united requires waiting several months after the injury [21, 22].

Another major complication results from the variety of treatment methods used. Internal fixation can in some situations achieve full weight bearing immediately. Internal standard plate fixation also creates an environment for direct healing. This is different to an external fixation device which encourages healing with a large amount of external callus formation [20]. Comparison of these two methods, especially visually, is difficult. Add to this the influence of complications such as the risk of infections in surgical treatment methods or malunions in conservative methods, and the reason why there is still no clear outcome measure in fracture treatment becomes better understood. In fact, in an insightful review on fracture healing outcome measures taking all these factors into account, Wade and Richardson go as far as to say that it is unlikely that one method of comparison will be developed to define and measure a suitable end point for the many different types of fractures and fracture treatment methods [22].

The aim of the clinician is to aid the body in its attempt to heal the fracture as quickly as possible. However, the lack of knowledge of a well defined and precise outcome measure can result in either the fixation device being removed too early, resulting in re-fracture, or the device being left on for too long, delaying a patient's return to normal activity. Both have implications in terms of temporal and financial costs as well as being detrimental to the

patient's lifestyle and general well being. Furthermore, accurate knowledge of the state and rate of fracture healing, especially for those with delayed union and other complications would be invaluable in providing the best treatment for each patient at the best time and avoiding unnecessary delays [3, 21, 22, 23, 24]. Knowledge of the state of bone healing and quality of fracture gap tissues can inform decisions such as a change of treatment or the necessity for surgical intervention. This would ensure that each patient gets the most appropriate treatment at the most advantageous time whilst avoiding costly interventions which are potentially unnecessary.

It is also important to have a reliable and sensitive way to evaluate fracture healing in the research setting. A clear, well defined and accurately assessable outcome measure is necessary when developing, testing or comparing different methods to aid fracture healing. Without this, it is impossible to design useful studies to evaluate the efficacy of different treatment methods because there is no way to compare them quantitatively [13, 20, 22, 25]. Tiedeman *et al.* blamed the lack of outcome measure on the lack of an objective, non-invasive technique to quantify the restoration of structural rigidity [15]. These studies indicate that a more sensitive and quantitative method for evaluation of fracture healing is necessary in both the clinical and research contexts.

2.5 POTENTIAL SOLUTIONS

Due to the described unreliability of existing fracture monitoring methods, many solutions, both invasive and non-invasive, have been attempted to improve diagnostic accuracy. Several of these are imaging methods that have been developed for the examination of bone density and fracture risk associated with osteoporosis.

2.5.1 Dual Energy X-ray Absorptiometry

Dual Energy X-ray Absorptiometry (DEXA) measures bone mineral density (BMD) and bone mineral content (BMC) and is most often employed for the diagnosis of osteoporosis. Due to the changing density of bone callus during healing, this technology also has the potential for monitoring the extent of healing. Some authors have found DEXA a useful tool for monitoring new bone formation and limb alignment and have found a high correlation between bending stiffness and DEXA derived stiffness values [26, 27]. However, other studies have shown only weak correlations between BMD as measured using DEXA and bone strength measured mechanically. This is because DEXA cannot measure small changes in BMD which could thus result in false positives or false negatives regarding bone strength in clinical practice. Furthermore, the accuracy of DEXA deteriorates greatly when applied

to fractures with metal implants such as internal nails. There is also a fundamental inability of bone density to predict the modulus of elasticity, and thus the bending stiffness, fully and this reduces the accuracy of DEXA and its ability to provide inter-patient healing comparisons [27].

2.5.2 Ultrasound

Studies into the use of ultrasound to monitor bone healing have been in progress for many years. Many of these have shown its potential in terms of a good correlation between speed of sound and healing bone [3]. Eyres *et al.* found that ultrasound could detect new bone in limb lengthening but lost accuracy further on in the healing process due to reflection against osseous structures [26], and this was confirmed by Kolbeck *et al.* [28]. However, Derbyshire and Simpson found that the extent to which the callus reflected sound could be used to monitor the rate of callus maturation during limb lengthening [29]. Kolbeck *et al.* also found the advantage of being able to view all aspects of the limb from multiple directions to be beneficial. Some researchers have also claimed that the speed of sound of ultrasound could be related to the mass, modulus of elasticity and resistance to deformation of bone which are measures of bone quality [30], although other groups state that there is a lack of any system that can do this effectively in a clinical setting as yet [31]. Several difficulties have prevented the widespread clinical use of ultrasound including the lack of reproducibility of measurement site, variable amounts of surrounding soft tissue in different patients, and other unaccounted for sources of error. Further research is required before this can be considered a viable clinical technique for the monitoring of fracture healing [3, 30, 32].

2.5.3 Computer Tomography

Computer Tomography (CT) has widely been shown to have an excellent accuracy in determining BMD but this has yet to be extended to healing callus. Quantitative Computer Tomography (QCT) provides CT numbers in Hounsfield Units (HU) which correspond to tissue densities. Investigators have used this relationship to verify that there is a high correlation between QCT numbers and apparent density in cortical bone over a wide range of densities achieved through distraction osteogenesis [33]. This accuracy has been used for the prediction of fracture risk and may extend to healing fractures although this has yet to be thoroughly investigated [30]. Lynch *et al.* performed a study on a small cohort of radial fracture patients and found HU useful in tracking density changes in healing fractures but recommended further research into the validity of the method for identifying patients at risk of delayed union [34]. Despite this, potential the cost and radiation involved in CT as well as its often restricted availability limits its clinical appeal [3, 13, 31].

2.5.4 Other Methods

Many other methods have been considered for monitoring fracture healing. One of these is the use of resonant frequency and impedance to provide information on the mechanical properties of bone, also known as vibrational analysis. Whilst some studies have shown potential in this regard there are several limiting factors including the necessity for readily accessible landmarks, the interference of adjacent soft tissues and bones and the lack of suitability when applied to externally or internally fixed fractures [3]. Roberts and Steele found resonant frequency a useful tool only in the early stages of healing where whole bone mechanical properties change rapidly [35]. However, despite the potential of this method, it has limited accuracy and has been found to be insufficient to measure fracture mechanical properties [25].

Finite Element (FE) analysis has been used to build (largely patient specific) computer models of bone structure. In general, a three dimensional (3D) imaging technique such as CT provides geometrical and tissue properties of an object. Further testing provides extra information such as mechanical properties. By estimating the potential loads on the elements in this object, the model can be used to predict the resulting mechanical behaviour. Models have been shown to agree with observed mechanical behaviour and to be able to distinguish between healthy and osteoporotic bone. Shefelbine *et al.* conducted a thorough study into the use of FE models and micro-CT as an *in vivo* predictor of the mechanical properties of healing fractures in 50 rat femoral fractures and found their method effective [25]. However, there is a lack of further studies confirming its potential and usefulness in the clinical setting. Furthermore, the potential of FE methods is limited by the large

amounts of computing time necessary and the high costs and radiation dose associated with intensive imaging and modelling. As such, no viable clinical systems are currently available [25, 32, 36].

Several other imaging methods have also been used to estimate bone mineral density. These include Single X-ray Absorptiometry (SXA), Positron Emission Tomography (PET) and Quantitative Magnetic Resonance Imaging (QMR). However, their use has yet to be extended to the monitoring of fracture healing. Several limitations occur such as the need for the scanned area to be submerged in a water bath in the case of SXA. This is not possible with several fracture treatment methods and depending on the fracture site may not be practical at all. In the case of QMR, fractures treated with metal fixators cannot be scanned and the techniques involved are time consuming. PET is expensive and not widely available. These factors and limitations combine to make these imaging methods unlikely choices for routine assessment of clinical fracture healing [30, 32].

2.6 SUMMARY

There are no reports in the literature of an effective method to monitor fracture healing accurately. Not only is the definition of a healed fracture unclear, current methods that are used to monitor this are unreliable and lack the quantitative detail necessary to optimise effective courses of treatment for patients. Whilst there are more advanced and accurate techniques available, these are yet to be validated and are impractical for every day use due to time and cost implications. Radiographs are readily available, cost effective, non-invasive, relatively harmless, quick to use and, importantly, are familiar to the medical profession. If their inherent imaging capabilities can be better harnessed in simple, cost effective techniques, they could provide better monitoring and quantification of fracture healing.

Chapter 3

Fracture Stiffness as an Indicator of Healing

3.1 INTRODUCTION

A variety of imaging methods to determine the density of the callus in a healing fracture have been reported. However, density *per se* does not relate to mechanical properties. It is therefore questionable how much information a density measure can give regarding the strength of a bone or fracture site [31]. Another property of bone that has been shown to be a good measure of fracture healing is stiffness [8, 22, 37, 38]. In order to explore this concept further, this chapter reviews the structural properties of bone and the mechanical engineering theory of bending and axial stiffness measurement. These concepts are then extended to monitoring the stiffness of healing fractures by considering previous studies, and the potential for further research is discussed.

3.2 PROPERTIES OF BONES

If researchers are to measure the stiffness of a fractured bone to determine state of healing, it is necessary to know what the properties of healthy bone are. A brief overview of the properties used to describe materials and of the structure of bone is presented.

3.2.1 Mechanical Analysis

There are three key aspects to mechanical analysis – the loads applied, the material they are applied to, and the geometry and support conditions.

Loads

When forces act on a body, they alter its size and shape. Although physiological loads are complex, there are three basic types of loading that make up most of them [39, 40, 41]. The first is torque where a twisting motion is applied to a beam. The second is axial loading where compression or tension are produced in the long axis of a beam. The final type is bending where forces are applied perpendicular to the long axis of a beam. Axial loading and bending are the loads of most interest in this discussion.

Material Properties

There are several basic response quantities that are used to describe the behaviour of materials in different load conditions [39, 40, 41, 42]. Two elemental descriptions regarding a material and the forces applied to it are stress and strain. Stress is the intensity of force acting on a particular plane and is measured as force per unit area in Pascals (Pa, N/m^2). Stress can be either normal to the plane of application, i.e. normal stress, σ, or tangential to it, i.e. shear stress, τ. If normal stress points away from the material (i.e. 'pulling') it is known as tensile stress whereas stress pointing towards the material (i.e. 'pushing') is compressive stress. Extensional strain, ε, is measured as the change in length in the direction of load divided by the original length and is dimensionless. If a contraction occurs, strain is negative, and if a stretch occurs, strain is positive. Shear strain measures the change in angle between two 'lines' in the material that were perpendicular before loading. Using these two basic properties a stress/strain curve can be plotted for any material. This curve has an elastic portion where, if the load was removed, the strain would return to zero. There is also a plastic section where, on removal of the load, a permanent strain is incurred. The value at which a material fails is the ultimate stress. Thus, this curve defines several further groups of properties.

The first group of properties are the Elastic Constants which are constants of proportionality relating stress and strain [39, 40, 41, 42, 43, 44, 45]. These constants may differ according to the direction in which testing is performed. There are different ways in which this can occur: anisotropy where the properties are different in every direction, orthotropy where the properties are different in three orthogonal directions, transverse isotropy where the properties are the same in every direction of a plane, and isotropy where there is no directional dependence. In this case, there are only two elastic constants: elastic (or Young's) modulus, E, and Poisson's ratio, υ. The elastic modulus of a material is the gradient of the stress/strain curve when loaded uniaxially, i.e. it is the ratio of axial stress to axial strain. The relationship (ratio) between stress and axial strain for a given material is linear up to a certain stress and the elastic modulus is the constant of this linearity, which

is an intrinsic property of each material. Poisson's ratio measures a material's ability to conserve volume when loaded, i.e. is the ratio of transverse contraction to axial extension. A material that deforms less for a given load is described as stiffer than one of the same structure that deforms more.

The second group are the viscoelastic parameters which relate stress and strain with time [43, 44, 45]. Viscoelasticity is a measure of how a material responds to the rate of loading. For a viscoelastic material lower strains (and higher elastic moduli) are obtained. The third group of properties are the plastic parameters which describe onset of yielding and post-elastic response such as permanent deformation, i.e. deformation that remains once a stressing load is released.

Geometry

The geometry of a material affects the way it will respond to different loads in different directions. The main measure of this in bending tests is the second moment of area, I, also known as the moment of inertia or area moment of inertia, which is a characteristic of the cross-section of a beam and is measured in mm^4. For axial loading, the geometrical measure of interest is cross-sectional area, A. This explains why stiffness relates to the structure of an object and not just its material properties [39, 40, 41, 42, 43, 44, 45].

3.2.2 Bone Structure

Bone consists of a fibrous, extracellular matrix (largely collagen) with cells such as osteoblasts, osteoclasts and osteocytes, and inorganic mineral salts consisting mainly of hydroxyapatite and calcium phosphate. Water makes up about 20% of bone, mineral salts 45% and organic substances 35%. The mineral salts are responsible for the strength and hardness of bone whilst the collagen matrix retains its structure [39, 43, 44, 45]. There are also two different types of bone tissue – cortical and trabecular (or cancellous) bone. Thus, a single bone is not homogeneous but made up of differing amounts of these two types of bone which have different mechanical behaviours. As these types of bone tissue change in proportion and microstructure during ageing and between different species and bones, so the mechanical properties vary accordingly [46].

Cortical bone is found largely on the surface and diaphysis of bones and is the more dense of the two types. It is considered to be an anisotropic material meaning its mechanical properties vary in different directions. In a study on whole human tibiae, Minns *et al.* found stiffness in the AP direction to be approximately one and a half times greater than that in the ML direction [47]. In a thorough mechanical analysis of 96 human tibial samples,

Hoffmeister *et al.* confirmed this and noted that it was most obvious in the axis parallel to the long axis of the tibia (a change of almost 100%) and less pronounced in the plane perpendicular to the long axis [48]. More recently, Shefelbine *et al.* also confirmed this finding. Using more sophisticated measurement techniques and FE models, they found the maximum rigidities almost twice as large as the minimum rigidities in a study on rat femurs [25]. This was explained by the 'form follows function' adaptation of the tibia to withstand loads in the AP direction, where they are experienced most commonly in the physiological setting [45, 47, 49]. Cortical bone is also a viscoelastic material, i.e. its strength and elastic properties are dependent on the rate and duration of applied loading [45].

Trabecular bone is generally found in the metaphyses and epiphyses of long bones, and is made up of porous trabeculae. It is difficult to characterise mechanically as its overall mechanical behaviour is due to the properties of each individual trabecule and its overall density. It can also be difficult to get samples of trabecular bone and to grip it without crushing it [44, 49]. Whilst the two types of bone are conventionally distinguished between, it should be noted that, as the bone is a continuous structure, the distinction between porous cortical bone and dense trabecular bone can be arbitrary and trabecular bone is continuous with the cortical shell [41, 45, 46].

In general, bone as a whole can be described as an anisotropic, viscolelastic structure that experiences plastic deformation in some conditions. The ultimate strength of bone depends on testing conditions, strain rate, bone age and mineral density [43].

3.3 BENDING AND AXIAL LOADING

Elastic modulus can be measured in two ways. The simplest is to load a specimen along its axis in tension or compression. This is perhaps the most fundamental and common way of testing a material's properties as it allows direct measurement of the material's stress/strain curve and load bearing capacity. Bending tests are also used, as deformations are often larger and therefore more easily measured. This section explores the engineering theory behind these two types of material loading.

3.3.1 Axial Loading

In engineering mechanics, loading a beam axially refers to applying either a compressive or tensile load to one or both ends of a material in the direction of the long axis. If the axial load is applied purely centrically, i.e. in the centre of the beam, then pure tension or compression results. If the load is applied slightly eccentrically, then a small bending moment is induced due to the fact that there is a lever arm between the force and the long

axis of the material. When the beam is loaded axially its length changes - it decreases in compression and increases in tension. Also, its area changes - it widens in compression and becomes narrower in tension. This is illustrated in Figure 3.1.

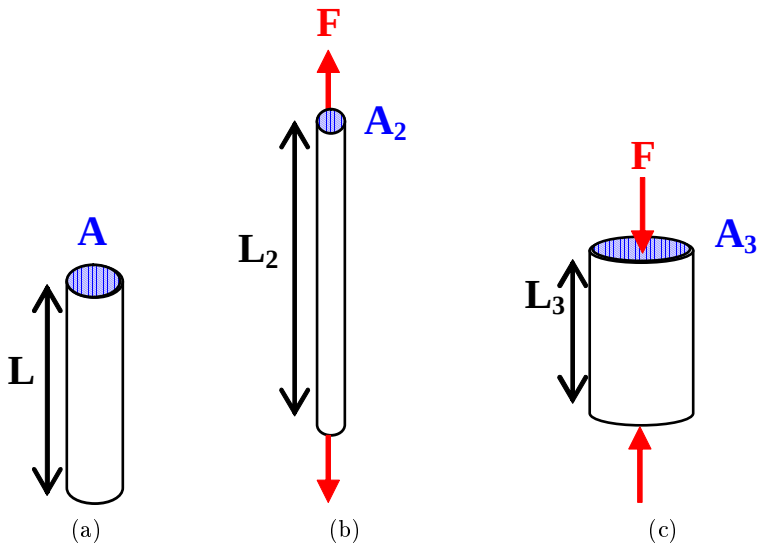

Figure 3.1: A beam a) unloaded, b) loaded axially in tension and c) loaded axially in compression.

The figure shows how, for a load F, the original cross-sectional area, A, decreases in tension (A_2) and increases in compression (A_3). Conversely the original length, L, increases in tension (L_2) and decreases in compression (L_3). From these changes, two strains are measurable in axial loading. The first is the strain along the loading axis

$$\varepsilon_1 = \frac{\triangle L}{L} \tag{3.1}$$

where $\triangle L$ is the change in length and L is the original length. In other words this measures the change in length due to the applied load. For tensile loading this is positive and for compressive loading it is negative. The second strain is the strain perpendicular to the loading axis

$$\varepsilon_2 = \nu\varepsilon_1 \tag{3.2}$$

where ν is Poisson's Ratio. Thus, the strain perpendicular to the longitudinal axis is related to the strain parallel to the longitudinal axis.

Stress is measured as the applied force on the cross-sectional area and changes as the cross-sectional area changes with deformation. Thus, stress and strain can be directly measured

using axial loading and can be used to derive a stress/strain curve. The curve is linear where the material properties are elastic and the gradient of this curve is E. This is illustrated in Figure 3.2.

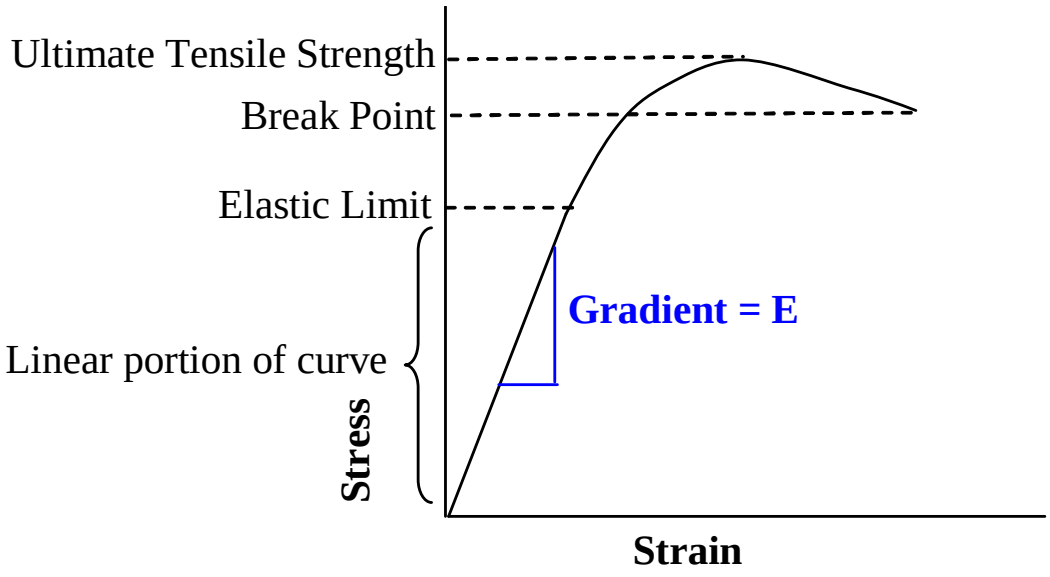

Figure 3.2: Stress/Strain curve showing measurement of the modulus of elasticity, E.

The axial stiffness, S_A, of a material is related to its elastic modulus [50]. It can also be simply defined as the force, F, divided by the induced change in length and is measured in N/mm where

$$\begin{aligned} S_A &= \frac{AE}{L} \\ &= \frac{F}{\triangle L} \end{aligned} \tag{3.3}$$

3.3.2 Bending

The bending of a beam refers to the application of a load perpendicular to the major axis. The forces applied to the beam cause internal stresses within it - there is tension on one side and compression on the other. These two forces create what is known as the bending moment. They decrease towards the centre of the beam where there is a neutral axis. In pure bending the neutral axis coincides with the beam axis. Analysis of bending in a beam is more complicated than the analysis of axial loading.

The theory used to analyse strains in a beam during bending is known as linear bending theory. Its main principle is that a plane perpendicular to the beam axis remains a plane and remains perpendicular to the axis after bending. Both the deformation and angle of curvature of a beam in bending can be calculated using this theory and knowledge of the material and cross-sectional properties of the beam. Composite beam theory can be used to make calculations where two or more materials are involved [40, 41, 42, 51, 52, 53].

The stiffness of the beam in linear beam theory is EI, measured in $\mathrm{Nm^2}$. However, in composite beam theory it becomes [40, 41, 42, 51].

$$EI_{xx} = \int_A E(x,y)x^2 dA \tag{3.4}$$

where $E(x,y)$is the two dimensional stiffness matrix. The bending moment, measured in Newton metres (Nm), can be calculated as

$$M = \frac{EI}{R} \tag{3.5}$$

where M is the bending moment, I is the second moment of area and R is the radius of curvature of bending. This shows that the deformation a beam undergoes during bending depends on its geometry, material properties and the force applied. It is important to note that the bending moment experienced along the length of the beam depends on the way in which force is applied to it. Wherever the force applied to a beam changes discontinuously, e.g. at a point of application of load or at a support, the expression for bending moment changes.

The bending moment is related to the deflection by the equation

$$M = EI\frac{d^2v}{dx^2} \tag{3.6}$$

where v is vertical deflection and x is distance along the beam measured from the chosen origin [40, 41, 42, 51].

There are two common bending configurations used when testing beams: three and four point bending.

Three Point Bending

Three point bending is commonly used to exert a bending moment on a beam due to its simplicity of set up. The configuration is shown in Figure 3.3 (a) where the beam of length L is held on supports at either end and a force, F, is applied at the centre. A diagram illustrating the change in bending moment across the length of the beam is shown in Figure 3.3 (b).

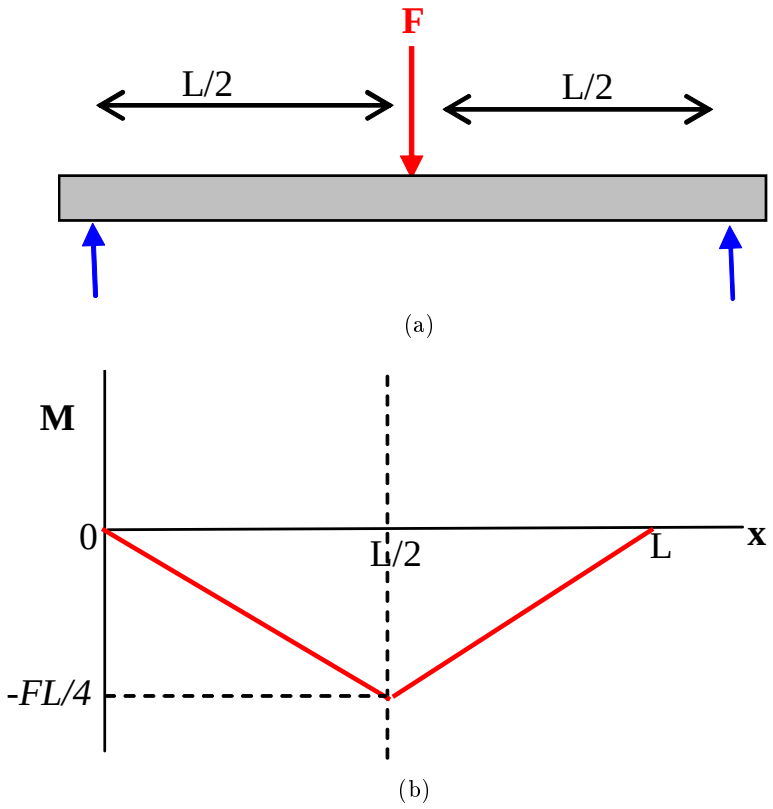

Figure 3.3: a) Three point bending configuration and b) bending moment diagram.

It can be seen from the diagram that at the point of load application, $L/2$, the bending moment changes abruptly. It can also be seen that the bending moment varies throughout the length of the beam. For three point bending, the bending moment is described as

$$M = -\frac{Fx}{2} \tag{3.7}$$

where F is the applied force and x is the distance from the origin.

The maximum bending moment occurs at the centre of the beam and is $M = -\frac{FL}{4}$. At this point the maximum deflection occurs and is

$$\delta = \frac{FL^3}{48EI} \tag{3.8}$$

In three point bending the maximum bending moment is only attained at a single point, the point where the force is applied, and decreases as distance from this point increases [53].

Four Point Bending

Four point bending is more complicated and is illustrated in Figure 3.4 (a). As can be seen in the figure, there are two supporting loads on either end of the beam. However, there are also two symmetrically placed points of application of the force. This creates a constant bending moment between the two force application points, as shown in Figure 3.4 (b) [40, 41, 42, 52, 51, 53].

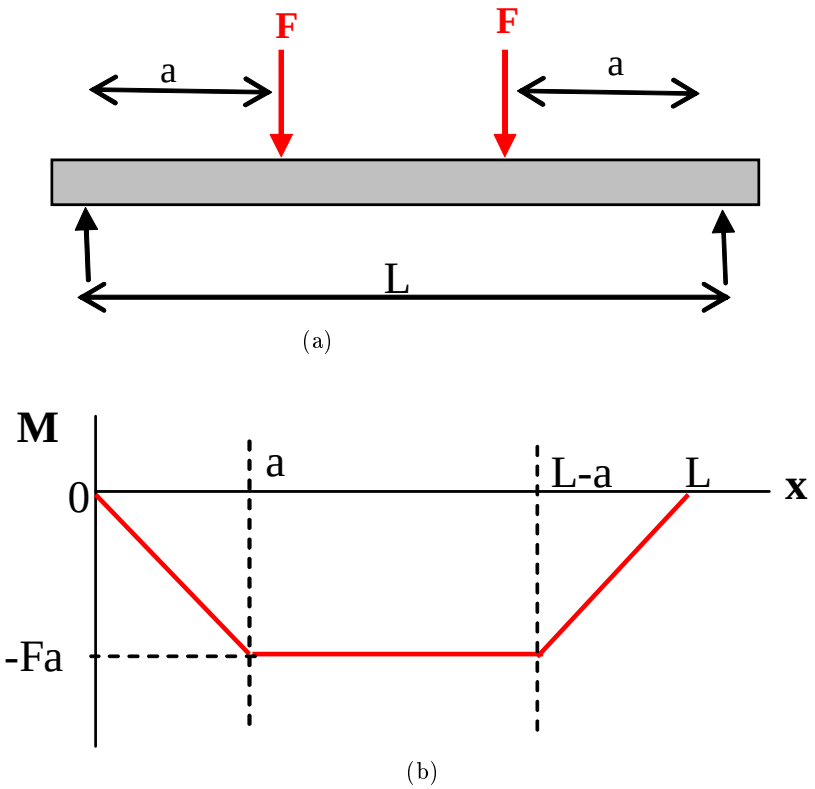

Figure 3.4: a) Four point bending configuration and b) bending moment diagram.

There is a constant bending moment in the portion of the beam between the application of load. The expression for the bending moment in four point bending is given as

$$M = -Fx \tag{3.9}$$

where x is the distance along the beam from the origin. Between the two loads this becomes $M = -Fa$ and causes the maximum deflection which is

$$\delta = \frac{FA(3L^2 - 4a^{2)}}{24EI} \tag{3.10}$$

Bending Stiffness and Elastic Modulus

A stress/strain and a load-deformation curve, which shows millimetres of deformation and the force applied, can be plotted. The information from these graphs can be used to calculate the bending stiffness, S_B, of a beam which relates the applied bending moment to the resultant deflection of the beam. Bending stiffness is the product of the elastic modulus and the second moment of area of the beam cross-section,

$$S_B = EI \tag{3.11}$$

Thus, the elastic modulus gives an indication of the elasticity of a beam and the bending stiffness describes its resistance to bending.

In clinical literature, the term bending stiffness is used to describe a variety of measures such as Nm/degree [10, 21, 38, 54, 55, 12, 56], Nm/mm [57], a stability ratio (deflection/bending moment) [18, 58, 59, 60] and rigidity ratio (test/contralateral) [15].

3.3.3 Measuring Stiffness in Bone

As described previously, bone is a complex structure and there are difficulties in assessing its mechanical properties precisely. This is illustrated in Table 3.1 which shows the values obtained for elastic modulus by different research groups.

Table 3.1: Comparison of values for elastic modulus in different studies.

Researcher	**Bone**	**Age**	**Elastic Modulus**
Hoffmeister *et al.* [48]	Tibial cortical, parallel to long axis, ultrasound measurement		20.9 GPa
Hoffmeister *et al.* [48]	Tibia, perpendicular to long axis		11.8 GPa
Ding *et al.* [61]	Tibial trabecular, in compression	Young (16 – 39 years)	654 MPa
Ding *et al.* [61]	Tibial trabecular, in compression	Middle (40 – 59 years)	829 MPa
Ding *et al.* [61]	Tibial trabecular, in compression	Old (60 – 83 years)	613 MPa
Keller *et al.* [46]	Femoral Cortical, Bending Strength	62 years mean	178.8 MPa
Keller *et al.* [46]	Femoral Cortical, elastic modulus	62 years mean	11.2 GPa
Choi *et al.* [62]	Tibial subchondral, three point bending	60 years	1.2 GPa
Choi *et al.* 1990 [62]	Tibial trabecular		4.6 GPa
Choi *et al.* 1990 [62]	Tibial cortical		5.4 GPa

As can be seen from the table, a wide range of elastic modulus values have been reported. These variations can be attributed to differences in testing methods, the use of whole bones, bone samples and machined samples, different patient groups and different measurement techniques. Choi *et al.* particularly stress the role that sample size has on influencing measurements [62]. This is due to the inhomogeneity of bone: values for cortical and trabecular samples differ and, as samples decrease in size, microstructure starts to play a

more important role. They repeated the important point made by Reilly and Burstein in their landmark paper on the properties of human cortical bone that the bone is an entire structure and that analysing different parts separately may introduce a misunderstanding of the mechanical effectiveness of the bone as a whole [43]. However, analysing the bone as a whole requires taking into account the complex structure and cross-section of the bone. These points are reinforced by many researchers into bone properties [44, 45]. Furthermore, all these experiments were conducted on extricated whole bones or bone samples. Minns *et al.* point to soft tissue contributions to the bending stiffness of bone [47]. This plays an important role in the bending stiffness that can be measured in patients. Additionally, the effect of ageing on bones has been widely recognised as correlating with a reduced stiffness value once middle age is reached. This means that bones at different levels of maturity will display different properties [43, 45, 61].

Keller *et al.* illustrated some of the difficulties in determining the material properties of bone [46] . They performed a study of the material properties of 155 femoral cortical bone samples loaded in four point bending in the AP direction and they calculated the elastic modulus using the following formula

$$E = \frac{1}{2}\frac{Fa(3l^2 - 4a^2)}{\delta b h^3} \tag{3.12}$$

where F is force, δ is deformation, l is distance between supports, a is distance from support to point of load, b is the width and h is the thickness of the specimen. They noted a major assumption with the use of Equation (3.12), namely that E is the same in tension and compression. However, the tensile and compressive characteristics of bone are in fact asymmetric. This means that the elastic modulus of bone as determined from bending tests is not a true material parameter. Other investigators echo this, warning that most bending equations are developed for isotropic, homogeneous engineering materials and since bone fulfills neither of these qualities calculations are only an estimate [62].

3.3.4 Stiffness versus Strength

An important distinction must be made between the stiffness and the strength of a material. Stiffness is related to the elastic modulus and is a measure of how much a material changes its size and shape in response to a force. It is affected by the geometry of the material. Strength is a measure of how much force is needed to damage or break a material. Thus, a material can have any combination of strengths and stiffnesses. For instance it can have a high strength and low stiffness (e.g. elastic band), a low strength and high stiffness (e.g. a biscuit), a high strength and high stiffness (e.g. concrete) or a low strength and low stiffness (e.g. jelly) [40, 41, 42, 51, 52, 53].

3.4 STIFFNESS AND FRACTURE HEALING

The stiffness of healing bone is widely regarded as the 'gold standard' in fracture assessment [37, 63]. Moorcroft *et al.* stated *"..the mechanical properties of the fracture..are of most importance since the primary function of long bones is weight bearing."* [38, p. 776]. This supports the idea that direct measurement of the stiffness of the healing callus will result in the most reliable measure of the functional capabilities of the bone in question. This further extends to the stiffness of potentially osteoporotic bones. Wade and Richardson clarify this, stating that healing is the return of function, and the function of the bone is the resistance to stress which is measured by elastic modulus (i.e. a measure of stiffness) [22].

To investigate this, Floerkemeier *et al.* measured the correlation between maximum torsional moment and torsional, bending and compressive stiffnesses in the fracture callus of sheep [57]. They found that all three can be used to predict the load bearing capacity of fracture callus. Chehade *et al.* performed a similar study on tibial sheep fractures [23]. They found a strong correlation between stiffness and strength regardless of loading pattern, and these results have been echoed by other researchers [20]. However, both groups as well as other authors cautioned that as healing progressed and bone regained the higher stiffness values of intact bone, the correlation was not as good [8, 23, 35].

These studies indicated that the monitoring of bone stiffness can be an effective tool in determining its strength in the early stages of fracture healing and that mechanical stiffness is an important characteristic of healing bone tissue. However, in a stiffness ranking study by Webb *et al.* it was shown that surgeons performed no better than medical students in ranking stiffness correctly, putting the patient at a high risk of re-fracture (see Section 2.3) [11]. This indicates the need for a quantitative method to assess fracture stiffness.

3.4.1 Direct and Indirect Measurement with an External Fixator

The concept of prediction of load bearing capability by measuring both axial and bending fracture stiffness has been applied to fractures treated with external fixators. Two methods have been used, direct and indirect stiffness measurement [55, 56]. In direct stiffness measurement the method involves temporarily removing the fixator and attaching electrogoniometers to the fixator pins across the fracture site. In the case of bending stiffness in tibial fractures, the heel of the patient is placed on a force plate. A force is applied by hand directly to the fracture site, perpendicular to the long axis of the bone, and the angular displacement at the fracture site is measured using the electrogoniometers. The applied force is recorded as the force measured on the force plate. 'Stiffness' is calculated as the

moment arm (Nm) divided by the angular displacement (degrees) to provide a reading in Nm/degree . This is essentially a three point bending configuration and an example of the equipment used by Richardson *et al.* is shown in Figure 3.5 [55, p. 390].

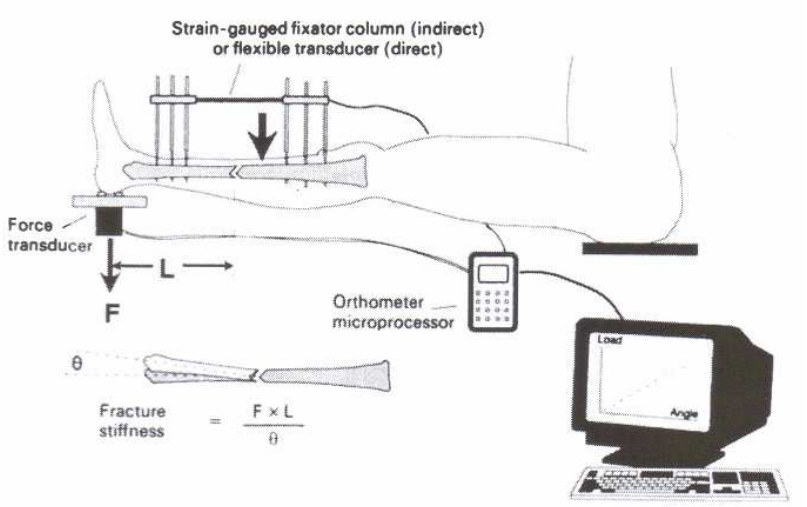

Figure 3.5: Application of load at the fracture site in externally fixed tibial fractures.

Dwyer *et al.* performed a study on distraction osteogenesis patients to determine callotasis stiffness. They found direct stiffness methods accurate and useful in monitoring patients' progress [56]. However, other authors have noted that the need to remove the fixator in order to perform the test is inconvenient. They also found that potential errors are introduced if the bone screws are loose [10, 21, 55].

Indirect measurements of both axial and bending stiffness have been made in the externally fixated tibiae of patients [10, 54, 63, 64, 65]. In indirect measurement, either an AP bending force or a compressive axial force have been applied to fractures with the fixator attached. Strain gauges attached to the fixator columns were used to measure the movement across the fixator bars and thus the stiffness of the fracture indirectly. This was possible since the stiffness of the fixator bars was constant. However, during the course of healing the stiffness of the fracture site increased. Any changes in measurement for a constant load were due to increased load being taken by the fracture site. For bending stiffness, the load application was similar to that shown in Figure 3.5 and measurements were made in Nm/degree. In the case of axial stiffness measurement in tibiae, the patient was in a sitting position with their foot resting on the force plate. A downward force was applied to the patient's knee and the electrogoniometers recorded the resulting displacement at the fracture site while the force plate recorded the applied force. Stiffness was calculated as the force divided by the displacement at the fracture and was measured in N/mm.

Indirect bending stiffness measurements were made on a small group of patients with humeral neck fractures treated with external fixation. Measurements of the deformation were seen to decrease as healing progressed except in a case where the fracture went on to non-union. These results indicated that the tests could be used to monitor healing changes [66]. In their well regarded study on 120 patients, Richardson *et al.* performed bending stiffness measurements on externally fixed tibial fractures [54]. They found that a stiffness of 15 Nm/degree indicated a level of healing advanced enough to remove the fixator. In a later study, they confirmed this and showed that the method provided superior guidance for fixator removal than conventional methods, avoiding refracture completely whilst decreasing the average time of fixator attachment. They also suggested its usefulness in predicting abnormal healing patterns. In addition, they found the indirect measurement of stiffness superior to the direct method [55].

In an earlier study, Evans *et al.* performed compressive axial stiffness tests on a similar group of patients [10]. They found that axial stiffness changes followed a similar pattern to bending stiffness and that fixator removal was considered safe at a stiffness of 1000 N/mm. Schmickal *et al.* performed similar tests in patients treated with distraction osteogenesis [64]. They measured compressive axial strength using partial weight bearing and AP bending stiffness through contraction of the foot flexors. They found the device useful in advising treatment strategy and alerting to slow healing. However, they emphasised that absolute measurement values must not be used but rather percentages of initial values should be monitored. This approach was also used by Kristiansen and Borgwardt [66].

The precision and accuracy of indirect measurements of fracture stiffness were assessed using Aluminium rods. It was found that in perfect set up conditions the error was below 10% of the true stiffness value but when set up differences were introduced this increased to 22% [12]. Tests in 33 distraction osteogenesis patients indicated that, in compressive testing, higher loads resulted in higher load-share ratios and that muscle interaction altered the indirect test outcome considerably. This illustrated that errors were easily introduced through testing method and patient interaction. Both results indicated that care must be taken when using the apparatus if serious errors are to be avoided. In both direct and indirect methods, stiffness in healing fractures has been shown to increase exponentially with time [55, 56, 63, 64].

Experiments with direct four point bending in Aluminium models have also been performed and found to give effective stiffness outputs. These have been extended to measurements on fractured sheep tibiae *in vivo* and the measurements were found to be sensitive to changes in stiffness and provide useful predictive value in terms of course of healing. Four point bending has also been found to be more robust to differences in callus location [35, 67].

Humeral axial loading models testing plate fixation have been made in cadaveric, Sawbones and epoxy models. All systems used compressive testing with loads ranges of 5 – 250 N and 10 – 100 N [68, 69, 70]. Beaupre *et al.* modelled an externally fixed humeral fracture using a plexiglass tube and neoprene 'fracture site' [71]. They applied a tensile load using hanging weights and found that, although displacements were small, they increased for neoprene of decreasing stiffness and therefore provided an indication of material properties.

3.4.2 Factors for Consideration

Moorcroft *et al.* stated that there were many factors to consider when taking stiffness measurements [38]. Firstly, a uni-planar (i.e. sagittal only) bending stiffness measurement may not detect the weakest plane and was therefore not a reliable indicator of fixator removal. Wade *et al.* confirmed this showing that patients with a 15 Nm/degree stiffness in one plane may have a much lower stiffness in another, thus causing a risk of re-fracture if the fixator was removed. Several authors supported this conclusion [9, 21, 54, 64]. The variation in readings was explained by the cross-sectional asymmetry of bones [31]. Some variation could also be explained by the presence or absence of an intact fibula, although authors investigating this have found the fibula's contribution to be less than 1.5% [24].

Authors also recommend consideration to be made of the viscoelastic nature of callus as well as the fact that fracture stiffness and strength increase at different rates. Since the stiffness of callus is dependent on loading rate this should always be made consistent and should be quoted with any given stiffness measurement [21, 38]. Chehade *et al.* conducted an investigation into the stiffness and strength relationship in fractured sheep tibiae using four point bending [23]. They found that at higher stiffnesses, stiffness changed according to load and loading rate, and that the correlation between strength and stiffness was only good at lower stiffnesses. They also found that strength and stiffness increased at different rates, especially at higher stiffnesses, and recommended that stiffness only be used to monitor strength until it reached about two thirds of its normal value. They reported that sequential monitoring, rather than isolated measurements, were necessary to provide progression towards a defined end point. Overall they found that stiffness could never be used as a measure of strength in the latter stages of healing. Similarly, Roberts and Steele performed a beam theory analysis on the accuracy of stiffness to provide healing information [35]. They found that for three point bending, stiffness increased more quickly than strength and recommended that stiffness was only used to monitor healing until it reached half the value of intact bone. However, as Richardson *et al.* pointed out, although a healing bone that achieves the stiffness of a healthy bone has only half its strength, it is stiffness which is the measure of functionality and thus the most clinically useful variable [54]. Chehade *et al.* view strength as the important variable and therefore find systems

which measure stiffness inherently limited [23]. Unfortunately, since strength is usually measured as load before failure, it is probably not practical to measure this in the clinical situation [54, 57].

Richardson *et al.* add further suggestions for improving the use of stiffness measurements to inform fracture treatment. They suggested consideration of the size of a patient when recommending fixator removal, heavier patients being advised to wait past the 15 Nm/degree healing point [55]. Simpson *et al.* and other researchers echo this point and in a mathematical simulation demonstrated that the value of 15 Nm/degree may not be an appropriate measure of healing for bones that are of a different size to an average adult tibia, and in bones of different ages and with different lengths of callus [35, 72].

A further improvement on the more commonly used clinical system to measure bending stiffness, which used three point bending, would be to use a four point bending application [6, 35, 41, 67]. Four point bending applied to the fracture would provide constant bending between the two inner fulcra, i.e. at the fracture site, providing a more accurate force application which would be unaffected by callus location. It is also less dependent on applying the load directly to the fracture site as well as being potentially more comfortable for the patient as it requires less direct force on the painful fracture area

Sources of error in axial stiffness measurements are similar to those in bending stiffness measurements. Aarnes *et al.* investigated the effect of load magnitude on measured stiffness and found that higher loads produce higher stiffness readings [63]. It is therefore important to ensure a consistent load throughout patient evaluations. Other investigators found that axial compressive loads are often applied a small distance from the centre of the longitudinal axis of the bone. This results in a small bending moment as well as axial compression, which is difficult to account for when making axial displacement measurements [41, 68]. Loading bones in tension, rather than compression, may reduce this effect. In a FE model of a fracture loaded in tension, Beaupre *et al.* found that 95% of the force passed through the fracture site [71].

The consideration of the effect of soft tissue is also important. Aarnes *et al.* showed that the axial force of tibiae in transducers can be increased by up to 5 N due to muscle interaction, which is enough to alter the calculated callus stiffness considerably, especially towards the end of healing [63]. They found this effect particularly noticeable when tests were performed with the patient standing as opposed to sitting. They recommended that loading was limited to reduce involuntary muscle contractions due to pain. Whilst difficult to quantify and control for, involuntary muscle interaction and other soft tissue effects affect stiffness measures and healing estimates in this type of assessment [25].

3.5 NON-EXTERNALLY FIXED FRACTURES

There is a strong and well accepted background in the use of stiffness as measure of fracture healing. However, there are several limitations with current methods. When measuring bending stiffness, a three point bending moment is applied whereas a four point application would provide a more predictable moment across the fracture site. A further problem with current bending stiffness methods is that, despite recommendations in the literature, most are only performed in one plane thus giving an incomplete picture of fracture stiffness. In axial stiffness measurements, the addition of a lever arm when loading off centre introduces some bending as opposed to pure axial load. Furthermore, measurements have concentrated on tibial fractures and are prone to errors due to muscle interactions and the differences between measurements made with the patient sitting versus those made when standing.

However, the most obvious problem with current methods is that they can only be applied to fractures treated with external fixators. Furthermore, direct stiffness measurements require removal of the frame, which cannot be done in the early stages of healing. This means that, as yet, no bending stiffness information is available for fractures not treated with an external fixator or for fractures in the early stages of healing being measured directly [15, 22]. This leaves a large group of patients to be monitored with conventional and inaccurate techniques. Studies show that fixation with an IM nail is up to four times less stiff in bending than fixation with a unilateral fixator, indicating the possibility that better bending stiffness values could be obtained with internally fixed fractures [73]. Coupled with this the use of force plates and electrogoniometers in current techniques, which are not routinely available in the clinical environment, seems to have reduced the widespread use of the existing bending stiffness technique to assess fractures. Tensile axial loading of fractures is potentially more comfortable for the patient and would allow limbs other than the tibia to be studied. Thus, there is room for expansion in the use of stiffness to assess fracture healing.

Some authors have noted the potential of stiffness to monitor fracture healing and also the limitations of an external fixation only measurement technique. In a small study of 11 patients, Shah *et al.* [24] performed a three point bending test on conservatively treated fractures using the same concept as Richardson *et al.* [54, 55] and Evans *et al.* [10]. A force, F, was applied at the tibial tuberosity, a distance y from the fracture. This force was measured by a load transducer at the ankle. The deflection at the fracture site was measured using an electrogoniometer to provide an angular deflection, θ. Stiffness, S, was calculated as

$$S = \frac{Fy}{\theta} \tag{3.13}$$

and measured in Nm/degree as in the Richardson *et al.* [54, 55] and Evans *et al.* [10] method. They used weights of approximately 5 kg on most patients and controlled for soft tissue involvement by asking patients to relax their muscles during testing and with the application of an elasticated cast sock. Readings were normalised to the contralateral leg as they felt the system was not accurate enough to provide direct stiffness readings. They found one of their major sources of error to be the attachment of the electrogoniometer to the soft tissue. Overall, their method correlated with the clinical image of healing and was useful in ensuring appropriate treatment methods for those with suspected delayed or non-unions. There were no reports in the literature of compressive or tensile axial stiffness measurements in fracture patients not treated with an external fixator.

3.5.1 Measuring Stiffness using X-ray

In 1984, Edholm *et al.* reported the use of a non-invasive radiographic measurement of the deflection of fractures treated with cast immobilisation [60]. In this method, patients' fractured tibiae were removed from their casts and X-rayed in the AP projection. A weight to induce a bending moment at the fracture was then applied to the leg at the ankle, directed medially, perpendicular to the longitudinal axis of the tibia and in the coronal plane. This system is shown in Figure 3.6 [18, p. 228]. It can be seen that this was a simple system that essentially applied a displaced bending moment to the fracture site in a three point bending configuration.

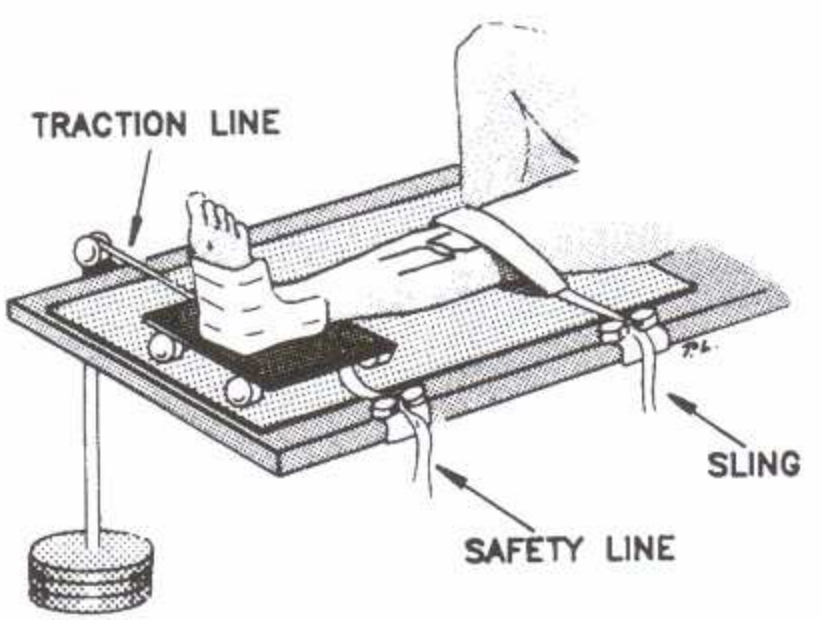

Figure 3.6: Apparatus used by Hammer *et al.* to apply load under X-ray in conservatively treated fractures.

The deflection caused by the weight was measured using a 'Shift Comparator' to align the two radiographs. This gave a measure of the angle of deflection with an accuracy of 0.19 degrees. The procedure was started with a 2 kg weight which was increased if, and until, the deflection exceeded 0.5 degrees, the weight exceeded 8 kg or the patient experienced pain. They also assigned a measure of the stability of union, the 'Deflection Ratio', which took into account the bending moment, deflection angle and patient's body weight. They found that when a patient had a deflection ratio of below 0.08, then it was probably stable. Using this method, they found it successful in recommending full weight bearing, monitoring healing, and predicting disturbances in healing. They also performed tests after loading to assess any potential effect of the measurement device on the patient, callus and subsequent healing. They found that the deflection produced no lasting deformation and did not interfere with the course of union.

In subsequent studies using the same measurement device on patients of varying age treated with cast immobilisation, external fixation and internal nailing, Hammer *et al.* [18, 58, 59] concluded that it was possible to define normal union, to differentiate between delayed union and true non-union, and to avoid unnecessary surgical procedures where increases in stability could be shown in suspected cases of non-union. They also used the system to compare to the accuracy of conventional radiographic methods and found it superior, with conventional radiographic methods being generally inconclusive.

A precedent for a useful means of measuring bending stiffness, and thus having an accurate measure of healing, has been set by these studies. Despite the somewhat cumbersome methods of applying loading, and especially of measuring angular deflection, Hammer *et al.* [18, 58, 59] and Edholm *et al.* [60] have achieved a high level of accuracy and clinical usefulness. No studies into similar methods have been conducted subsequently, the radiographic method being abandoned for the electrogoniometer method described in Section 3.4.1. These results indicate that, with current improvements in both radiographic quality and digital image analysis techniques, the method of Hammer *et al.* [18, 58, 59] and Edholm *et al.* [60] could be re-applied to fractures treated with a variety of stabilising devices and in both bending and axial configurations. Despite the potential to monitor stiffness changes using X-ray, no examples of this in axially loaded fractures have been identified.

3.6 SUMMARY

It has been reported that even with accurate laboratory techniques, researchers have found a wide range of values for the stiffness of human bone. It has also been noted that due to the anisotropy and inhomogeneity of bone, traditional engineering equations are not entirely accurate when used to calculate bending stiffness or elastic modulus. Adding these uncertainties to the clinical environment, where factors such as patient size, muscle strength, soft tissue involvement and testing inconsistencies play a role, adds further errors to the measurement. However, the potential of stiffness to provide at least intra-patient comparative data during the healing process has been shown and consistency in experimental results supports this concept. Furthermore, initial work with the use of X-rays to measure bending stiffness in fractures not treated with an external fixator showed that this method could be a simple, non-invasive way to monitor fracture healing without the need for complex measurement equipment.

Chapter 4

X-ray Analysis of Fracture Healing

4.1 INTRODUCTION

Radiographic analysis is one of the three common techniques used by surgeons to assess fracture healing due to its low cost, availability and flexibility. It is heavily relied upon despite its proven inaccuracies [74]. Several authors have attempted to improve the quality and reliability of radiographic images and to use them to attain more useful, quantitative information. The advent of digital radiography has increased the possibility of quantitative bone healing assessment due to improved detector efficiency and digital processing capabilities [28]. This chapter reviews the basic physics of X-ray imaging, together with sources of image inaccuracies, and this is further extended to Digital Radiography. The use of an Aluminium step wedge to provide calibration is also discussed.

4.2 PRINCIPLES OF RADIOGRAPHY

4.2.1 Production and Beam Quality

Roentgen discovered X-rays in 1896 and soon afterwards X-rays began to be used for medical diagnostic imaging [75]. When X-rays pass through a body they are attenuated to different extents, thereby forming a 2D 'shadow'. When the transmitted X-rays are converted to a visible image they provide useful medical information. X-rays result from the conversion of kinetic energy attained by electrons accelerated under a potential difference (voltage) into electromagnetic radiation. They are electromagnetic radiation at high energies and short wavelengths which means they behave more like particles than waves and interact with other particles through collisions that transfer energy. In diagnostic imaging, the electron

volt (eV) is used to describe the energy of the X-ray and 1eV is equal to the kinetic energy gained by an electron in a vacuum accelerated by a potential difference of 1V and is equal to 1.6 x 10^{-19} J.

Generation of X-rays occurs in three steps [76]. First, free electrons are supplied by the heated filament of the X-ray beam emitter. In the second step, the generator supplies a high voltage which is applied to the cathode and anode in the X-ray tube causing the negative electrons to accelerate towards the positive anode. The anode is generally made of tungsten and can take one of two configurations: fixed geometry or the more common rotating anode which provides better heat dissipation. The tube current (measured in milliamperes, mA) expresses the number of electrons travelling between the electrodes. Each electron attains a kinetic energy (in keV) equal to the applied tube voltage. The amount of time the electrons are produced for is the exposure and is measured in seconds (s). Tube current and exposure time are measured together in milli-ampere seconds (mAs). The third step in X-ray production occurs when the electrons interact with the anode or target. The kinetic energy that is lost is principally lost as heat and the rest is converted to electromagnetic radiation in a process known as bremsstrahlung. The resulting X-ray energy is determined by the energy level at which the interaction occurs. This results in a polyenergetic spectrum of X-rays which is emitted from the target surface in the area known as the focal spot. A collimator, consisting of adjustable lead shutters, is adjacent to the focal spot and is used to shape and size the beam incident on the patient and detector.

4.2.2 Interactions and Image Formation

Primary radiation is defined as the X-rays that are transmitted through a patient without interaction. However, some X-rays are removed from the beam through attenuation by absorption and scatter. The most basic type of interaction, Photoelectric Absorption, occurs when the X-ray photon transfers its energy to an electron in the inner shell of an atom. In tissues this results in the incident photon depositing all of its energy, i.e. total absorption. As well as absorption, there are two types of scatter that can occur. In Rayleigh Scattering the incident X-ray photon is deflected off an electron with no loss of energy. The X-ray photons are scattered at a small angle and there is a low probability of this happening in soft tissue. However, in Compton Scattering the incident photon transfers some of its energy to the electron and is then deflected from the atom at an angle which can range from 0 degrees to 180 degrees. These scattered X-rays can affect image quality by reducing contrast.

Due to these interactions, there is a difference between the incident (N_x) and transmitted (N_o) X-ray beam. This relationship is exponential depending on the thickness of the material and is

$$N_x = N_0 e^{-\mu x} \tag{4.1}$$

where μ is the linear attenuation coefficient (cm^{-1}) and represents the probability of attenuation per centimetre of a material. μ is dependent on the incident X-ray energy and the physical density and atomic number of the material the beam passes through. The mass attenuation coefficient, μ/ρ, normalises the linear attenuation coefficient by the density of the material and is measured in cm^2/g. Radiation dose is a measure of the absorbed energy per unit mass, in Joules/kilogram (J/kg) which equals 1 Gray (Gy) [77].

4.2.3 X-ray Image Inhomogeneities

There are several factors in the production and transmission of X-rays which create intensity variations in the resulting image which are not solely due to attenuation by the body of interest. Some of these are easily measured or predicted, whilst others are anomalous.

Beam Hardening

As the X-ray beam passes through attenuators of increasing thickness a process called beam hardening occurs. This means that X-rays with lower energies are attenuated more than X-rays with higher energies. Therefore, a beam passing through a thick attenuator will result in a greater proportion of high energy photons than the same beam passing through a thinner attenuator. Beam hardening occurs to a greater extent in higher density objects [77].

Magnification and Path Length

X-rays emerge from a single point of the X-ray tube and the resulting X-rays diverge into a fan shaped beam. This results in blurring of the edges of objects as the X-rays hit them at an angle (the resulting blur is known as the penumbra). It also results in the magnification of some objects, especially when the detector is placed far from the object. Furthermore, beams at the edge of the image travel a longer path length from the source than those in the centre, resulting in a reduction in X-ray intensity on the edges of the image. All of these effects are stronger the further from the centre of the beam the object of interest is placed [77].

Anode Heel Effect

The anode heel effect is an inhomogeneity in intensity and is a smoothly varying function of spatial location. It is due to the angle of the source so that X-rays emerging from the anode side of the source travel through a greater thickness of target material, and are therefore attenuated more, than those emerging from the cathode side. It causes a drop in the X-ray intensity on the anode side compared with the cathode side and means that the relative brightness of an object is dependent on its position within the field of view. This is illustrated in Figure 4.1.

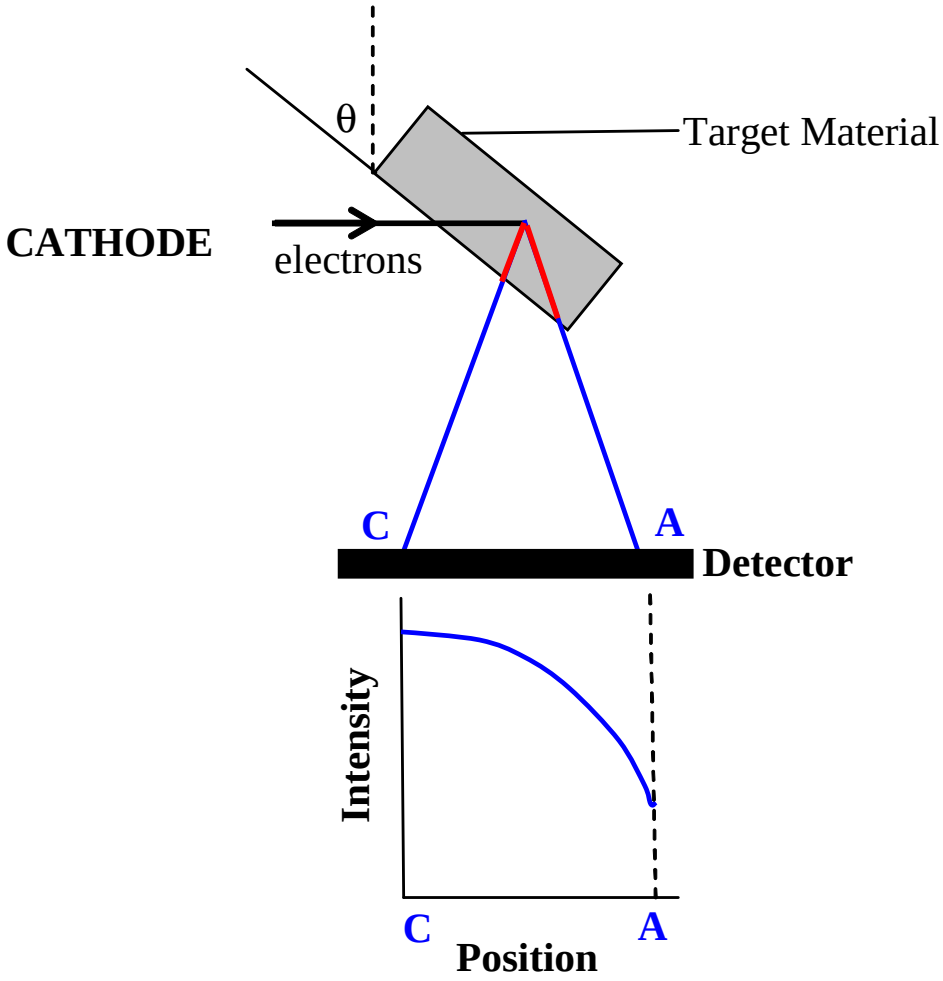

Figure 4.1: Diagram illustrating the anode heel effect for a target at an angle θ showing the change in intensity on the detector from cathode to anode side.

The figure shows how electrons on the cathode side, C, travel through less target material than those on the anode side, A (illustrated in red). This results in a variation in intensity on the detector which can be seen in the graph. However, due to beam hardening effects, the radiation from the anode side is more penetrating than that on the cathode side of the beam and so the heel effect can be less noticeable at depths within an object due to attenuation being balanced by penetration. The effect is predominantly in the anode-cathode direction with the maximum difference between anode and cathode ends being estimated at approximately 45%. Variations in X-ray intensity perpendicular to the anode-cathode axis are small and generally considered not significant [77, 78, 79, 80, 81]. The anode heel effect increases with large field sizes at short focal object distances and as target angle decreases, as well as in older X-ray tubes due to 'pitting' of the anode [81, 82].

Scatter Degradation

In the ideal case, only primary radiation contributes to the formation of an image. However, at most diagnostic imaging energies a large amount of attenuation is due to Compton scattering and this reduces subject contrast adding background signals which are not representative of patient anatomy. Air and detector scatter also contribute to background inhomogeneities, resulting in more scattered radiation in the centre of the field than on the outer edges. The amount of scatter and its degrading effect increases with increased object thickness and field size [77]. In a Monte-Carlo (repeated, random) simulation of scatter, Boone and Seibert found the Point Spread Function (PSF) of scatter to be approximately Gaussian in distribution [83]. It was highly dependent on the imaging parameters used and a function of object thickness, object-to-detector distance and X-ray spectrum. An important measure of the effect of scatter on an image is the scatter-to-primary ratio (S/P) which indicates the proportion of X-rays scattered compared to the proportion transmitted as primary radiation.

4.2.4 Image Detection

X-ray images are formed by the detection of transmitted X-rays and conversion into a signal which is used to produce a 2D image. However, this process is prone to losses of signal and thus is not 100% efficient. The efficiency of X-ray detectors can be described in three ways. The first is Quantum Detection Efficiency (QDE) which is the probability of detecting the radiation incident on the detector at a given energy. The second is Conversion Efficiency (CE) which is the transfer of this energy into an amplified signal used to create the X-ray image. Finally, a measure of the overall detector efficiency is called Detective Quantum

Efficiency (DQE). It measures the efficiency with which information is captured, i.e. the signal-to-noise ratio achieved in the image as compared to that incident on the detector.

Analogue data are those which are continuously variable. The screen film cassette is the most commonly used analogue X-ray detector. In this analogue system, incident X-rays are converted to light by an intensifying luminescent screen which has direct contact with a light-sensitive film. When processed, this film contains a 2D image representing the concentration of light in different parts of the image which in turn corresponds to the X-ray attenuation. In analogue systems, the grey scale display range of the image is dependent on the response characteristics of the film and the chemical exposure methods used. Once produced, this cannot be changed [77].

4.3 DIGITAL RADIOGRAPHY

Although screen film systems are still used, over the last few decades X-ray systems which form X-ray images without the use of films and chemical exposure have been implemented clinically. This is due to the limits on the information that can be captured by film which include fixed dose latitude, fixed non-linear grey scale responses and limited potential for dose reduction to the patient. This is combined with the inherent difficulties of films such as expense, dangerous materials for processing, labour requirements and difficult long term storage, retrieval and transfer. The physics behind X-ray production in digital and analogue X-ray systems is the same, but methods of detection and formation of an X-ray image using digital systems have changed. In digital radiography there are two major stages to imaging namely data acquisition and image display [84].

4.3.1 Data Acquisition

The signal from the attenuated X-ray beam must be stored. Instead of the light sensitive film used in conventional radiography, an imaging plate (IP) is used in digital radiography. There are two types of digital radiography systems. The most common system is known as Computed Radiography (CR) which uses an IP made of photostimulable phosphor (PSP) crystals to obtain a digital signal. These crystals store energy when excited by X-rays and emit luminescence corresponding to the absorbed radiation when stimulated by visible or infra-red radiation [85]. This system is similar to the screen film cassette system and the IP is generally housed in a light tight cassette. The charges stored in the plate must be read by a CR reader in order to be formed into an on-screen image and this is done by scanning the IP with a helium neon laser and collecting the emitted light through a photomultiplier tube

which converts it to an analogue signal. This is known as Photostimulated Luminescence (PSL)

The major difference between conventional and computed radiography is that the continuous signal used by analogue systems is now sampled using an Analogue to Digital Converter (ADC) to form a discrete, digital signal. This digital information is then used to display and process images on a computer screen. Although there is a small loss of data inherent in the sampling process, this is offset by the display and processing options offered by a digital display.

More recently, direct Digital Radiography (DR) systems which use charge-coupled devices and thin film transistor arrays have been developed. These allow the direct acquisition and display of the digital image by converting the X-ray energy directly into electrical signals without the need for a cassette reader [77]. They have been quoted as having nearly perfect DQE, and this, together with their ease of use, means they are challenging CR for popularity in radiology [86].

4.3.2 Image Display

The signals stored on either PSP plates or in digital radiography are converted to a grey scale image where the number of possible grey values depends on the number of bits used to define an image. This ranges typically between 2^8 (256 shades of grey) and 2^{16} (65 536 shades of grey). Black (full exposure) is assigned the value zero, and white (no exposure) is assigned the highest value (e.g. 255 or 65 535) [87, 88, 89].

The dynamic range in digital systems is wide, and therefore conversion to a grey scale image often includes some automatic processing (Automatic Gain Control) that scales the signal to a grey range that will lie in the visually useful range of optical densities for viewing by clinicians. In the Fuji CR system this is done by analysing a histogram of the image to decide on two defining parameters: Latitude (L) and Sensitivity (S) of the reader system. Latitude is $\log_{10}$ of the range of intensities imaged while Sensitivity determines the level within the dynamic range to be the centre of the X-ray intensities. Both these parameters depend on the reading mode chosen by the operator. This is normally set to an automatic mode so that the intensities are relevant for examination by clinicians. However, settings that allow some or complete manual manipulation of these parameters are also possible [85, 90].

4.3.3 Advantages

DR systems have excellent qualities in terms of transferring the detected intensities to an X-ray image. On the other hand, CR systems only manage to match screen-film systems in this regard, although newer systems are gradually overcoming this problem [84, 86, 90]. Many of the advantages of these systems lie, not only in image transfer capabilities or image quality, but on their day to day ease of use and the way images are displayed, processed and stored.

Some of the main advantages of digital radiography stem from the digital 'soft copy' format of the images as opposed to the unalterable 'hard copy' of an X-ray film. Potential post-processing options include correction for under or over exposed images, modification of image contrast to enhance certain anatomical features, and direct availability of the digital grey scale data which can be used for quantitative analysis [77, 87, 89]. A further advantage is that DR and CR systems offer a higher resolution and greater dynamic range than X-ray film. Added to this they provide consistent radiograph 'development'. Unlike traditional film development, which varies due to exposure and development characteristics, digital images can be produced consistently using the same X-ray settings thus making them useful for quantitative studies [85, 87, 89, 91].

Digital radiography is also of benefit to the patient. Since the detector has a greater sensitivity, it is possible to obtain the same quality of image by using a lower exposure (lower patient radiation dose) than would be necessary in conventional film radiography [84, 85, 87]. In a more practical sense foreseen by Kato *et al.*, digital radiography allows the viewing, archiving and filing of images in digital format [85]. This can reduce the number of films that are printed and stored and also facilitates the exchange of information between clinicians and hospitals anywhere in the world. Standardised image formats following the Digital Imaging in Communications and Medicine (DICOM) standard which governs image formation, storage and transfer ensure consistency between different departments and hospitals around the world [92]. The electronic management of digital images is now widespread and performed using picture archiving and communication systems (PACS) which would not be possible without the advent of digital radiography. The benefits are twofold, firstly there is lower cost due to reduced film usage, storage needs and staff requirements and secondly, speed and flexibility in viewing images is significantly improved over retrieving hard copy films [84].

4.4 MEASURING CALLUS

Digital X-ray systems offer improvements over conventional radiography as well as high quality digital data which lends itself to modern image processing and analysis techniques. Since X-ray images are commonplace in the clinical environment, it would be useful to harness some of these capabilities in improving the monitoring of fracture healing. There are two broad areas concerning fracture callus analysis which have been looked at in the literature: analysis of callus size and callus density.

4.4.1 Fracture Size

It has been suggested that a larger callus results in a faster and better healed fracture. Many authors have attempted to correlate the size of callus with the extent of healing, with varying degrees of success. Some studies found a good correlation between fracture size measured radiographically and that measured by histomorphometry but this size measurement does not correlate at all with the chemical composition [93]. However, as Aro *et al.* noted, chemical analysis of callus composition is of little use in the evaluation of mechanical stiffness which is the primary outcome measure in fracture healing [93].

One measure of the callus size is the Callus Index, which is the ratio of maximum callus width to the diameter of the original shaft at the same level [20, 94, 95]. Marsh reported that this measure produced the strongest correlation to bone stiffness compared to other radiographic measures. However, they noted that the correlation was not significant and that, although callus index was more predictive of healing at ten weeks than leg stiffness, the size of periosteal callus could not be used as an independent indicator of healing but should be supported with other measures of healing progression [20].

In a prospective study on fifty closed tibial shaft fractures, Oni *et al.* found no statistically significant relationship between either callus volume or callus index and fracture union [95]. They noted the wide variety of callus shapes and sizes in patients with tibial shaft fractures treated in casts. They also noted that there is no change in callus size after six weeks, only in its density. This lends support to the theory that callus stiffness cannot be related to size or density alone since a callus of a small size might have a greater density thus making it as stiff as a large callus of low density [17, 96].

Other authors have analysed a range of different radiographic measures of callus geometry and found that none can be used usefully to predict the strength of a healing fracture [17, 37]. Furthermore, different treatment methods produce healing with little or no callus formation, for instance internal plate fixation. This illustrates that callus formation is dependent on the mechanical healing environment and therefore not applicable as a general measure of fracture healing [20, 22].

4.4.2 Fracture Density

It has been shown in a variety of studies that bone density is highly correlated with bone strength in several mechanical aspects. Carter and Hayes, like many investigators before them, compared the compressive strength and elastic modulus of a range of bone types and densities and found a strong correlation between density, strength and stiffness [97]. This was confirmed by other investigators using mechanical strength tests and quantitative density analyses such as ash weight [6, 43, 46, 61, 96]. However, due to the need to perform strength tests to destruction, these results are not necessarily extendable to the patient situation *in vivo*. Some animal studies have been performed to compare density with strength. Powell *et al.* examined the relationship between mechanical strength and calcium content in fractures of rat metatarsals using microinterferometry [96]. Microinterferometry measures the refractive index and composition of a substance by creating two identical optical beams. The reference beam passes through an empty microscopic section and the sample beam passes through a histological section of the substance of interest. The optical path difference between the two is due to the composition of the substance traversed by the sample beam. This is used to find the calcium content of the histological section. They found that calcium content at the level of the fracture increased in a corresponding way to mechanical strength increase and concluded that monitoring of the calcium content of fractures could enable diagnosis of the onset of mechanical recovery. Other studies on fracture healing and osteotomies in animals used various density measurement techniques to confirm that mineral density has a significant effect on fracture rigidity [6, 28].

A number of studies have attempted to validate radiographic 'density' as a measure that is indicative of mechanical stiffness. In a study on the ability of X-ray images to provide mineral density measurements, Vose found that low intensity X-ray measurements were exponentially related to mineral content measured using ash weight [98]. In a later study they performed bending tests on human cadaveric femurs. Samples of bone from these femurs were X-rayed and a statistically significant exponential relationship was found relating bone strength and X-ray determined mineral density [99].

Further studies have shown a good correlation between bone stiffness and density measured using DEXA, which is one of the most commonly used methods to evaluate bone density non-invasively [2, 36]. Shah *et al.* measured the three point bending strength of feline bone segments decalcified using Ethylene Diaminatetra Acetic Acid (EDTA) and compared it to DEXA readings of BMC [100]. They found a high correlation between the two readings and concluded that calcium content is a reliable indicator of the mechanical strength of bones. Tselentakis *et al.* supported these findings *in vivo* and found a strong correlation between DEXA-derived density measures and bending stiffness in patients undergoing callotasis [27]. However, it has been suggested that the use of smaller regions of interest are necessary when applying DEXA to healing fractures. It is also possible to obtain erroneous results due to the fact that DEXA is not sensitive to small changes in BMC [2]. Further consideration must be taken when measuring bone density around a fracture as there is often a loss of mineralisation in surrounding bone due to disuse osteoporosis [34].

Whilst these studies show the relationship between bone strength and bone density, there is a paucity of studies illustrating the two important concepts necessary to validate the use of X-ray to evaluate fracture healing. The first is whether X-ray can be accurately used to assess bone density while the second is whether bone density in fractures, as opposed to whole bones, is a useful indicator of mechanical stiffness. In their study on the bending strength of feline femurs throughout decalcification, Shah *et al.* took X-ray images of the decalcified bones to document the change in radiodensity throughout the decalcification process [100]. Although they also took DEXA scans of the same bones at regular intervals, they did not correlate the two density measures. Other authors monitored changes in radiographic density over the healing course of osteotomies and in dental studies but failed to correlate this with actual density [74, 101, 102].

In a well designed study, Tiedeman *et al.* attempted to address both of these questions in evaluating roentgenographic density as a potential quantitative fracture healing outcome measure [15]. They performed their tests on sixty four osteotomised canine tibiae and fibulae at various stages of fracture healing. They obtained roentgenographic densities using digital photometer readings from film X-rays to give illuminance values which they corrected for background intensity variations and calibrated using a step tablet. Their first test compared illuminance with ash weight density of decalcified bone samples and they found a high linear correlation between the two readings (i.e. a correlation coefficient of r = 0.95). In their second test they compared illuminance of the least dense area of the fracture gap to the three point bending rigidity at various stages of healing and found a statistically significant exponential correlation between the two (i.e. a correlation coefficient of r = -0.99). The results using illuminance to evaluate healing were more accurate than those from clinicians' evaluation of radiographs of the whole bones. They concluded that their

method was a quantifiable way of using roentgenographic density to assess healing in bone. However, they cautioned that their animal model was of a simple osteotomy so conclusions regarding clinical usefulness in more complicated fracture patterns could not be drawn.

Although only limited studies have been made investigating the usefulness of bone density as a measure of fracture healing, and X-ray as a means to measure this, conclusions as to the potential of these methods have been positive. However, several authors have noted that, as healing progresses, increase in calcium content (equivalent to bone mineral density) levels off, indicating that any further healing is due to changes in bone micro-architecture. This suggests that monitoring the changes in bone density would only be useful in the early parts of fracture healing [15, 96].

Whilst some studies have shown that bone density is a useful way of monitoring the healing of osteotomies, in the more complex situation of traumatic fractures where there are no clear fracture gaps, the predictive power of bone density with regard to healing is not as clear [25, 28]. This would also seem to be the case in areas such as fracture risk analysis (e.g. osteoporosis), where bone density does not always correlate well with the likelihood of fracture. This could be due to the effect of changes in bone architecture on the mechanical properties of the bone [36]. Whilst methods such as QCT and DEXA are in use clinically to determine bone mineral density, there is still potential for an accurate and reliable method based on X-ray imaging. According to Haidekker *et al.*, many of the areas needing this type of imaging are in the research field, using small animals which they reported as unsuitable for use with DEXA or QCT [103]. They noted that one of the problems involved in the use of these computerised methods is the limited resolution. The bone averaging that is used for large areas such as the hip in osteoporosis monitoring is not suitable when accurate measures of small areas are needed. This is especially true in the case of fracture monitoring where the inclusion of metal implants in the averaging process may distort any density assessment. Thus, an affordable and reliable method of assessing, or at least quantifiying, bone mineral density using X-ray systems would be of value.

4.5 ALUMINIUM STEP WEDGE CALIBRATION

One of the most commonly used methods of gaining quantitative information from X-rays is to include a step wedge, usually made of Aluminium, in the image. This wedge is then used as a calibration device to normalise radiographs between the same patient at different times and between different patients. The wedge provides a relationship between optical density/grey value in the radiographs and equivalent Aluminium thickness (AlEq). It can be used to obtain a value for bone or fracture callus density in terms of equivalent Aluminium thickness which might be useful in the assessment of fracture healing.

4.5.1 Calibration with Optical Densities

Many studies have used Aluminium wedges to calibrate X-ray images for various purposes from as far back as 1901. One of the most comprehensive papers describing the measurement of bone density using a step wedge is by Colbert *et al.* [104]. They used a 14 step Aluminium wedge in X-ray images of bone. The resulting film images were scanned using a microdensitometer to yield optical density which was then modelled using the exponential Lambert-Beer law governing the intensity of X-rays hitting the film, and a linear exposure characteristic. Combining these two relationships and taking logs results in

$$ln(D–D_0) = ln(D_m–D_0)–\mu d \tag{4.2}$$

where D is optical density, D_0 is background optical density due to chemical fog, scatter etc., D_m is maximum film density, μ is the linear attenuation coefficient and d is the thickness of material.

Colbert fitted Equation (4.2) with a straight line by recursively estimating the D_0 term until the plot of $ln(D–D_0)$ versus step thickness reduced from a second to a first order polynomial. The gradient of the straight line was used as an accuracy check, as it should be the linear attenuation coefficient for Aluminium. The curve was used as a calibration relationship between optical density and Aluminium so that any optical density in the X-ray could be assigned an equivalent Aluminium thickness. By normalising density values according to the background optical density (D_0), this method also included a crude correction for varying imaging and film development parameters. However, it is important to note that use of the attenuation coefficient as accuracy verification is not entirely precise as its determination is dependent on both the purity of the Aluminium used in the wedge and the assumption of a monochromatic X-ray beam [87, 105]. Neither of these factors were taken into account by Colbert *et al.* However, other authors and existing industry standards in fields such as dentistry recommend the logarithmic calibration procedure as opposed to the straightforward optical density versus Aluminium thickness curve, despite giving no clear reasons for this [89, 106].

Haidekker *et al.* used six 0.5 mm steps of an Aluminium step wedge to calibrate X-ray images in small animal studies [103]. The X-ray films were digitised using an optical scanner which provided optical density information. Their step segmentation method was semi-automatic, and they used the relationship described by Colbert *et al.* to fit the log of optical density to step thickness with a straight line by minimising the squared deviation [104]. A semi-automatic segmentation of the boundaries of bone and soft tissue was used to provide soft tissue correction in the density measurements. They found their algorithms robust and useful, especially in providing the detail necessary to analyse small

anatomies and in minimising the effects of random scatter. However, they noted several shortcomings including variations in film development and density fluctuations according to the positioning of objects in the film. Various similar calibration methods have been used with conventional films digitised into optical densities to observe changes in bone density [15, 102, 105, 107]. These results point to the potential of this method to monitor healing in fracture patients.

4.5.2 Calibration with Grey Levels

When films of optical densities are digitised, the resulting image appears as a matrix of grey scales. Most previous studies have relied on using the original optical density values for calibration. With digitisation, as well as allowing for the effects of the digitiser, the major change here is that the grey scale is inverted in comparison to optical density. In the same way as film processing produces a roughly logarithmic conversion from X-ray intensity (dose) to optical density, digitisation uses a roughly logarithmic relationship to convert dose to grey level. This means that high grey levels relate to low doses and vice versa. This change required a review of the applicability of methods previously used in optical density based systems [87].

The same basic calibration used with optical density was used by Symmons with a 15, 1 mm step wedge in images of animal bones [108] . He updated the method by referring to grey level rather than optical density. He also measured the thickness of the bone in an orthogonal view and used this to take bone thickness into account in the density measurements. Furthermore, he considered magnification and image distortion effects and found a significant correlation between actual (mass/volume) and digitally measured density which was superior to DEXA. This was despite the fact that he did not seem to include any corrections for background variations, i.e. heel effect and scatter.

Other authors reported some success with the basic grey level to Aluminium thickness calibration but noted that inaccuracies can occur due to differing 'base' grey levels, a lack of knowledge of the relationship between incident X-ray intensity and radiograph density, and noise. Solutions using linear interpolation and extrapolation showed an acceptable degree of accuracy [109].

In a comprehensive analysis, Martin *et al.* presented a different method of assessing the Aluminium thickness versus grey level (as opposed to optical density) relationship [88]. Their images were attained from digitising X-ray films. They modelled the digitiser characteristic and combined this with the attenuation and exposure relationships to form a

straight line relationship

$$ln(\frac{V_g}{V_{max} - V_g}) = ln(\frac{V_0}{V_{max} - V_0}) + q(V_{max})x \tag{4.3}$$

where V_g is pixel grey level, V_{max} is highest grey level (corresponding to white), V_0 is lowest grey level (corresponding to black), q is a constant depending on imaging parameters and x is thickness.

They also corrected for varying background intensity by performing an 'empty field' (i.e. a fully exposed image with nothing between the beam and detector) assessment and measured section thickness accurately. Although they did not perform any direct comparison with other bone density measuring systems, they found their method precise and repeatable (i.e. a correlation coefficient = 0.997) and an improvement on more complicated calibration procedures. The accuracy of their results was confirmed by Nackaerts *et al.* who compared their results to BMD assessed by DEXA [110]. They also assessed the effect of different numbers of steps on the calibration procedure and found that decreasing from nine to three steps made no significant difference on accuracy. Gu *et al.* confirmed this finding attributing it to the highly linear relationship of the calibration graph [91]. However, this is contrary to other findings which suggested that the inclusion of more than three points on the calibration curve is important for maintaining accuracy [88] and that a thickness range exceeding the highest expected equivalent thickness of samples should be used for best accuracy [105].

The use of an Aluminium step wedge in conventional radiography is a technique that has been investigated by a wide range of researchers in varying degrees of detail. Many of these, especially those working more recently with film to grey level digitisers, have noted the major sources of inaccuracy as the noise and the dynamic range of the digitiser [88, 111].

4.5.3 Aluminium Calibration Using Digital X-ray Systems

The advent of digital radiography, where images are directly converted to digital format, has eliminated some of the sources of inaccuracy described above. With the removal of sources of variation such as film development, digitiser response curves etc. has come the introduction of new problems and unknowns such as the effects of automatic (and often 'black boxed') processing and digitisation. Fewer authors have examined the advantages and disadvantages of digital X-ray imaging in the context of density calibration. Nomoto *et al.* [87] and Carvalho-Junior *et al.* [89] made the observation that, in dentistry, although radiography and digital radiography is used extensively, no thorough investigation into the accuracy of digital systems for determining the radio-opacity of materials has been con-

ducted despite there being thorough International Organisation for Standardisation (ISO) and American Dental Association (ADA) protocols for such evaluations on film radiography [112, 113]. They stressed that the previously used methods cannot be blindly applied to digital radiography but must be updated with careful consideration of both the new processing features and the direct use of grey scale as opposed to optical density.

Kolbeck *et al.* performed a simple square regression fitting to step thickness versus grey level using an Aluminium wedge of ten 2 mm steps imaged using a digital radiography system, though they did not take into account bone thickness or background variation [28]. They used this to assess the changing density of 24 tibiae undergoing distraction osteogenesis in a micropig animal model and found their method useful and sensitive in assessing day to day healing progress with a statistically significant correlation between equivalent Aluminium thickness and torsional stiffness (i.e. a coefficient of determination $r^2 = 0.8$). They recommended additional evaluation of the use of digital radiography in the monitoring of fracture healing.

In a critical evaluation of current standards, Gu *et al.* used an approach recommended in dental standards [91] , i.e. to convert grey level into absorbance

$$A = -\log_{10}(1 - \frac{G}{255}) \tag{4.4}$$

where A is absorbance and G is grey level. Linear regression was used to provide a calibration graph between absorbance and Aluminium thickness. In the study on a 15, 1 mm step wedge to assess the radiopacity of dental materials, they found the method precise and repeatable with no statistical difference between measurements of the same materials taken with different exposure settings and at different times.

In a more comprehensive paper dealing with dentistry materials, Nomoto *et al.* assessed the use of computed radiography to perform X-ray calibration with a ten 0.5mm step Aluminium wedge [87]. They corrected the equations used by Colbert *et al.* for use with grey levels and found

$$\ln(g - G) = \ln(atI_o) - \mu x \tag{4.5}$$

where g is the grey level for a non-irradiated area, G is grey level, atI_0 is the exposure characteristic, μ is the attenuation coefficient and x is Aluminium thickness. They used this linear relationship to assess the accuracy of conventional X-ray and digital X-ray with and without processing by comparing manufacturer specified and measured Aluminium equivalent densities of various substances. It was found that digital imaging with no processing provided the lowest variation in density measurements. However, they cautioned that the use of Automatic Gain Control (AGC) processing in digital imaging caused distortion of

the expected step thickness versus grey level relationship, rendering this method unreliable and inaccurate.

Nackaerts *et al.* evaluated whether a step wedge was necessary in acquiring accurate densitometric results in digital imaging [110]. Results using Aluminium calibrated grey levels and directly assessed grey levels were compared to DEXA scan results. They reported a superior result when using a step wedge. Other authors have also suggested that since digital radiography provides such consistent images for the same target distance and exposure time, wedge calibration is unnecessary and values could be measured directly from the image as they should remain constant in each radiograph [91]. Beltrame *et al.* attempted this using a semi-automated method whereby the background of the X-ray and the surrounding healthy bone were assumed constant and used to normalise the radiographs of healing bone grafts [74]. Compared to a step wedge method, they had good results and used their method to monitor bone deposition in osteoconductive grafts of animal models. However, the basis of using bone as a time invariant calibration area is questionable since effects such as disuse osteoporosis could change the optical density of this reference area which would result in inconsistencies over time.

4.6 CORRECTION OF IMAGE INHOMOGENEITIES

Previous attempts have been made to improve the information gained from X-rays by using various calibration methods, although the inherent non uniformities of X-ray exposure are rarely taken into account. As discussed previously, an X-ray image is created by the detection of the beam that has been changed by attenuation through the body. An ideal X-ray image assumes a point source, no modification of the beam by the target, no scatter, and complete detection of the beam that strikes the detector. Even in digital radiography, actual image X-ray acquisition differs greatly from this ideal [77]. In order for any grey level calibration technique to be accurate, these anomalies in image formation need to be measured and corrected for as far as possible. In digital radiography, problems resulting from film characteristics, film exposure techniques and digitiser response curves have been removed. However, two issues inherent to X-ray formation and propogation remain: the anode heel effect and scatter.

4.6.1 Anode Heel Effect

Several methods to correct for the intensity variation due to the heel effect exist and have varying degrees of complexity. A basic approach used in both conventional and digital radiography is to correct the background based on a pixel-by-pixel correction matrix formed

from an empty field image [15]. Martin *et al.* used this approach with success in a video microscopy system [88]. However, they cautioned that the beam of the empty field should be filtered with an object of similar density to the radiographic image of interest. The disadvantage of this type of method is that it relies on calibration images that represent the background accurately. More complex corrections have been attempted to overcome the need for calibration X-rays. Behiels *et al.* performed a thorough evaluation of the heel effect and various retrospective correction techniques for digital hand radiography [78, 114]. Since the main contribution to the field variation is in the anode-cathode direction, a 1D model in this direction was constructed. Based on the physical geometry of the X-ray tube, the incident radiation was modelled with an exponential function. The assumption of no variation perpendicular to this axis was justified by empty field experiments which showed it to be relatively small. They also extended this to an exponential model in two dimensions. They found both 1D and 2D models robust and effective at eliminating the heel effect to allow for further analysis. However, they cautioned that the retrospective aspect of their technique should only be used in images with sufficient background area.

Similarly, do Nascimento *et al.* performed an automatic heel effect correction in digital mammograms. They modelled the effect as a Gaussian distribution in the anode-cathode direction and a logarithmic distribution perpendicular to this and reported their method as effective and useful in normalising background measures [115]. De Josselin and ten Bosch took a more simplistic approach [105]. Whilst they noted that background inhomogeneity was a critical factor in the accuracy of their method, they did not attempt to correct for it, but simply ensured that both specimen and wedge were placed near to each other and near the centre of the image to minimise the effect.

Although the heel effect has previously been considered by authors, there is no straightforward correction method that takes into account the various aspects of the effect whilst also taking advantage of the digital nature of modern X-rays, specifically for use with step wedge calibration techniques.

4.6.2 Scatter

Several methods to reduce the effect of scatter during the image formation process exist. These include using smaller field size, which is not always appropriate, and anti-scatter grids, which allow a majority of primary X-rays to be transmitted whilst most of the scatter is absorbed by lead strips. However, this also requires increased patient dose to achieve the same image quality [77]. As a result of digital radiography, computerised techniques for the quantification and reduction of scatter have become more commonplace. Many of these techniques required the PSF to be known and used as a deconvolution filter. However,

PSFs are image dependent and change according to object thickness and object-to-detector air gap. Boone and Seibert used these parameters and the linear attenuation coefficients of the primary and scattered radiation to develop image-specific PSFs for scatter correction [116]. They found their technique gave a good approximation to the actual PSF and thus had potential in correcting X-ray images. However they reported that the results might not be as good in more complicated clinical situations.

4.7 SUMMARY

It has been reported that digital radiography provides new opportunities in obtaining quantitative information from X-rays. Of the radiographic measures of bone healing, density is the best correlated to strength and healing. Several studies have investigated obtaining calibrated density measures from conventional radiographs and digitised radiographs. A few have extended this to digital radiography. However, there remains a lack of consensus on the best calibration methods to use and a lack of thorough investigation into the effects of different factors on X-ray calibration. Furthermore, few authors took into account the effect of various X-ray inhomogeneities. Thus, although previous studies show potential, the question of whether X-ray can be accurately used to monitor healing through fracture density monitoring is still unclear. A thorough investigation of the use of an Aluminium step wedge in computed radiography, and the associated corrections, would be of value.

Part II

X-ray Based Measurement of Fracture Stiffness

Chapter 5

Stiffness Testing Apparatus

5.1 INTRODUCTION

This chapter describes the equipment developed to perform stiffness tests on fracture patients using digital X-ray. The design of a frame to apply a four point bending moment to tibial fractures is discussed and equipment to apply a tensile axial load to humeral fractures is explained. Models of both an IM nailed tibial fracture and a conservatively treated humeral fracture are presented, and equipment developed for the Zwick materials testing machine to perform mechanical tests is also described.

5.2 INVESTIGATIVE TOOLS

This section gives details of the investigative tools used during this study.

5.2.1 X-ray Imaging

All test and patient X-rays were taken in Outpatient Department 6 (OPD6) at the Royal Infirmary of Edinburgh (RIE). A Philips Bucky Diagnost X-ray set with Optimus generator (Philips Electronics, Netherlands) and Siemens Multix Top with Polydorus LX50 generator (Siemens, Germany) were used. Pre-clinical X-rays were taken using a Sterne Acu-ray Junior (Model 31-BLD-C) X-ray tube (Sterne Manufacturers, Canada). All X-rays were taken using the Fuji Computed Radiography cassettes and processed using the FCR XG-5000 Fuji Computed Radiography processor (Fuji Film Ltd., Japan).

5.2.2 Image Analysis

All programming was performed in the Matlab technical computing language (Mathworks, USA). Some image analysis was also carried out using the freeware program Image J (National Institute of Health, USA). DICOM format images of 10-bits (1024 grey levels) were taken from the Fuji CR system and read into both programs.

On analysis it was noticed that the Fuji CR system produced images with an inverted look-up table (LUT). In other words, black was assigned the value 1023 as opposed to 0. Whilst Image J automatically recognised this and displayed the images in the correct way, Matlab did not. In order for the images to match their clinical appearance and to create images where areas of no attenuation (i.e. black) have a grey level of 0 and areas of complete attenuation (i.e. white) have a grey level of 1023 an image inverting function was written in Matlab. This function read an image and replaced each pixel with 1023 minus the pixel's original grey level. All images taken on the Fuji system were processed in this way for analysis in this thesis.

5.2.3 Mechanical Testing

Mechanical bending stiffness and tensile axial stiffness tests were performed using the Zwick/Roell Z005 materials testing machine (Zwick GmbH & Co., Germany) and measured using the accompanying testXpert software.

5.3 TIBIAL BENDING

As discussed in Section 3.4, previous researchers have applied stiffness tests to fractures. The equipment and methods used in their studies, as well as the specific aims of this project, were taken into account when designing a frame to apply bending in the X-ray environment. This section gives an overview of the equipment used previously and the changes necessary due to the design considerations of this project. The final design of a four point bending frame for use on IM nailed tibial fracture patients is presented together with the mechanical calculations used to obtain stiffness measurements using this frame.

5.3.1 Previous Equipment

The equipment used by previous researchers measuring the bending stiffness of tibiae was discussed in Sections 3.4.1 and 3.5.1. Researchers measuring mechanical stiffness in externally fixed tibial fractures applied a three point bending load and used electrogoniometers

to measure deflections at the fracture site [54, 55]. Since the force was applied by hand at the fracture site, this equipment would not be suitable for use in X-ray. Hammer *et al.* applied a three point bending load during X-ray and used a comparison between loaded and unloaded images to measure stiffness [18, 58, 59].

5.3.2 Design Considerations

Having examined the equipment and techniques used by previous researchers, several design considerations were addressed: the patients to be studied, the type of bending moment to be applied, the directions in which it should be applied and the way the system would work in the clinical radiography setting.

Patients

Previous studies have been performed on tibial fracture patients. This is due to the accessibility of the limb and the ease of applying loads to it as well as the fact that tibial fractures have a relatively high rate of impaired healing, i.e. delayed or non-union. There was good documentation of previous results with which to compare a new technique and therefore tibial fracture patients were selected as the subject group for this study.

The technique of Richardson *et al.* can only be applied to patients treated with an external fixator, and cannot be applied under X-ray due to the need to apply the load to the fracture site manually [54, 55]. The technique of Hammer *et al.* was applied to conservatively treated patients. However, at each study point these patients had to have their plaster casts removed before imaging, and then replaced. This was not ideal. Therefore in this study, patients treated with an IM nail were selected. Whilst the nail might prove problematic in terms of allowing motion at the fracture site, patients could be studied directly, with no intervention.

Three Point versus Four Point Bending

Both sets of equipment reported in the literature used a three point bending configuration. However, it has also been reported that the accuracy of three point bending depends on how accurately the load can be applied to the fracture site (Section 3.4.2). Away from the point of load application, the moment changes rapidly. Thus, if clinicians were not applying the load exactly on the point of fracture, which may not always be easy to determine, their calculations of bending stiffness would have been inaccurate as they would have been over estimating the applied moment. On the other hand, it has been reported that four point

bending provides a method whereby the bending moment remains constant between the two points of load application. As long as the fracture site is within these two points, then a known moment is applied across it. In addition, a load applied directly to the tender fracture site may cause more pain to the patient. For these reasons it was decided that a four point bending configuration would be the most suitable in order to provide accurate and potentially more comfortable loading.

Measuring Force in Different Planes

The third point for consideration was in which planes to measure the stiffness of the fracture. Previous methods measured the stiffness in only a single plane. In the case of Richardson *et al.* (and the investigators who used his method) this was the AP (or sagittal) plane. On the other hand, Hammer *et al.* applied a load in the lateral (or coronal) plane. However, as discussed in Section 3.4.2, a more complete picture of bending stiffness can be obtained by measuring in two different planes. Researchers have shown that measurements in a single plane were not reflective of the bending stiffness in all planes [9, 54]. Thus, a bone may be regarded as clinically healed when measured in one direction when it still has very low stiffness in another. This can result in an inaccurate picture of fracture healing and might lead to re-fracture. Based on these findings, it was decided that the most accurate measure of fracture healing would be obtained by applying a bending moment in two directions: AP and lateral.

Clinical Radiography Requirements

The aim of this system was to provide a simple tool that could be applied easily in the conventional clinical environment. The necessity for complex equipment such as force plates and electrogoniometers, which are foreign to the normal clinical environment, seems to have restricted the use of the Richardson *et al.* method, despite their results being encouraging. Therefore a major design consideration was how the system would work in the radiography setting where it would be used.

Conventionally, two X-ray views of tibial fracture patients are taken: an AP and a lateral view. Since these views also measure the directions of loading that are of interest, the only change necessary was for both an unloaded and a loaded image to be taken in each view. The equipment would ideally allow for both views to be taken without the patient having to move and without any effect on the X-ray equipment. It also needed to be simple and quick to operate so as not to cause delay in a busy radiography setting, as well as be easy to manoeuvre in and out of position for use with the patients. All these factors were considered in the design of the equipment.

5.3.3 Frame Design

From consideration of the four previously discussed aspects, a frame to apply a four point bending moment in the AP and lateral directions to internally nailed tibial fracture patients was designed. Schematic drawings of the frame are shown in Figures 5.1.

Photographs of the frame in the AP and lateral loading positions are shown in Figure 5.2. The frame consisted of three main components. The first was a set of supporting bars where the patient's leg was placed. These were made of metal rods onto which disposable sections of foam padding were placed which could be changed for each patient to ensure the hygiene of the equipment. The position of all four fulcra was adjustable. The outer rods were the support points which supported the leg and provided a comfortable positioning for the patient while the inner rods were the outer fulcra of the four point bending system. These could be adjusted to be equal distances from the inner loading fulcra.

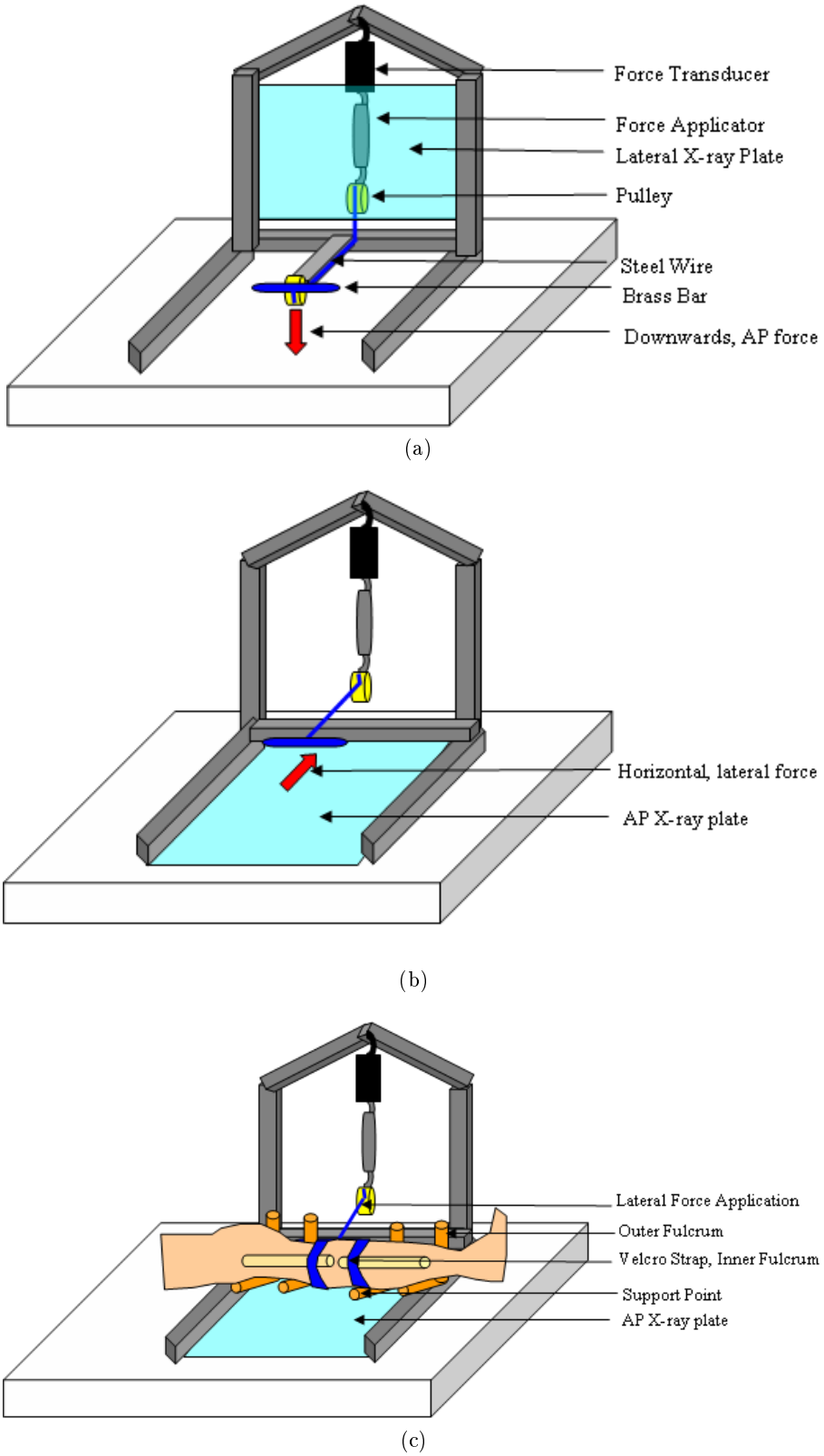

Figure 5.1: X-ray frame in a) the AP force configuration, b) the lateral force configuration and c) the lateral force configuration showing leg position and fulcra.

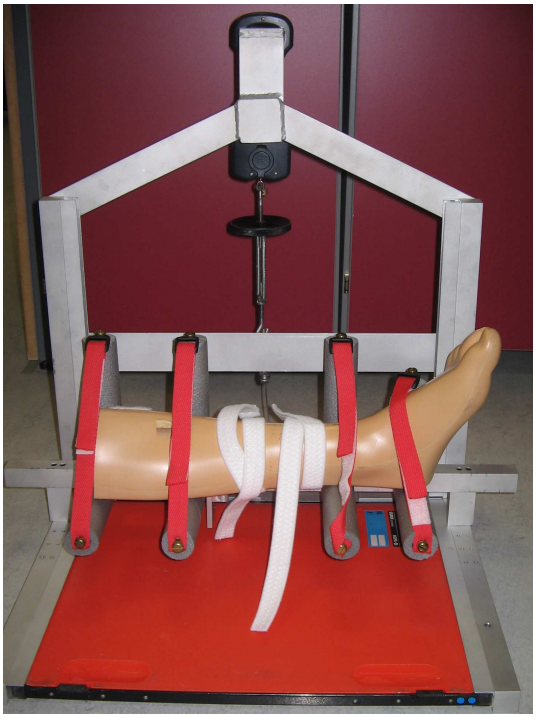

(a)

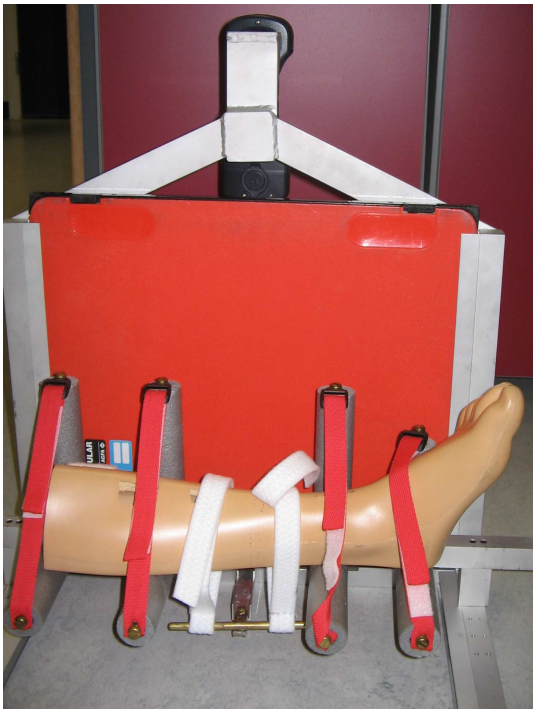

(b)

Figure 5.2: The frame with a foam leg in the a) lateral and b) AP loading directions. The position of the X-ray plate (red) is also shown.

The second part of the system was the force application section and consisted of two adjustable velcro bands that were placed on either side of the fracture site. These were the inner fulcra of the four point bending configuration. If the outer fulcra were positioned equal distances on either side of the inner fulcra, and the load applied was divided evenly between the two inner fulcra, then the moment across the fracture site should be constant (See Section 3.3.2). The three sets of fulcra are shown in Figure 5.3.

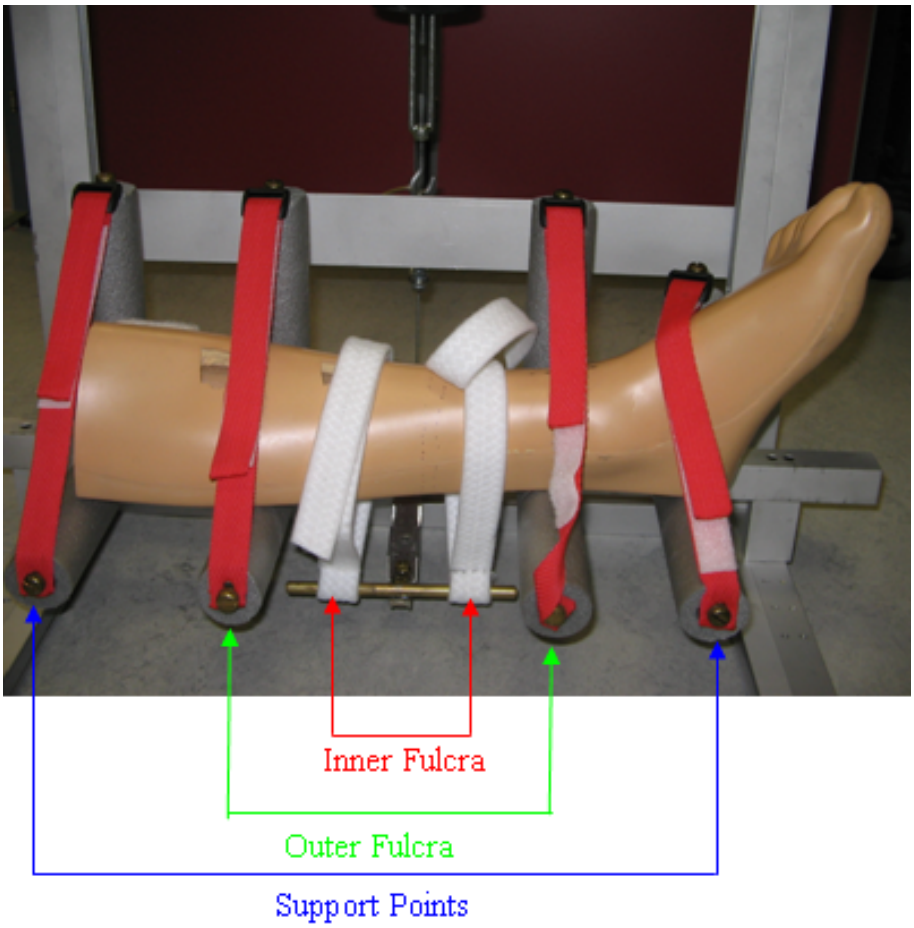

Figure 5.3: Image of the bending frame showing the inner and outer fulcra and support points.

The velcro bands of the inner fulcra were connected to a brass bar which was in turn connected via a pulley to a tensioning device. This consisted of a wheel that was turned to tighten the steel wires connecting the brass bar to the tensioning device. In other words, it increased (or decreased) the force applied to the inner fulcra. This force was measured by a digital spring balance (SmartSensor Electronic Digital Scale, Model AR815, Maximum Capacity 25kgs, accuracy $\pm$ 2%). Figure 5.4 shows the position of the tensioning device on the frame.

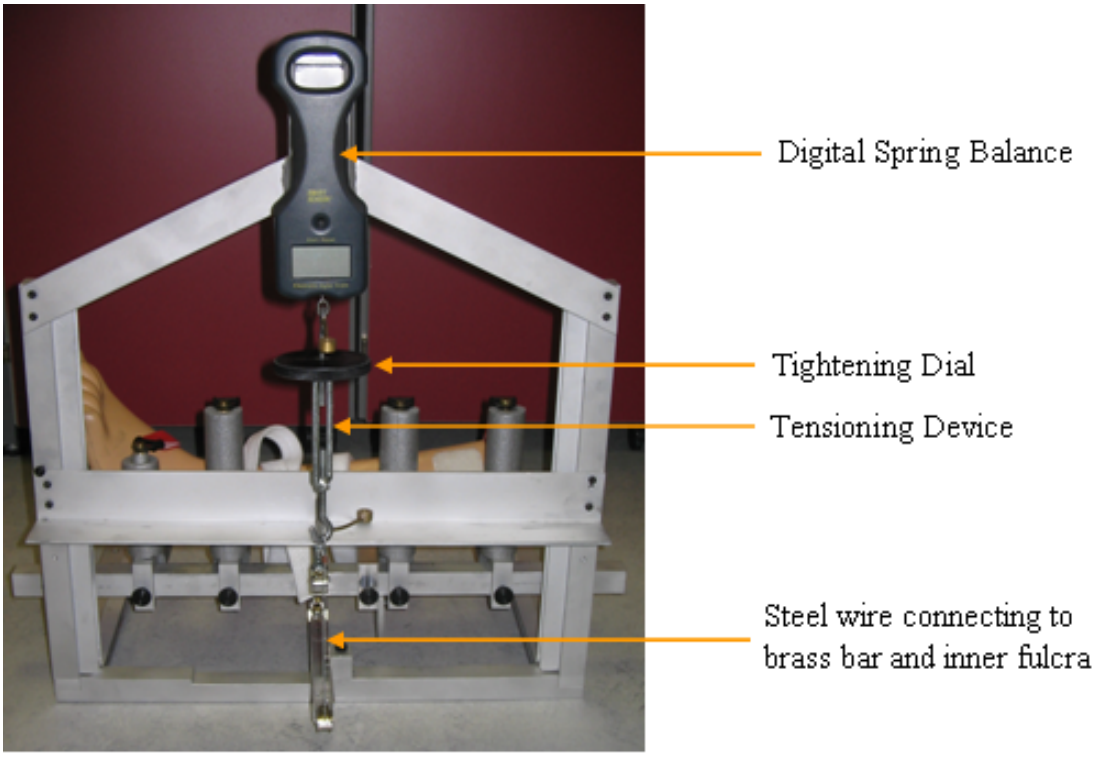

Figure 5.4: Image of the frame showing the inter-connection of the steel wires, tensioning device and digital spring balance.

There were two brass bars for the two directions of force application. The first setting allowed a downwards pulling AP force across the fracture site, this was monitored using a lateral projection of X-ray. The second setting applied a horizontal lateral force which was monitored using an AP projection of X-ray. Figure 5.5 shows the position of the brass bar for the two different directions of force.

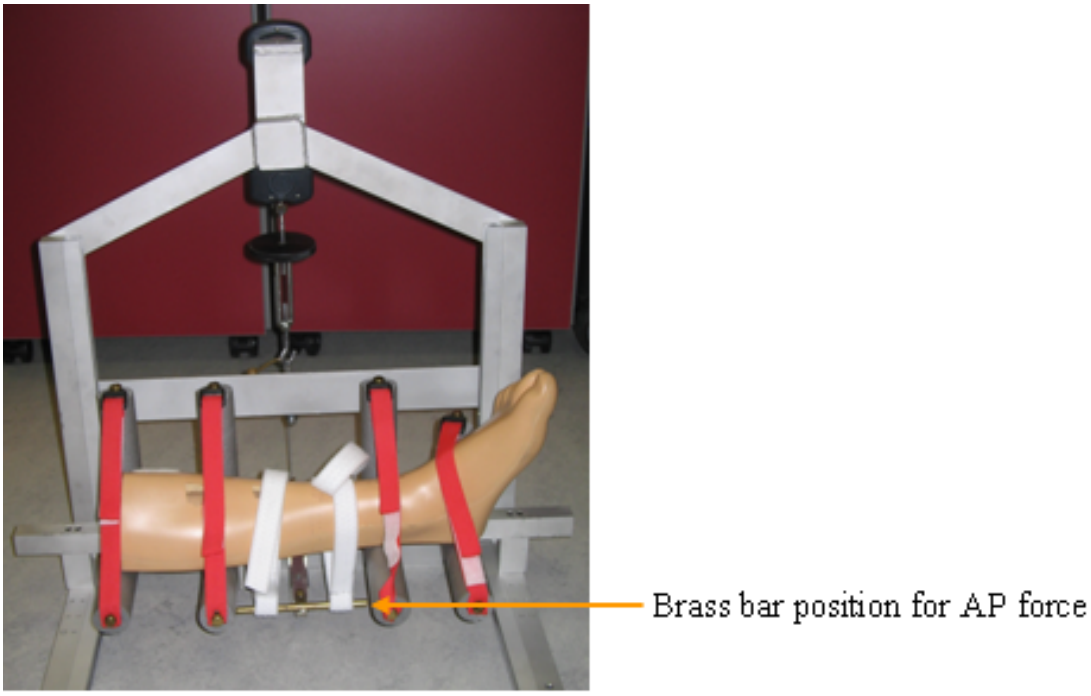

(a)

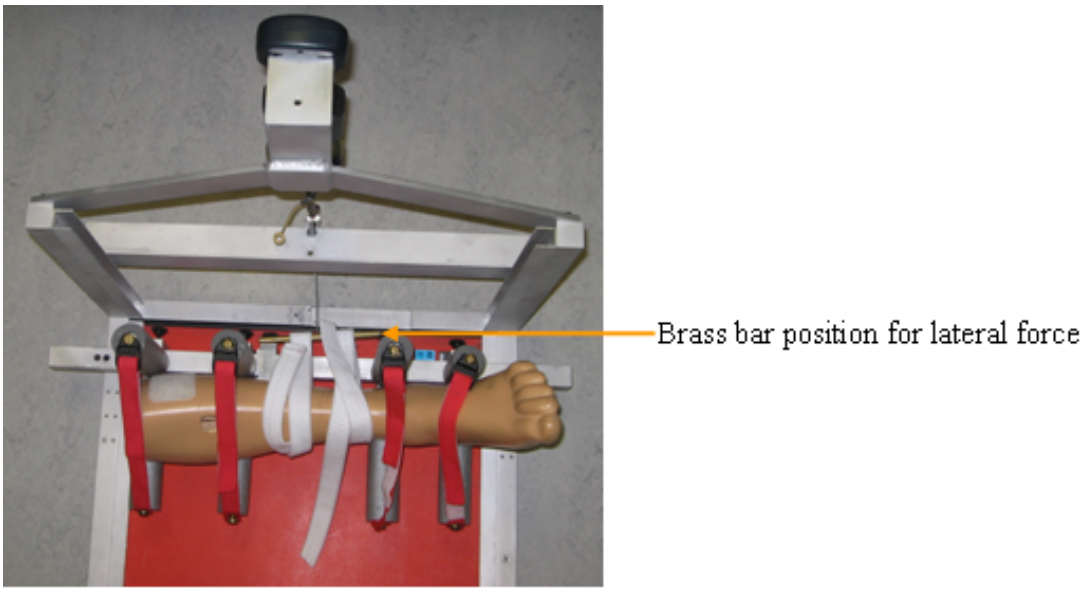

(b)

Figure 5.5: The brass bar positioned a) below the leg to give a downwards, AP force and b) to the side of the leg to give a horizontal, lateral force.

The final parts of the frame were the X-ray cassette holders. These provided slots for the X-ray cassettes to be inserted either below the patient's leg in the case of an AP radiograph, or to the side of the patient's leg in the case of a lateral radiograph. In order to take

the AP projection (i.e. lateral load), the X-ray source was positioned above the patient, aiming vertically downwards. For the lateral projection (i.e. AP load), the X-ray source was positioned to the side of the patient, aiming horizontally.

The entire frame was made of Aluminium. The steel wires were tightly wound and the velcro material firmly sewn to reduce stretching of these elements of the frame in response to loading. Plans for the frame in both the AP and lateral loading configurations are presented in Appendix A.

5.3.4 Mechanical Calculations

Symmetrical Four Point Bending

To operate the frame, a load was applied by the force applicator and divided between the two inner fulcra and the resulting deflection was measured using X-ray. The ideal configuration is shown in Figure 5.6 which shows the patient set up and the corresponding model used to make mechanical calculations. The inner fulcra are evenly spaced from the fracture site and the outer fulcra are evenly spaced from the inner fulcra. This set up creates a symmetrical four point bend that will result in a constant moment between the two inner fulcra and thus the fracture site. Typical calculations of the applied forces, reaction forces and bending moments are given in Appendix B.

Several assumptions were made about the leg under assessment to enable the mechanical calculations to be made. Firstly, it was assumed that the leg ended at the outer fulcra points and that these were simply supported, or hinged, ends which allowed four point bending to take place. This assumption was valid for the distal end of the leg since the leg ends at the ankle and foot, so it is free to react to a bending moment. Proximally the leg continues to the knee and the rest of the body, which could result in a fixed, rather than hinged end. However, an assumption was made that the articulation at the knee joint would allow sufficient movement to describe the proximal part of the lower leg as hinged.

The second assumption was that the load applied to the brass bar was divided evenly between the two velcro bands, i.e. inner fulcra. This assumption would be true for a completely uniform beam, whereas the leg varies in cross-section along its length. Therefore it was possible that one fulcrum would experience more load than the other. However, the division of this load would be difficult to calculate considering the complicated structure of the leg so, for simplicity of calculation, it was assumed that the same force was applied by each of the inner fulcra.

The third assumption was that the leg could be described as a homogeneous beam. Again this was not the case since the leg is made up of soft tissues, two types of bone (cortical

and trabecular), an IM nail and a fracture with callus. Although the soft tissues provided some resistance to bending, this was difficult to quantify separately and was instead added to the resistance provided by the bone as a whole. It was assumed that bending would not occur at a magnitude where the bone ends come into contact with the nail and it would therefore play a minor role in the system. The fracture site could potentially be modelled as a hinge in the early stages of healing. However, as callus matures this becomes less accurate. Since the callus material is weaker than the bony material it was assumed that any bending that occurred would happen at the callus site. Calculating the response to forces based on the callus properties rather than the bony properties was valid as the bony areas would not undergo enough force to experience any bending. Although it may seem to be an oversimplifying assumption, it was relevant to model the leg under load as a single, composite beam with hinged ends supported at the outer fulcra and loaded at the inner fulcra.

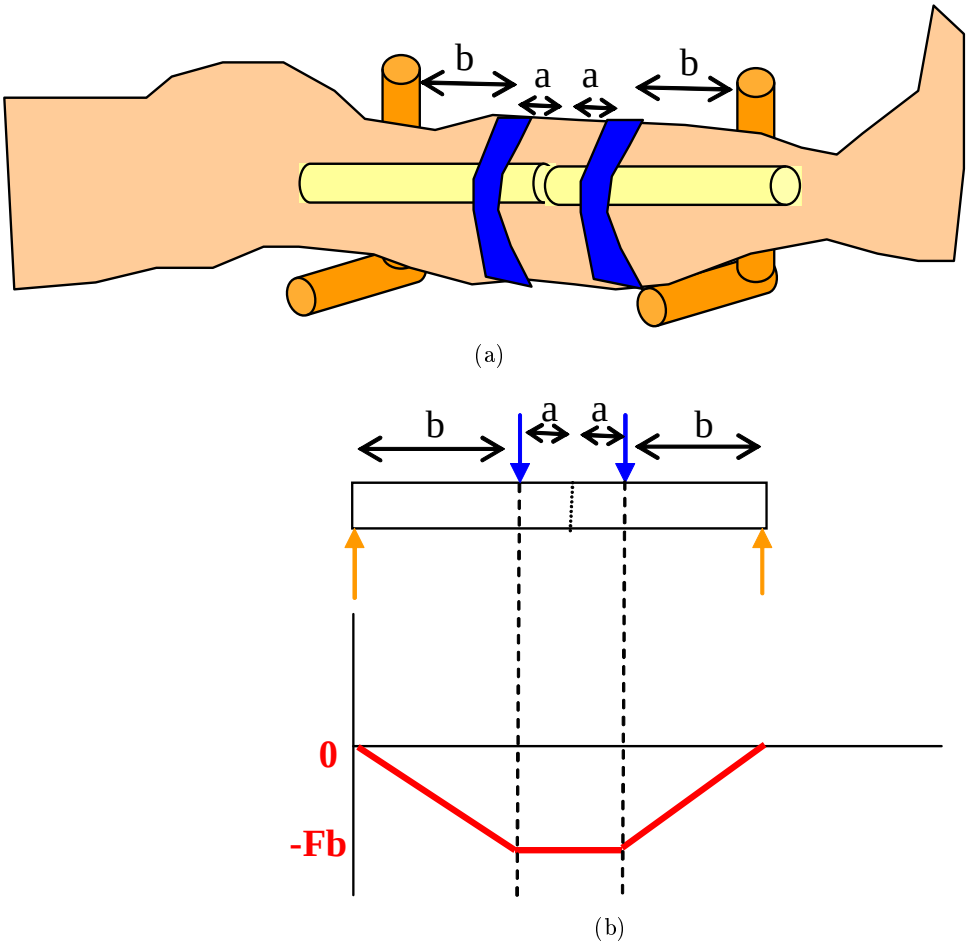

Figure 5.6: a) A patient's leg showing the fracture and inner and outer fulcra and b) the corresponding force and bending moment diagrams.

Asymmetrical Four Point Bending

In the previous model, the outer and inner fulcra were symmetrically placed. However, in a clinical situation it was likely that a patient may not be ideally aligned in the frame or that the position of the fracture (for instance, very close to the ankle or knee) would not allow for equal spacing of all the fulcra. This circumstance is shown in Figure 5.7 and when this happens, constant bending does not occur across the fracture site. However, if the distances a, b, c and d are known, the force that does occur at the fracture site can be calculated as shown in Appendix B. This illustrates that even with an asymmetrical set up of the four point bending frame, the measurements from the X-ray images can still be used to give the forces and bending moments at the fracture site.

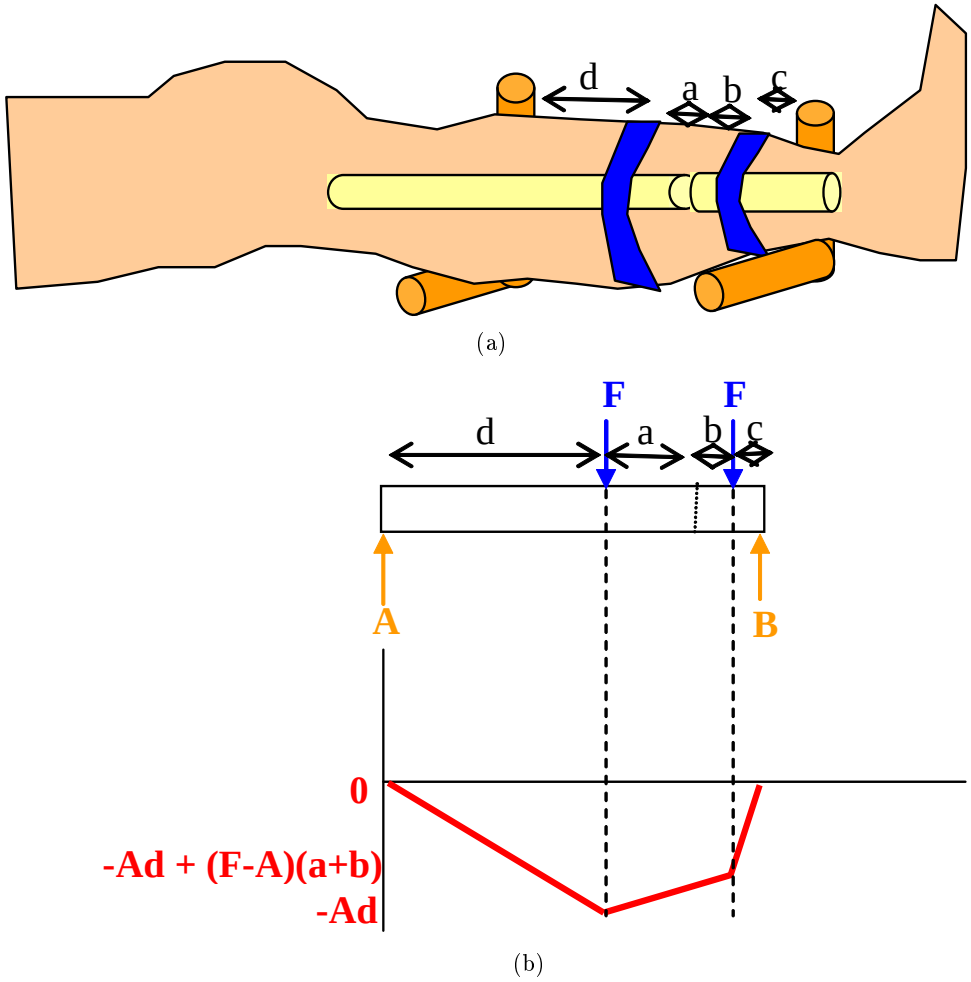

Figure 5.7: a) A patient's leg in a non-ideal position and b) the corresponding force and bending moment diagrams.

5.4 HUMERAL TENSIONING

Unlike the case of the tibial bending frame, there was little previous research on which to base the application of a tensile axial load to a humeral fracture. This meant that constructions and flaws in previous equipment could not be used to guide the design process. This section describes the points considered in the design of the humeral apparatus and the final system that was developed. A discussion of the mechanical calculations to get stiffness measurements using this equipment is also given.

5.4.1 Design Considerations

As with the tibial frame, four areas were considered in the design of the humeral apparatus.

Patients

Suitable patients for the study were considered from the point of view of ease of applying an axial load. The first aspect of this was that the limb in question should be accessible for axial load application. The second was that it could be fairly well isolated from surrounding joints so that joint involvement in response to load did not affect measurements. Thirdly, the fracture needed to be treated in such a way that measurements could be easily made and imaged clearly on X-ray. This eliminated patient groups that had been rigidly fixed surgically and left primarily those treated conservatively. Although a conservatively treated tibial fracture could have been appropriate, most tibial fractures are treated operatively at the RIE. Instead it was decided to study conservatively treated humeral fracture patients. This was due to the ease of accessibility of the limb, as well as the fact that since the arm hangs down during X-ray the simple use of gravity could provide an appropriate tensioning force. Therefore, conservatively treated humeral shaft fractures were chosen for the study.

Type of Force

As discussed in Section 3.3.1, axial loading is the most fundamental type of loading which provides a direct assessment of material properties. Axial loads are applied vertically in the direction of the long axis of the beam and can be either compressive or extensive. Compression tests have been performed previously on fractured bones and bone-fracture models, especially with regard to ascertaining whether axial micro-motion might be beneficial to the healing process and also in the case of measuring healing in distraction osteogenesis [117]. However, there is an inherent limit in the movement possible when 'pushing' the two sections of fragment together – in a well aligned and reduced fracture, this will be almost

nothing, making X-ray measurement of any movement difficult. A tensile axial load allows a greater potential for displacement and therefore an easier measurement of the movement of the fracture ends. Load application is also simple since gravity and hanging weights can be used to apply downwards force. For these reasons, a tensile axial loading direction was chosen.

Measuring Force in Different Planes

In the case of four point bending, measuring the bending motion in more than one plane provided a clearer picture of healing. However, in the case of axial loading this might not be true. Although different views of an axial load can be taken, the load and resulting movement is the same as long as it is applied centrally, since the cross-sectional area will remain the same. Thus, in tensile axial loading there was essentially only one possible direction of loading and two separate measurements of this were unnecessary.

Clinical Radiography Requirements

A key aspect of the design was how to implement the loading of the fracture site whilst an X-ray was being taken, and how this design would fit into the clinical environment with as little disruption as possible. For conservatively treated humeral X-rays, two views are conventionally taken, AP and lateral, using a vertical bucky with the patient standing upright and being manoeuvred to allow both views to be obtained. This is already a fairly complicated process so the loaded X-rays needed to be as simple as possible. After some experimentation, it was found that obtaining a loaded lateral X-ray would be difficult for both radiographer and patient, and in the case of larger patients, would be almost impossible. Therefore, it was decided to image the fracture site using the AP view only.

5.4.2 Equipment Design

From consideration of these four aspects, a set of equipment was designed to apply a downwards axial force to a conservatively treated humeral fracture. The loaded fracture was X-rayed in the AP direction only. In order to apply a load to the humerus, potential movement at the elbow and wrist had to be eliminated. Although many humeral fractures are treated using a collar-and-cuff arrangement, plaster casts are also used. To satisfy both these situations and eliminate joint involvement, the concept of applying a downward load to a bent arm at the elbow was used. The resulting force through the arm was measured with the hand resting on a force plate, as shown in Figure 5.8.

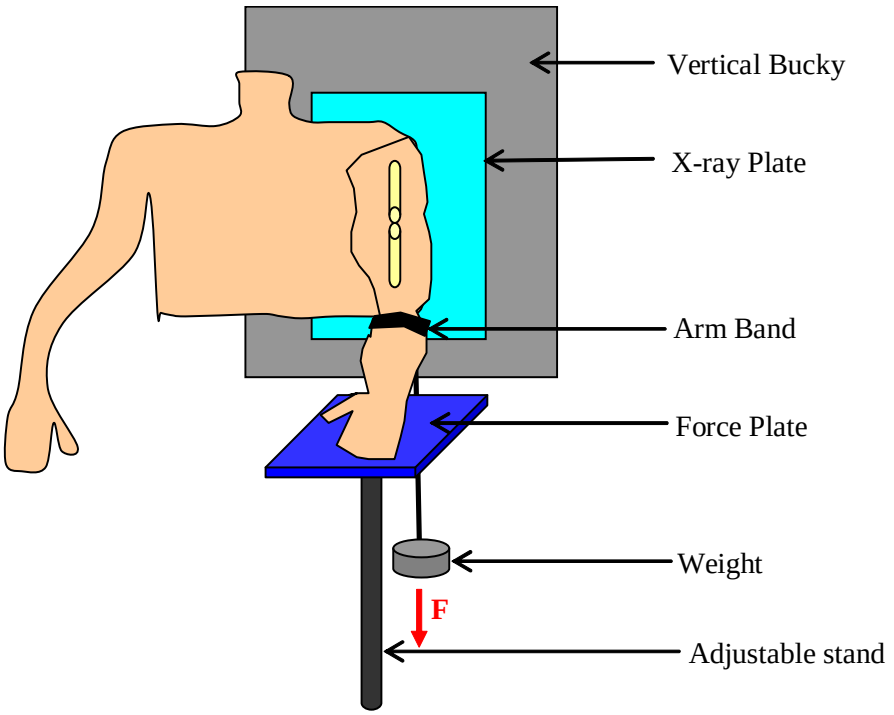

Figure 5.8: Positioning of the equipment to measure humeral axial stiffness.

As the figure shows, the patient stood in front of the bucky containing the X-ray plate, as they would for a conventional AP X-ray. If they were wearing a collar-and-cuff, the strapping was released to allow their arm to hang freely. If they were treated using either a brace or a cast, this remained in place during the X-ray examination. Their arm was bent at the elbow and the height of the force plate (Terraillon Supreme Stainless Steel scale, maximum capacity 10kg, precision 2g (0 – 1kg), 5g (1 – 4kg), 10g (4 – 10kg)) was adjusted so that their hand rested on the force plate with the angle at the elbow as close to 90 degrees as possible and the arm in front of them.

A tightly woven polyester band was placed around the arm, as close as possible to the elbow joint. In the case of plaster casts this might have been slightly further down the forearm. A small hanging weight was attached to the arm band and the weight on this could be increased until the desired level was reached. The weight could be quickly and easily removed if the patient felt discomfort at any stage. The material of the band allowed little stretching in response to loading. An X-ray was taken both before and after the load was applied with no other parts of the system changed. This allowed the comparison of the two X-rays in order to measure the axial displacement that occurred at the fracture site.

5.4.3 Mechanical Calculations

In order to relate the axial displacement at the fracture site with the stiffness of the fracture or stage of healing, it was also necessary to know the force experienced at the fracture site. Figure 5.9 illustrates the forces acting in this system from the lateral view.

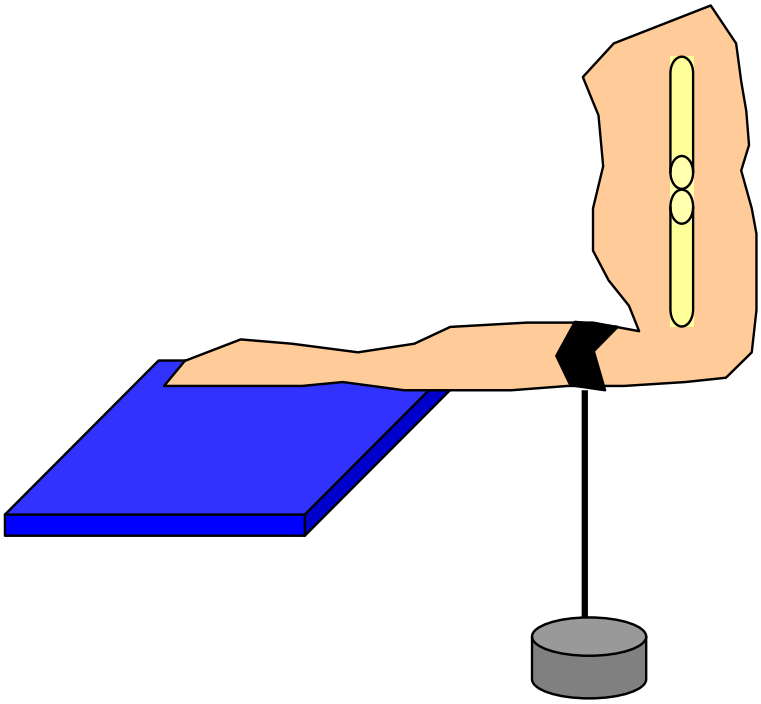

(a)

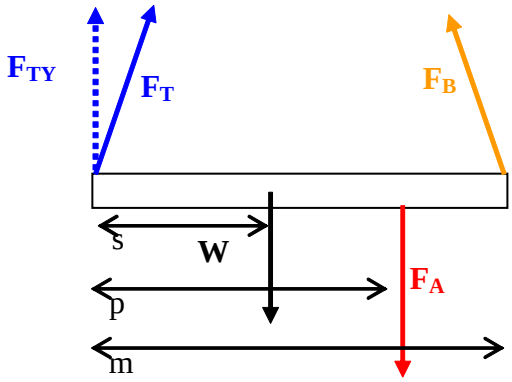

(b)

Figure 5.9: a) The position of the arm, force plate and applied force and b) the corresponding free body force diagram in the lateral view.

The figure shows the different forces acting on each point of the arm in the lateral view. F_{T_Y} is the force measured by the force plate and F_B is the force of interest (i.e. the force through the fracture site when the load, F_A, is applied). In the ideal situation, both of these forces are purely vertical and mechanical calculations showed that assuming these forces to be vertical, even if they were not, introduced a negligibly small error for small angles (2% error for $\theta < 10$ degrees, see Appendix C).

The measurements required to make a full force calculation for F_B, the force through the fracture, required knowledge of the distances s, p and m. However, these are not measurable directly on an AP radiograph, which shows the upper arm only. Unless measurements were made directly on the patient, calculations of the force through the humerus had to be made without this knowledge. It was therefore necessary to make some assumptions when calculating the force through the fracture. Firstly, as discussed above, it was assumed that both the force at the force plate and the force through the arm were perpendicular to the horizontal, i.e. at 90 degrees. Secondly, that the applied force was placed at the elbow joint, i.e. the distances m and p were equal. Thirdly, that the difference between the forces measured at the force plate before and during loading indicated the quantity of applied force through the hand and that the humerus was subjected to the remainder of the applied force. Figure 5.10 shows the simplified free body diagram used to make force calculations on an AP humeral radiograph.

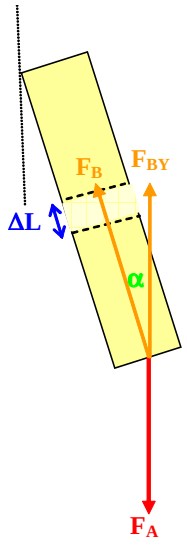

Figure 5.10: Simplified free body diagram of the loaded humeral fracture system in the AP view.

The final force calculations from this diagram are

$$F_B = \frac{F_{B_Y}}{\cos\alpha} \tag{5.1}$$

and

$$S_H = \frac{F_B}{\triangle L} \tag{5.2}$$

where F_{B_Y} is the vertical force due to the applied weight, α is the angle of the arm to the vertical in the AP view, S_H is the stiffness of the humerus, F_B is the force through the humerus, and $\triangle L$ is the displacement at the fracture site. Further assessment showed that negligible error was introduced by assuming $\alpha = 0$ degrees (2% for $\alpha < 10$ degrees). Thus, a reasonable and simple way to obtain an estimate of the axial stiffness of the loaded humeral fracture was

$$S_H = \frac{F_A - (F_{T_{YL}} - F_{T_{Y0}})}{\triangle L} \tag{5.3}$$

where $F_{T_{YL}}$and $F_{T_{Y0}}$ are the forces measured at the force plate with and without applied load, F_A, respectively. Therefore, with some simplifying assumptions, the force through the fracture site could be calculated and this could be related to the resulting displacement and stiffness (see Appendix C for full calculations).

5.5 FRACTURE MODELS AND TEST EQUIPMENT

This section discusses the equipment developed to test the tibial bending frame and humeral tensioning apparatus in X-ray. Phantoms of tibial and humeral fractures which anatomically and mechanically modelled patient fractures and were visible in X-ray images are described. The equipment designed to perform four point bending on the tibial model using the Zwick materials testing machine is also explained.

5.5.1 Internally Nailed Tibial Fracture

The patient group selected for study was those treated with an IM nail. This treatment is usually used for oblique or spiral fractures that cannot be maintained in re-alignment using plaster alone. In the most commonly used closed technique, a guide wire inserted into the medullary canal from the proximal end of the proximal fragment to the distal fragment guides re-alignment of the fracture and reaming of the IM canal (usually to approximately 12 mm diameter). A nail of the correct size is placed into this canal and locked into place

using cross-screws at the proximal and distal ends [7]. Patients in this study had their fractures treated in this way and were placed in the mechanical loading frame to measure bending stiffness.

A model of an IM nailed tibial fracture that could be loaded in the tibial frame was designed using a Sawbones (Pacific Research Laboratories Inc.) fourth generation composite tibia which modelled the external anatomy of a human tibia closely and replicated its physical responses (i.e. tensile and compressive strength and density) using a simulated natural cortical bone shell and rigid polyurethane cancellous core material with an IM canal. The bone was reamed by an orthopaedic surgeon in order to place a Stryker T_2 locking IM nail (Stryker Corporation, USA) down the centre of the bone. This was secured using interlocking screws at the proximal and distal ends. The procedure followed was as similar to the normal surgical technique as possible. The bone was then 'fractured' by making a horizontal cut leaving two separate bone fragments connected only by the IM nail. This modelled a newly fractured tibia. This bone was then placed in a Sawbones anatomical foam lower leg model to mimic the effect of soft tissue surrounding the leg. Phantoms modelling fractures in the proximal and distal thirds were also created. The bone models are shown in Figure 5.11.

The surgical and anatomical situations were well reflected in this model. For the purposes of testing the X-ray frame it was necessary that this phantom not only modelled the anatomical and geometrical situation but was also visible on X-ray. Both Sawbones biomechanical bones and the foam lower leg fulfilled these criteria as Figure 5.12 shows. All parts of the phantom could be seen clearly in the image and were of similar X-ray grey levels to a true patient image.

(a)

(b)

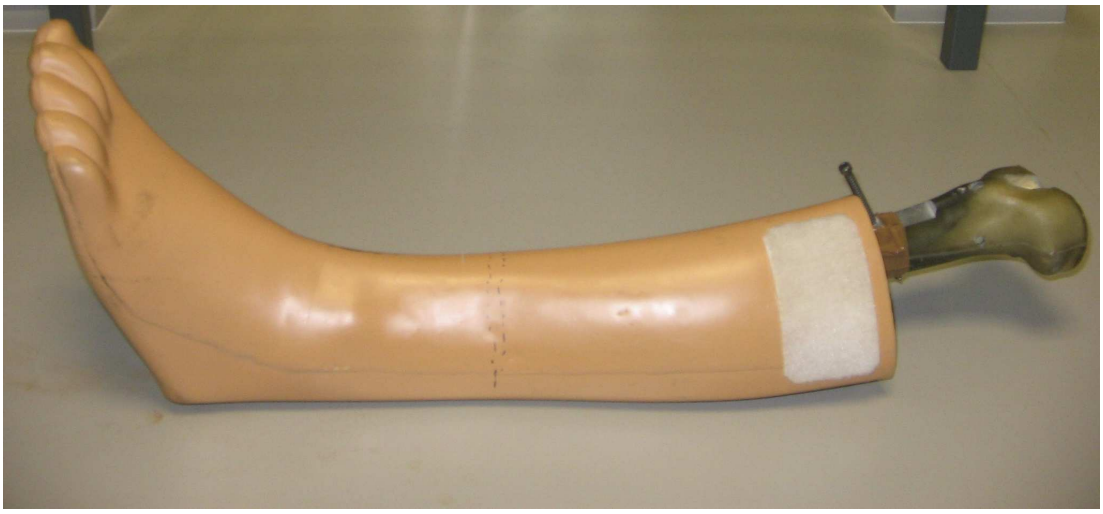

(c)

Figure 5.11: The Sawbones composite bone with IM nail with a) a proximal fracture, b) a distal fracture and c) in the foam soft tissue leg.

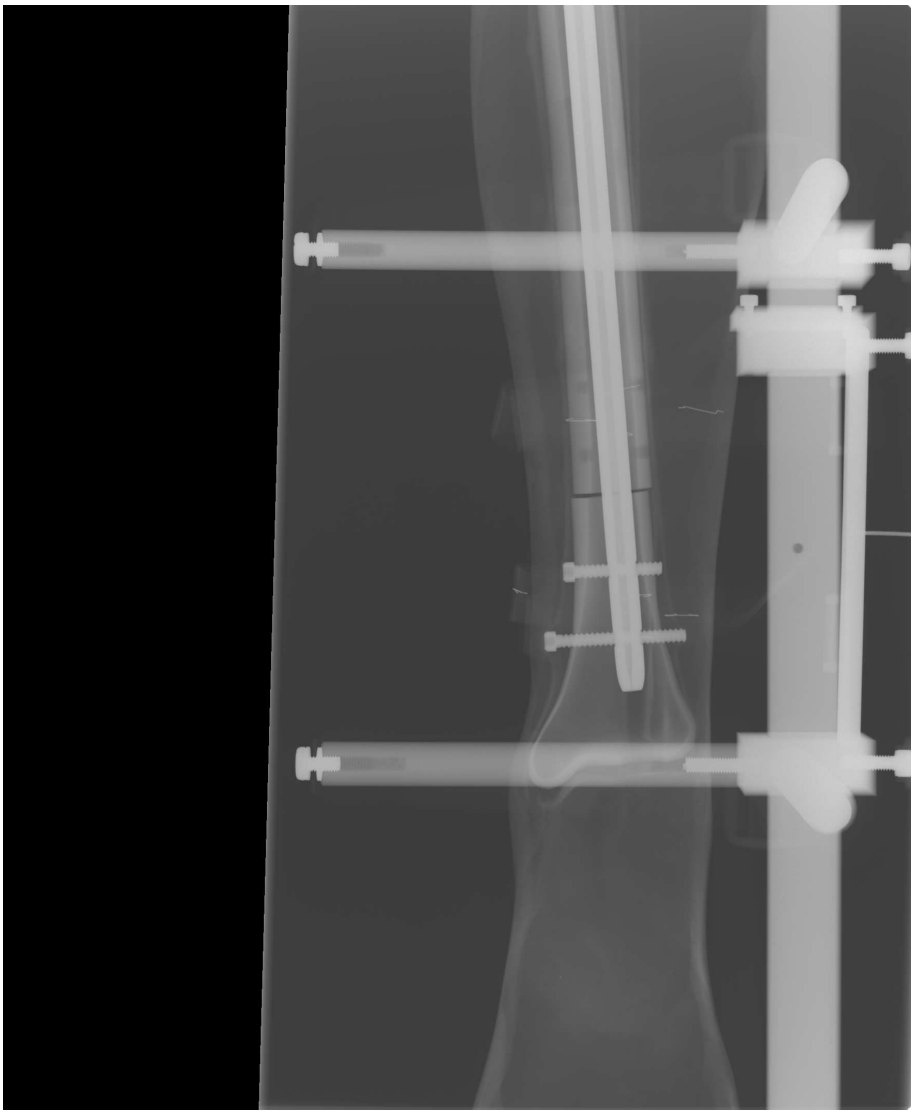

Figure 5.12: Image of the nailed distal fracture in the soft tissue leg placed in the X-ray frame.

5.5.2 Conservatively Treated Humeral Fracture

As with the IM nailed tibial fracture, little literature was available discussing the axial stiffness of conservatively treated fractures. In order to test the magnitude and type of responses expected in a conservatively treated humerus it was necessary to develop a mechanical model of one that was also visible on X-ray. To model the mechanical responses expected in a humerus accurately, the anatomy of the humerus itself had to be replicated as far as possible. A transverse mid-shaft fracture was created in a preserved human humerus using a saw resulting in two distinct segments: proximal and distal. As these segments were not bound together with any surgical fixation device, it was necessary to fix them together with material to model the soft tissue connection.

Physiological callus is a complex material and its properties are difficult to model using commonly available synthetic materials. However, based on the work of Gardner *et al.* in modelling tibial fractures using Aluminium rods and polyurethane foam, it was decided that this approach would provide the best approximation to healing callus [118] . Unfortunately Gardner *et al.* quote only the axial stiffness values in N/mm for the polyurethane foams used in their compressive axial tests on fracture models. Other sources in the literature quote a variety of elastic moduli for callus in the early stages of healing. Some of these are given in Table 5.1. The table shows that values ranging from 0.2 – 76 MPa have been reported for the various tissue types involved in callus healing. The studies quoted in the table all describe the creation of FE models of healing callus. No studies dealing with the elastic modulus of callus in humeral fractures were found.

Table 5.1: Values for the elastic modulus of healing callus.

Author	**Callus Material**	**Time of Healing [weeks]**	**Elastic Modulus [MPa]**
Gardner *et al.*[119]	Tibial, Central material	4	0.2
	Tibial, Adjacent	4	3.8
	Tibial, Peripheral	4	76.0
Lowet *et al.* [120]	Tibial, non-mineralised callus	1 - 2	1.1
Beilin *et al.* [121]	Shaft of long bone	-	0.5

The earliest stage of healing mentioned was 1 – 2 weeks with an elastic modulus of 1.1 MPa and the lowest elastic modulus reported was 0.2 MPa, but none of these studies dealt with humeral fractures. Considering this, it was decided that the ideal elastic modulus

value to model immature callus in a conservatively treated fracture in the early stages of healing would be below 1 MPa. Tests were carried out on a variety of polyurethane foams of a constant geometry (40 mm long, cross-sectional area of 80 mm^2). These were securely fastened into the grips of the Zwick machine, with 15 mm of foam within each grip and a grip-to-grip separation distance of 20 mm, as shown in Figure 5.13. The foam was loaded at 0.2 mm/s until a 5 mm displacement was reached. This was repeated five times and the results were presented in the form of a Force versus Displacement graph over the time of testing. An example graph is shown in Figure 5.14. Values for stress, strain and geometry were calculated and used to find the elastic modulus for each material. The results are given in Table 5.2. Each material is referred to by its manufacturer's code.

Figure 5.13: a) View and b) close up of the Zwick machine with a foam sample secured in the axial grips.

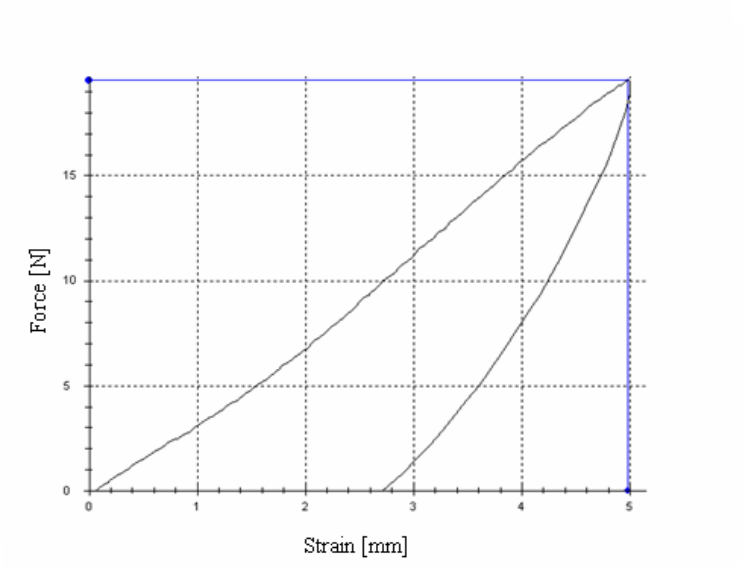

Figure 5.14: The force versus displacement graph for a foam sample loaded until a displacement of 5 mm was reached.

Table 5.2: The elastic modulus of a range of polyurethane foams.

Material	**Elastic Modulus [MPa]**
RL10	0.39
BL22	0.53
EV30	0.65
VA25	0.93
LD45	1.89

The table shows that a variety of suitable values were found. The foam with the lowest modulus (RL10) was chosen to represent callus in the early stages of healing to model the low stiffness values expected in this type of fracture soon after trauma. A 20 mm x 13 mm section of this foam was cut to fit the cross-sectional area of the humerus. This had a thickness of 8 mm. The foam was fixed to each side of the fracture gap using instant contact adhesive. The entire model formed a simulation of a humeral fracture with early stage callus between the two bone ends and is shown in Figure 5.15.

Figure 5.15: Model of a humeral fracture with polyurethane foam representing the callus material.

In order to use this model to measure the expected movement at the fracture site when loaded axially, a holding frame was utilised. This consisted of a height adjustable stand with a side arm at 90 degrees. Two wires were passed through the proximal and distal ends of the humerus. The proximal end was attached to the side arm of the frame and the distal wire was used to attach hanging weights of varying magnitudes. The holding frame, humerus and weights are shown in Figure 5.16. The humerus could be adjusted to the required height for an X-ray to be taken, and weights could be attached for axial loading.

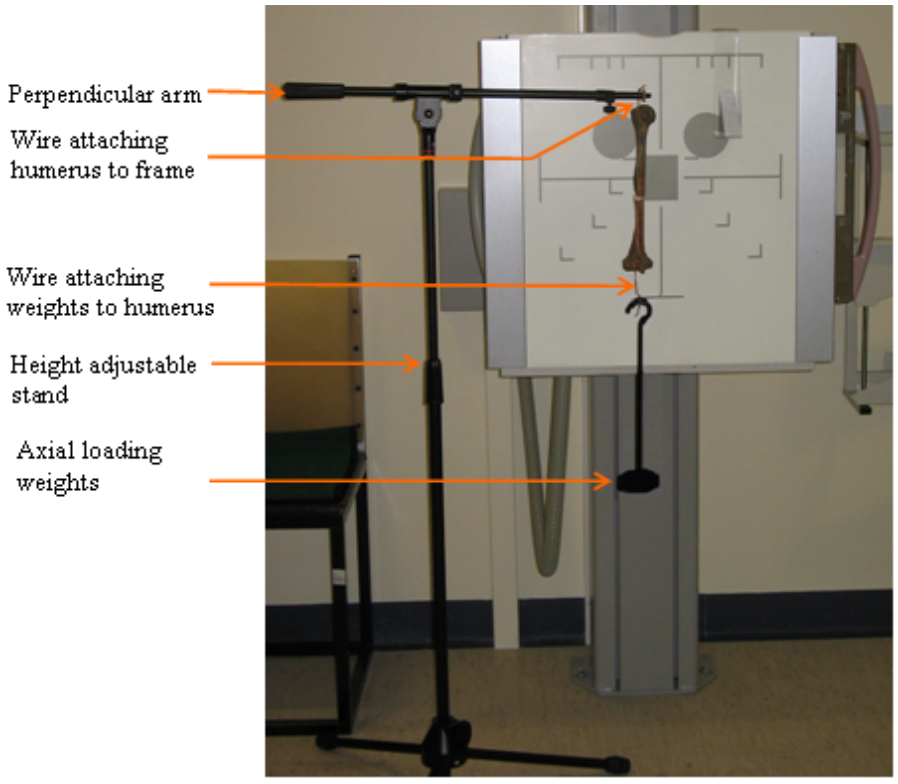

Figure 5.16: The humeral fracture X-ray set up.

Figure 5.17 shows an X-ray image of this humeral model. The bone is radio-opaque whereas the callus foam is not, although changes between the bone ends are still visible for monitoring response to load.

Figure 5.17: X-ray image of the model of an axially loaded humeral fracture.

5.5.3 Materials Testing Machine

In order to validate the measurements obtained using the bending frame, they were compared to four point bend tests using the Zwick materials testing machine. An adjustable four point bending attachment to allow for variable fulcra positioning was designed so that the tibial fracture models could be positioned for bending tests and is shown in Figure 5.18. The lower fulcra could be moved by placing them in any of the screw-hole positions. For the upper, inner fulcra, a sliding system allowing the fulcra to be adjusted to any position was provided. The upper fulcra were applied on a tilting connection to allow both fulcra to make contact with the uneven surface of the bone. This allowed the application of evenly displaced forces.

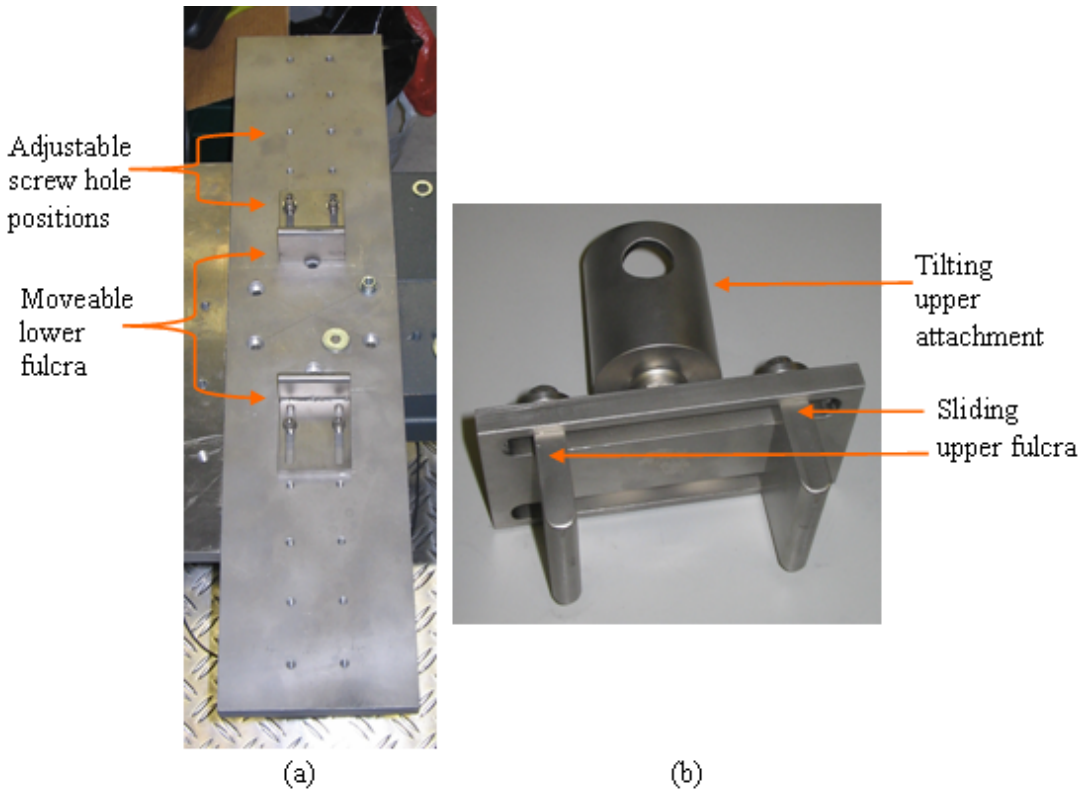

Figure 5.18: The adjustable four point bending apparatus designed for the Zwick testing machine showing a) fixed lower attachment and b) pivoting upper attachment.

5.6 DISCUSSION

5.6.1 Use in the Clinical Setting

The frame to apply bending to tibiae under X-ray was easily manoeuvrable as it was light and small enough to lift onto and off the X-ray table as required. Slots provided for the different projections of X-ray images made the two different loading directions easy to image without the patient having to move and without causing discomfort. The support fulcra of the frame meant the patient's leg could rest comfortably whilst being X-rayed. Outer fulcra were easily adjusted to the correct position for each patient's fracture. Inner fulcra (velcro bands) were easily applied and attached to the brass bar and underwent minimal stretching as the load was applied, whilst at the same time being comfortable for the patient. Both fulcra and velcro could be changed for each patient making the frame hygienic for use in a hospital setting. The steel wires connecting the inner fulcra to the tensioning device experienced little change during loading. The tensioning device was simple to use in terms of increasing or decreasing the load, and this could be easily monitored using the digital

screen output of the spring balance. In case of emergency, the load could be instantly removed by detaching the spring balance from the top of the frame.

The humeral equipment to apply tensile load worked well in a radiography environment. It was light and simple to move in and out of an X-ray room. It was quick to set up and adjustable for patients of a variety of heights. It allowed the loaded and unloaded X-rays to be taken with little change to the conventional radiographic procedure. The different parts of the apparatus were simple and offered a robust way of applying axial load. Little absorption of load occurred in the tightly woven loading strap. The load could be increased and monitored easily and, in case of emergency, removed quickly. The load experienced at the hand was accurately measured using the force plate and easy to monitor using the digital screen.

5.6.2 Measurement of Displacement and Calculation of Stiffness

With the measurements from X-rays, the load and stiffness at the fracture site could be calculated for both sets of apparatus. However, several simplifying assumptions were necessary.

Bending Stiffness

For four point bending it was assumed that the bone-fracture system was an isolated and homogeneous beam, which would respond to load at the site of the callus and was simply supported at both ends. It was also assumed that the applied load was divided evenly between the two inner fulcra. Whilst there were some potential inaccuracies with these assumptions, they were necessary in order to make a simple measurement of the displacement and stiffness at the fracture site based on four point bending theory.

Mechanical engineering theory defines bending stiffness as EI (See Section 3.3). In order to find both E and I, the cross-sectional area of the object under load must be calculated. This was difficult to determine in the case of a tibial bone with an IM nail. One approximation could be as shown in Figure 5.19 where the tibial cross-section is modelled as a triangle and the central nail as a circle. However, there were several problems with this approximation. Firstly, the dimensions of the 'triangular' tibia vary throughout its length and these could not be easily measured using X-ray. Secondly, the tibia is made up of both cortical and trabecular bone, each with different material properties. Finally, there was not only a nail in the centre but also a reamed IM canal. The dimensions of these structures could not be measured from X-ray images or estimated satisfactorily.

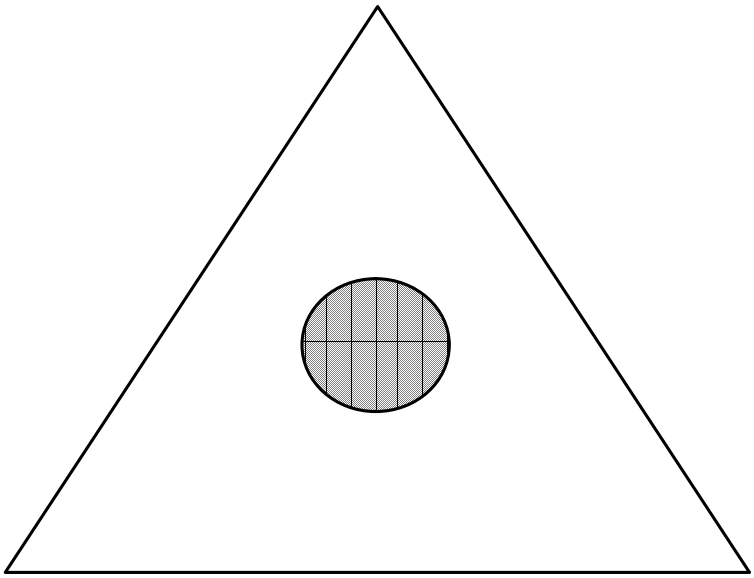

Figure 5.19: Simple model of the cross section of an IM nailed tibia.

It was therefore overly simplistic to make assumptions about the cross-sectional area of the bone in order to get the elastic modulus or stiffness information, and it would be difficult to relate this to the actual properties of the fracture material. Instead, for bending calculations, an approach similar to that used by Richardson *et al.* was chosen where a nominal 'bending stiffness' value was given in Nm/degree, as these are the two quantities (i.e. bending moment and bending angle) which could be measured with some precision [55].

Axial Stiffness

For the axial calculations it was assumed that the arm was at 90 degrees to the horizontal as viewed laterally, and 0 degrees to the vertical as viewed in the AP direction. Calculations simulating the likely deviations from this in the clinical environment showed these to be valid assumptions for angles less than 10 degrees. It was also assumed that the callus would be the major contributor to stiffness and displacement measurements, since its elastic modulus is much lower than that of bone. Further complications were introduced since the loading occurred across two joints. It was assumed that the arm and forearm operated in isolation to the rest of the body. This assumption was valid for loads applied close to the elbow and situations where the patient is relaxed and does not respond to load application with movement at the shoulder.

Axial stiffness is also dependent on the measurement of cross-sectional area of the object under load (see Section 3.3.1) which was not possible from the available X-ray views. There-

fore a nominal 'axial stiffness' value in N/mm was given, as these were the two quantities (i.e. force and displacement) that could be calculated with some precision. This approach was supported in the literature by authors such as Gardner *et al.* and others working with compressive axial forces [63, 68, 69, 118]. However, these values were still dependent on the geometry of the callus and fracture for each patient being measured, and normalisation for geometry would be necessary to standardise all measurements for inter-patient comparisons.

5.6.3 Fracture Models

There are no previous reports of studies on either IM nailed tibial fracture patients or conservatively treated humeral fractures loaded in tension. In order to test the possibility of measuring responses to load in these patients, models of an internally nailed tibial fracture and conservatively treated humeral fracture were designed. Previous researchers have modelled fractures using Aluminium, plastic or plexiglass rods [25, 71, 118]. Stiffness depends on the geometry of an object. This is especially important when modelling the anatomy as the geometry is complex and difficult to mimic with conventional materials such as rods. Use of the human humerus allowed the anatomy of the bone to be modelled realistically. The Sawbones biomechanical tibia mimicked the biomechanical nature and anatomy of a human tibia.

Although the complex mechanical nature of callus is difficult to replicate using a synthetic material, polyurethane foam has previously been used effectively [118]. However, it has also been reported in the literature that callus is viscoelastic in nature [38]. Thus, any attempt to model it accurately using artificial material would require a careful study of the mechanical response of the callus in various loading environments. Although necessarily simplistic, evaluation of the elastic modulus of the foam used in the humeral fracture model showed that it gave an acceptable representation of callus in the early stages of healing in terms of its mechanical response to axial load.

The effects of soft tissue on mechanical measurements have also been mentioned by several research groups [25, 63]. In the tibial fracture model, the foam surrounding of the tibia was used to mimic soft tissue, but unlike a true leg, it was flattened on the underside. Perhaps more importantly, the casing was made of simple foam. This was not a true reflection of *in vivo* soft tissue which contains combinations of muscles, fat, nerves and blood vessels. The humeral fracture model did not take into account soft tissue effects but this was not considered to be essential with axial loading. Furthermore, loading in this fracture occurs across the elbow and shoulder joints, which were not modelled in the fracture phantom.

Both fracture models have clean, transverse fractures. However, most traumatic fractures do not occur in this fashion and complex fracture patterns resulting from trauma to the

bone create a variety of different fracture anatomies which were not feasible to model in these simple studies. Oblique, spiral, comminuted, compacted or avulsion fractures can occur, often including bony fragments [7]. Beaupre *et al.* noted that the configuration of the fracture surfaces is an important issue when applying stiffness tests clinically to fractures as opposed to in models [71]. The anatomy of the fracture will alter the response of the fracture to load, and these various anatomies were not taken into account in these fracture models. This is less likely to affect the measurement with axial loading compared to bending.

All these factors created a complex mechanical environment which was difficult to model in a simple fashion for feasibility tests. Despite these shortcomings, these phantoms provided a sufficiently accurate reflection of the underlying structures of interest to give approximate predictions of the response of an IM nailed tibial fracture and a conservatively treated humeral fracture to loading, as well as how this could be measured using X-ray imaging.

5.7 SUMMARY

This chapter described the equipment that was designed to investigate mechanical stiffness measurements using digital X-ray. An Aluminium frame to apply a four point bending moment to an IM nailed tibial fracture was constructed and apparatus to apply a tensile axial load to a conservatively treated humeral fracture was designed. Models of both types of fracture were made using Sawbones and preserved human bone. These were designed to mimic the mechanical environment of a healing fracture and to be visualised using X-ray. Limitations are placed on the information available during this type of testing due to the complicated geometrical considerations of human anatomy. However, useful measures, especially of intra-patient healing, are still possible. The use and testing of the apparatus described here is discussed in the following chapters.

Chapter 6

Image Analysis of Loaded and Unloaded X-rays

6.1 INTRODUCTION

One of the aims of this study was to determine whether the degree of healing of a fracture could be measured by examining its response to load. The previous chapter described the equipment developed to load fractures and the phantoms designed to model tibial and humeral fractures. This chapter describes the computerised procedures that were developed to analyse the digital X-ray images of loaded and unloaded fractures to acquire stiffness information. Programs to measure the angle and offset induced between fracture fragments were designed and tested on X-ray images of modelled fractures.

6.2 COMPARING LOADED AND UNLOADED IMAGES

6.2.1 Previous Methods

In the 1980s, Hammer, Edholm *et al.* attempted to use X-rays to measure response to load [18, 58, 59, 60]. In their method they used 'X-ray overlay' to compare loaded and unloaded images which involved viewing the X-rays alternately using a semi-transparent mirror and two light boxes. One image was rotated until only the proximal fragment appeared to move and the degree of rotation of this image was used as the measurement of deflection of the fracture under load. The potential of digital X-ray imaging and the associated image processing techniques available suggested that a more efficient way of measuring the change in fracture could be developed.

6.2.2 Cross-Correlation

A conceptually similar approach to that used by Hammer, Edholm *et al.* is cross-correlation. Cross-correlation is a method of comparing two different functions and is commonly used in signal processing to determine the similarity between different signals [122, 123, 124]. In the discrete case (as with digital images) it is defined as

$$r_{fg} = (f * g)[n] = \sum_{m=-\infty}^{\infty} f[m]g[n+m] \tag{6.1}$$

where r_{fg} is the cross-correlation of f and g, f and g are the signals of interest and n is a shifting factor.

Equation (6.1) shows that the shifting factor, n, is used to 'slide' the two signals across each other while m is a dummy variable and disappears during the summation. This creates a cross-correlation function with a peak which occurs where the waveforms match up. Essentially, the cross-correlation is a measure of the sum of the products of the two signals. Two unrelated signals will tend to have randomly varying products which will sum to zero. However, signals with a degree of similarity will create a final product sum and this is a measure of their similarity.

For 2D images, by shifting function g across function f, a 3D plot is formed illustrating the points at which the two functions are most similar. An example is shown in Figure 6.1 where the peak (indicated in red) is at the position of the images where the result of the cross-correlation is greatest. The (x, y) position of this peak gives the information required to align the two images. This principle of cross-correlation was used to identify the optimal way to align the X-ray images of loaded and unloaded fractures.

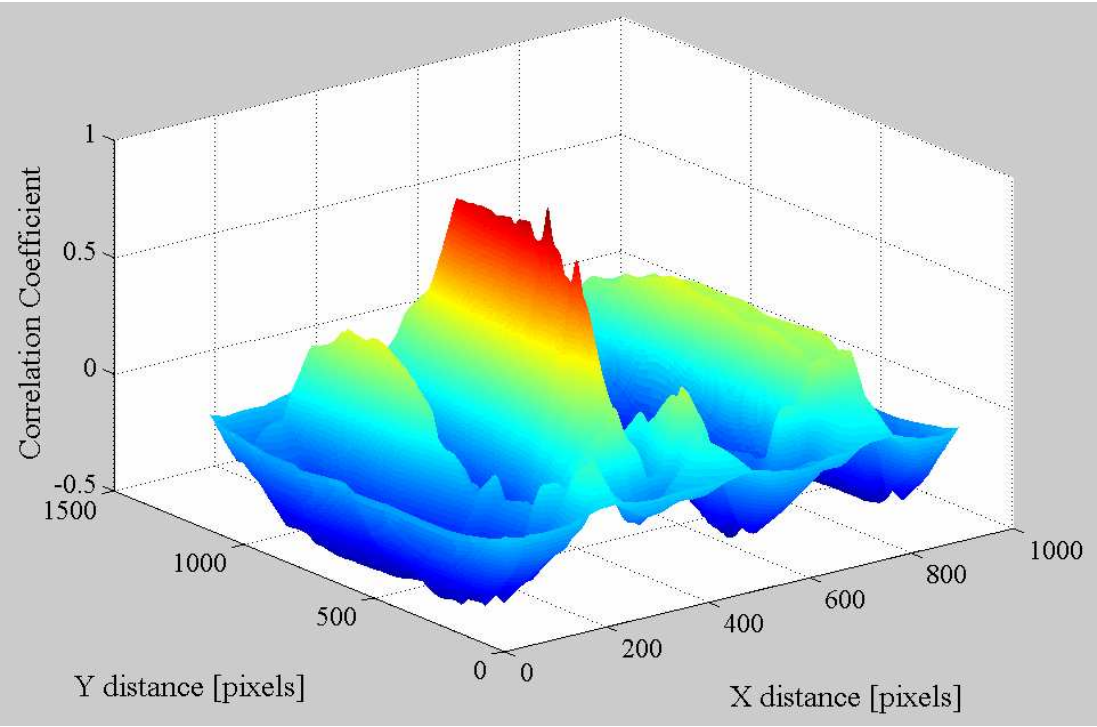

Figure 6.1: A three dimensional cross-correlation plot generated in Matlab.

6.3 MEASURING OFFSET

Three types of movement needed to be analysed when comparing loaded and unloaded X-rays. In the case of four point bending, angular movement and lateral (or horizontal) displacement had to be derived. In the case of humeral fractures loaded in tension, axial displacement had to be detected. This section describes the methods used to measure these quantities on X-ray images.

6.3.1 Bending Angle of a Loaded Tibial Fracture

The first type of fracture considered is the IM nailed tibial fracture which was placed under four point bending. The radiographic phantom described in Chapter 5 was X-rayed in the frame to obtain images of this. According to previous authors working on conservatively treated and externally fixated fractures, force applied to a fracture results in a bending angle. Therefore, the first method attempted was one to measure bending angle.

A computerised procedure was designed which attempted to measure the angular deflection induced by four point bending. In this program, both sections of the fracture were selected in the unloaded X-ray, and the proximal section of the bone was selected in the loaded X-ray.

This proximal section was then rotated in increments of 0.1 degrees and the cross-correlation with the unloaded image was calculated. The degree of rotation where the cross-correlation returned the highest peak was used as the angular movement of the fracture under load. However, on closer visual analysis of the images, it was noticed that a displacement, rather than an angular bend, was occurring at the fracture site. This is illustrated in the X-rays in Figure 6.2 which show that although little angular variation occurs, a more measurable lateral displacement is visible. This can also be seen by the movement of the nail within the IM canal of the bone. For this reason, it was decided that a measurement of both angle and lateral displacement was necessary.

(a)

(b)

Figure 6.2: a) Unloaded and b) loaded Sawbone tibial fractures.

6.3.2 Displacement of a Loaded Tibial Fracture

Two approaches for measuring the lateral displacement were attempted. The first used simple geometry. In this approach, the user was asked to select the four 'corners' of the bone fragments, as shown in Figure 6.3.

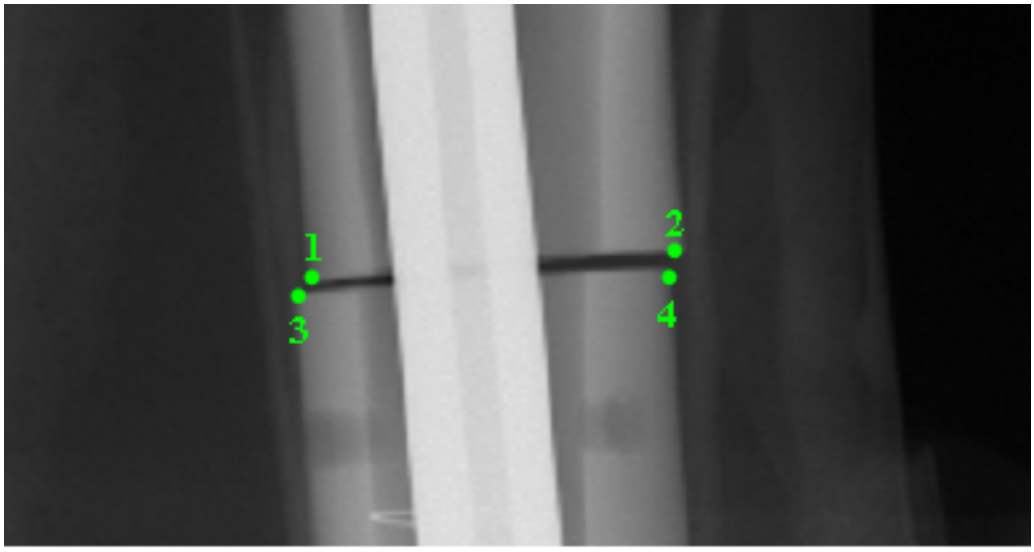

Figure 6.3: The four 'corners' of the fracture segments.

The image shows the four corners labelled 1 to 4. The upper points (1 and 2) were used to calculate the angle of the upper segment to the image's x-axis (horizontal axis) by

$$\theta = \arctan(\frac{y_1 - y_2}{x_1 - x_2}) \tag{6.2}$$

This angle was used to transform all the points to a new co-ordinate system with an origin at 1 and with x-axis, x', in the direction of 1-2 and y-axis, y', perpendicular to this. Figure 6.4 shows the original image axes, and the new transformed axes which were at an angle to the image axes. The calculations to perform these transformations can be found in Appendix D. The lateral displacement of the segments was the x' displacements between the two lines 1'-2' and 3'-4'. The displacement between the bone segments was calculated for the loaded and unloaded images and the difference between these was used as a measure of the displacement caused by loading the fracture.

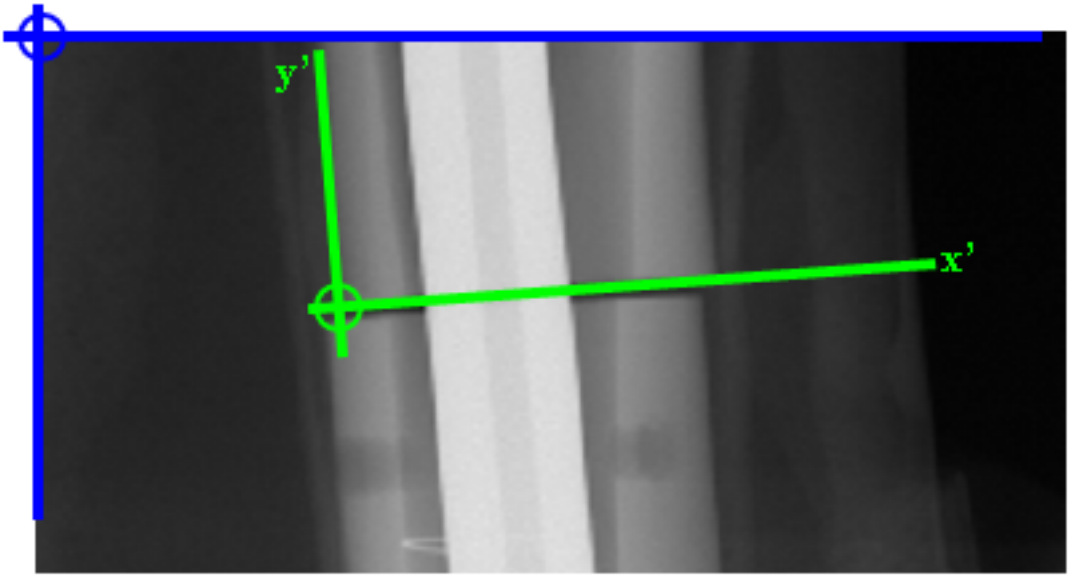

Figure 6.4: The image co-ordinate system (blue) and the transformed co-ordinate system (green).

In order to investigate the repeatability of the technique, it was executed five times on the same image. The standard deviation (SD) of the measurements was calculated and found to be 35% of the mean displacement measurement. This represented an unacceptable variation in the offset returned by the program for the same image. It was decided that the inaccuracy and variability introduced by the user's marking of the four points was undesirable and that better, more consistent results could be achieved if this was eliminated.

The second method designed to measure lateral movement between the two bone segments was cross-correlation. Since the cross-correlation function measures the displacement between two images, it could also be used to measure the offset between the bone ends of the loaded and unloaded X-rays. However, it was first necessary to ensure that the co-ordinate systems of both images were the same so that accurate comparisons could be made. To do this, the images were first aligned according to the proximal segment using cross-correlation. They then had the same co-ordinate system, related to the proximal segment, which was unchanged in each image. Cross-correlation was performed on the distal segment to calculate the offset between the two fracture segments.

The algorithm of this procedure was as follows:

1. Crop the unloaded image between the two outer fulcra. The co-ordinates of the cropping rectangle are used to crop the loaded image to the same size.
2. Crop the proximal segment of the loaded image.
3. Rotate the proximal segment incrementally, cross-correlating with the unloaded image until the best angle for alignment is found.
4. Rotate the entire unloaded image by this angle.
5. Use the position of the peak of cross-correlation (which gives the offset between the two images) and the co-ordinates of the cropping rectangle (which gives the offset of the cropped portion from the origin) to calculate how much the loaded image must be offset from the unloaded image so that the upper segments align exactly (see Appendix E).
6. The result is two images of identical size and equivalent co-ordinate systems, defined by the proximal segment of the bone.
7. Crop the distal segment of the padded loaded image.
8. Rotate the unloaded image incrementally, cross–correlating with the distal segment to find the best angle of rotation to align the images.
9. Rotate the entire padded loaded image by this angle, which is the total bending angle.
10. Calculate the offset between the distal segments using the position of the cross-correlation peak and the cropping rectangle. Since the co-ordinate systems are the same, this is the change in offset between the proximal and distal segments between the loaded and unloaded images.
11. The final images are padded with zeros and overlaid to illustrate the accuracy of alignment.

Images illustrating the cropping stages of this program are shown in Figure 6.5. When cropping the distal segment, the black borders of the image, which are delineated with a blue dotted line in Figure 6.5 (c), illustrate the zero padding used to create images of identical sizes.

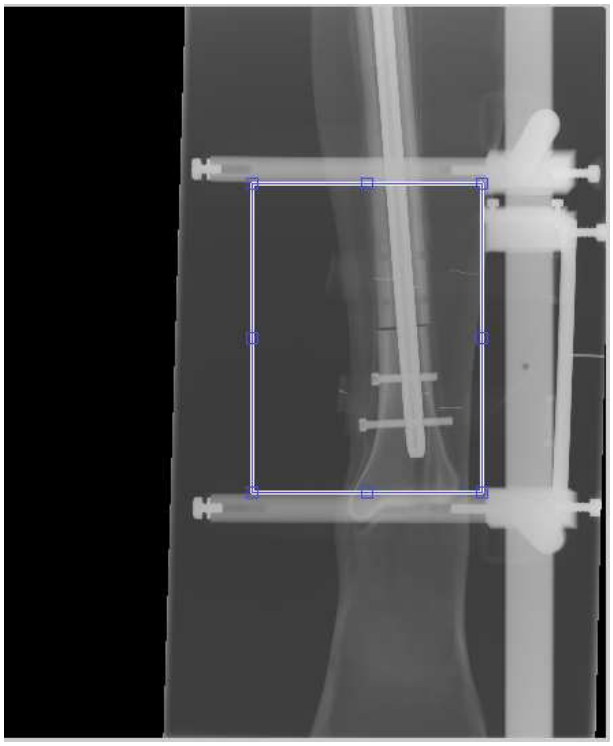

(a)

(b)

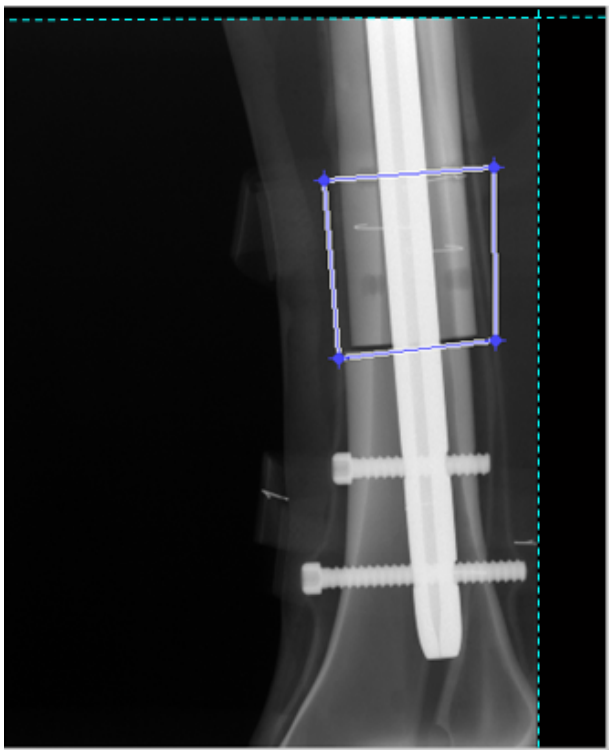

(c)

Figure 6.5: Cropping a) the image between the bars, b) the proximal segment and c) the distal segment showing the areas of zero padding (dotted lines).

6.3.3 Displacement of an Axially Loaded Humeral Fracture

The movement expected in a conservatively treated humeral fracture under tensile axial load was an axial (or vertical) displacement. The program described above used cross-correlation to measure the angle and offset of a loaded tibial fracture. It was also suitable to measure the axial offset of the distracted humerus as well as any angular or lateral displacements that might be induced. Therefore the same method used to measure tibial movement was used to measure humeral movement.

6.4 ASSESSING THE PROCEDURE

This section describes the tests to determine the precision, accuracy and repeatability of the computerised procedures described in Section 6.3. An initial evaluation of the efficacy of the program in correctly re-sizing and aligning the images was made by a visual check of the aligned images displayed in Red Green Blue (RGB) colour channels. The precision of the cross-correlation program was calculated by combining the precisions of the cross-correlation and rotation procedures.

6.4.1 Accuracy

The accuracy of a method is the difference between measurements produced by the method and those produced by another reliable approach. In order to determine how accurately the program can measure offsets and bending angles, a series of X-rays of known displacements and bending angles were taken. These were performed using a human humerus and a Sawbones composite tibia, both of which had been 'fractured' in the mid-shaft using a saw to create two separate segments. Three sets of tests were performed. In the first, the accuracy of displacement measurement was tested, the second measured the accuracy of angular measurement and the third measured the effect of rotation of the bone on measurement accuracy.

In the first test, the proximal and distal segments of each bone were placed a known distance apart, as shown in Figure 6.6.

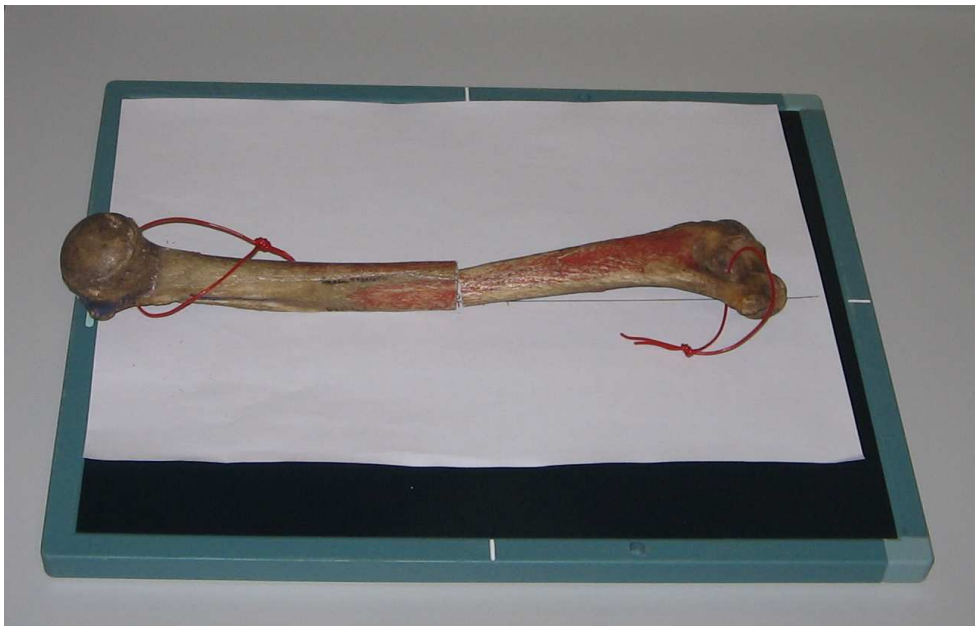

Figure 6.6: The humeral fracture model placed for axial offset measurement.

As the image shows, exact alignment of the two separate bone ends was not easily achievable. A measurement of the alignment was made using a ruler measuring the distance between the two fracture segments. Due to the difficulty of alignment, further measurements were made manually on the X-ray images to confirm the initial ruler derived measurements.

An X-ray was taken of approximately 0 mm, 3 mm, 5 mm and 10 mm displacements for the humerus and 0 mm, 5 mm, 10 mm, and 20 mm displacements for the tibia. Examples of these images are shown in Figure 6.7. The cross-correlation procedure was executed to compare each image to the 0 mm displaced image and therefore obtain an axial displacement measurement. These were then compared to the measurements made manually.

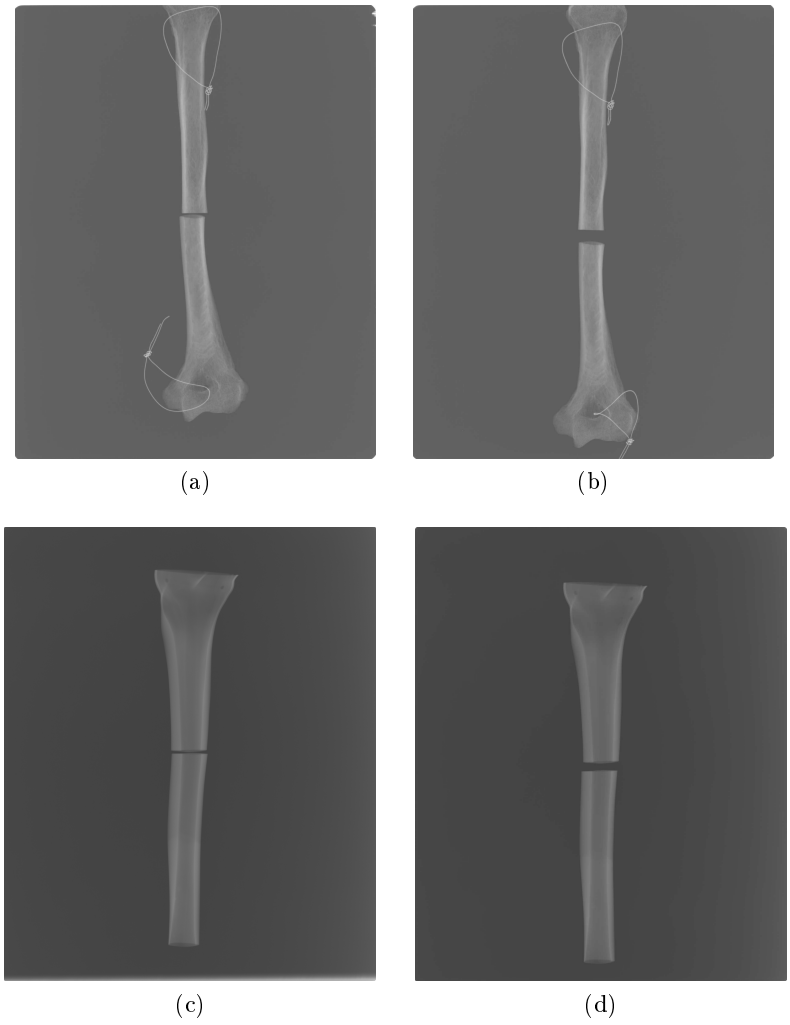

Figure 6.7: The humeral bone segments at a) 0 mm and b) 10 mm displacement. The tibial bone segments at c) 0 mm and d) 10 mm displacement.

In the second test the segments of the tibia were placed to create different bending angles, as shown in Figure 6.8. The angular offset was achieved by moving the distal segment. Again, the fact that the two segments were irregular made exact alignment difficult. Physical measurements with a protractor and verification using manual measurements from X-ray were used to obtain the true angular offset.

X-rays were taken for 0 degrees, 5 degrees, 10 degrees, 15 degrees, 20 degrees and 30 degrees. Examples of these X-rays are shown in the Figure 6.9. The program was executed comparing each image to the 0 degrees image to get a measure of the bending angle. These measurements were compared to those made physically to calculate the differences between the two methods.

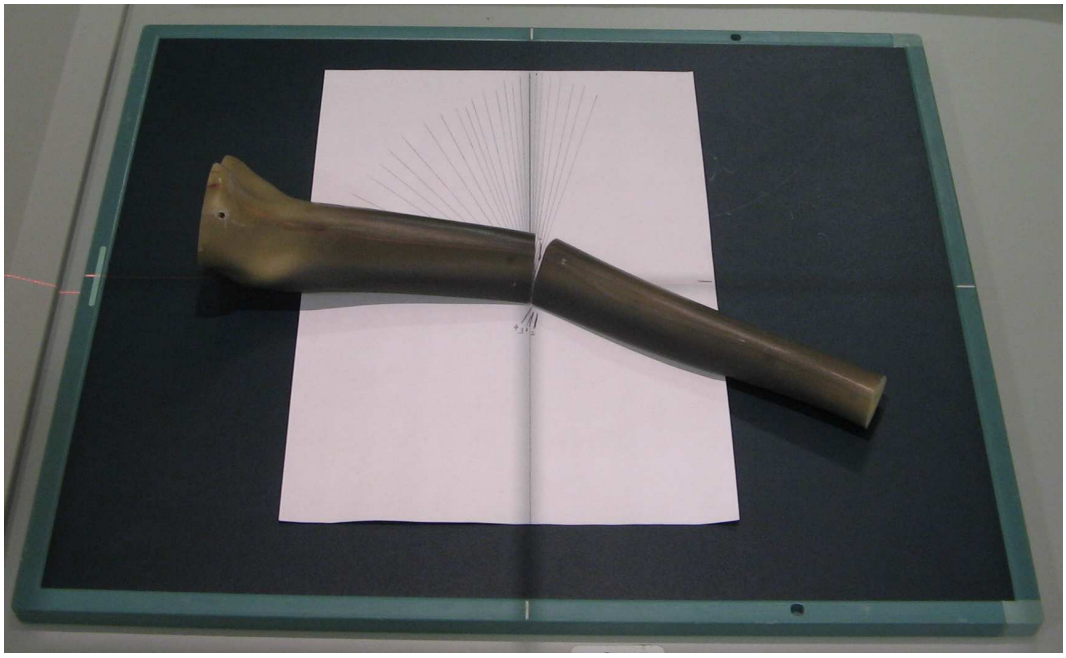

Figure 6.8: The tibial fracture model placed for bending angle measurement.

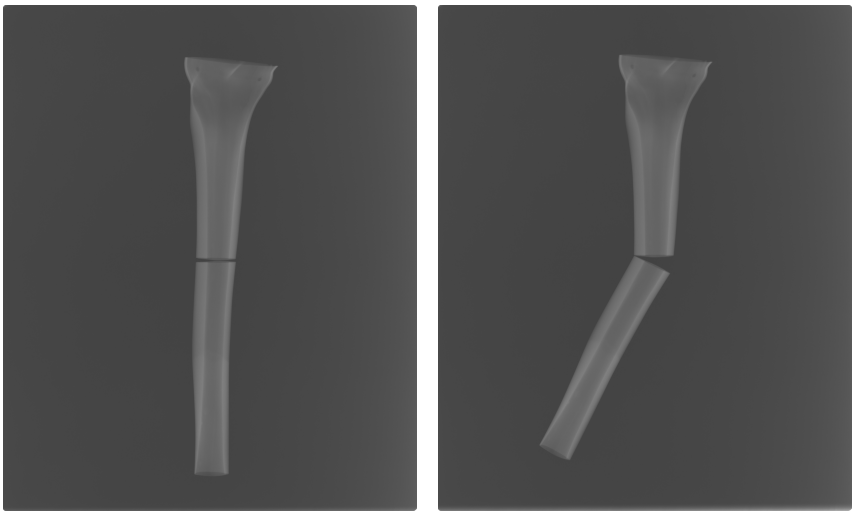

(a) (b)

Figure 6.9: The tibial segments at a) 0 degrees and b) 30 degrees bending angle.

In the third test, two bending angles (10 degrees and 20 degrees) were recreated. However, in this test, the proximal segment of the tibia was rotated axially through 0 degrees, 10 degrees and 30 degrees, as shown in Figure 6.10. The rotation of the tibia was measured using a laser beam to provide a reference 0 degree point. Examples of the X-ray images

are shown in Figure 6.11. Each rotated image was compared to the 0 degrees rotation to provide a measure of the uncertainty introduced.

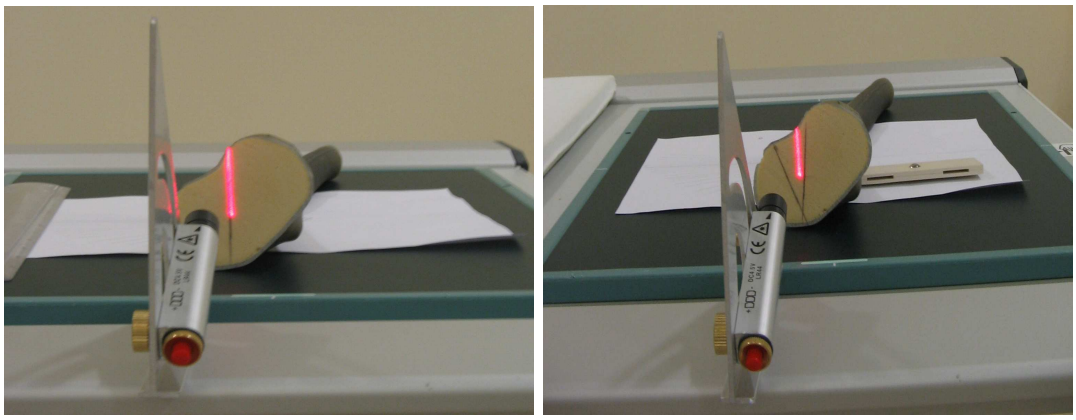

(a) (b)

Figure 6.10: The tibial fracture rotated axially by a) 0 degrees and b) 10 degrees, as measured by a laser.

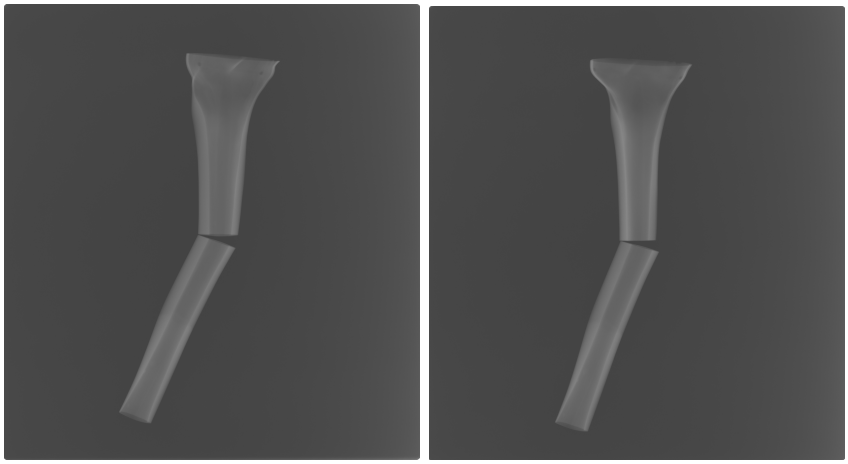

(a) (b)

Figure 6.11: The tibial segments at 20 degrees bending angle and a) 0 degrees and b) 30 degrees axial rotation.

6.4.2 Repeatability

In order to ascertain how consistently the program returned measurements of bending angle and offset, it was executed three times for each of the images described above. The SD in the measurements was used as an indicator of the repeatability. Measurements of bending angle and axial offset were also made manually in Image J to provide a comparison of the repeatability achieved with a recognised X-ray measurement tool.

6.5 RESULTS

The initial evaluation of the cross-correlation program was made by examining the final overlaid images, which are shown in Figure 6.12. The unloaded image is displayed in the green colour channel and the loaded image in the red colour channel. Where these images align, the image appears yellow due to the colour overlay. Areas where the images do not align appear in red or green. Visual inspection of the image showed a good alignment of the loaded and unloaded X-rays.

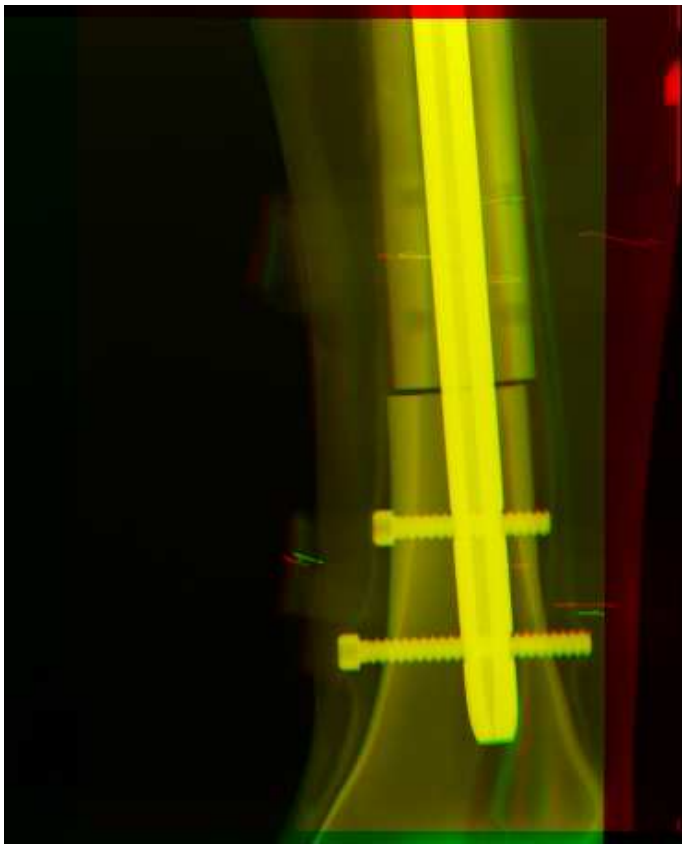

Figure 6.12: Colour overlay of the shifted and rotated images.

6.5.1 Precision

The precision of the cross-correlation system was the degree of uncertainty with which it produced measurements. The cross-correlation operation treated each image as a matrix of numbers. It returned the position of optimal alignment as an (x, y) position of these numbers. Since each number is a pixel, it could be said that the program could measure offset to within a pixel. Since there were 5 pixels per mm, the offset precision was 0.2 mm. In terms of angle, in order to ascertain the ideal angular offset the images were rotated in steps of 0.1 degrees so this was the angular precision of the procedure.

6.5.2 Accuracy

The results of the first accuracy test are given in Table 6.1. The difference between the manually measured displacement and that calculated by the cross-correlation procedure is shown. A dash indicates that no images were taken for the given offset. The table shows that using the procedure to calculate the axial offset gives an approximate difference of 2.3 mm from the physical measurement. The largest measured difference was 3.0 mm.

Table 6.1: Differences in axial offset measurements between manual evaluation and the cross-correlation.

Axial Offset [mm]	**Difference [mm]**	
	Humerus	**Tibia**
0	1.2	1.6
3	1.9	-
5	1.7	2.4
10	1.5	2.0
20	-	3.0

The results of the second accuracy test are shown in Table 6.2. The difference between the angular offset calculated using cross-correlation and that measured manually is given. The difference in measuring the bending angle using the two techniques was approximately 1.5 degrees, with the largest error of 4 degrees occurring at the small angle measurement of 5 degrees.

Table 6.2: Differences in angle measurement between cross-correlation and manual measurement.

Angle [degrees]	**Difference [degrees]**
0	0.0
5	4.0
10	1.3
15	0.9
20	1.4
30	0.1

The results of the third accuracy test are shown in Table 6.3. The difference between the angular offset measured with no rotation and that measured with rotation of the proximal segment are shown. The maximum difference introduced by rotating one segment of the tibia was an underestimation of bending angle of 3.4 degrees. The mean difference was an underestimation of 1.3 degrees. The table shows that the difference introduced by axial rotation is larger at smaller degrees of rotation. However, no result could be obtained for 30 degrees rotation since the cross-correlation failed to match the proximal segments correctly because rotation had changed the geometry. This is shown in Figure 6.13. Due to the change in appearance of the proximal segment after rotation, the procedure erroneously aligned the proximal segment of the rotated tibia with the distal segment of the non-rotated tibia.

Table 6.3: Differences introduced by axial rotation compared to 0 degrees axial rotation.

Rotation [degrees]	**Angle [degrees]**	**Difference [degrees]**
10	10	-0.6
	20	-3.4
30	10	No Result
	20	-0.6

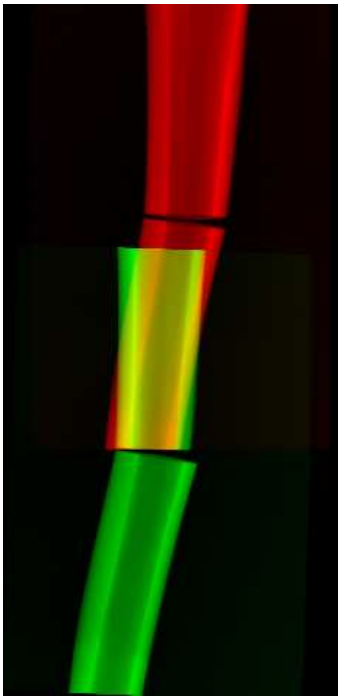

Figure 6.13: Image showing the mis-alignment of the proximal segment of the rotated tibia (green) with the non-rotated tibia (red).

6.5.3 Repeatability

The results of analysing X-rays three times for each angle and offset measurement are given in Table 6.4. The repeatability of both offset and angle measurements was indicated by the SD of the measurements. Using the cross-correlation procedure gave lower SDs than when making measurements manually. The improvement in repeatability was greater for angle measurements than offset measurements. Compared to the mean measurements, both results showed acceptably low SDs between repeated measurements.

Table 6.4: Mean and SD of displacement measurements made with the cross-correlation procedure compared to Image J.

Measurement	**Mean (SD)**	
	Cross-Correlation	**Image J**
Axial Offset [mm]	3.5 (0.1)	5.4 (0.4)
Angle [degrees]	10.7 (0.1)	12.7 (0.9)

6.6 DISCUSSION

The final procedure developed to analyse and align loaded and unloaded images was cross-correlation. The differences in alignment of the upper and lower segments of the fracture provided measurements of the angular and displacement offsets caused by loading of the fracture. The previous sections have given results for the precision, accuracy and repeatability of the cross-correlation program to measure bending angle and offset. These are three distinct but important measurements of the performance of a system. When combined, they gave an indication of the effectiveness of the computerised procedure.

The accuracy of the procedure was found to be within 2.3 mm and 1.5 degrees for tibial measurements and within 1.6 mm for humeral measurements. The differences between measurements returned by the procedure and those made manually using a ruler and protractor on the phantoms themselves were high. A possible explanation for this was that in the set up of this test, the irregular geometry of the bones made an accurate manual measurement of offset and bending angle difficult. For instance, one side of the distal segment end might have been closer to the proximal segment than the other side. This made the measurement of the 'true' offset difficult and these difficulties were noted at the time of performing the experiments. The differences between the measurements from the cross-correlation procedure and those made manually may not be as large as these tests indicated since the original manual measurements may not have been very precise. Furthermore, these measurements were limited by the precision of basic tools such as rulers and protractors, which was only 1 degree or 1 mm, whereas the computerised procedure had a precision of 0.2 mm and 0.1 degrees.

The repeatability of the procedure was very good, giving consistent measurements for both angle and offset in the same images. The repeatability was found to be ± 0.1 mm for displacement measurements ± 0.1 degrees for angular measurements which was an improvement on the repeatability of measurements made manually. This was probably due to the fact that the manual measurements were prone to user error and inconsistency in selecting the points to measure. Furthermore, with manual X-ray measurement, displacement and angle were measured using single points of the X-ray, whereas with cross-correlation, the entire image was used to calculate the displacements. This gave a greater consistency between repeated angle and displacement measurements.

The accuracy and repeatability results in this study indicated that whilst the computerised procedure could reliably give the same measurement, this might not be an exact measurement. This suggested that the procedure was best suited to provide longitudinal comparisons, rather than accurate quantitative measures which could be used to derive meaningful values for material properties. However, a reliable reference measurement technique with which to compare the values calculated by the cross-correlation procedure would be necessary to get a true measure its quantitative accuracy.

Previous reports of the use of X-ray to perform similar measurements in loaded and unloaded X-rays were those of Hammer *et al.* who used a procedure conceptually similar to the cross-correlation used in this study, termed X-ray 'overlay' [18, 58, 59]. After the completion of this study, results were published reporting the use of radiostereometric analysis (RSA) to monitor fracture movement in X-rays [125, 126]. Two studies reported investigations of axial loading of internally plated femoral fractures and hand grip tests of internally plated distal radial fractures respectively. Both required the insertion of tantalum marker beads to the ROIs and the use of RSA X-ray equipment and software to calculate motion at the fracture site. No validation tests were carried out in the femoral study, and repeatability results in the radial study indicated that measurements could be made within 0.06 - 1.3 mm and 0.5 - 1.0 degrees. The repeatability of the technique in this study is similar. The RSA results indicated the feasibility of the method to monitor within-patient changes in fracture healing, although noted the high cost and invasiveness of the RSA procedure and the small magnitude of measured displacements. This supports the findings of this study and further indicates that the use of X-ray to monitor fracture healing properties is an area with potential for further investigation.

6.7 SUMMARY

This chapter discussed the methods used to analyse loaded and unloaded X-rays of tibial and humeral fractures. A computerised procedure to measure the bending angle and offset induced by loading a fracture under X-ray was developed using cross-correlation. Accuracy and repeatability tests were performed on X-ray phantoms of tibial and humeral fractures and the results showed this to be a repeatable method to make measurements of the effect of loading on digital X-rays. The following chapter describes the comparison of this measurement technique to standard methods of testing materials.

Chapter 7

Pre-Clinical Stiffness Testing

7.1 INTRODUCTION

The previous chapters described the development of the physical apparatus and image processing tools necessary to perform investigations into the use of digital X-ray to measure movement at a fracture site under load. This chapter describes preliminary studies that were conducted to ascertain the effectiveness of these devices and processes. These include mechanical and simulated X-ray tests of the Sawbones models of tibial and humeral fractures under load to compare expected and measured displacements.

7.2 ASSESSMENT METHODS

7.2.1 Tibial Bending Frame

The tibial bending frame has been described in Section 5.3. It was shown that accurate placement of the inner and outer fulcra would result in a four point bending application of force across the fracture site. The digital spring balance recorded the force applied and the X-ray images were used to measure the distances necessary to calculate bending moment. These images were also analysed to provide the bending angle induced and the displacement occurring between the segments using cross-correlation. In order to verify the usefulness of the bending frame, it was necessary to ascertain how it performed in comparison to conventional methods of applying and measuring bending moment. For this reason it was decided to compare measurements made on the Sawbones proximal and distal tibial fracture phantoms using the bending frame to measurements made using the Zwick materials testing machine.

The two Sawbones phantoms which modelled fractured tibiae were used (see Section 5.5). One was fractured in the proximal third segment and the other in the distal third segment. Both were fixed securely with an IM nail using the normal surgical procedure. Each fractured Sawbone was placed inside a foam, 'soft tissue' leg and these were placed in the tibial bending frame. The straps were placed securely around the fracture site at approximately 70 mm apart, and the outer fulcra were placed symmetrically on either side of these at approximately 200 mm apart. For each phantom, a 10 kg load was applied. This was repeated three times for X-rays in the AP direction and three times in the lateral direction. The resulting X-ray images were used to obtain measurements of fulcra spacing using the pixel to mm conversion information given in the DICOM file header. Examples of these measurements are shown in Figure 7.1. A is the distance between the outer fulcra, B is the distance between the inner fulcra and C is the distance from outer to inner fulcrum.

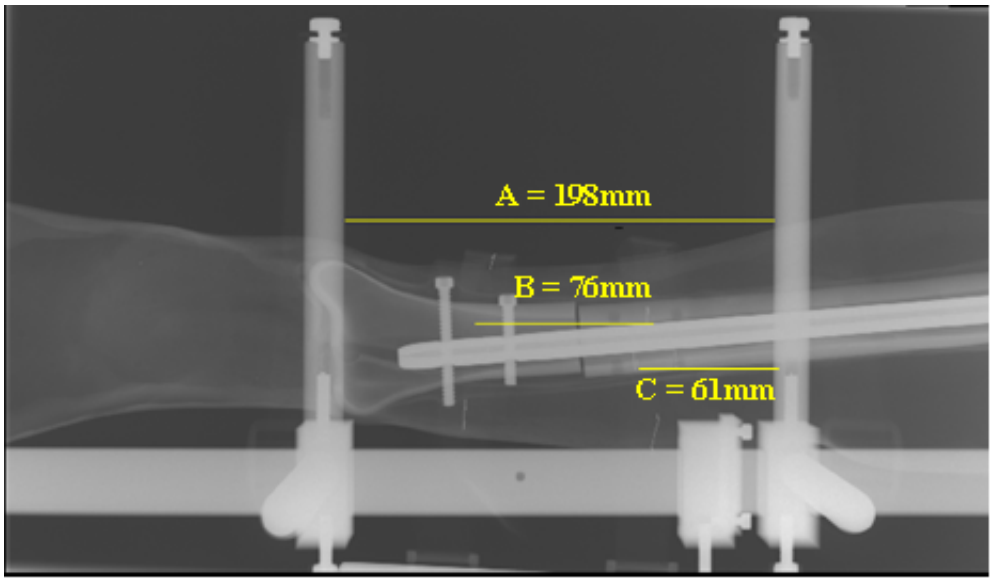

Figure 7.1: An example of the measurements of the fulcra placements on an X-ray image.

Measurements of the fulcra spacing allowed the bending moment to be calculated. For example, for the measurements in Figure 7.1, the bending moment across the fracture gap was $M = Fd = (\frac{100}{2}) \times (0.61) = 30.5$ Nm.

X-rays were also used to measure the bending angle and displacement caused by loading. These measurements were combined to provide the final measurements of stiffness of the phantoms at the fracture site, namely the bending moment per degree of angulation in (Nm/degree), and the bending moment per millimetre of displacement (in Nm/mm).

After X-raying, the same two phantoms were measured using the Zwick materials testing machine and the adjustable four point bending fulcra, as described in Section 5.5. In both

tests the outer fulcra were placed 150 mm apart and the inner fulcra 65 mm apart. This set up is shown in Figure 7.2.

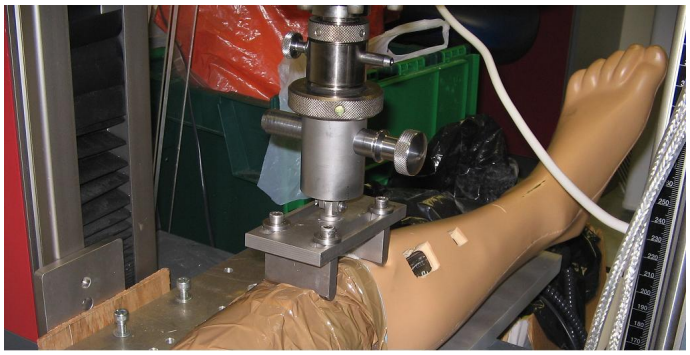

(a)

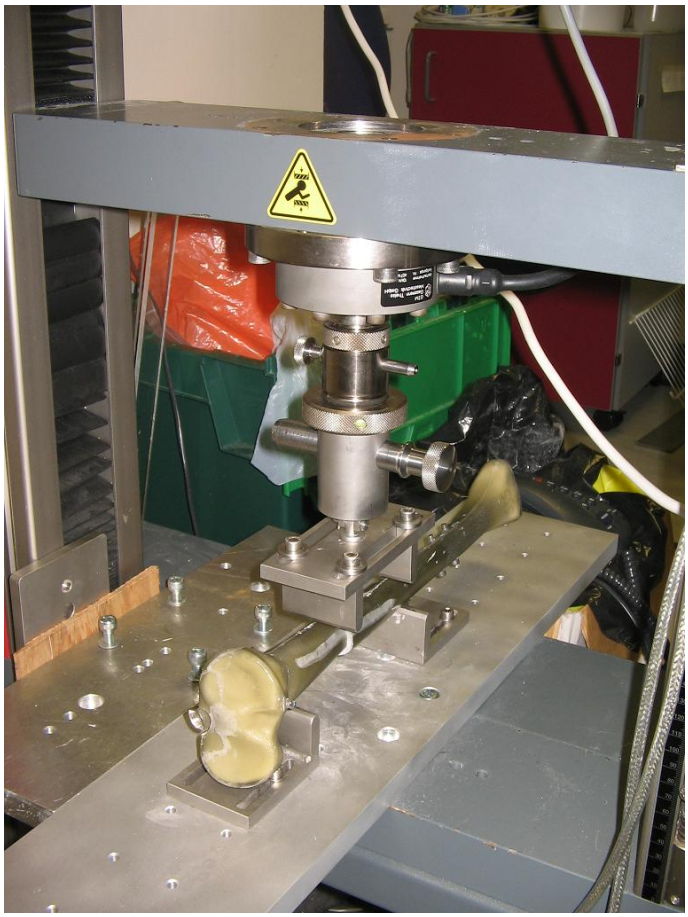

(b)

Figure 7.2: Four point bending set up in the Zwick machine with a) the foam leg in AP loading and b) the Sawbones proximal fracture in lateral loading.

The phantoms were initially measured within the soft tissue leg with a force of 200 N applied at 10 N/s. A large amount of compression of the foam by the fulcra meant that no true measurement of the bending or displacement at the Sawbone fracture was possible with the foam leg in place so these results were discarded. The test was repeated for the fractured Sawbone alone, with no outer soft tissue leg. Measurements were repeated three times in both the AP and lateral directions. The results were presented in the form of a force versus displacement graph. An example of this graph is shown in Figure 7.3.

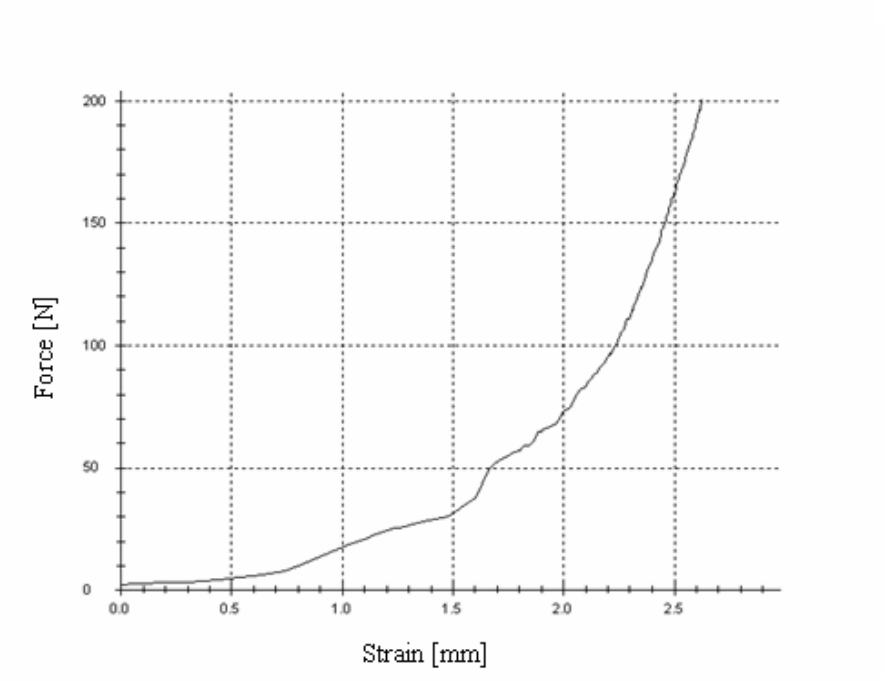

Figure 7.3: Force versus displacement graph for the proximal fracture with no soft tissue.

For each test, the displacement that occurred at 100 N was measured and used to calculate the axial displacement and the bending angle induced at the fracture site. Figure 7.4 shows how this was achieved. The diagrams show the measurements necessary to calculate the bending angle, β, and displacement at the fracture site, δ.

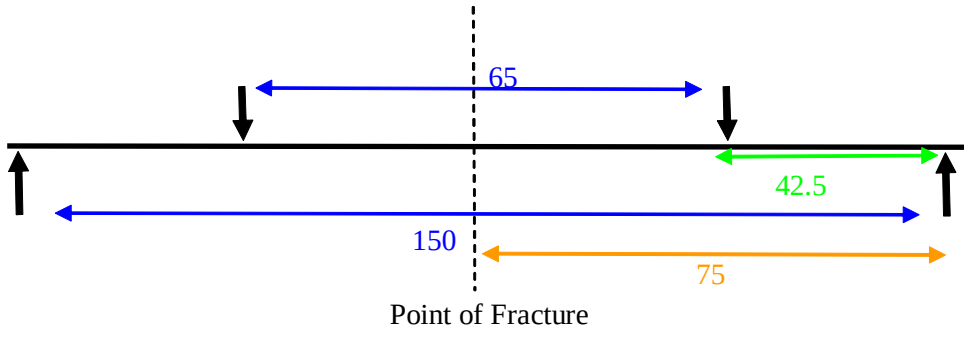

(a)

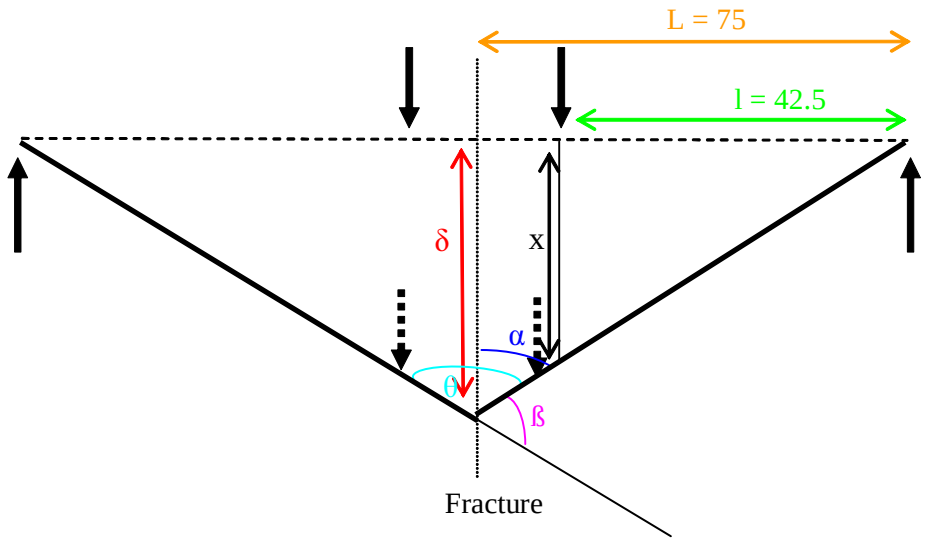

(b)

Figure 7.4: Four point bending set up with a) no load applied and b) load applied causing deflection.

As can be seen in Figure 7.4, x is the displacement measured by the Zwick machine. As discussed previously, it is assumed that the callus is the least stiff material and therefore responds to loading first, resulting in a triangular movement at the fracture site. It can be seen that $\delta = L/\tan\alpha$, where $\tan\alpha = l/x$, and $\beta = 180–\theta$, where $\theta = 2\alpha$. These formulae, together with the Zwick force versus displacement graph, were used to calculate the bending angle and the displacement at the fracture site so that they could be compared to the measurements made using the frame. As with the frame measurements, these were combined with the fulcra spacings to provide the final measurements of stiffness of the phantoms in Nm/degree and Nm/mm.

7.2.2 Humeral Loading Apparatus

The set up of a system to apply axial force to a humeral fracture was described in Section 5.4. It has been shown how careful placement of the downwards pulling weights results in a tensile force through the humerus and that the magnitude of this force could be calculated using the force plate on which the hand is placed. X-ray measurements allow a calculation of the displacement induced by the loading of the fracture and the stiffness at the fracture site. To investigate how useful this method was, measurements were made on the humeral phantom (see Section 5.5) using the X-ray based method.

To test the apparatus, the fracture model of the humerus with callus was suspended using the holding frame to allow X-ray measurements. Unfortunately it was difficult to produce a model of a patient's arm in a clinical-type situation, so the force plate method of measuring force could not be used. However, since the weights were applied directly to the humerus it was assumed that a purely vertical load equal to the applied weight occurred across the fracture site. In the test, the humerus in the holding frame was X-rayed with no weights attached. A 0.5 kg weight was then attached to the distal end of the humerus and an X-ray taken. This was repeated twice. Three more levels of weights increasing in steps of 0.5 kg were attached and X-rayed in this way. The images were then used to measure the axial displacement induced by loading. This, combined with the force applied at the distal end of the humerus, was used to give a measurement of axial stiffness in N/mm.

The bone ends of the humerus were too large to be securely gripped by the axial grips of the Zwick machine, so no comparative tests could be made. Calculations based on the material properties of the foam experiencing the same tensile loads as during the X-ray tests were made.

7.3 RESULTS

7.3.1 Tibial Frame

The angular and lateral displacements and bending stiffness results using the frame and the Zwick machine were compared for both proximal and distal fractures in the AP and lateral directions. The results of the repeated displacement measurements are given in Table 7.1. Angular measurements from the frame were smaller than those measured by Zwick while displacements were larger. Repeatability was assessed using the SD between the repeated measurements. Since the SDs for the frame were lower, this indicated a better repeatability using the frame versus using the Zwick machine.

Table 7.1: Measurements of angular and lateral displacement using the Zwick machine with Sawbone and the bending frame with Sawbone and foam casing.

		Angle (SD) [degrees]		**Displacement (SD) [mm]**	
		Zwick	**Frame**	**Zwick**	**Frame**
Proximal	**AP**	4.4 (1.1)	0.2 (0.1)	2.9 (0.7)	4.7 (0.6)
	Lateral	3.6 (2.5)	0.1 (0.1)	2.4 (1.7)	7.0 (1.0)
Distal	**AP**	1.5 (0.5)	0.3 (0.0)	1.0 (0.3)	2.0 (0.0)
	Lateral	6.0 (0.9)	0.1 (0.1)	3.9 (0.6)	5.7 (0.6)

The bending moment in the Zwick machine was a constant value of 21.5 Nm in all tests due to the consistent fulcra placing and force application. Differences in fulcra placing using the tibial frame resulted in bending moments varying from 27 Nm to 34 Nm, with a mean of 31 Nm. These bending moments and the angular and displacement measurements were used to calculate the angular and lateral stiffness at the fracture site. The results for the Zwick and frame measurements are given in Table 7.2.

Table 7.2: Angular and displacement stiffness values using the tibial phantom for the Zwick machine and the tibial frame.

		Angular Stiffness [Nm/degree]		**Displacement Stiffness [Nm/mm]**	
		Zwick	**Frame**	**Zwick**	**Frame**
Proximal	**AP**	5.0	189.4	7.7	6.7
	Lateral	8.0	49.0	8.9	4.9
Distal	**AP**	15.3	90.6	23.3	13.6
	Lateral	3.5	227.0	5.4	5.0

The results show that, due to the bigger angles measured by the Zwick machine, smaller bending stiffnesses were found. The very small angular measurements detected by the frame resulted in very high stiffness values. Measurements of displacement stiffness were more similar between the two systems than the angular measurements.

Conducting these tests gave an indication of the angular and lateral displacements that could be expected in an IM nailed tibial fracture patient. The results using the frame are summarised in Table 7.3. The table shows small angular displacements of less than 1 degree, and lateral displacement measurements from 1.0 – 8.0 mm.

Table 7.3: Angulation and displacement at the fracture site for the AP and lateral loading situations in the frame.

	Angle [degrees]	Displacement [mm]
Max AP	0.3	5.2
Min AP	0.1	2.1
Max Lateral	0.8	8.0
Min Lateral	0.1	1.0

7.3.2 Humeral Equipment

The elastic modulus of the foam was calculated as 0.39 MPa using the Zwick tests and the predicted displacement values varied from 0.7 mm to 2.8 mm for 5 N to 20 N with a stiffness of 7.2 N/mm. The results showing the displacement and stiffness values measured using the humeral apparatus, together with the SD of the displacement measurements, are given in Table 7.4. The results show that both displacement and stiffness increased as the applied force increased. Low SDs between repeated measurements at a variety of forces indicated that the repeatability of the humeral frame system was good.

Table 7.4: Mean displacement and stiffness measurements using the humeral phantom loaded using the humeral apparatus.

Force (N)	Displacement (SD) [mm]	Stiffness [N/mm]
5.0	1.1 (0.1)	4.4
10.0	2.2 (0.1)	4.6
15.0	2.5 (0.1)	5.9
20.0	3.0 (0.3)	6.7

7.4 DISCUSSION

7.4.1 Accuracy of the Tibial Bending Frame

A direct comparison between the measurements made using both systems was limited by the fact that the Zwick tests could not be performed using the foam leg and the frame measurements could not be made without it. This limitation was illustrated in the discrepancies between measurements made using the two systems. The biggest of these occurred with the bending angle. The frame produced much smaller bending angle measurements which resulted in low stiffness values. This might in part be due to some compression of the foam leg in the frame so that the fracture site was not experiencing the same force in

the frame as it was in the Zwick set up. It may also be because the technique was not as sensitive to angle changes as the Zwick fulcra, which were in direct contact with the bone. It is also possible that some slippage of the Zwick fulcra on the Sawbones caused measurement of a bigger angular displacement than was actually occurring.

Most investigators have reported their fracture bending assessments as stiffnesses in Nm/degree. The only angular deflection measurement given in the literature was a deflection of 0.4 degrees - 1 degree found by Edholm *et al.* using loads of 2 – 8 kg [60]. These results were similar to those found using the bending frame whereas the Zwick measurements were much larger. Taking bending moment into account allowed a comparison of stiffness. Both Evans *et al.* and Richardson *et al.* found stiffnesses of between 2 and 20 Nm/degree throughout the course of healing [10, 55], although Hammer *et al.* recorded stiffnesses below 15 Nm/degree [58] . It was unclear whether this was because the X-ray measurement used by Hammer *et al.* was less sensitive than the electrogoniometers used by Evans *et al.* and Richardson *et al.*, or whether measurements of slightly different properties were being made. The bending stiffnesses found using Zwick agree with these reported stiffness results better than those using the frame. Lateral displacements in bending stiffness tests were not recorded by previous investigators, so it was difficult to compare the results from this test to an expected value, although there was less discrepancy between the results measured using the frame and Zwick than in the bending angle results.

Examination of the X-ray images allowed analysis of the movement at the fracture site. This indicated that a true angular bend was not occurring, and that, instead, a lateral displacement around the nail took place. In other words, despite the fact that the mechanical tests were set up as four point bend applications, a true four point bend response was not being seen at the fracture site. It was therefore possible that the calculations of bending moment and stiffness at the fracture site were more complicated than first assumed using conventional four point bending mathematics. It was decided to analyse this problem further after examination of patient results.

7.4.2 Accuracy of the Humeral Equipment

Since the humeral fracture phantom could not be secured in the Zwick machine due to the size of the grips, a direct comparison of the the humeral apparatus and the Zwick was not possible. In the direct humeral measurements, an increasing displacement and stiffness occurred as the load increased and the displacement measurements were larger than those predicted by Zwick. This could have been due to the fact that pre-loading of the foam in the earlier tests caused stretching and plastic deformation. Further inaccuracy could have been added by the securing of the foam to the bone ends. It is possible that the entire cross-

sectional area of foam was not bonded to the bone, resulting in a smaller cross-sectional area reacting during loading. Tearing might also have occurred at the bone ends where the foam was secured. The increasing stiffness with increasing load is consistent with tearing and destruction of elastic components which would increase the stiffness of the material through the course of testing. Measurements of the tensile stiffness of callus were not given in the literature so no comparison could be made between the values found in these tests with those in previous studies.

7.4.3 Repeatability

Low SDs between repeated measurements using both the tibial frame and the humeral apparatus indicated a good repeatability of the bending and tensile stiffness tests using these sets of equipment.

7.4.4 Expected Results in Patients

The fracture phantoms were designed to model the physiological fracture situation closely. Since the measurements on patients would be made using the tibial and humeral apparatus, they were used to give an indication of the expected results in the clinical situation as a guide to the feasibility of conducting the tests on patients. In the case of tibial tests, results showed that a maximum angle of 0.8 degrees and a maximum displacement of 8.0 mm was caused by loading. This confirmed the visual examination of X-rays which suggested that little actual bending occurred at the fracture site and more lateral offset displacement took place. It therefore seemed that this might be the most useful and easily detected measurement with which to compare a patient's X-rays, although it deviated from a true four point bending response. Since previous authors have not visually measured the response of the fracture to loading, it is hard to say whether they were measuring bending or displacement – it could be that in previous studies it was an offset displacement rather than a bending movement that occurred. The low bending angle results recorded by Edholm *et al.* using an X-ray measurement system support this [60].

The results using the humeral frame also gave an indication of typical displacement in a patient. The humeral phantom did not model soft tissue responses and the polyurethane foam was only an approximate model for callus in the early stages of healing. Despite these deviations from the physiological situation, this represented the most appropriate model of a fracture patient that could be manufactured. The measurements made using the humeral frame indicated that displacements between 1.1 mm and 3.0 mm could be measured. There was no previous data to guide the ideal size of force to apply to the patient. The phantom

results suggested that 20 N would result in a measureable displacement. However, taking into account the offset of the force from the humerus in the patient situation, as well as the force absorption that might occur through soft tissue, a slightly higher load might be required.

7.5 SUMMARY

Tests on the X-ray apparatus to perform four point bending on tibial fractures and to axially load humeral fractures have been described in this chapter. Accuracy, repeatability and initial measurements on fracture models were performed using the X-ray apparatus and the Zwick materials testing machine. Accuracy results were difficult to analyse due to the different loading methods applied using the two types of system. However, tests indicated that the loading apparatus had a comparable or better repeatability than the Zwick apparatus. This indicated the potential of the apparatus to measure and monitor changes in response to loading throughout a patient's course of healing. Initial calculations of the stiffness in fracture models gave an indication of the displacements that could be expected in patient tests. Feasibility studies carried out on patients using these methods are described in the following chapter.

Chapter 8

Patient Studies

8.1 INTRODUCTION

This chapter describes how the loading apparatus and image analysis methods developed in Chapters 5 and 6 and evaluated in Chapter 7 were used in preliminary clinical studies. The tibial four point bending apparatus was tested on a series of tibial fracture patients treated with an IM nail and the humeral apparatus was used to apply axial load to two conservatively treated humeral fractures. These studies were applied as proof of concept investigations into the feasibility of using these devices to obtain stiffness information in healing fractures.

8.2 BENDING STIFFNESS OF TIBIAL FRACTURES

A quantitative measurement of fracture stiffness throughout the course of healing would be useful in providing surgeons with a direct measurement of the success of the fracture treatment as well as providing predictions of problems such as delayed or non-union. Previous methods to provide this information in the tibia have been restricted to fractures treated with an external fixator. The design of a frame to apply four point bending in the X-ray environment to tibial fractures treated in other ways has been described in Chapter 5. The results of initial tests indicated that it was feasible to apply load to IM nailed fractures and to measure the resulting movement using X-ray analysis (see Chapter 7). These tests also suggested that a displacement, rather than an angular bend, may occur at the fracture site. In order to test the application of this apparatus in the clinical setting a feasibility study was performed on a series of IM nailed tibial fracture patients.

8.2.1 Materials and Methods

The patients selected to participate in this trial were all patients with fractures in the proximal or distal third of the tibia which had been treated with an IM nail. They were recruited in the orthopaedic wards of the RIE over a period of six months. Appropriate permission for the study was obtained from the NHS Lothian Research Ethics Committee (see Appendix F). Five male patients aged 21 – 39 years (median 32 years) were recruited. Each patient was followed up at their first return to fracture clinic, approximately four weeks after their initial fracture and surgery ('early' follow-up), and again towards the end of their healing, at approximately eight weeks after their surgery ('late' follow-up). Details of the patients giving their identification (ID) numbers are shown in Table 8.1. One patient did not attend (DNA) their late follow-up.

Table 8.1: Tibial fracture trial patients.

Patient ID Number	**Early Follow-Up (days after surgery)**	**Late Follow-Up (days after surgery)**
1	60	122
2	36	107
3	30	95
4	21	99
5	36	DNA

At each return visit to clinic, the patients were X-rayed using the tibial frame. The normal X-ray protocol for tibial fracture patients was that AP and lateral views of the fracture were taken. This procedure was adhered to with two additional, loaded X-rays being taken. The procedure for each patient was as follows:

1. The position of the fracture was determined from existing X-rays to allow accurate fulcra placement.
2. The patient lay on the X-ray bed and their fractured leg was placed securely in the tibial frame.
3. The moveable bolsters were adjusted so the patient was comfortable and the outer fulcra were as evenly spaced on either side of the fracture site as possible.
4. The velcro straps were attached firmly on either side of the fracture site.
5. Each strap was attached to the central brass bar which connected to the AP loading pulley, the tensioning device and the digital spring balance.

6. An X-ray cassette was placed in the lateral cassette holder and a lateral X-ray was taken with no load applied.

7. Once the correct positioning had been verified from this X-ray, the force through the velcro straps was slowly increased by turning the dial on the tensioning device.

8. This was monitored using the digital spring balance and once the highest force that could be comfortably tolerated by the patient was attained, a further, loaded, lateral X-ray was taken.

9. The force was released after the X-ray and the velcro straps were now attached to the brass bar connected to the lateral loading pulley.

10. An X-ray cassette was placed in the AP X-ray cassette holder and an unloaded AP X-ray was taken.

11. As before, the force through the velcro straps was increased to the highest force comfortably tolerated by the patient and a further, loaded AP X-ray was taken.

12. The force was released.

An image of a patient positioned in the frame is show in Figure 8.1.

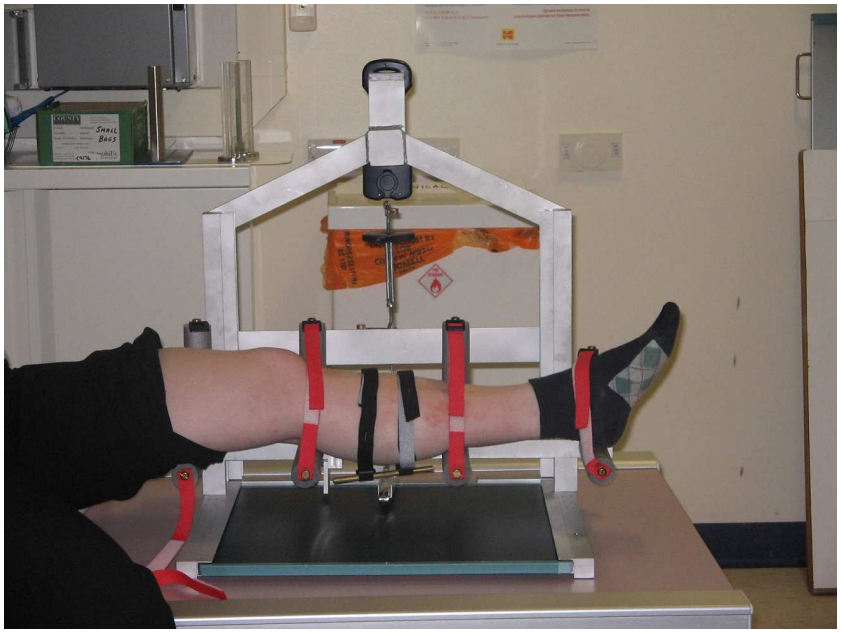

Figure 8.1: Photograph of the positioning of a patient in the tibial bending frame.

Each set of loaded and unloaded images was analysed using the cross-correlation method described in Section 6.3. This gave a measurement of the angular movement and the lateral

offset at the fracture site. Additionally, the procedure was executed three times for each set of images for patient 1 to assess repeatability. Examples of the aligned loaded and unloaded images are shown in Figure 8.2.

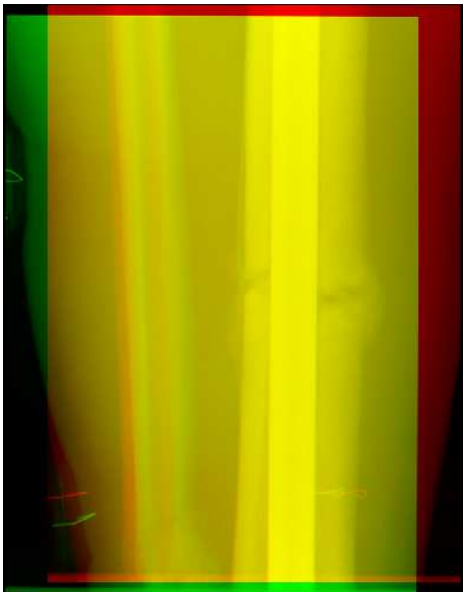

(a)

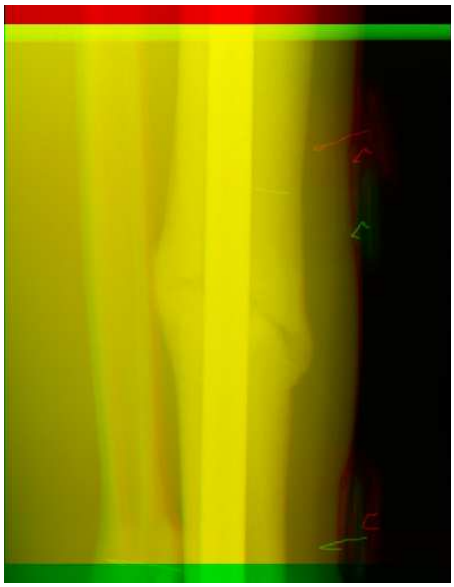

(b)

Figure 8.2: Aligned X-rays of a patient fracture in a) the AP view and b) the lateral view. In both images, yellow indicates where the loaded and unloaded X-rays are aligned, red indicates the unloaded image and green indicates the loaded image.

To provide a comparative measure, analyses of the X-ray were also performed manually using the Image J program. Using this software, a measurement of the change in angle of the nail within the IM canal was obtained. This was achieved by drawing lines against the side of the intramedullary canal and intramedullary nail in the unloaded image. The difference in angle between these two lines was taken as the unloaded angle. The procedure was repeated in the loaded X-ray, and the difference between the unloaded and loaded angles was used as a measurement of the bending angle. A measure of the lateral displacement was made by measuring the perpendicular distance between the most medial part of the fracture and the most medial part of the IM nail. This was executed in both unloaded and loaded X-rays and the difference taken as a measurement of the lateral displacement. An example of these measurements is shown in Figure 8.3 which shows the unloaded AP image where angular measurement was 1 degree (89 degrees – 88 degrees) and the unloaded lateral displacement offset was 16.2 mm. These measurements were repeated in the loaded X-ray and the difference between the two taken as the final angle and lateral offset measurement.

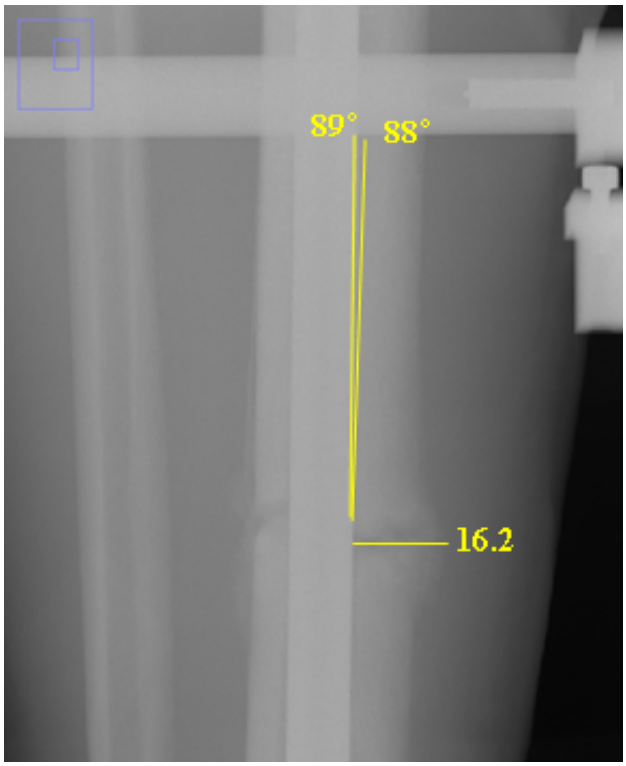

Figure 8.3: AP X-ray image showing the position of measurements for the angular and lateral offsets measured manually using Image J.

8.2.2 Results

This section gives the measurements obtained from the patient X-rays. The results are described according to the X-ray view in which they were taken, i.e. measurements taken on an AP X-ray are described as AP measurements although the loading in this view is in the lateral direction.

Angle and Lateral Displacement Measurements

The first step in analysing the X-rays was to measure the angular and lateral movements between the loaded and unloaded X-rays in both the AP and lateral directions. This was performed using the developed cross-correlation procedure and the results for all five patients are given in Table 8.2.

Table 8.2: Lateral displacement and angular measurements for patient X-rays.

Patient	Image	Lateral Displacement [mm]	Angular Bend [degrees]
1	AP1	0.4	0.2
	AP2	0.4	0.2
	Lat1	0.4	0.0
	Lat2	0.4	0.0
2	AP1	0.4	0.6
	AP2	0.2	0.2
	Lat1	0.2	0.0
	Lat2	0.4	0.2
3	AP1	1.2	0.4
	AP2	1.2	0.2
	Lat1	0.6	0.0
	Lat2	1.0	0.0
4	AP1	0.6	0.6
	AP2	1.2	0.0
	Lat1	0.6	0.0
	Lat2	0.4	0.0
5	AP1	0.4	0.0
	AP2	DNA	DNA
	Lat1	0.2	0.0
	Lat2	DNA	DNA

The results showed that the cross-correlation procedure was successful in obtaining angular and displacement measurements for all images. However, both measurements were

extremely small - on average less than 1 mm. The lateral displacement measurements were higher than the angular measurements, as expected, but were still very low. The results also showed that measurements in the AP X-rays (i.e. lateral loading direction) were higher than those in the lateral X-rays by an average of 0.2 mm.

Changes in Angle and Displacement Measurements

The next step was to compute the difference between the measurements in the early and late X-rays, which should provide a measure of the increase in stiffness of the fracture. Table 8.3 shows the differences between measurements made in the early and late X-rays measured using the cross-correlation method and Image J. Negative readings indicated an increased measurement in the second set of measurements.

Table 8.3: Angular and lateral displacement differences between early and late X-rays measured using a) the cross-correlation method and b) Image J.

(a)

Patient	**AP Difference**		**Lateral Difference**	
	Angle [degrees]	**Displacement [mm]**	**Angle [degrees]**	**Displacement [mm]**
1	0.0	0.0	0.0	0.0
2	-0.4	-0.2	0.2	0.2
3	-0.2	0.0	0.0	0.4
4	-0.6	0.6	0.0	-0.2

(b)

Patient	**AP Difference**		**Lateral Difference**	
	Angle [degrees]	**Displacement [mm]**	**Angle [degrees]**	**Displacement [mm]**
1	0.0	0.1	1.0	0.6
2	0.0	0.6	-0.7	-0.6
3	0.0	2.5	0.2	0.0
4	0.0	4.3	1.0	0.0

The results using both methods showed very small changes in induced angular offset and lateral displacement between early and late X-rays. This was as expected since the measurements in both images were small. Negative readings occurred fairly frequently and showed that the angular or lateral displacement was larger in the late follow-up X-rays

than in the early ones, which was opposite to the expected result of decreased response to loading over the course of healing. The measured changes between early and late X-rays were different for each patient and this, combined with the very small readings, made it difficult to describe an overall trend.

Repeatability

The image measurements were repeated three times for the late X-rays of patient 1 to test the repeatability of the cross-correlation approach. The results indicated that in AP X-rays a mean angle of 0.0 degrees with a SD of 0.0 degrees and a mean displacement of 0.4 mm with SD of 0.0 mm was calculated. In lateral X-rays a mean angle of 0.0 degrees with SD of 0.0 degrees and mean displacement of 0.3 mm with SD of 0.1 mm was calculated.

Change in Stiffness Measurements

In order to relate angle and displacement measurements to healing they were converted to a mechanical stiffness measurement. To do this, the bending moment in each X-ray was calculated using the known force applied and the distances that were measured on the X-rays. The mean applied bending moment was 57 Nm. The resulting changes in stiffness between the early and late X-rays are shown in Table 8.4. A second stiffness reading for patient 5 could not be obtained since the patient did not attend the late follow-up. Negative readings indicate a decrease in stiffness.

Table 8.4: Difference between angular and displacement stiffness readings between early and late X-rays measured using a) the cross-correlation procedure and b) Image J.

(a)

Patient	AP Stiffness Difference		Lateral Stiffness Difference	
	Angle [Nm/degree]	Displacement [Nm/mm]	Angle [Nm/degree]	Displacement [Nm/mm]
1	-31.5	-15.8	No Reading	15.0
2	80.0	60.0	No Reading	-250.0
3	59.5	-4.7	No Reading	-49.6
4	No Reading	-85.0	No Reading	148.3
5	DNA	DNA	DNA	DNA

(b)

Patient	AP Stiffness Difference		Lateral Stiffness Difference	
	Angle [Nm/degree]	Displacement [Nm/mm]	Angle [Nm/degree]	Displacement [Nm/mm]
1	No Reading	16.7	8.8	No Reading
2	0.0	33.3	-16.5	No Reading
3	No Reading	No Reading	No Reading	No Reading
4	-8.0	59.8	17.0	No Reading
5	DNA	DNA	DNA	DNA

The results show a large variation in measurements. Taking into account the measurement accuracy of the system (± 1.5 degrees and ± 2.3 mm, see Chapter 6), early and late stiffness measurements could vary by an average of ± 37.7 Nm/degree and ± 23.6 Nm/mm. Negative results indicated that the stiffness in the early X-rays was larger than that in the late, which was contrary to the expected increase as healing progressed, although the low stiffness measurement precision might have occluded any true stiffness changes. Table entries which show 'No Reading' occurred when one or both stiffnesses could not be calculated due to the measured angular or lateral displacement being zero. This resulted in division by zero when calculating stiffness (bending moment divided by displacement). It could be argued that this was essentially a measurement of infinite stiffness, since no displacement occurred, but it was decided to record the results with no measurement value. Again, due to the erratic results it was difficult to compare measurements between Image J and the cross-correlation method – they both resulted in similar numbers of 'No Reading' and negative results.

Scatter plots illustrating the lateral stiffness readings obtained for the early and late AP images using both Image J and the cross-correlation method are shown in Figure 8.4 and for the lateral images in Figure 8.5.

Comparison between Image J and the cross-correlation method showed no consistency between measurement methods. Some readings showed higher stiffnesses in the late measurements using cross-correlation, but showed the opposite result using Image J and vice versa. Both measurement techniques gave some results where early stiffnesses were higher than late stiffnesses. Measurements using cross-correlation could be made for every image, whereas measurements of 'No Reading' indicated that no change between loaded and unloaded images could be detected using Image J. Although this was represented as zero on the graph, it could be interpreted as an infinitely high stiffness. In the AP Image J measurements, a trend of increased stiffness in late readings was seen, although the case of no measurement in patient 3 and lack of late follow-up in patient 5 made it difficult to draw meaningful conclusions. The high number of 'No Readings' using Image J made it difficult to compare the two techniques in any detail.

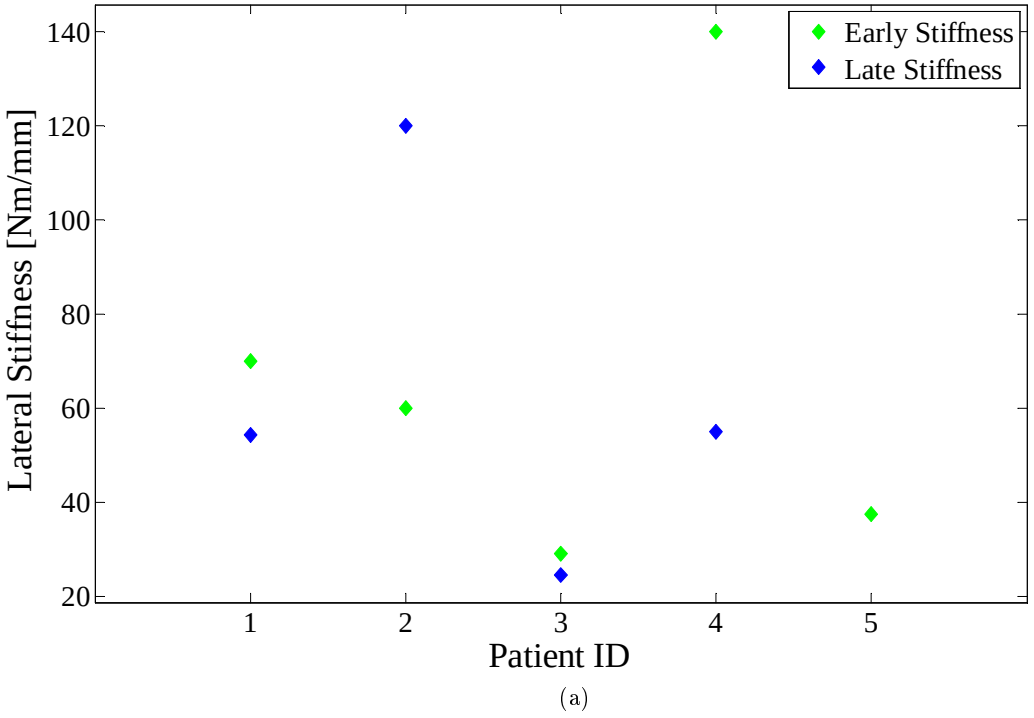

(a)

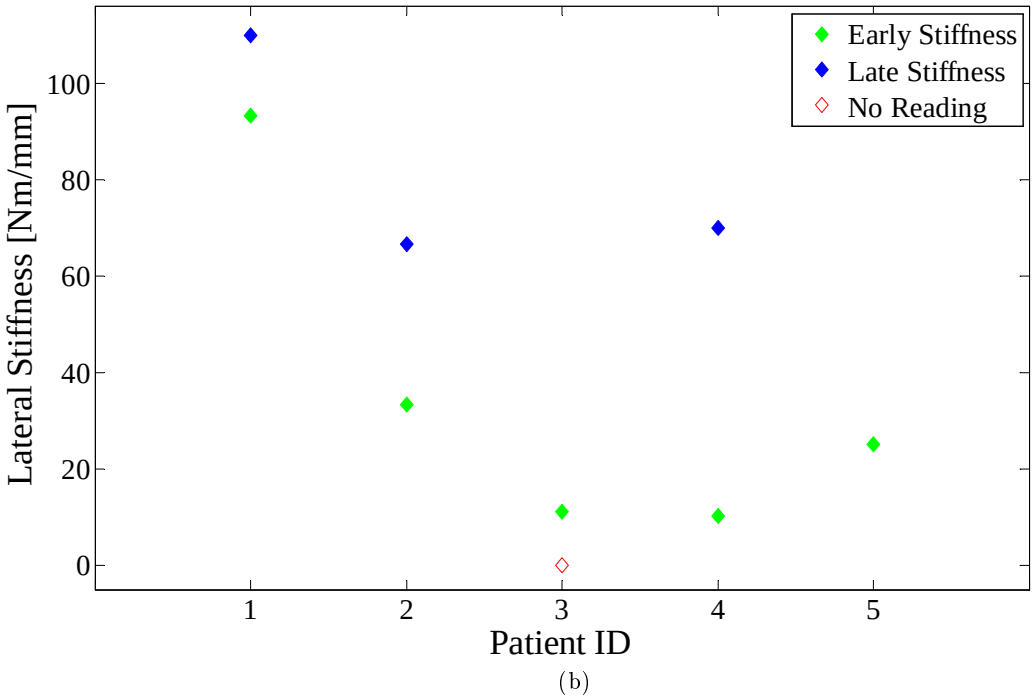

(b)

Figure 8.4: Lateral stiffness measured on AP X-rays using a) the cross-correlation method and b) Image J.

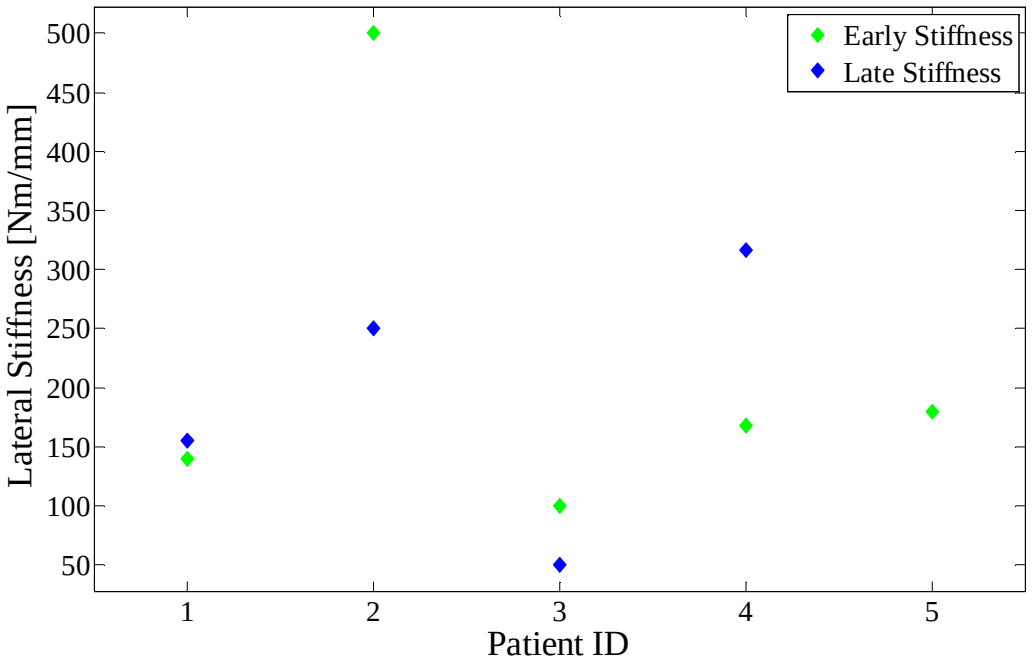

(a)

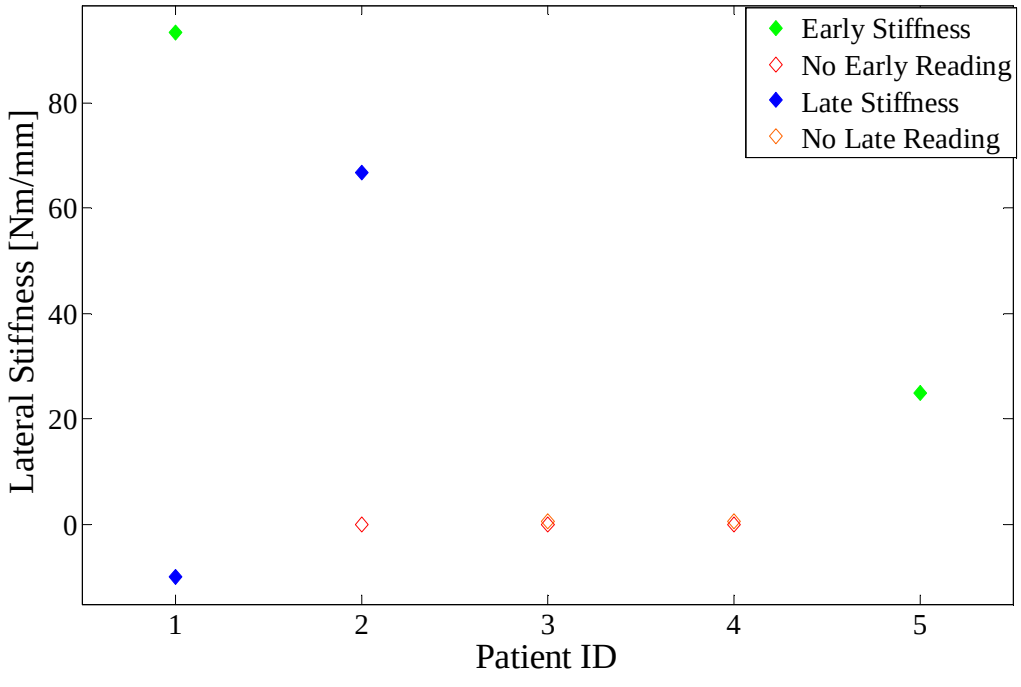

(b)

Figure 8.5: Lateral stiffness measured on lateral X-rays using a) the cross-correlation method and b) Image J.

8.2.3 Discussion

This section described the use of the tibial four point bending frame in the clinical environment on tibial fracture patients treated with an IM nail. The X-ray frame worked well in the radiography environment and interfered minimally with normal practice. Radiographers were happy to use the frame and did not find it intrusive or time consuming to add the loading measurements to the routine X-rays they would take for a fracture patient. They also found it very useful to be able to take a lateral view using the lateral X-ray cassette slot without asking the patient to change position. Furthermore, the frame effectively and comfortably applied load to the patients and maintained this load during the X-ray without the need for any extra radiation exposure to the operator. This illustrated that the design of the frame, both for ease of use in the clinical radiography setting and for comfort to the patient whilst applying load, was effective.

The displacement results showed that, although a bending moment was theoretically being applied to the fracture site, a displacement rather than a bending angle was measured. This indicated that four point bending might not be occurring in this system, which was possible if several of the assumptions made about the system were inaccurate. A major assumption was that the 'ends' of the leg were simply supported. Whilst this was probably accurate for the ankle and foot, the results indicated that the assumption that the knee was simply supported could have been inaccurate and that it was instead 'anchored' by the rest of the body. This would result in the situation of the 'beam' having one fixed and one hinged end, which results in an indeterminate system that cannot be resolved without knowledge of E and I . It is likely that this might have resulted in different moments on either side of the fracture. This difference in moments would be bigger if the assumption of an evenly divided load between the inner fulcra was incorrect. Since the leg is not completely uniform, one fulcrum was possibly experiencing a higher load than the other. Both these factors made it likely that the assumption of a true four point bending set up was inaccurate and that a greater shear force occurred than theoretically predicted. A further consideration should be made of the fact that the leg is a relatively thick structure. The equations used to calculate moments and deflections were developed for thin structures, and become inaccurate for thicker structures, where shear stresses play a greater role [127]. This, combined with the complex loading pattern and asymmetrical load distribution could explain why a displacement, rather than an angulation, occurred at the fracture site.

The first set of results examined the magnitude of measurements made using the frame. Test experiments on Sawbones phantoms (see Chapter 7) indicated that the angular measurement in nailed tibial fractures would be small, and this was confirmed in these patient images. However, the pre-clinical tests on phantoms indicated a measurable amount of lateral displacement whereas this was much lower in the patient X-rays. The reason for

this reduction in displacement was possibly due to soft tissue factors. The patients had a more robust surrounding of muscle, fat, skin, nerves and blood vessels than the Sawbones phantom, which modelled this soft tissue using a simple foam outer shell. It was likely that the soft tissue in the patient prevented the inner bone being loaded directly. Direct resistance of the musculature to the bending movement may also have occurred. It is also possible that the IM nails in the patients were placed in more closely reamed holes than in the Sawbones model, allowing less room for 'pivoting' within the intramedullary canal. Finally, the fracture lines in the patients were more complex and irregular than those used in the Sawbones phantoms.

The reduction in measured displacement values in comparison to the pre-clinical tests meant that the accuracy of measuring tibial displacement was low. In Chapter 6 it was found that the procedure could measure small displacements of the tibia with an accuracy of 2.3 mm. All of the readings in the patient group were lower than this. The low measurement accuracy was illustrated in the comparison between early and late stiffness measurements for each patient. In both the AP and lateral X-rays, measurements were inconsistent and did not reflect increasing stiffness over the course of healing. However, the low accuracy of stiffness measurements resulting from the low displacement measurement accuracy meant that high errors in either early or late stiffness calculations might have been made that would have occluded any indications of increasing stiffness. Measurements using the Image J system were also unreliable due to their small size.

Despite the small amount of deflection that occurred in the IM nailed patients, the computerised method detected displacement changes in all patients, whereas manual detection using Image J was not always possible. Furthermore, the repeatability tests illustrated that these measurements could be consistently detected using the cross-correlation procedure. However, it would seem that application of the loading technique in IM nailed tibial fracture patients is inappropriate as not enough movement occurred to provide useful clinical measurements of stiffness. It is possible that applying a higher force to the inner fulcra may have resulted in greater movement, although it is questionable whether patients would have tolerated this. Rather, it seems that the frame may be better applied to conservatively treated fractures where more movement can be expected. Application of the frame to patients treated with an external fixator would also be useful since successful stiffness measurements have been made manually on this group of patients before [54, 55]. It would be interesting to compare the method of measurement between previous systems and the system in this study. The X-ray images allowed visualisation of the actual movement at the fracture site whereas previous systems measured the 'superficial' movement of the bone and leg or external fixator system. Examination of whether a true bending or displacement movement occurs at the fracture site could be conducted using this X-ray based system.

Furthermore, the system would allow a measurement of stiffness in the lateral view to be conducted easily to allow comparative measurements between the AP and lateral stiffnesses which might indicate which is the most useful for tracking healing changes.

8.3 AXIAL LOADING OF HUMERAL FRACTURES

Chapters 5 and 6 described the development of equipment and imaging techniques to measure the axial stiffness in humeral fractures. This section describes a pilot study which was designed to evaluate the effectiveness of measuring axial stiffness in conservatively treated humeral fracture patients using these methods.

8.3.1 Materials and Methods

From results with tibial fractures it has been shown that fractures treated surgically with internal splints offer a lower likelihood of having detectable displacement under load than those left untreated. Humeral fractures are often treated non-surgically and fractures of the humerus are easily visualised in X-ray images. Humeral fractures are also accessible for the application of load. For these reasons, the patient group studied was those with conservatively treated humeral fractures.

Patients were recruited over a period of six months at the RIE. Appropriate permission for the study was obtained from the NHS Lothian Research Ethics Committee (Appendix F). During recruitment it was found that mid shaft humeral fractures occur rarely and, if displaced, were often surgically treated. Patients experiencing humeral fractures were also often elderly with associated frailty and medical and mental complications. This reduced the patient group for recruitment considerably. The result was that only two female patients, 42 and 70 years old, were successfully recruited. These patients were treated as case studies for the application of axial load to humeral fractures. The X-ray procedure followed was similar to that for tibial patients. The aim was to take one set of X-rays at the earliest possible return to the fracture clinic, and a further set when the humerus was judged to be well healed (usually approximately eight weeks). Unfortunately, due to the recruitment process, the first X-ray could only be obtained approximately one month after fracture. For patient 7, her second follow-up appointment was scheduled for after the completion of the study, so no measurement could be obtained. Details of the recruited patients are shown in Table 8.5.

Table 8.5: Humeral fracture feasibility study patient details.

Patient ID Number	First Follow-Up (days after fracture)	Second Follow-Up (days after fracture)
6	36	62
7	34	N/A

Routine humeral fracture X-rays are taken in both AP and lateral views with the patient standing. After some experimentation with the radiographers it was found that obtaining a loaded lateral view would be impossible whilst maintaining a clear image of the fracture, especially for larger patients. Thus, only a loaded AP view was taken. The X-ray procedure was as follows:

1. The patient was positioned in front of vertical X-ray bucky with their back to the X-ray cassette.
2. Strapping holding the forearm upwards was removed leaving the brace or cast in place, as in the normal radiography procedure.
3. The band was placed around the patient's forearm, as close to the elbow as possible.
4. The patient's hand was placed on the scale with the elbow at approximately 90 degrees.
5. The weight on the scale was recorded.
6. An AP X-ray was taken (unloaded X-ray).
7. Weight was added to the strap, increasing gradually and stopping if the patient experienced discomfort.
8. When the maximum weight that could be tolerated by the patient was reached, the reading on the scale and the total applied weight was recorded.
9. A second AP X-ray was taken (loaded X-ray).
10. All weight and equipment was removed allowing a normal lateral X-ray to be taken.

A photograph of how a patient would be positioned for an axially loaded X-ray is shown in Figure 8.6.

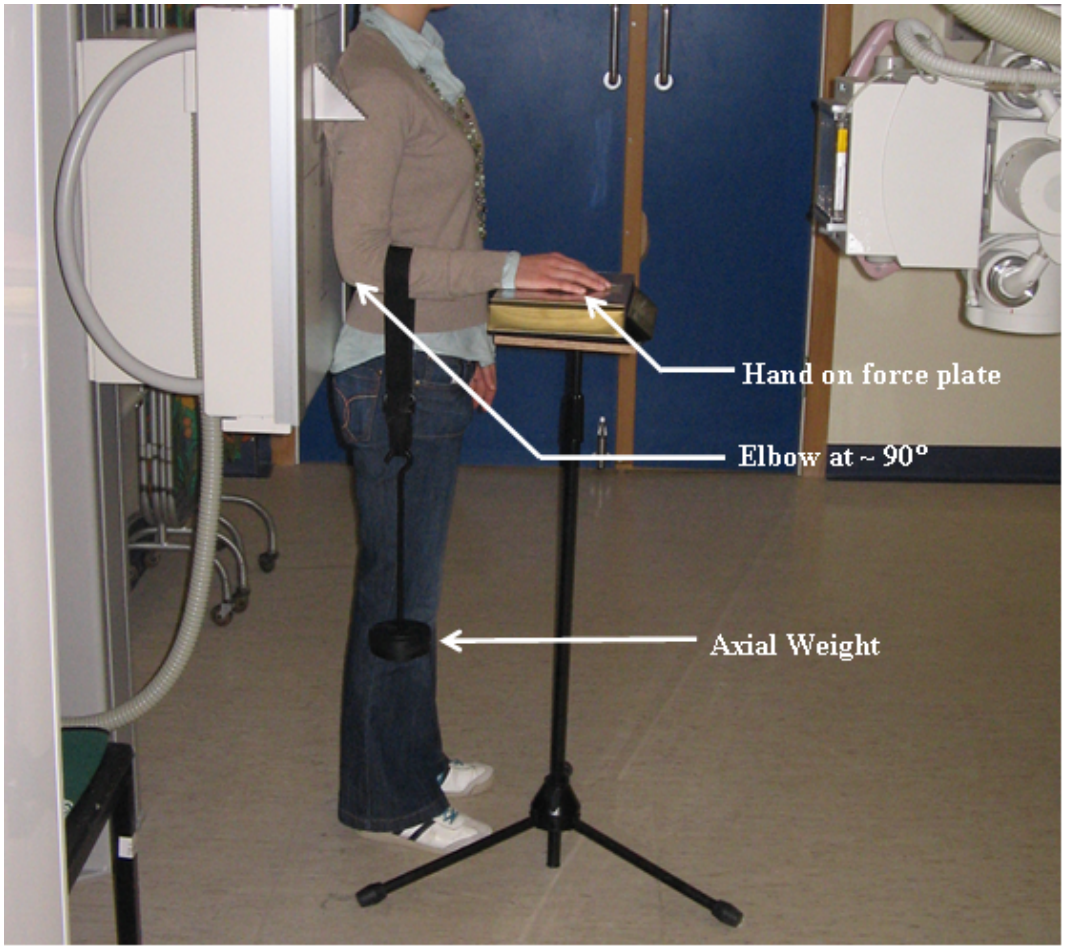

Figure 8.6: Positioning of a patient for an AP, axially loaded humeral fracture X-ray.

The X-rays were analysed using the computerised cross-correlation procedure described in Section 6.3. This gave a measurement of the induced angle and axial and lateral offsets due to loading. The procedure was executed three times to get an indication of repeatability. The changes that occurred at the shoulder joint were also examined using this software.

To provide a comparative measurement to the computerised cross-correlation method, manual measurements were also made using Image J. Measurements of the offset between the bone ends were conducted along the fracture line for loaded and unloaded X-rays. For each fracture, three repeat measurements of axial offset at the medial, midline and lateral sections of the fracture were made. The difference between these for loaded and unloaded X-rays was calculated. The angular measurements gave the angle of the proximal and distal fracture lines to the horizontal. Again, each measurement was repeated three times for each image and the difference between unloaded and loaded was calculated. Examples of the measurements are shown in Figure 8.7.

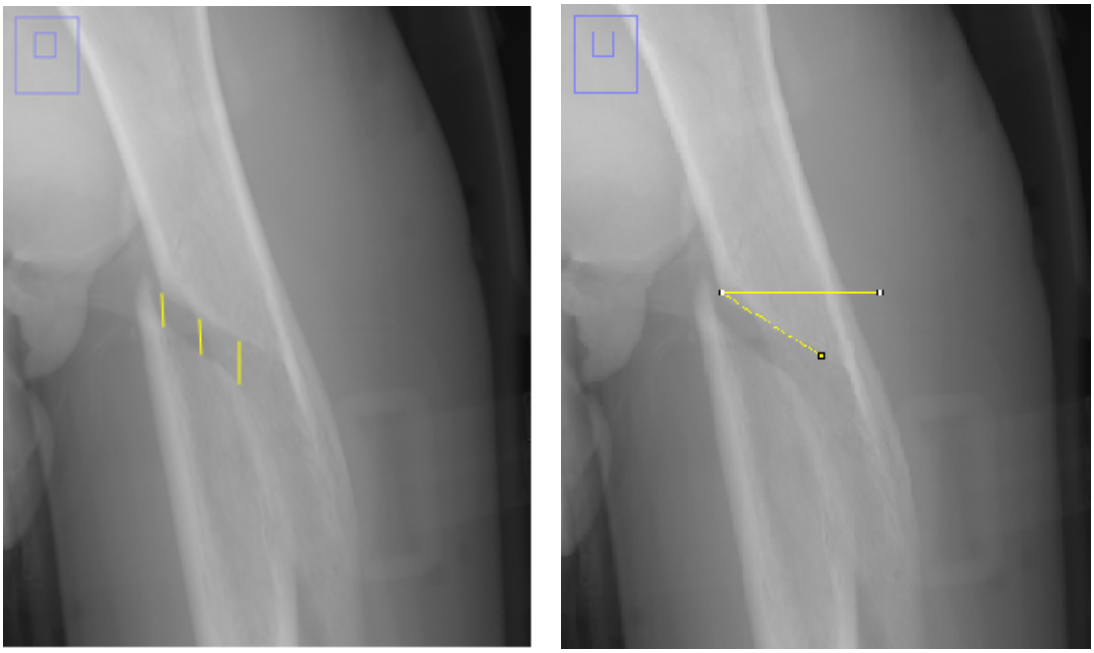

(a) (b)

Figure 8.7: a) Axial offset measurements between the bone ends showing (from left to right), medial, midline and lateral measurements and b) angular measurement of the proximal section of the humerus with the horizontal.

8.3.2 Results

The humeral X-ray apparatus worked well in the radiography environment and the patients were comfortable during the X-ray procedure. Both patients tolerated a maximum load of 2.5 kg. Close up views of the fracture sites in early and late testing are shown in Figure 8.8.

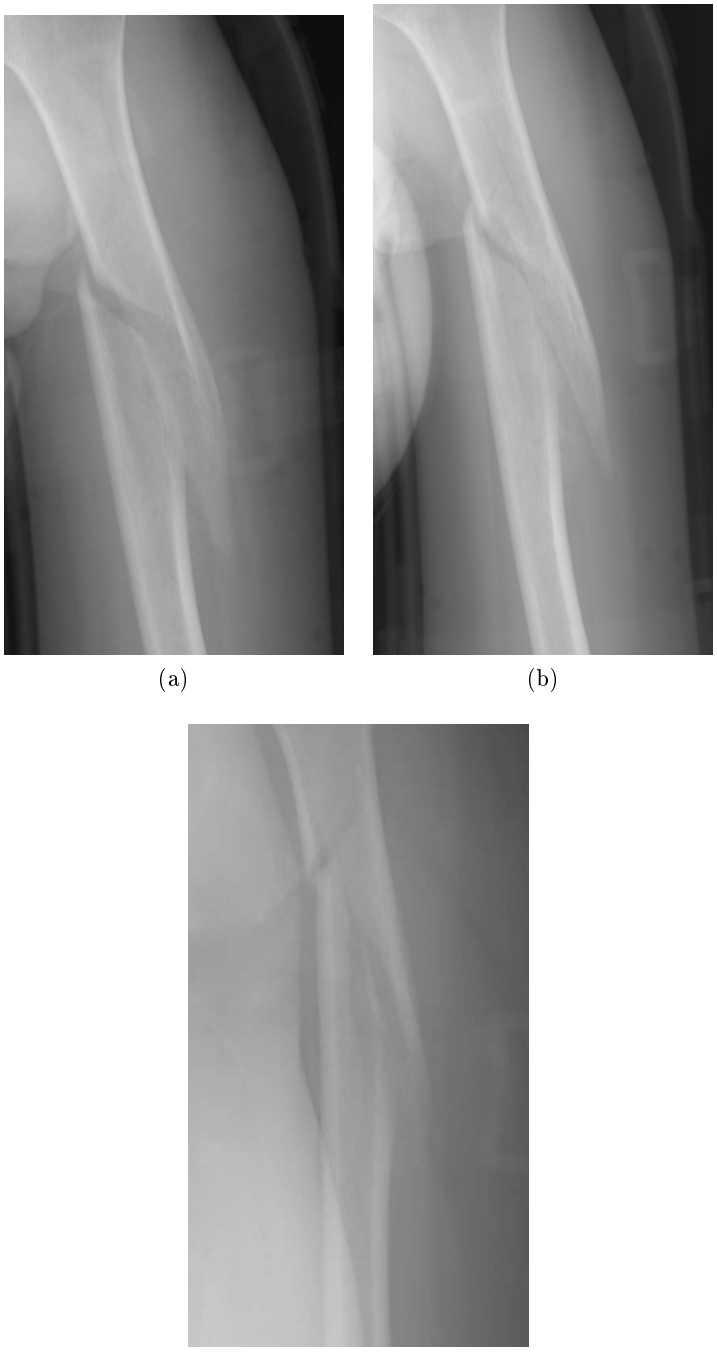

(a) (b)

(c)

Figure 8.8: AP view of the fracture site with load applied for a) the first follow-up of patient 6, b) the second follow-up of patient 6 and c) the first follow-up of patient 7.

Matlab Cross-Correlation Procedure

The procedure was executed successfully on the humeral images, i.e. it gave values for lateral and axial offset as well as angular deflection. Images from the program are shown in Figure 8.9.

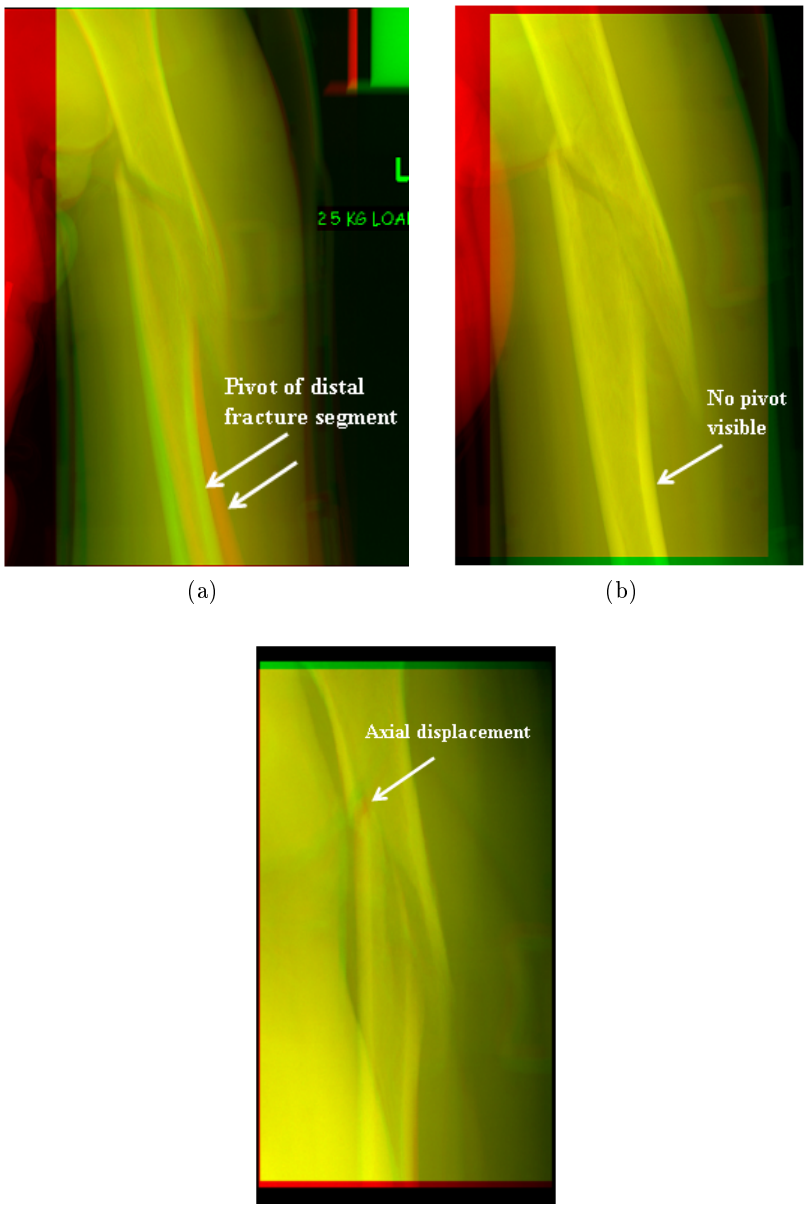

(a) (b)

(c)

Figure 8.9: Alignment of the loaded and unloaded X-rays for a) patient 6 first follow-up, b) patient 6 second follow-up and c) patient 7 first follow-up.

The figures show that a good alignment was achieved using the cross-correlation method. Figure 8.9 (a) shows that for the first follow-up of patient 6, when the proximal segments of the loaded and unloaded X-rays were aligned, there was a 'pivot' or angular offset between the distal segment in the loaded and unloaded images. This effect was reduced in the late follow-up, shown in Figure 8.9 (b). The pivoting effect did not occur to the same extent in patient 7's X-rays. Although smaller changes were visible in this patient, a small axial offset at the medial border of the fracture was seen.

The measurements made of the angular movement and lateral and axial displacement using the cross-correlation method are shown in Table 8.6. For patient 6, the smallest deflection measured in the first test was an axial offset. Both angular and lateral offsets were fairly large. In the second test the vertical offset had increased slightly but both angular and lateral changes decreased. This was consistent with the 'pivot' effect seen in the X-ray images. For patient 7, no angular movement occurred in the first test. Lateral displacement was 1.7 mm and axial displacement was large at 2.8 mm which was expected from an axial load. Again, this was consistent with the radiographic evidence. All measurements had a low SD indicating good repeatability of the computerised procedure.

Table 8.6: Angular and offset measurements and SDs made using the cross-correlation method.

Patient	**Test**	**Angle (SD) [degrees]**	**Axial Offset (SD) [mm]**	**Lateral Offset (SD) [mm]**
6	1	2.1 (0.1)	0.7 (0.1)	2.9 (0.1)
	2	0.1 (0.0)	0.9 (0.1)	0.5 (0.1)
7	1	0.0 (0.0)	2.8 (0.2)	1.7 (0.2)

The cross-correlation method was also executed on the shoulder joint to measure any displacement of the humerus occurring there. The alignment of the acromion process in the loaded and unloaded images of the first test for both patients is shown in Figure 8.10.

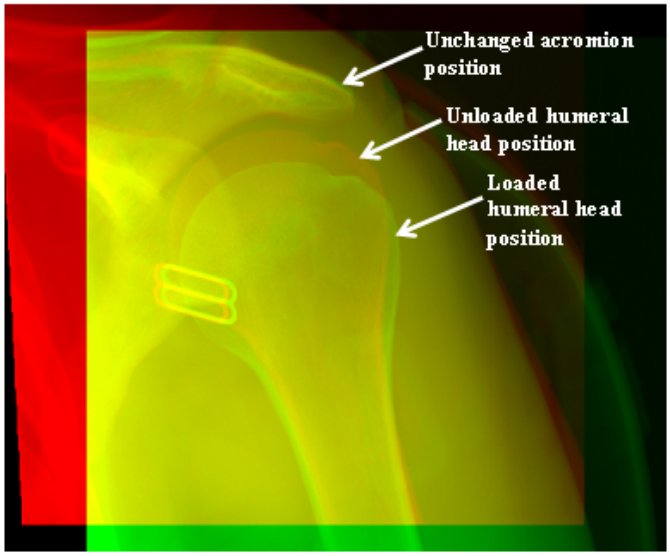

(a)

(b)

Figure 8.10: Alignment of the acromion process and humeral head in the unloaded and loaded X-rays using the cross-correlation program in a) patient 6 and b) patient 7.

Figure 8.10 (a) shows that extension occurred at the shoulder joint of patient 6. The red 'shadow' image is the unloaded image. The head of the humerus can be seen to be in normal position within the joint. The green 'shadow' image is the loaded image, where it can be seen that the humeral head had moved downwards. Areas of yellow are where the two images have aligned well, i.e. the acromion had not changed in position. Contrastingly, the alignment of the second patient's images showed mostly yellow regions indicating little movement of the humeral head or extension at the shoulder joint.

Image J Measurements

The measurements made manually using Image J were used to provide a comparative assessment of the images to the cross-correlation program. Results from the measurements are shown in Table 8.7. For the first test on patient 6, the results showed only a small change in angle between loaded and unloaded X-rays for the proximal section of humerus. However, this increased almost seven times for the distal segment. Displacement changes across the fracture line increased as the measurements moved laterally. The offset between proximal and distal fragments decreased in the most medial measurement. The pattern of displacements was similar for the second test on this patient, but the measured displacements were bigger. The angle change was similar in proximal and distal segments. An increase in displacement from medial to lateral also occurred in the first test of patient 7. However, only very small angular changes occurred.

Table 8.7: Change in angular and displacement measurements between X-rays using Image J.

		Displacement [mm]			**Angle [degrees]**	
Patient	**Test**	**Medial**	**Midline**	**Lateral**	**Proximal**	**Distal**
6	1	-0.7	0.6	1.3	1.6	7.7
	2	-0.3	1.7	2.0	-5.0	-9.0
7	1	1.0	6.1	12.3	-1.0	1.0

Mechanical Stiffness Measurements

Using the angle and distance measurements and the applied loads, mechanical stiffness calculations were made. These are shown in Table 8.8. For patient 6, the results show an increase in stiffness measured by axial and lateral displacements, as expected. However, the angular stiffness, although similar between the two tests, decreased by a small amount.

Table 8.8: Mechanical Stiffness measurements for the first and second follow-ups.

		Patient 6			Patient 7
	Follow-Up	**1**	**2**	**Change**	**1**
F_B **[N]**		21.5	20.5		14.0
	Axial [N/mm]	29.1	23.5	-5.6	5.1
Stiffness	**Lateral [N/mm]**	7.4	43.6	36.1	8.3
	Angular [N/deg]	10.1	205.0	194.9	No Reading

8.3.3 Discussion

Radiographers found the system easy to use and that the extra equipment was not difficult to set up or manoeuvre. Furthermore, the patients were comfortable throughout the X-ray procedure. Application of the weight did not cause discomfort, although it is possible that attempting the test earlier in the fracture healing process may be difficult due to patient discomfort. A potential limitation of the humeral equipment was whether patient compensation would reduce the load experienced at the fracture. Examination of the X-rays showed that the patients maintained their shoulders in a level position suggesting that little alteration of the load experienced at the fracture occurred due to flinching or angling of the shoulder. A further potential limitation of the equipment was the fact that no loaded lateral view could be taken. However, having two views was not as necessary with axial loading as it was in the case of four point bending. In axial loading, the fracture is always loaded in the same direction and it would therefore be the image of the fracture that changed in a different view and not the direction of loading. In some fracture configurations alternative views may allow a better visualisation of the fracture gap.

In the first test on patient 6, analysis of the X-rays both visually and using the cross-correlation procedure showed little axial movement at the fracture site due to loading. This indicated that there was some bridging between the two fracture segments allowing the force to be transmitted to the proximal segment of the humerus, although little callus was visible on the X-rays. This possibility was reinforced when analysing the angular movement that occurred in the distal segment where the distal part of the humerus seemed to pivot on the medial part of the fracture. The cross-correlation measurements confirmed this, showing a lateral and angular movement, rather than an axial offset. Manual Image J measurements were also illustrative of this movement and showed no change in the angular orientation of the proximal segment but that the displacement between the segments increased from medial to lateral and decreased medially on loading. This could have been due to loading

occurring at an offset to the longitudinal axis of the humerus, although it also seemed likely that there was some early bridging callus material in the medial side of the fracture which caused the load to transfer to the proximal segment resulting in a pivot of the distal segment about the medial callus. The prediction of medial bridging callus from these early X-rays was confirmed on visual examination of the X-rays at the second follow-up, which showed visible callus in this area. The loading tests indicated that callus on the lateral fracture border also increased during healing. This resulted in a decreased pivoting movement and slightly increased axial displacement which could be more easily measured due to the lack of angular movement. In general, the displacements between the first and second tests decreased resulting in measurement of increased stiffness which was consistent with the radiographic evidence and the expected change during the healing process.

In the first test on patient 7, a more typical displacement pattern was seen with axial displacement being the major displacement measured. X-rays at the shoulder showed that the humeral head was unaffected by loading, indicating that no load was being transmitted to the proximal segment and that most was being absorbed at the fracture site. The comparison between the different types of displacements measured in each patient indicated that the anatomy of the fracture is important in determining the movement that will occur during loading. since comminuted areas will limit movement. This could result in pivoting or angular movements which might be early indicators of healing. Although these differences in displacements made it difficult to compare results between patients, the changes between early and late tests still showed a decrease in displacements and increase in stiffness in patient 6. This, combined with a qualitative assessment of the response of the fracture to loading, could provide clinicians with an indication of the healing progress of fractures or alert them to potential delayed or non-unions should the stiffness not increase at later follow-ups. However, further testing on a larger patient group would be necessary to confirm this.

8.4 SUMMARY

This chapter has presented the results of two clinical pilot studies. The first described four point bending stiffness tests performed on five IM nailed fracture patients. The second described axial stiffness tests performed on two conservatively treated humeral fracture patients. The results from these tests and the previous chapters are used to make conclusions and recommendations in Part IV. The following section presents the investigation into Aluminium step wedge analysis.

Part III

Aluminium Step Wedge Calibration in Digital X-ray

Chapter 9

Experimental Apparatus

9.1 INTRODUCTION

This chapter describes the equipment developed to perform Aluminium step wedge calibration in digital X-rays and the assessment of the accuracy of the resulting information. The optimal design of an Aluminium step wedge is discussed and the apparatus that was constructed to test the effect of scatter and overlying soft tissue on the calibration technique is also presented. The investigative tools used are the same as those discussed in Section 5.2.

9.2 ALUMINIUM STEP WEDGE DESIGN

The design of the step wedge was based on experience from previous investigations and models from previous studies. The goal was to develop step wedges that could be used in both pre-clinical and patient studies. It was necessary for the wedges to have the precision to detect changes in Aluminium-equivalent thickness across a wide range of values. The wedges also needed to provide enough information to form an accurate calibration graph whilst not being cumbersome in the clinical environment.

Various different designs of wedge have been reported in the literature. These are summarised in Table 9.1. The table shows that a wide variety of step numbers and thicknesses have been used in previous studies. However, none of these are specified for patient based fracture research.

Table 9.1: Description of step wedges reported in the literature.

Source	**Number of Steps**	**Step thickness [mm]**	**Study Group**
Haidekker *et al.* [103]	6	0.5	Mice
Nomoto *et al.* [87]	10	0.5	Dentistry
Kolbeck *et al.* [28]	10	2.0	Pigs
Colbert *et al.* [104]	14	Not specified	Bone Samples
Symmons *et al.* [108]	15	1.0	Various animals
Gu *et al.* [91]	15	1.0	Dentistry

In this investigation two different wedges were designed and tested. The first was a 25 mm wide wedge of ten steps, each 5 mm thick. Based on examination of X-rays, this thickness was chosen to be the thickest visible on X-ray and the highest value necessary for patient based density evaluation. Although the 50 mm thick top step was thick enough to completely block X-rays, the possibility of high scatter interference due to its being on the edge of the wedge was considered. To attempt to solve this problem, another wedge, 30 mm wide with 15, 5 mm steps, was designed. Although this exceeded the visually useful range of densities, the extra layers of top steps provided some scatter protection for the steps to be used in calibration. For pre-clinical studies on small anatomies, a 10 mm wide wedge of ten steps, each 2 mm thick was chosen based on an average of the designs of previous researchers. The smaller steps allowed the greater precision necessary when dealing with small bone samples. Images of the three wedges are shown in Figure 9.1 and X-rays of each of the wedges are shown in Figure 9.2. The figure shows the difference in saturation levels achieved by the greater thicknesses of steps and the bigger range of grey levels (GLs) visible with smaller steps. The wedges were milled in a workshop using Aluminium alloy 6082 (97% Aluminium, density 2.7 g/cm^3) and with a precision of 0.1 mm.

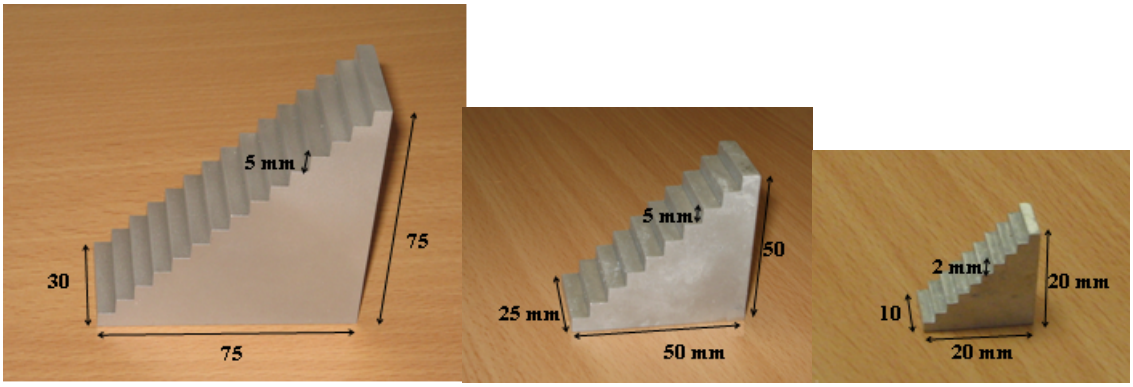

(a) (b) (c)

Figure 9.1: Photographs of the three wedges; a) the fifteen 5 mm step, b) the ten 5 mm step and c) the ten 2 mm step.

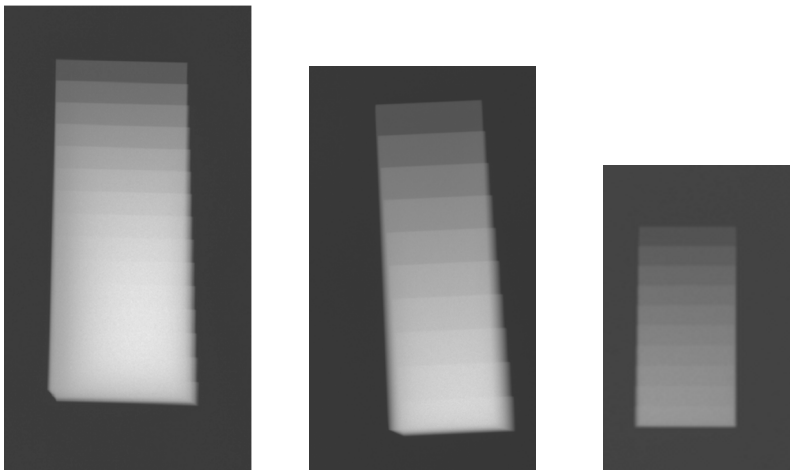

(a) (b) (c)

Figure 9.2: X-rays of the three wedges; a) fifteen 5 mm step, b) ten 5 mm step and c) ten 2 mm step.

9.2.1 Vertical Placement

In most X-ray examinations the patient lies horizontally and an X-ray is taken from above. In this situation the wedge could be easily placed next to the patient, lying directly on the imaging cassette or bed. However, in other cases, such as for humeral fractures, images are taken with the patient standing up and the X-ray source pointed horizontally. In this situation, specific equipment was necessary to position the wedge near to the point of interest. In the Orthopaedic X-ray department of the RIE, vertical X-rays were taken using

a chest X-ray plate holder. This had a width of 511 mm, a height of 570 mm and a depth of 5 mm. It was also height adjustable so that it could be positioned specifically for each patient. In order to include the wedge in vertical X-rays, a wedge holder was designed to fit over the chest X-ray bucky. The design of the wedge holder is shown in Figure 9.3. The wedge holder hooked over the end of the bucky and was constructed of 1 mm thick Perspex so it did not distort or attenuate the X-rays passing through the wedge. Strengthening corners of Perspex were used on the sides to maintain stability.

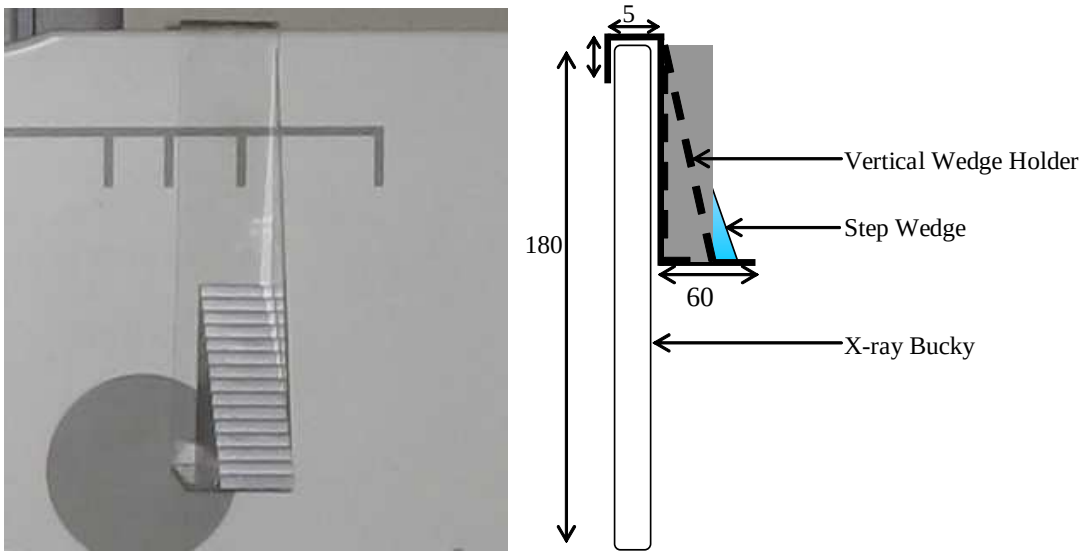

(a) (b)

Figure 9.3: a) Photograph of the vertical X-ray wedge holder over a chest bucky and b) side view schematic diagram.

9.3 SCATTER PHANTOM

In examining the use of the Aluminium step wedge to measure bone and fracture equivalent thickness accurately, the effects and contributions of scatter, soft tissue and bone thickness had to be investigated. Since some fractures were also treated using plaster, polytape or fibreglass casts, the effects of these on measured equivalent thickness also needed to be considered. Two X-ray phantoms were developed to do this. The first was of a human tibia placed in a watertight box made with 5 mm thick Perspex (40 mm x 10 mm x 10 mm) with a lid. This box was filled with varying levels of water to mimic the effect of different thicknesses of soft tissue overlying the bone. Figure 9.4 below shows this phantom and a corresponding X-ray image.

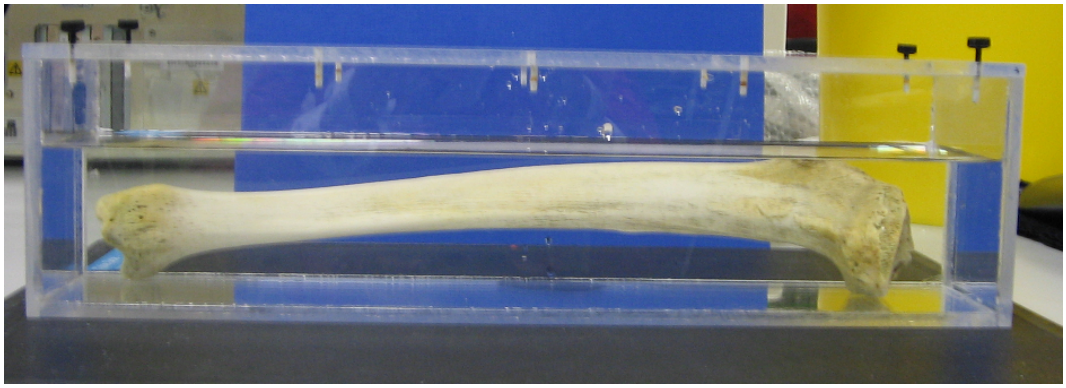

(a)

(b)

Figure 9.4: a) The Perspex box with tibia filled with 60 mm of water and b)the corresponding X-ray image.

The X-ray image shows the bone, box borders, and how the water around the bone provided a good estimation of the X-ray attenuation caused by soft tissue. The figure also shows that a constant level of water provided a different covering over the bone in different areas. In analysing the images from this phantom, these inconsistencies due to the varying bone shape, as well as the possible absorption of some water during the course of experiments, made it difficult to assess the effects of scatter and soft tissue thickness.

For this reason a second, more uniform phantom was designed and is shown in Figure 9.5. It consisted of a solid Perspex box with a central cylindrical section made from polyvinyl chloride (PVC) with a density of 1.43 g/cm^3. PVC was chosen as it mimicked the X-ray grey level of bone closely. This phantom was equipped with several 2 mm thick sections of Perspex. Since Perspex has a similar atomic number, and therefore similar X-ray attenuation properties, to soft tissue it was used to represent different soft tissue thicknesses. Sections of polytape, fibreglass and plaster were also made to fit over the phantom, representing a bone treated with a cast made from these materials. This was a more uniform model

allowing for an estimation of the contributions of scatter, soft tissue and bone thickness. Furthermore, it allowed modelling of the effect of adding plaster, polytape or fibreglass and was an improvement on the anatomical model for the purposes of measuring scatter contributions. The investigations made using this phantom are discussed in the following chapter.

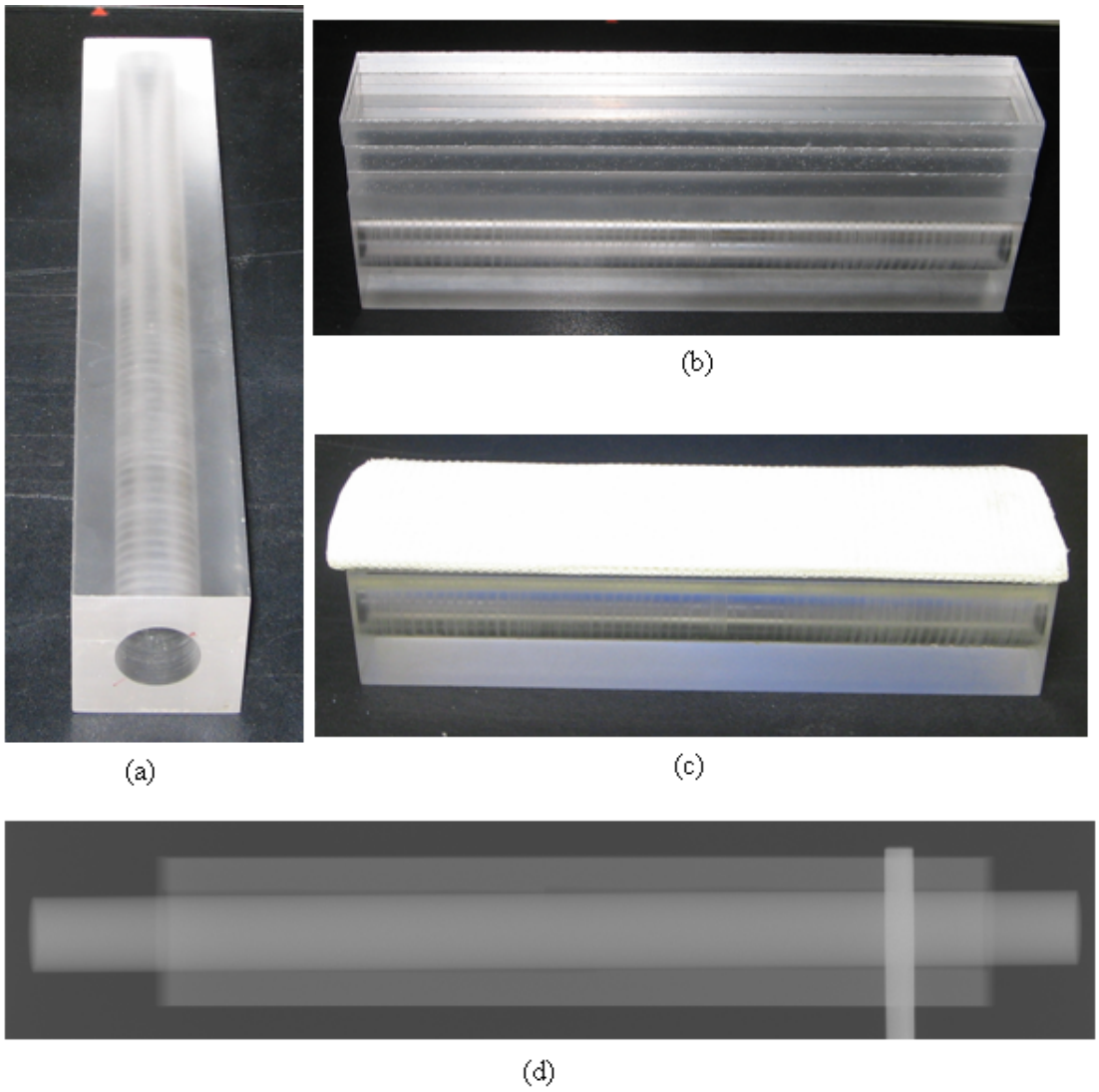

Figure 9.5: The Perspex box phantom a) showing central tunnel, b) with four layers of Perspex overlaying it, c) with a layer of fibreglass overlaying it and d) an X-ray image of the phantom with the central bone-equivalent rod in place.

9.4 SUMMARY

This chapter described apparatus that was designed and manufactured to investigate the use of an Aluminium step wedge included in digital X-ray images in order to give information on fracture healing. Several designs of step wedge were made to cover the range of measurements in both pre-clinical models and patient studies. X-ray phantoms to test the effects of scatter and overlying soft tissue were also constructed. The use and testing of the apparatus is described and discussed in the following chapters.

Chapter 10

Image Analysis of Digital Step Wedge X-rays

10.1 INTRODUCTION

This chapter discusses computerised procedures that were developed to use a step wedge to provide a consistent calibration of grey level to Aluminium thickness in digital X-ray images. This included identifying the steps of the wedge, investigating the best method of calibration, correcting for sources of error in the X-ray imaging process and analysing the automatic processing performed by a Fuji CR system. Correcting for the contributions of scatter, soft tissue and bone thickness was also investigated. Except where otherwise indicated, all exposures were taken using 63 kV and 1.8 mAs.

10.2 STEP WEDGE IDENTIFICATION

As discussed in Section 4.5, the basic concept behind using a step wedge in X-rays is to relate the Aluminium thickness of each step to the grey level in the X-ray image. In theory this information forms a calibration graph that can be used to relate all other grey levels in the image to an equivalent Aluminium thickness. It also means that measurements in different X-ray images can be compared, as they are all calibrated using the same Aluminium step wedge. In this study, there were two major steps involved in performing the calibration: i) identifying the steps of the wedge in radiographs and ii) relating the X-ray grey levels of these steps to Aluminium thickness in a meaningful way. The task of identifying the steps of the wedge and their grey levels is addressed in this section.

10.2.1 Step Segmentation

For the accurate segmentation of steps of the wedge, a limited amount of user interaction was necessary to crop an area containing the wedge from the X-ray image. Several methods were then investigated to identify and locate the steps of the wedge. Procedures were implemented using Matlab.

Edge detection

Canny edge detection computes the gradient of an image using the derivative of a Gaussian filter. It applies upper and lower thresholds to this gradient for greater edge sensitivity and was found to give the best results as the methods it employs are most robust at overcoming noise problems [128, 129]. The best results were found with Matlab's default threshold values and a sigma equal to two (where the wedge dimensions are 75 pixels x 25 pixels and sigma is the SD of the Gaussian filter). An example of the wedge after Canny edge detection is shown in Figure 10.1. Although edges were identified, it did not delineate them with enough clarity to use for step detection.

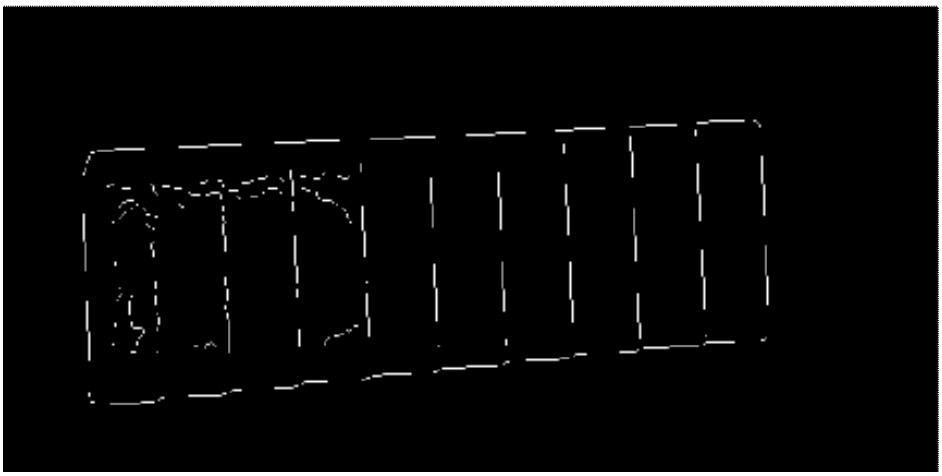

Figure 10.1: Step wedge after Canny edge detection

Kmeans Clustering

Kmeans clustering was attempted to group grey levels according to a set number of clusters. Kmeans clustering works by grouping a specified number of objects into a specified number of partitions according to certain attributes [130]. This was attempted with six clusters and the result is shown in Figure 10.2. As the image shows, results were only clear up to the third step and it was concluded that this method was unsuitable for further use.

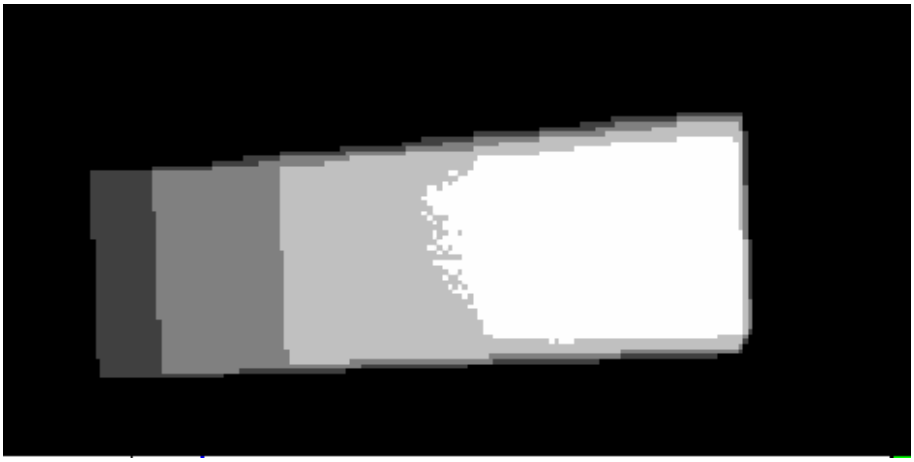

Figure 10.2: Wedge after six cluster kmeans analysis.

Hough Transform

The Hough transform is a mathematical algorithm that is commonly used in image processing to detect geometrical features such as lines [131, 132]. It was useful in this application because it is tolerant of gaps in lines and noise in the image. The Hough transform works by converting lines in Cartesian space (x, y) to points in Hough space (r, θ), where r is the length of a perpendicular line joining the origin to a point and θ is the angle of this line. The use of the Hough transform is based on the fact that any line in Cartesian space can be described uniquely by two parameters, r and θ, as shown in Figure 10.3. The angle and distance description obtained from Cartesian space is plotted in Hough space to create a single point.

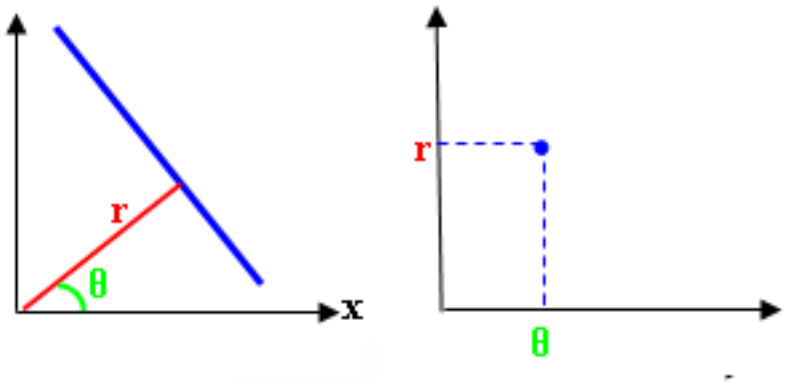

(a) (b)

Figure 10.3: a) A line in Cartesian space converted to b) a point in Hough space.

A single point in Cartesian space forms a single sinusoidal curve of points in Hough space and a group of points that lie on the same line in Cartesian space form sinusoids that intersect at a common (r, θ) point in Hough space. It is this feature of Hough space that allows easy identification of lines. Examples of the Hough transforms of a point, four points that lie on the same line, and the line they lie on are shown in Figure 10.4. This demonstrates how identification of a line in Cartesian space becomes identification of intersecting sinusoids in Hough space.

When applied to an entire image, the Hough transform counts the number of r and θ parameters in bins. Bins with the highest counts are likely to correspond to lines in Cartesian space. A variety of thresholding methods can be used to aid in identifying the correct bins, and therefore lines, in a given image. In this application, the Hough transform was applied to the Canny edge detected image of the wedge. The result is shown in Figure 10.5.

The intersections of partial sine waves in the image show the possible locations of lines of the edge detected wedge. Analysis of this resulted in an array of line segments with r and θ values. According to the image attributes (average step size, line length, number of steps, spacing of steps etc.), the best bins of the transform in which to search for line segments were found. The lines identified by these bins were then merged or discarded according to the image attributes, resulting in an array of lines representing the edges of the wedge. Using this method, the start and end point of each line segment were known and could therefore be used to identify each step individually. In the images, higher thicknesses of Aluminium became saturated by X-rays and it was found that ten steps, with thicknesses from 5 - 50 mm, could be identified. However, the Hough transform did not perfectly identify the edges of the wedge, and often offered incorrect options as to the steps of the wedge. Several methods were used to overcome this problem.

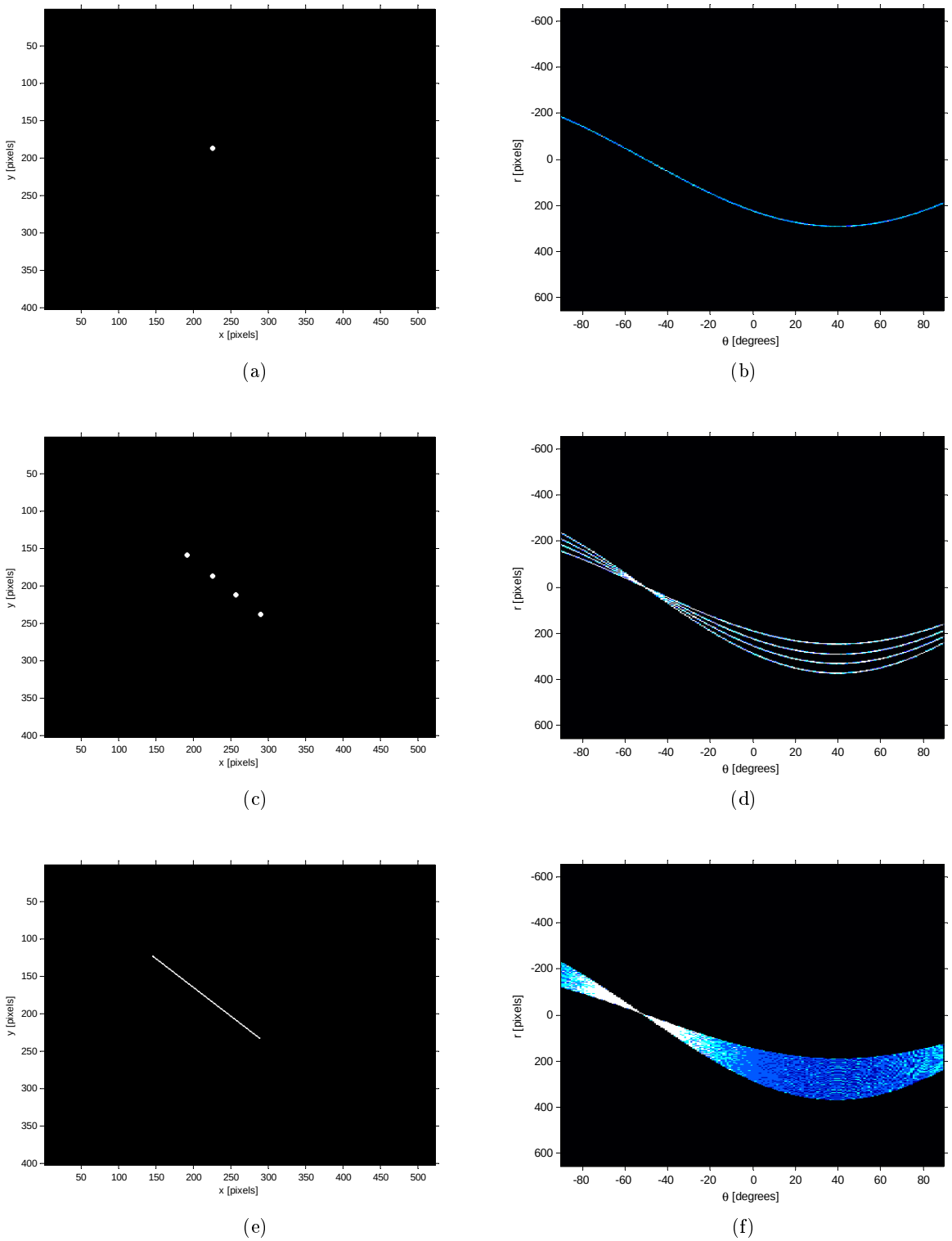

Figure 10.4: a) A single point in Cartesian space transformed to b) a sinusoid in Hough space, c) a group of points on the same line transformed to d) a set of sine waves intersecting at a single point in Hough space and e) a line and f) group of sine waves showing the point of intersection in Hough space.

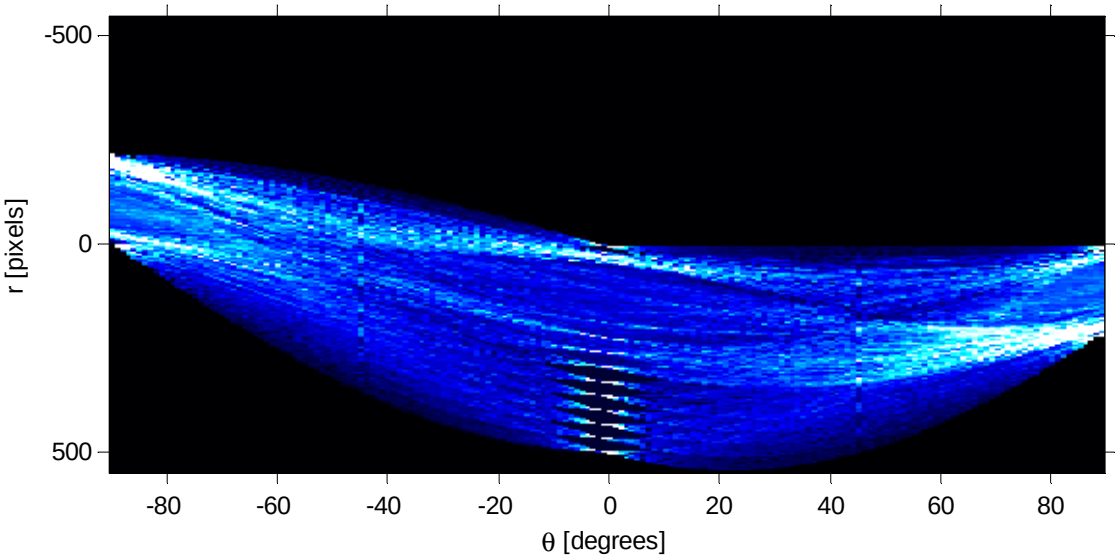

Figure 10.5: Hough transform of the edge detected step wedge.

i) Re-orientation of the wedge

Each time the user cropped the wedge from an image, a slightly different area was selected. This meant that the Hough transform was calculated differently, since the origin used to calculate the (r, θ) parameters was in a different position in relation to the wedge. This is illustrated in Figure 10.6 (a) and (b). Thus, different lines were chosen as steps in an unpredictable manner. To eliminate this problem, only the area containing the wedge (and no surrounding space) was used. This was achieved, firstly, by ensuring the wedge was always horizontally positioned and secondly, the selected area was converted into a binary image of which the bounding box (i.e. the smallest box which could be drawn around the object) was identified and the wedge subimage was cropped to this. This meant that the same area and origin was used for calculating the steps of the wedge each time the procedure was executed, since the same bounding box was calculated independent of the user selected area. See Figure 10.6 (c).

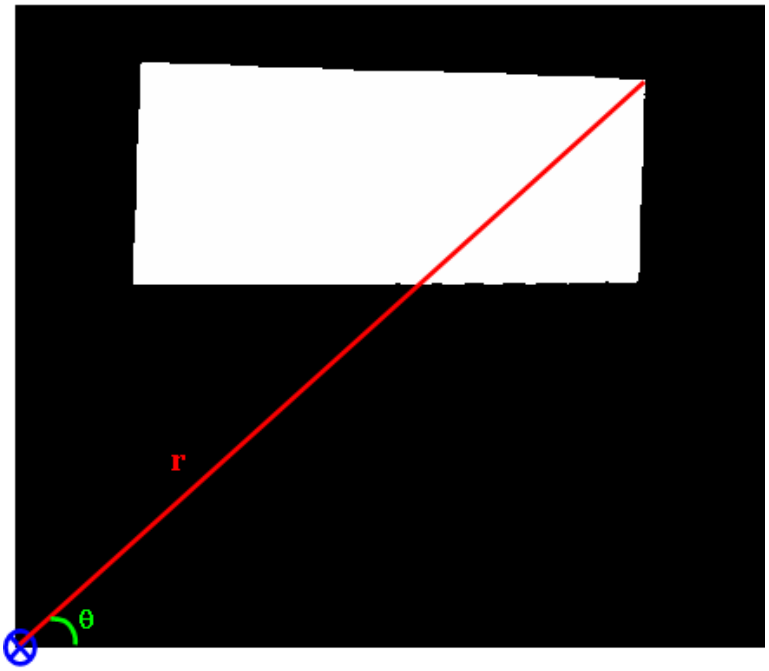

(a)

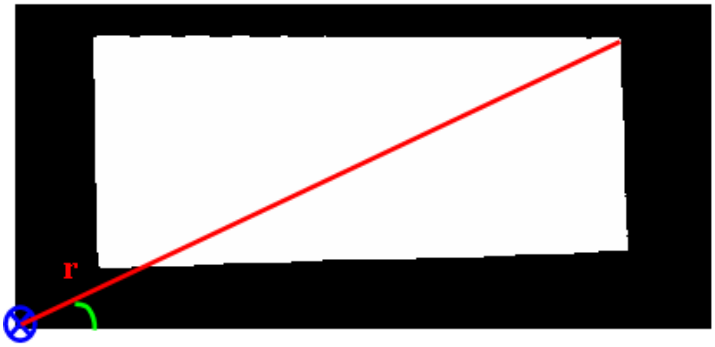

(b)

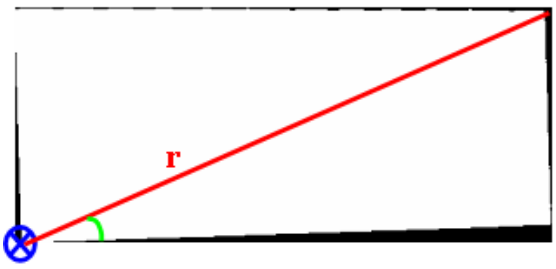

(c)

Figure 10.6: User selected wedge regions showing different origins (blue) and (r, θ) values for the top right corner of the wedge (red and green) in a) a large region selection and b) a small region selection. c) Consistent bounding box resulting from any user selected wedge region.

ii) Rejection of Incorrect Steps

Despite the improvement in consistency of cropping the wedge, incorrect lines were still identified as step edges. To eliminate these, the minimum and maximum pixel measurements of wedge step lines were determined by measuring the wedge. Any lines selected by the Hough process that fell outside this range were rejected, leaving only the true steps.

iii) User Controlled Step Selection

In cases of noisy images or different X-ray settings, the first two methods did not always succeed in identifying all the steps correctly with no spurious lines. As a final check, an option was added to allow the user to select only the lines that were correct, and to manually add any lines that had been left out. This ensured that the correct steps were always chosen.

10.2.2 Grey Level Calculation

The co-ordinates of each line identified by the Hough transform were used to identify the steps of the wedge. The first procedure was to ensure that the 'start' and 'end' co-ordinates of each line were in the correct orientation and that the lines were sorted in the correct order. This was achieved by analysing each set of co-ordinates to ensure the 'start' co-ordinate was always placed vertically higher than the 'end' co-ordinate. Secondly, the lines were ordered according to which 'start' co-ordinate lay closest to the left hand edge of the image. This resulted in a set of lines directed in the same orientation and in a specified order. Figure 10.7 shows an accurate delineation of the relevant steps performed by the computerised procedure. This was then used to determine the mean grey level of each step for subsequent calibration purposes.

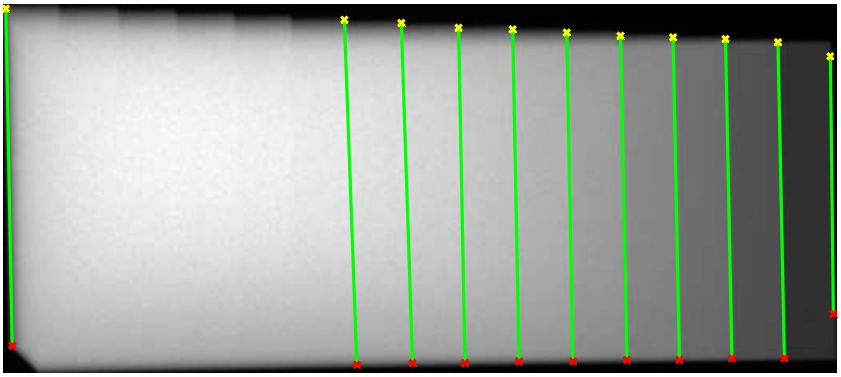

Figure 10.7: The X-ray image of the wedge showing the selected step boundaries (green). Start (yellow) and end (red) co-ordinates are also marked.

Mean of the Entire Step

To find the mean grey level for each step, an average of all the pixels in a step was found using the boundary co-ordinates derived from the Hough transform. Typical grey levels and the associated SDs are shown in Table 10.1. As the table shows, the SDs were high, i.e. ~13%, especially with greater step thicknesses. This was due to scattering and shadowing effects at the edge of each step creating a range of pixel values on the step boundaries.

Table 10.1: The mean grey level and SD for each step of the wedge.

Step Number	**Mean Grey Level**	**SD**
1	370	2
2	458	12
3	531	22
4	592	36
5	643	48
6	683	66
7	717	75
8	743	92
9	759	103
10	799	98

Mean of an Inner Region of a Step

To minimise inconsistencies due to scatter and shadowing, it was decided that a better approach was to use the inner part of each step where a more homogeneous grey level could be found. However, since the wedge was not perfectly horizontal in X-ray images, identification of this area was non-trivial. Figure 10.8 illustrates the geometrical situation for a single step of the wedge.

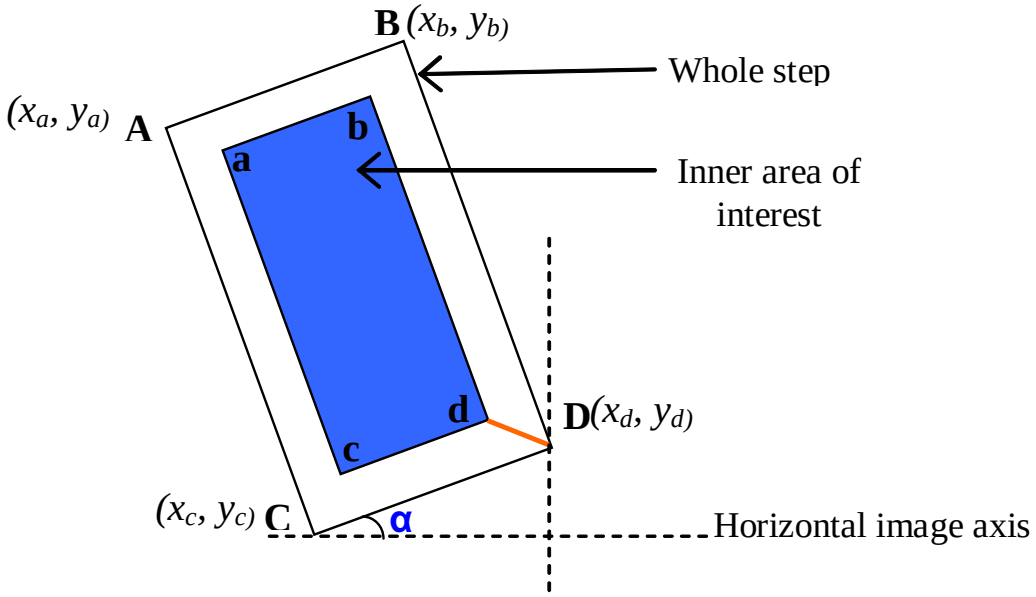

Figure 10.8: The orientation of a step at an angle α to the horizontal image axis and the inner area (blue) used for grey level measurement.

As can be seen in Figure 10.8, the wedge is at an orientation of α degrees to the horizontal image axis. The position of the four corners of the outer step (A, B, C, D) are known from the Hough lines identification. The problem was to determine the co-ordinates of the four corners of the inner area of the step (a, b, c, d) that would allow for a more representative determination of mean grey level. Figure 10.9 shows the point D and the associated angles used for calculating the inner point d.

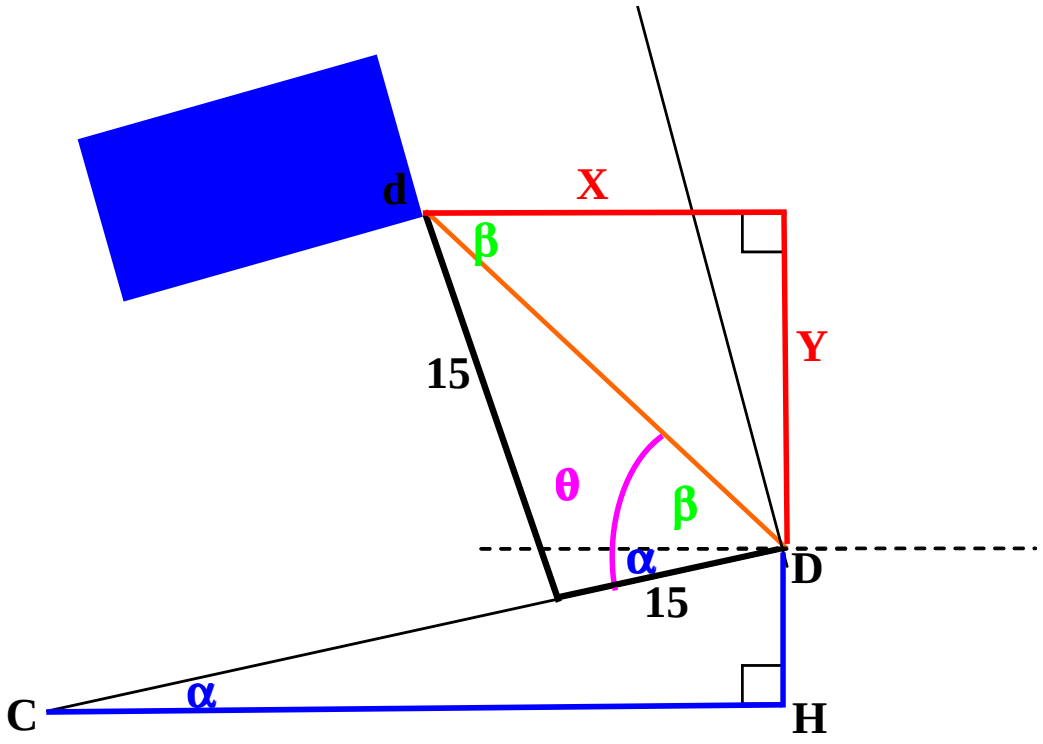

Figure 10.9: Angles and distances used to determine the vertical and horizontal distances from D to d.

The distances to relate corner D to corner d in the step co-ordinate system are known. Considering the dimensions of the wedge, a distance of 15 pixels along the width and 15 pixels along the length of the step was chosen. As has been shown, the wedge is rotated by α degrees to the horizontal image axis. In Matlab, co-ordinates are specified according to the right-angled (x, y) image co-ordinate system. Therefore, the vertical and horizontal distances from D to d (X and Y, shown in red) required calculation.

From the blue triangle

$$\begin{aligned} \tan\alpha &= \frac{DH}{CH} \\ \alpha &= \arctan\frac{DH}{CH} \end{aligned} \tag{10.1}$$

From the black triangle

$$\begin{aligned} Dd &= \sqrt{15^2 + 15^2} \\ &= 21.21 \end{aligned} \tag{10.2}$$

Also

$$\begin{aligned} \sin\theta &= \frac{15}{Dd} \\ \theta &= \arcsin\frac{15}{Dd} \\ \beta &= \theta - \alpha \end{aligned} \tag{10.3}$$

Therefore, in the red triangle

$$\begin{aligned} \cos\beta &= \frac{X}{Dd} \\ X &= Dd(\cos\beta) \end{aligned} \tag{10.4}$$

$$Y = Dd(\sin\beta) \tag{10.5}$$

Thus, the vertical and horizontal distances in the image co-ordinate system that must be moved in order to accurately isolate a central portion of each step of the wedge were determined.

On applying this algorithm it was found that a more stable mean grey level reading was obtained, as illustrated in the Table 10.2. Typically, mean grey level was also found to be higher, indicating that some of the background areas surrounding the steps were previously being taken into account in mean grey level calculations. Furthermore, the SD was reduced by an average of 75% and the largest SD was now only 4% of the corresponding mean grey level value.

Table 10.2: Table showing the mean grey level and SD for the inner rectangle of the steps.

Step Number	Mean Grey Level	SD
1	369	9
2	462	3
3	540	4
4	609	7
5	670	10
6	724	15
7	768	20
8	811	23
9	837	29
10	871	36

10.2.3 Final Algorithm

The algorithm of the final procedure used to detect the steps of the wedge is as follows:

1. The user selects the region of the image containing the wedge.
2. Thresholding is performed to select the smallest possible region containing the wedge.
3. Canny edge detection isolates the edges.
4. The Hough transform identifies the possible positions of the steps.
5. Unlikely lines are rejected based on length and geometric properties.
6. The user has the opportunity to reject or add lines to form a final set defining the steps.
7. Lines are re-ordered and re-orientated so that they are positioned from left to right and with start co-ordinates at the top of the image.
8. An inner area of each step is located.
9. Mean grey level and SD of each step are returned.

The resulting steps and inner regions used to calculate grey level are shown in Figure 10.10 where the selected steps are in magenta and the corners of the inner area used to calculate the grey level are in yellow, red, green and blue crosses.

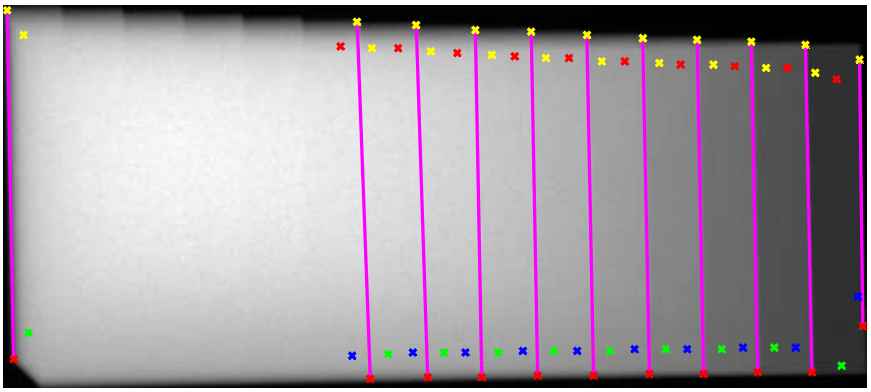

Figure 10.10: The step wedge with identified steps (magenta) and the boundary points of the inner rectangles used to calculate grey level (yellow, red, green and blue).

10.2.4 Discussion

This section described the procedure to semi-automatically obtain mean grey level information for each step on the wedge using Canny edge detection and the Hough transform. Most previous reports of the use of step wedges in radiographs involved manual selection for subsequent optical density or grey level calculation [87, 89, 106, 108]. For instance, de Josselin de Jong and ten Bosch used operator determined means from 1D densitometer scans [105] and Kolbeck *et al.* manually positioned circular regions of interest to calculate the mean grey level in each step of the wedge [28] . However, some authors have reported semi-automated methods of step detection. Haidekker *et al.* used Sobel edge detection on the image of the wedge and then analysed repeated scan lines perpendicular to the wedge to identify each step and its mean grey level, although the details of the procedures were not described [103]. Use of the Hough transform has not previously been reported despite its suitability for edge and line detection. The procedure presented here is robust to noise, non-ideal imaging conditions, inconsistencies in user selected wedge regions and variations in wedge positioning to the horizontal. Any possible errors in step selection can be overridden by the user in an efficient manner. Calculation of the mean grey level for each step is not a subject that has been dealt with in any detail in the literature, despite the fact that it is central to obtaining a valid and reliable calibration graph. An accurate automatic algorithm for selecting only the inner area of each step for mean grey level calculation has been developed to reduce the inconsistencies related to scatter that occur when the full step area is used.

10.3 CALIBRATION

In order for the Aluminium wedge to provide a useful calibration tool, the grey levels of the steps must be related to the corresponding thickness of Aluminium. Several methods were attempted.

10.3.1 Fitting a Straight Line

The method of calibration used by most authors [103, 104] involves fitting wedge data with a straight line. This is based on the reasoning that the relationship between incident intensity and emitted intensity (also known as the Lambert-Beer law) is

$$I = I_m e^{-\mu d} \tag{10.6}$$

where I is the intensity incident on the X-ray plate, I_m is the emitted X-ray intensity, μ is the linear attenuation coefficient (a property of the material and the X-ray energy) and d is the thickness of the material.

In the case of film X-ray, the measure of intensity on the film is made in terms of optical density, where the following relationship holds

$$D = mIt + D_0 \tag{10.7}$$

and D is optical density, m is the slope, It is the exposure and D_0 is the background fog due to processing and other film anomalies. It is important to note that optical density is high for areas of high exposure and low for areas of low exposure, i.e. it is proportional to exposure.

By combining Equations (10.6) and (10.7) and taking logs of each side, the following relationship emerges. From Equation (10.7)

$$\begin{aligned} D_m &= mI_m t + D_0 \\ mI_m t &= D_m - D_0 \end{aligned} \tag{10.8}$$

where D_m is the maximum film density. Combining Equations (10.6) and (10.7)

$$\begin{aligned} D &= D_0 - mI_m te^{-\mu d} \\ D - D_0 &= (D_m - D_0)e^{-\mu d} \\ \ln(D - D_0) &= \ln(D_m - D_0) - \mu d \end{aligned} \tag{10.9}$$

This is a straight line relationship with a negative slope equal to the linear attenuation coefficient, μ. The approach taken by Colbert *et al.* and most subsequent authors was therefore to fit the relationship between step thickness and optical density with a straight line. This was achieved in various ways, but primarily by iteratively calculating a value of D_0 that caused the exponential (or, in the case of Colbert *et al.*, second order polynomial) relationship to reduce to a straight line. This process resulted in a value for D_0 which 'corrected' for the effects of background fog and a slope for the straight line that should be equal to the linear attenuation coefficient of Aluminium.

In this study, this was attempted with grey levels. However, it is important to note that grey levels are the inverse of optical density, i.e. a high exposure gives a low grey level and a low exposure gives a high grey level. Thus, the relationship between grey level and exposure is the inverse of that between optical density and exposure seen in Equation (10.7) [90]

$$G = -mIt + G_0 \tag{10.10}$$

and combining this with the Lambert-Beer law (Equation (10.6)) and taking logs gives

$$\ln(G_0–G) = \ln(G_0 - G_m) - \mu d \tag{10.11}$$

However, since the relationship between grey level and step thickness is the inverse of that between optical density and step thickness, a positive gradient is required to model the data, so

$$-\ln(G_0–G) = -\ln(G_0 - G_m) + \mu d \tag{10.12}$$

Therefore, to find the straight line fit and calculate G_0, a value for G_0 was selected iteratively until a straight line fit of the data was obtained. This method was implemented and whilst a good fit was obtainable, the resulting graph was plotted on a negative grey level axis which was not reflective of the positive grey levels that occur in the image.

In order to relate step thickness to grey level accurately, it was necessary to consider the differences in image characteristics between optical density and grey level. Figure 10.11 illustrates the relationships between step thickness and optical density versus step thickness and grey level.

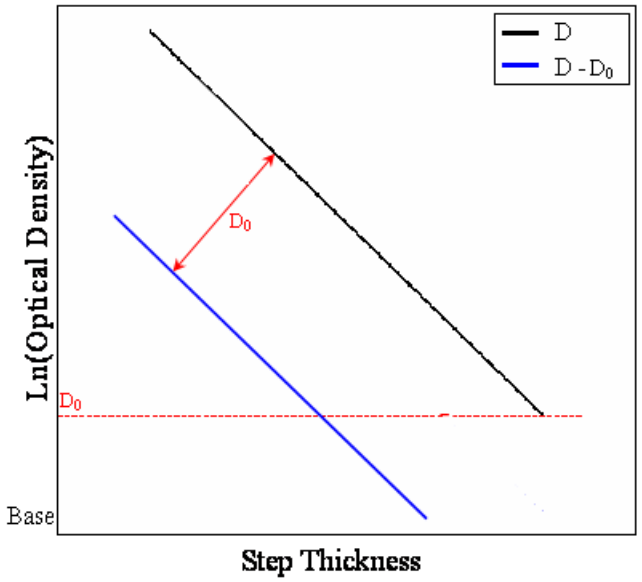

(a)

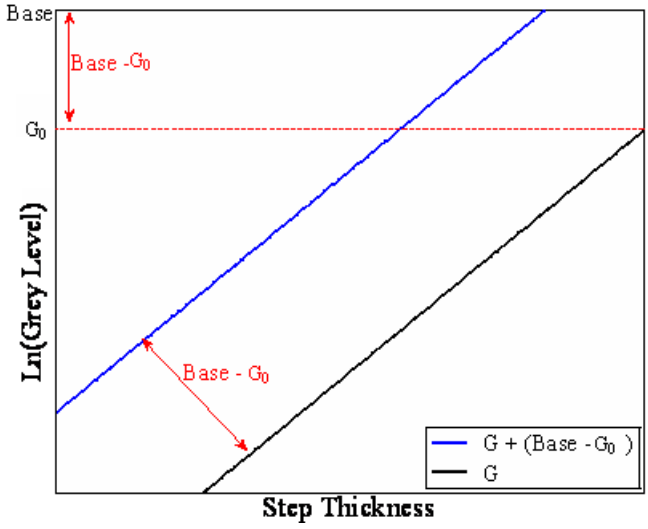

(b)

Figure 10.11: Representation of the relationship with step thickness for a) optical density and b) grey level.

As the figure shows, the situation with grey level is more complicated, since the 'base' (area of no exposure) is not 0, but the highest grey level (i.e. in a 10 bit image, this is $2^{10} - 1 = 1023$, since the lowest level is numbered from 0).

Various methods to overcome this problem were attempted, including fitting with $1023 - \ln(G_0–G)$ and $\ln(G–G_0)$. Whilst good straight line fits and a positive gradient were achieved with both of these methods, the resulting calibration graphs were plotted on a negative y-axis which was not a good reflection of the data and the relationship between grey level and step thickness, since these are both positive values.

10.3.2 Fitting an Exponential

The correction for D_0, the background fog due to chemical exposure, may not be necessary since these are mainly film based anomalies which are eliminated with the use of digital X-ray. Previous methods were based on optical density and since grey levels were now being used, a reconsideration of the calibration procedure was appropriate. One of the major reasons that previous investigators attempted to find a straight line fit was due to the inferior computing power available at the time of development. More complex curve fitting was not available, so simple ways of modelling data were necessary. It is clear from the Lambert-Beer law that the relationship between exposure and X-ray intensity is exponential. The method of modelling this with a straight line graph requires the assumption of both a mono-energetic, narrow X-ray beam and a homogeneous material. Neither of these assumptions is particularly accurate.

To eliminate the inaccuracies added by making these assumptions, the grey level and step thickness data were modelled with an exponential graph that better reflects the nature of the relationship. Therefore, the final equation chosen to fit grey level to Aluminium-equivalent thickness was

$$G = ae^{-bx} + c \tag{10.13}$$

where G is grey level, a is mI_mt, x is step thickness and c is G_0.

10.3.3 Discussion

Most step wedge techniques reported in the literature were based on film X-rays which measure optical density [103, 104, 105, 106, 107]. These fitted the exponential optical density versus step thickness relationship with a linear model of the log of the optical density. Several investigators who reported step wedge calibration using grey level, usually from film

digitisers, have shown an exponential relationship between step thickness and grey level, although they have modelled this in different ways. For instance, Kolbeck *et al.* used a square regression [28] and Carvalho-Junior *et al.* used a logarithmic regression [89]. Most investigators using grey level continued to recommend the formation of a linear calibration graph although the reasons for this were not clear [87, 88]. From an examination of the previous techniques based on optical densities it has been shown that implementing the extra computative step in attempting to fit the data with a straight line is not necessary. Not only does this not model the physical reality, but any further transformation of the data can only add uncertainty and error into the calibration process. Modern computing techniques can efficiently process more complex curve fitting so that modelling the grey levels of an X-ray image versus Aluminium thickness using an exponential curve, and subsequent calculation and extrapolation of Aluminium-equivalent thickness, is appropriate and reliable.

10.4 WEDGE DESIGN EVALUATION

As discussed in Section 9.2 previous studies have used wedges with a variety of different step numbers and step thicknesses, although few have justified the reasons for choosing a particular design. Since the information from the wedge is central to the calibration, and therefore resulting accuracy with which X-ray images can be compared, an investigation into the factors affecting wedge suitability was undertaken to determine the best design for this study. A comparison between different wedges to analyse the effects of grey level SD and scatter and a theoretical analysis of the effect of different step numbers and step thicknesses were performed. Finally, an evaluation of the precision of the calibration of the wedge is discussed.

10.4.1 Comparison of Designs

Two different wedges for patient based studies were designed in this study: one with 15, 5 mm steps and the other with ten, 5 mm steps (see Section 9.2). Analyses of the SD of mean grey level, percentage scatter and accuracy of curve fitting were performed to decide which wedge was most effective in providing density comparison information.

Standard Deviation

For each wedge, the SD of the mean grey level for each step was calculated. On comparison it was found that the ten-step wedge had a lower mean SD by approximately 9 GLs. This is probably due to the fact that the steps of the 15-step wedge are wider by 5 mm and the bigger pixel sample size therefore contributes to the greater SD. This is not necessarily an indicator of lower accuracy but a result of taking the mean of a larger area. Despite the increased SD, it is likely that sampling a larger area to get the mean grey level of each step results in a more reliable result than using a small area which could be prone to localised errors or inaccuracies.

Scatter

To analyse the scatter effects in each wedge, X-ray images were taken with the wedge covered with a piece of 2 mm thick lead overlying half longitudinally as shown in Figure 10.12 (a). For these X-ray conditions, analysis shows the expected transmission of direct radiation to be much less than 10^{-8}, in other words, that no direct radiation will penetrate the lead [133]. This was confirmed from images of the lead placed directly on the imaging plate, which showed the grey level under the lead to be 1023 GLs, the highest possible value in a 2^{10}bit image. When placed on the Perspex table above the imaging plate, the grey level under the lead was measured to be 980 GLs. This difference is due to scatter from the Perspex table, but contributes only 4% additional scatter to that due to the wedge alone. The experimental set-up allowed measurement of the covered and uncovered grey levels of each step to be compared. Measurement of the uncovered grey levels is a measure of the primary and scattered X-rays incident on the X-ray plate. The measurement under the lead covered part of the wedge is a measure of the scatter contributions only, since the lead blocks all direct radiation from the source, as shown in Figure 10.12 (b).

For each step, the covered and uncovered grey level was converted to dose and the scatter dose (covered) was calculated as a percentage of the total dose (uncovered). On comparison it was found that in each step, the 15-step wedge had an average of 3% less scatter than the ten-step wedge. This indicated that the larger design provided better protection against scatter interference in the areas of interest.

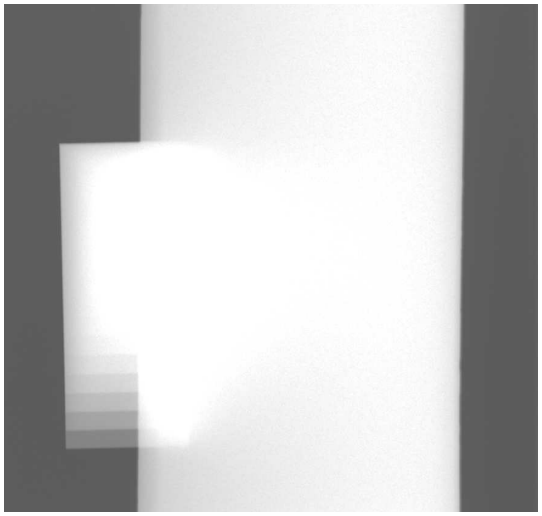

(a)

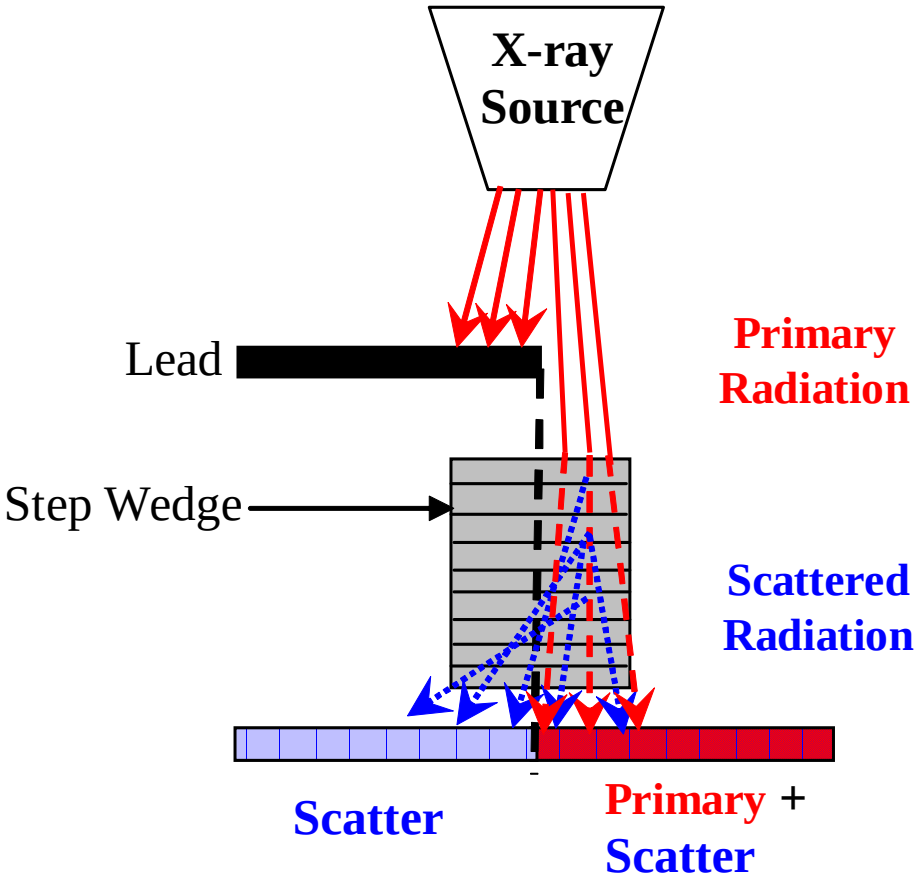

(b)

Figure 10.12: a) X-ray image showing the wedge with an overlying piece of lead blocking all emitted radiation and b) diagram showing the primary (red) and scattered (blue) X-rays incident on the cassette.

Calibration Curve Fitting

To analyse the effect of wedge design on calibration curve accuracy, the step detection computerised procedure was executed on both wedges. In each case, the first nine steps as well as the outer border of the thickest step were found automatically by the program. This indicated that above ten steps (i.e. 50 mm of Aluminium) saturation was reached since steps could no longer be clearly delineated from each other. This confirmed that the first ten steps of Aluminium (i.e. thickness 5 – 50 mm) span the grey levels of interest and above this range the wedge is fully saturated. Therefore, it is these steps which provide the necessary curve fitting information. However, manual detection of all of the steps of both wedges was performed to ensure a complete data set for robust comparison between the two designs.

The values from each step were fitted with Equation (10.13). The coefficients and R^2 value for curve fitting operations were calculated. The R^2 value is the coefficient of determination and indicates how well a model fits the original data. Values range between 0 and 1, with 1 indicating a perfect fit. The 95% prediction bounds in the fitted curve were also calculated, indicating the uncertainty with which the model fits the data. The maximum interval between these for Aluminium thicknesses from 0 - 50 mm and 0 - 100 mm were used as an indication of the uncertainty in the curve fitting and are expressed as the 95% Prediction Interval (PI). The results for fitting calibration curves to the steps of each wedge are given in Table 10.3. An example of the calibration graph for the first ten steps of the 15-step wedge, showing 95% PI over 100mm, is shown in Figure 10.13.

Table 10.3: Results for curve fitting with the different wedges.

		Wedge		
		Ten step	**15 step**	**Ten steps of 15 step**
Co-efficients	**a [GL]**	-684	-693	-763
	b [mm^{-1}]	0.05	0.04	0.03
	c [GL]	895	937	1027
95% PI [GL]	**50 mm**	85	49	7
	100 mm	293	155	24
R^2		0.970	0.996	0.999

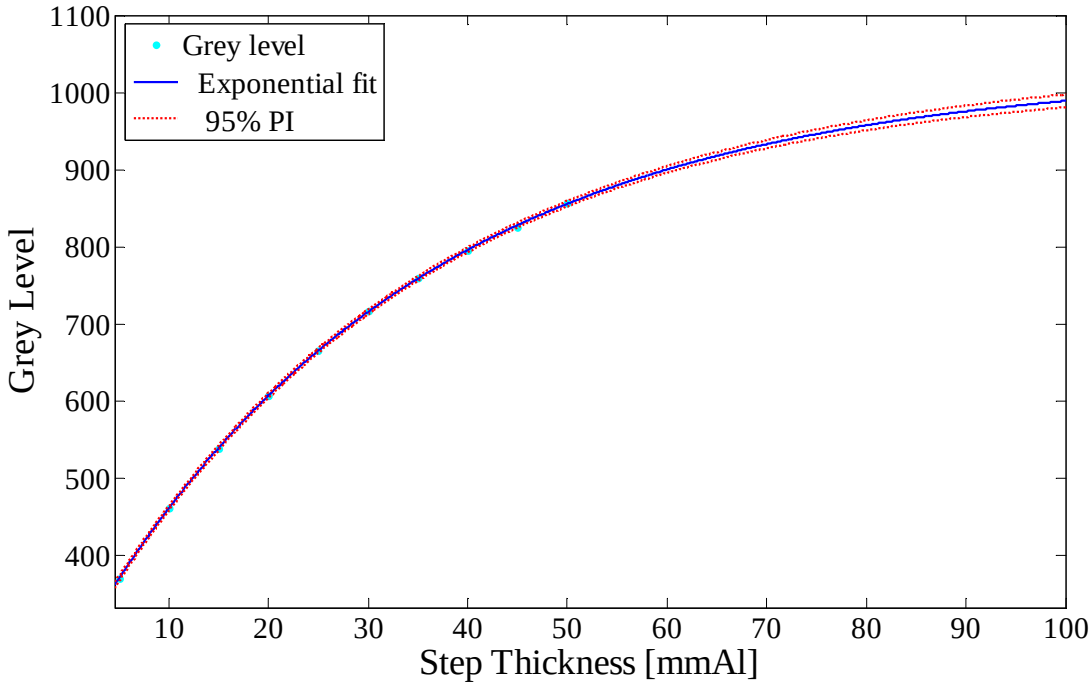

Figure 10.13: Exponential calibration graph for the first ten steps of the 15-step wedge. Also shown is the 95% PI.

As the table shows, curve fitting accuracy improved when using the 15-step wedge. This was particularly true using only the ten detectable steps of the 15-step wedge. Reduced scatter contributions became apparent, and a near perfect fit with an R^2 of 0.999 was achieved. The improved accuracy of fit was also indicated by the decreasing prediction intervals showing a maximum uncertainty of only 7 GLs for the first ten steps of the 15-step wedge over 50 mm Aluminium. It is also interesting to note that the y-axis intercept occurs at 1027. This is close to 1023, the highest possible grey level in the image, and is what was expected theoretically. Therefore, these tests show that using the first ten steps of the 15-step wedge provides the most reliable curve fitting calibration graph.

10.4.2 Changing the Steps

Having decided on the design of the wedge, it was necessary to justify the choice of the number and thickness of steps to show that this was adequate and that a smaller wedge with fewer or thicker steps would not provide a similarly accurate calibration.

Step Thickness

To model the effect of increasing the thickness of steps on the calibration process, existing steps of the wedge were analysed and others excluded to mimic thicker steps. An intrinsic limitation of this comparison is that the curve fitting process requires the number of data points to be greater than the number of coefficients (three) in order to perform a calculation of the 95% prediction bounds. Therefore, models of ten-, six-, five- and four-step wedges, ranging from 5 to 50 mm but with steps thicker than 5 mm, were chosen. Visual models of how these steps would look in the six- and four-step wedges are shown in Figure 10.14. The grey levels for each wedge were fitted with the exponential calibration curve. The results for the different wedges are given in Table 10.4.

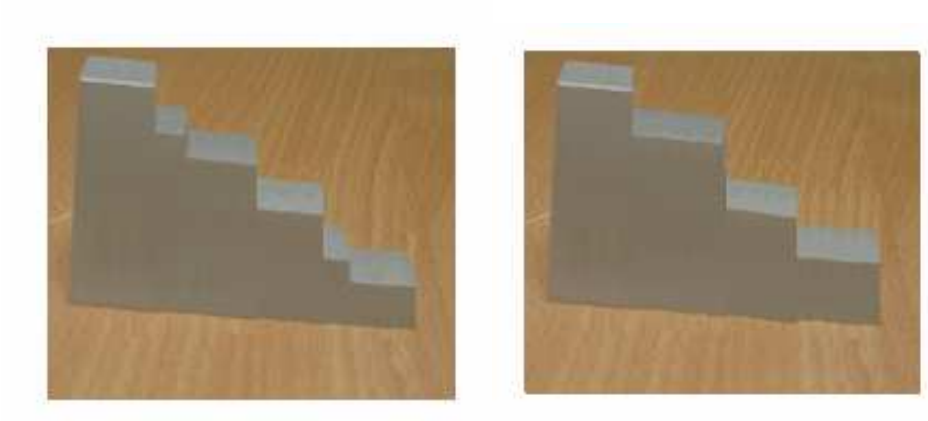

(a) (b)

Figure 10.14: Visual models of a) the six-step and b) the four-step wedge.

Table 10.4: Changes due to step thickness.

Wedge	**95% Prediction Interval [GL]**	
	50 mm	**100 mm**
Ten-step	7	24
Six-step	8	35
Five-step	14	64
Four-step	50	348

As the table shows, an increase in the uncertainty of the calibration occurred when fewer, thicker steps were used, even if the same total thickness of wedge was maintained. This is illustrated in Figure 10.15.

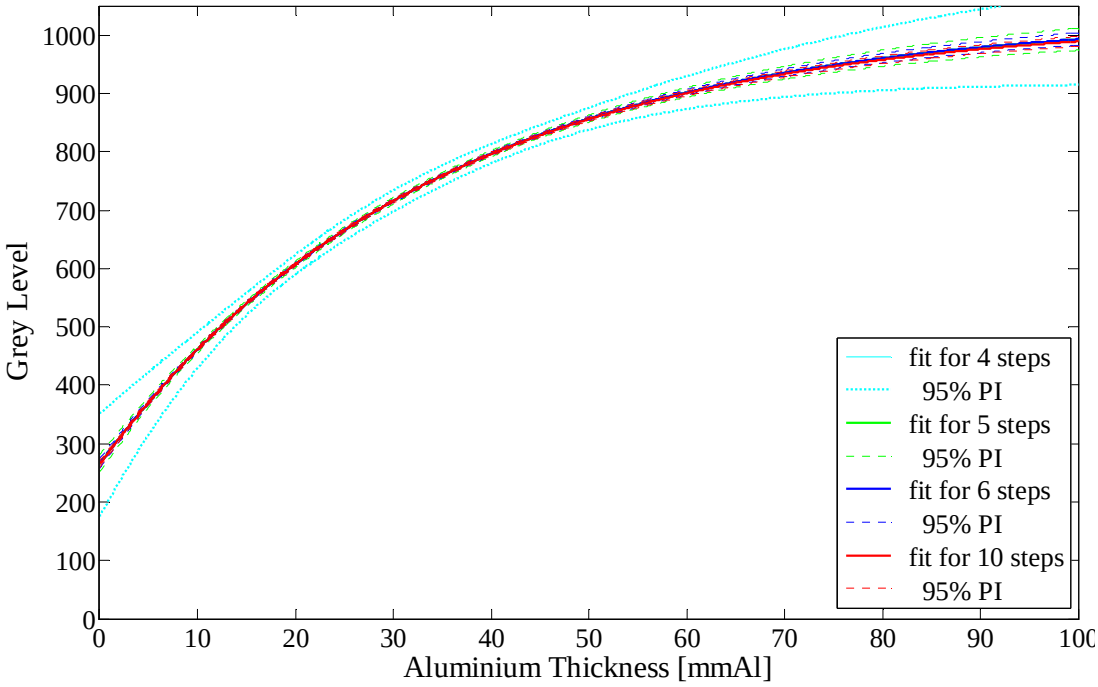

Figure 10.15: Changes in 95% prediction interval for wedges with thicker steps.

As this figure shows, the prediction interval increased when plotting calibration graphs for wedges with steps thicker than 5 mm. Furthermore, the thicker the steps, the bigger the PI, showing that the calibration graphs resulting from the six-, five- and four-step wedges could not be as confidently used to find equivalent thickness levels as the ten-step wedge. This justifies the choice of 5 mm thick steps as being a good thickness to provide a calibration model.

Number of Steps

The next aspect of the wedge design was to verify whether a sufficient number of steps had been used. It has already been shown that using a bigger wedge reduced the effects of scatter. However, it has not been clearly shown how many steps of this wedge are necessary to provide an accurate calibration. Models of wedges with decreasing numbers of 5 mm thick steps (i.e. lower overall wedge thicknesses) were made using the existing grey level measurements. With ten steps as the top of the range, wedges modelling eight, six, five, and four 5 mm steps were tested and fitted using the exponential method. The results of curve fitting and the maximum 95% PI are given in Table 10.5.

Table 10.5: Changes in 95% prediction interval if fewer steps are used.

Wedge	**95% Prediction Interval [GL]**	
	50 mm	**100 mm**
Ten-step	7	24
Eight-step	10	32
Six-step	23	65
Five-step	70	185
Four-step	520	1243

The table shows that a large increase in the uncertainty of the calibration graph occurred if fewer than ten steps were used, even though these steps were no thicker than the original steps (i.e. 5 mm thick). This is illustrated when fitting the calibration data, as shown in Figure 10.16. The graph shows that decreasing the number of steps increased uncertainty in the calibration, especially at greater thicknesses of Aluminium. This justified the choice of ten steps as a suitable number to use to achieve a reliable calibration.

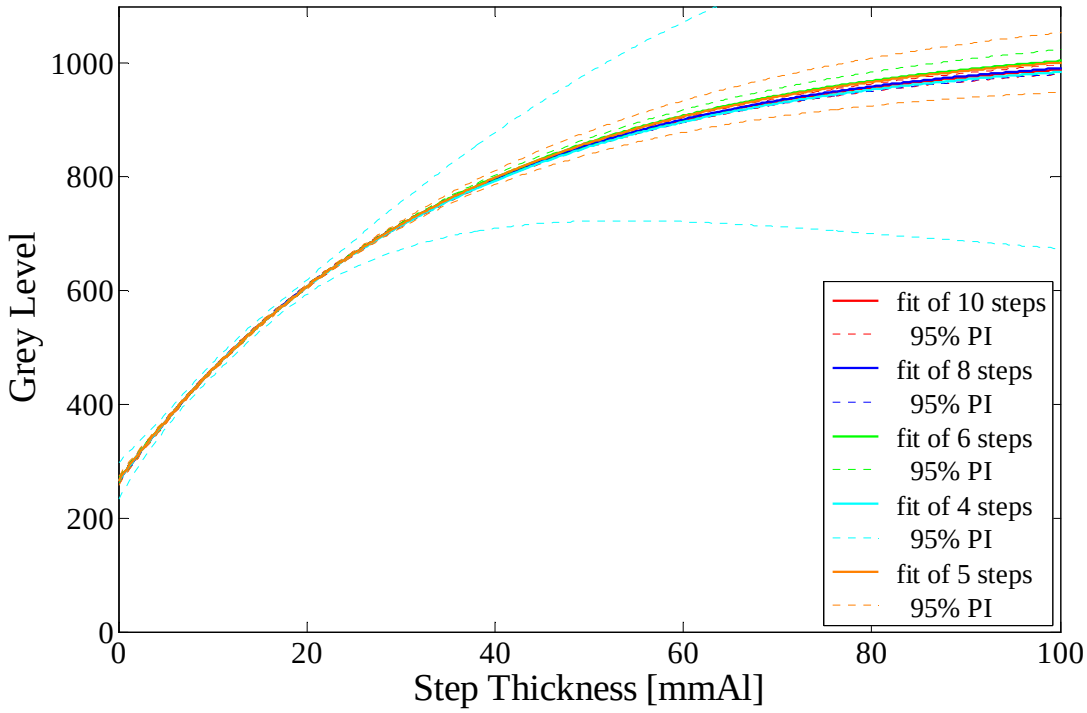

Figure 10.16: Changes in 95% PI when reducing step number from ten to four.

10.4.3 Precision

To determine how confidently the conversion of grey level to millimetres of Aluminium could be obtained it was necessary to calculate the precision of the wedge calibration graph. Since the calibration graph was fitted extremely well (R^2 =0.999), the fitting process could be neglected as a sizeable source of error. Errors contributing to uncertainty in the calculation of equivalent Aluminium thickness were due to the manufacture of the wedge and the calculation of the grey level of each step. Steps in the wedge were manufactured to a precision of ±0.1 mm. The precision of determining the grey level of each step is a function of the SD incurred when averaging the grey levels of pixels. These two values allowed calculation of the maximum possible error for each step as illustrated in Figure 10.17.

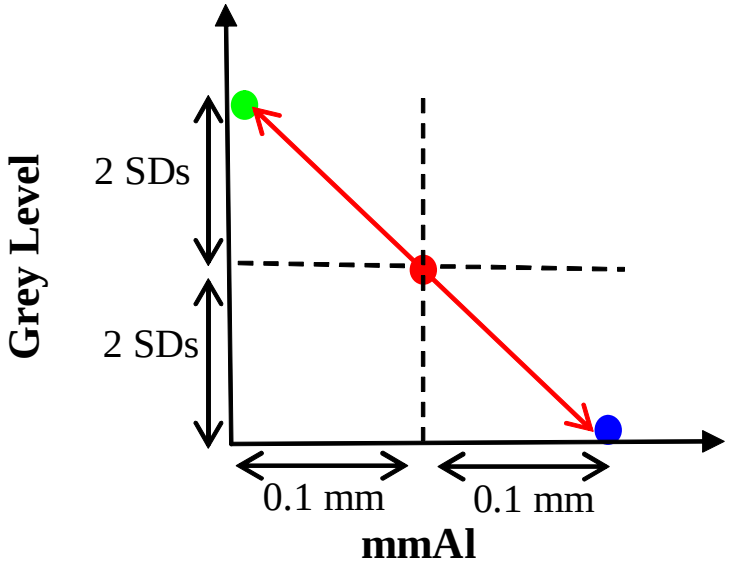

Figure 10.17: Calculated Aluminium-equivalent thickness value (red), possible underestimation (blue), possible overestimation (green) and resulting uncertainty in measurement (red arrow).

The figure shows how the values could be used to determine two separate calibration graphs that could be correct if the SD or precision in manufacture resulted in an over- or underestimation of the grey level or step thickness. These two graphs calculated for the first ten steps of the 15-step wedge are shown below in Figure 10.18 and are effectively the 95% Confidence Intervals (CI).

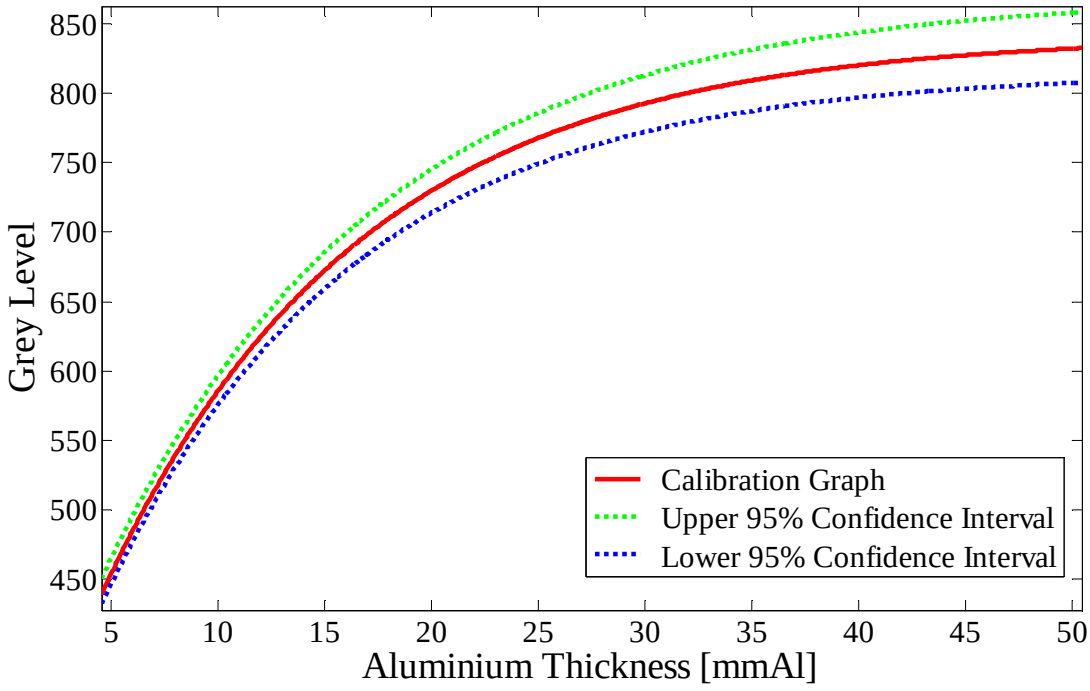

Figure 10.18: Calculated calibration graph and 95% Confidence Intervals.

The graph shows that the uncertainties are small for low grey levels, due to the low SDs in the grey levels. As the higher steps become increasingly saturated, the SD increases and the uncertainty in the calibration increases correspondingly.

From a study of clinical X-rays it was determined that the typical grey level range of interest lies between 300 and 700 for patient images. Table 10.6 shows the uncertainty in calculating equivalent Aluminium thickness for these levels. The maximum uncertainty in the clinical range of grey levels is 1.3 mm occurring at a grey level of 700, i.e. measurements of equivalent Aluminium thickness in clinical X-rays could be quoted as ±1.3 mmAl.

Table 10.6: Grey levels and the associated uncertainties in equivalent Aluminium thickness.

Grey level	**Uncertainty [mmAl]**
300	0.2
400	0.2
500	0.3
600	0.5
700	1.3

10.4.4 Discussion

It is important to examine the factors that contribute to a reliable calibration between grey level and Aluminium thickness as this is fundamental to the use of an Aluminium step wedge as a calibration tool. However, previous literature describing these types of investigations has been lacking. A comparison between the ten- and 15-step wedges showed that using ten 5 mm steps (i.e. a total thickness of 50 mm) covered the range of grey levels of clinical interest and that steps above this level became saturated with X-rays, offering no new information for a calibration graph. Whilst the larger width of the 15-step wedge resulted in larger SDs in grey level calculation, it was possible that the provision of a larger set of pixels from which to calculate mean grey level could have reduced potential localised inaccuracies that might occur in smaller steps. It could also be seen that the larger wedge design provided some reduction in the inaccuracies due to scatter. This was especially the case when the first ten steps of the 15-step wedge were used for calibration calculations, as the upper end of the wedge shields the lower steps of interest from scatter effects. Previous investigations into these effects on ideal step wedge design have not been found in the literature.

Also important in using a step wedge is whether size is influential on calibration. To optimise computing time and radiographic simplicity, it is important to verify that a simpler wedge design would not be more appropriate. De Josselin and ten Bosch recommended the use of a total step thickness exceeding the highest thickness expected in samples [105]. However, both Gu *et al.* and Nackaerts *et al.* reported negligible loss in calibration accuracy for decreasing step number and attributed this to the highly linear calibration relationship used [91, 110]. In this study, tests comparing the accuracy of exponential calibration for wedges modelling decreasing numbers of steps (i.e. lower total wedge thickness) were performed and provided an illustration of the loss of precision in fitting the exponential model when using too few steps. The difference between these results and those reported by Gu *et al.* and Nackaerts *et al.* could be due to two factors. Firstly, the added step in forming their linear models may obscure some of the effects of reducing wedge thickness. Furthermore, their evaluations were only performed over a small range of possible thicknesses whereas this study has looked at the effect on precision up to 100 mmAl. A further investigation into wedge design which has not previously been reported in the literature illustrated that increasing the thickness of steps reduced the precision with which the exponential model could be fitted, even if the same total wedge thickness was maintained. It could be seen from these tests that ten 5 mm steps were an appropriate design to provide an accurate calibration.

Finally, the precision of the calibration process based on the manufacturing precision and grey level averaging errors was calculated. Knowledge of this is important so that the confidence in Aluminium-equivalent thickness can be quoted. Results indicated that for the clinical range of grey levels, the calibration values can be quoted to ± 1.3 mmAl. Similar precision measurements were not previously reported in the literature, so no comparisons could be made. Similarly, little data was found giving an indication of the expected Aluminium-equivalent thickness of areas of interest in patients, or to what degree this changed over the course of fracture healing. Nackaerts *et al.* reported that the Aluminium thickness of dried adult mandible sections varied from 2 mmAl to 5 mmAl, which corresponded to 0.55 g/cm^2 to 0.8 g/cm^2 as measured by DEXA [110]. Kolbeck *et al.* showed that the equivalent Aluminium thickness in distraction osteogenesis in a micropig animal model varied from 6 mmAl to 7.5 mmAl over ten days of fracture consolidation [28]. However, it was not reported how this related to stage of healing or expected values in human fractures. It is therefore difficult to say with patient based fracture investigation whether an accuracy of $\pm$ 1.3 mmAl is sufficient to detect the necessary bone changes in humans.

10.5 AUTOMATIC PROCESSING

The first problem in dealing with digital X-rays as opposed to conventional film X-rays was the use of grey levels instead of optical density. This has been addressed in Section 10.3. The second problem was accounting for the automatic post-processing applied by the Fuji X-ray system used in this study. One of the major advantages of digital X-ray is the opportunity to apply post-processing to the raw images. This adjusts the window level and size so that contrast and brightness are enhanced in order to make the image more clinically useful. Most of this processing is applied automatically depending on the setting chosen and the objects in the image, but some can also be applied interactively by the user. The automatic processing applied by the Fuji system is called Histogram Analysis. With this analysis, the characteristics of the X-ray are calculated by the Exposure Data Recogniser (EDR) and are used to determine the Latitude (L) and Sensitivity (S) values [134]. The L value is the range of dose values assigned to the 0 to 1023 grey levels of the display image and the S value is inversely related to the mean of this range.

Although this processing is beneficial when viewing clinical images, it can distort the relationship between grey value and dose depending on what is X-rayed. This is detrimental to any method such as step wedge calibration which aims to consistently relate grey level to step thickness. Thus, it was important to determine what automatic processing the Fuji system applied to an X-ray image and whether this could be corrected for or removed.

10.5.1 Sensitivity and Linearity

In order to test whether placing different objects in the image would alter the dose to grey level relationship, different thicknesses of copper were used, as shown in Figure 10.19. The X-ray cassette was placed under a Perspex table on which four copper plates of different thicknesses were arranged. An X-ray was taken at 80 kV and 2 mAs, recording the grey level that represented each copper thickness in the image. For a given setting in computed radiography, if the processing is not dependent on the objects in the image, then the relationship between the grey level and copper thickness should be the same no matter what combination of thicknesses is imaged. To test this, an experiment was performed for two arrangements of copper thicknesses. The first had a small range of thicknesses (i.e. 0.05 mm - 0.3 mm) and the second had a wider range (i.e. 0.1 mm - 1.5 mm).

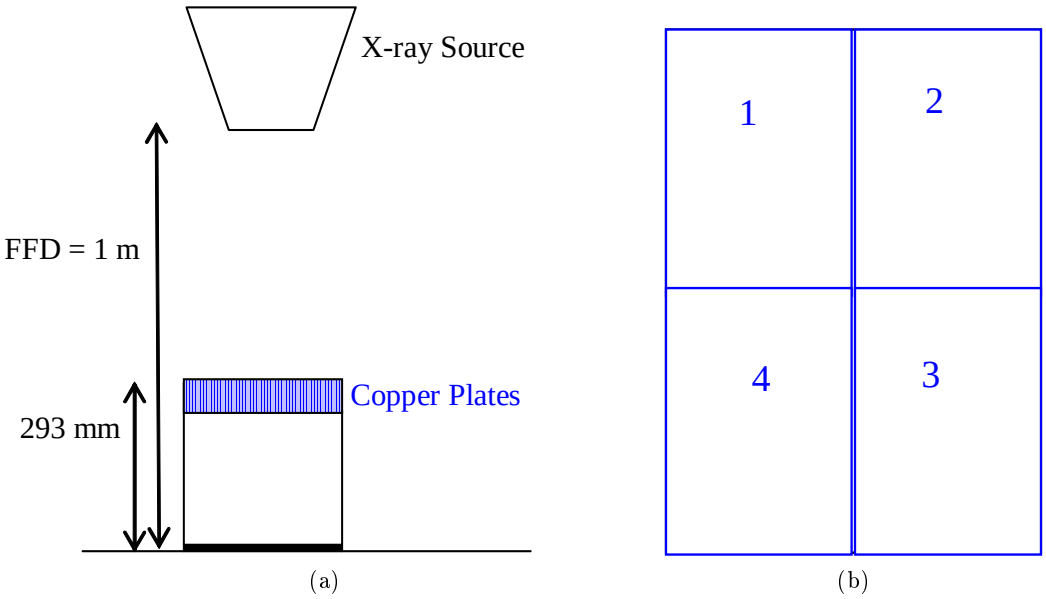

Figure 10.19: a) The X-ray set up of the automatic processing experiment and b) the arrangement of copper sheeting above the X-ray plate.

The first setting that the images were processed on was 'Sensitivity', which is the setting used for Quality Assurance purposes in the RIE. In this setting the L value is fixed at 1 and only the S value is adjusted. The resulting grey levels from the images are shown in Table 10.7.

Table 10.7: Grey levels for images with two different copper thickness ranges on the 'Sensitivity' setting.

	Copper Thickness [mm]	Grey Level	SD
Test 1	0.05	297	4.6
	0.10	462	5.5
	0.30	756	5.9
	0.53	857	5.1
Test 2	0.10	0	0.0
	0.30	432	4.2
	1.00	983	6.4
	1.50	1019	0.0

The results show that for the thicknesses of copper which were the same in each image, i.e. 0.1 mm and 0.3 mm, the system produced a different grey level depending on the other copper thicknesses in the image. This showed that the 'Sensitivity' setting applied histogram analysis and was not processing free.

In order for the calibration curve of the step wedge to be unaffected by automatic processing, it was necessary to find a processing free setting on the Fuji system. After some experimentation, the 'Linearity' setting was selected. This takes images with a constant L value of 3.0 and S of 200. The same two experiments with different copper thicknesses were processed using 'Linearity' and the results are shown in Table 10.8.

Table 10.8: Grey levels for images with two different copper thickness ranges on the 'Linearity' setting.

	Copper Thickness [mm]	Grey Level	SD
Test 1	0.05	123	1.7
	0.10	156	2.1
	0.30	252	1.9
	0.53	306	1.5
Test 2	0.10	159	2.3
	0.30	253	1.5
	1.00	435	1.7
	1.50	629	4.9

The results show that in the case of the 'Linearity' setting, very similar grey levels were obtained for the same thicknesses of copper and were not influenced by other objects in the image. This lack of automatic post-processing made the 'Linearity' setting ideal for use in step wedge calibration experiments.

Experiments were also performed to check whether images taken on clinical settings (i.e. settings which perform processing to enhance the clinical appearance of the image) could be changed to the 'Linearity' setting at a later stage without any effect on the raw image data. Exposures of several thicknesses of copper were taken on the 'Linearity' setting. The same exposures were then repeated on the 'Sensitivity' setting and only changed to 'Linearity' after imaging. The grey levels of the two sets of images were compared, as shown in Figure 10.20.

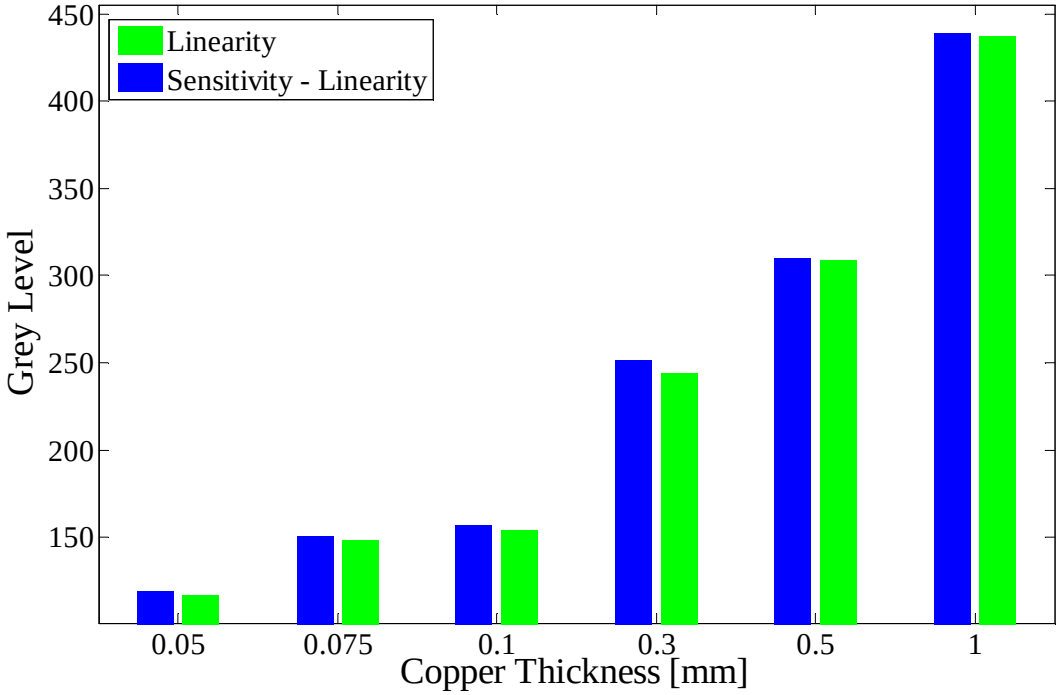

Figure 10.20: Graph comparing grey levels obtained using the 'Linearity' setting versus the grey levels obtained when the setting was changed from 'Sensitivity' to 'Linearity' post-exposure.

As the figure shows, the grey levels were almost identical in both images. This means that even if an image was originally taken with a clinical setting to aid diagnosis, it could later be changed to the 'Linearity' setting for analysis with no loss of information and without a further exposure.

10.5.2 Dose to Grey Level

To check various aspects of the image settings (such as the heel effect and scatter contributions) it was necessary to know what relationship between the grey level and the incident dose on the X-ray plate for the 'Linearity' setting was. This was checked by taking exposures of a number of different thicknesses of copper, as in the previous set up. However, in this situation, a measure of the dose in micro-Grays (μGy) was also taken using a dosimeter underneath the copper. The result were fitted with an exponential curve and are shown in Figure 10.21.

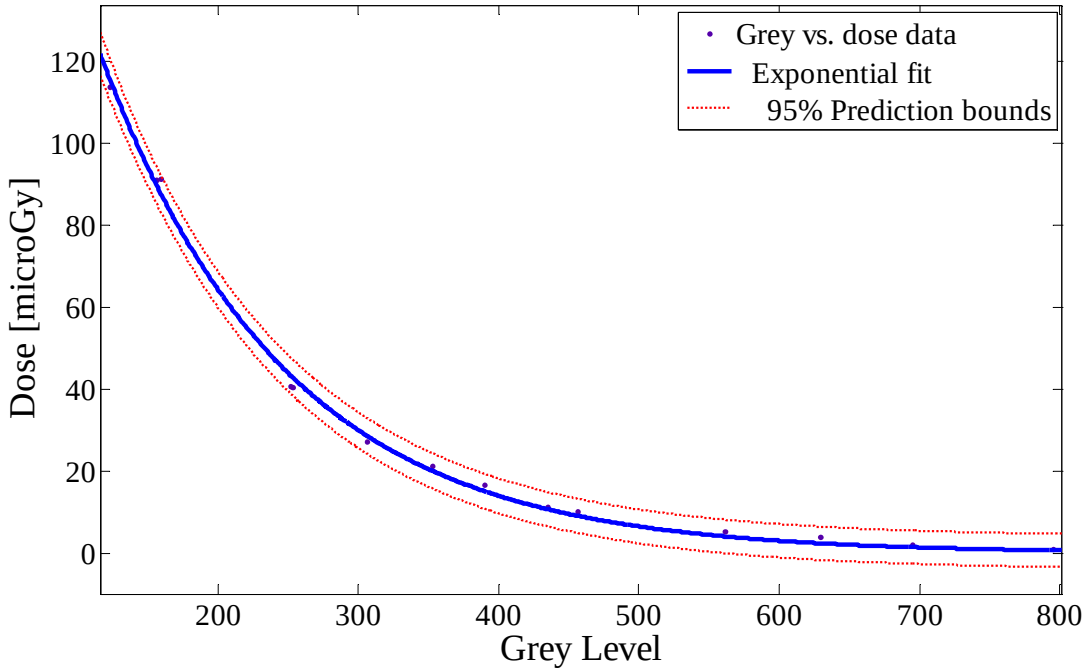

Figure 10.21: Graph showing the relationship between grey level and dose fitted with an exponential curve with 95% prediction bounds.

The figure illustrates the exponential relationship between dose and grey level (i.e. $y = ae^{bx}$ where a=295, b=-0.0076; $R^2 = 0.99$). This was simplified to a straight line relationship between ln(dose) and grey level, as shown in Figure 10.22.

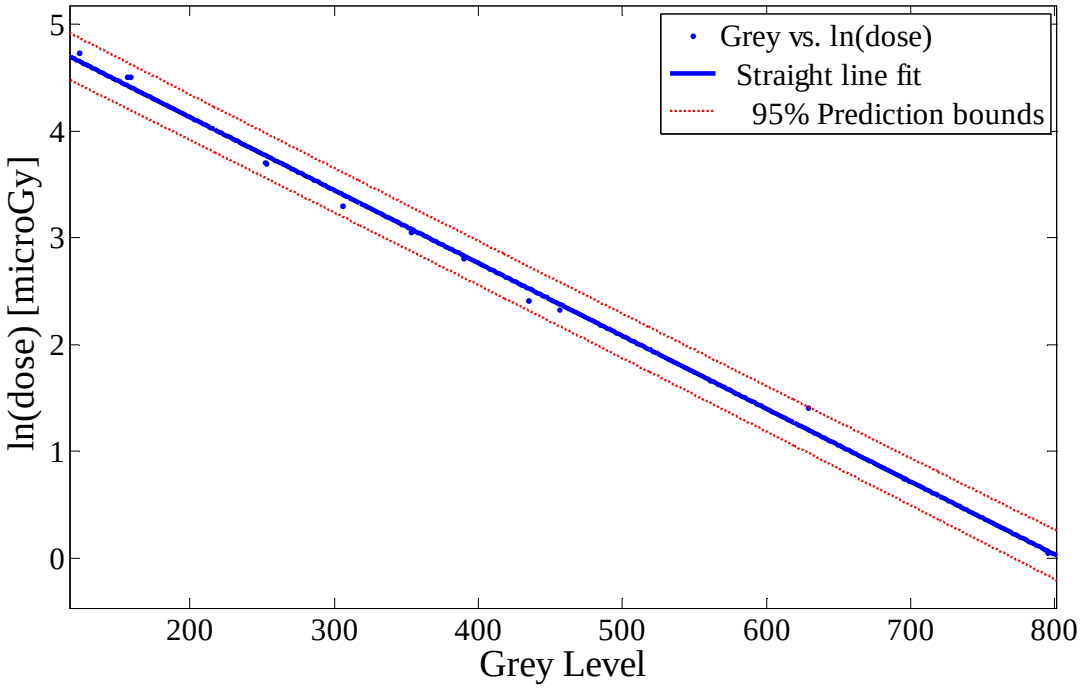

Figure 10.22: Graph showing the relationship between ln(dose) and grey level fitted with a straight line with 95% prediction bounds.

As the graph shows, this relationship was linear (i.e. $y = mx + c$, m=-0.0068, c=5.49, R^2 = 0.99) which could be used to simply and easily convert between grey level and dose with a maximum error of ± 1.11 μGy.

10.5.3 Discussion

An investigation into the processing applied by the Fuji CR system was undertaken. One previous report in the literature investigating the differences between digital and film X-ray systems has mentioned the effect of automatic post-processing and showed that this must be eliminated when performing step wedge calibration as the processing is essentially arbitrary and does not allow for a reliable calibration relationship to be formed [87]. In the current study, the nature of this type of processing has been investigated and a method to obtain processing free images for calibration without the need for extra exposures or the loss of clinically useful images was developed. Furthermore, the dose to grey level relationship using the processing free 'Linearity' setting of the Fuji CR system has been investigated. Previous reports of this have not been found in the literature. A reliable linear relationship between grey level and ln(dose) has been found.

10.6 HEEL EFFECT CORRECTION

As discussed in Section 4.6, one factor that can affect image quality in digital X-ray images is the anode heel effect. This causes the X-ray intensity on the anode side of the field to be less than that on the cathode side. This difference is sometimes visible in an empty field X-ray image as shown in Figure 10.23.

Figure 10.23: X-ray image illustrating the heel effect.

As can be seen in the image, the background varies from light on the left (anode side) to dark on the right (cathode side). When using a step wedge to relate grey levels to Aluminium-equivalent thicknesses throughout an image, a difference in intensity in different parts of the image will cause errors in the calibration. Therefore, it was important to account for this variation using data available in routine clinical X-rays. This section discusses how the heel effect was analysed and the correction techniques that were utilised.

10.6.1 Dose Modelling

In order to get a full picture of the magnitude of heel effect, a 2D measure of the dose in an empty field X-ray image was taken. This was performed by positioning the tube at a height of 430 mm above the floor and opening both collimators fully, to a field size of 400 mm x 400 mm. An exposure was taken at 63 kV and 1.8 mAs (the routine clinical values used when imaging a tibia) with a dosimeter in the ROI measuring the corresponding dose value in μGy. This was repeated 49 times, with the dosimeter moved throughout the exposure region of the tube. The dose values were tabulated and used to create a 3D plot of the heel effect, as shown in Figure 10.24.

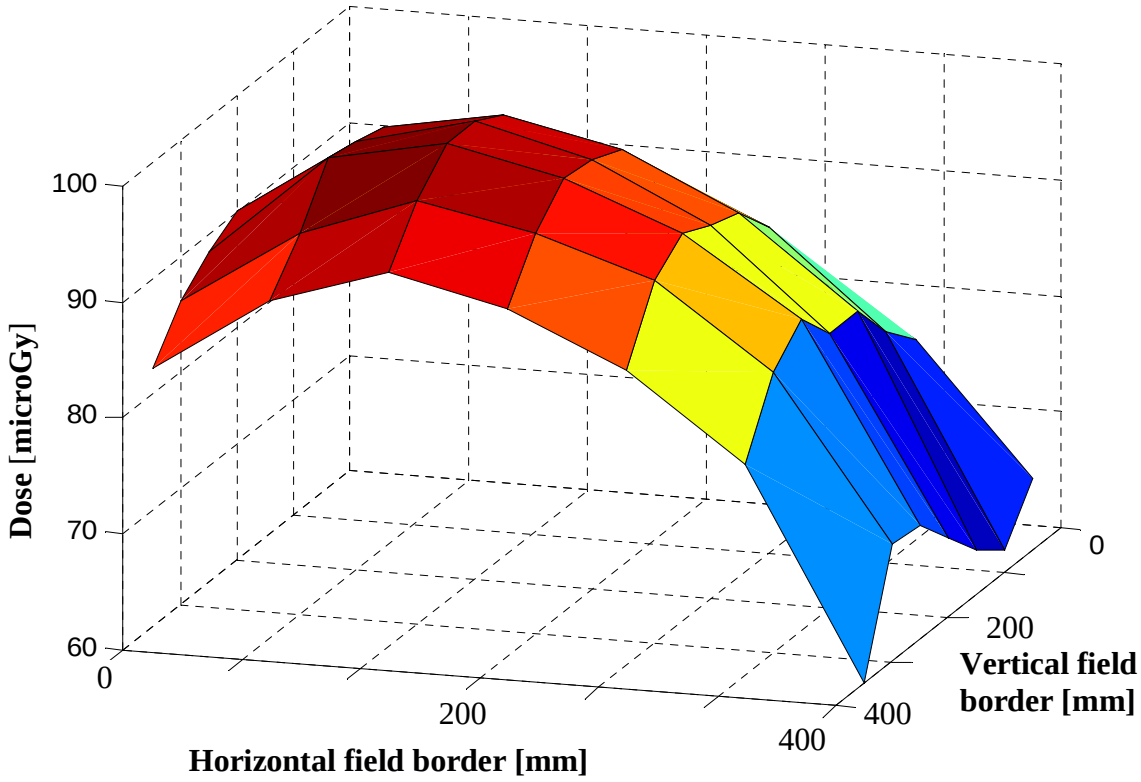

Figure 10.24: 3D representation of the heel effect measured in dose [μGy].

The figure shows how the exposure, and hence dose, varies according to where in the image an object is placed. It also shows how the effect is greater in the horizontal (anode-cathode) direction than in the opposite direction due to the physics of the heel effect. Some of the anode-cathode variation, and most of the variation perpendicular to this, is due to the effects of scatter and the path length of the beam in various parts of the field. These result

in a greater intensity in the centre of the field than on its borders (see Section 4.2.3). These further sources of inhomogeneity were grouped with the heel effect in this study and the dose model illustrated the need to correct for these.

10.6.2 Grey Level Modelling

Since the images produced by the CR are digital images, the effect could be modelled and this was achieved using empty field X-rays. These were taken at the same clinical settings as before (63 kV and 1.8 mAs) with a 1 m distance between the tube and the X-ray table. The resulting images were imported into Matlab and analysed by tracing through and recording the grey level value for each pixel in the image. This resulted in an image inverse to that obtained using dose.

The rows of the image were averaged to give a horizontal 1D profile, i.e. a profile in the anode-cathode direction. A similar procedure was repeated for the columns to give a vertical 1D profile, i.e. a profile perpendicular to the anode-cathode direction. These images are shown in Figure 10.25. Since the magnitude of the intensity profile in the vertical direction was small, it was assumed that this would have a negligible influence on the grey levels of the image.

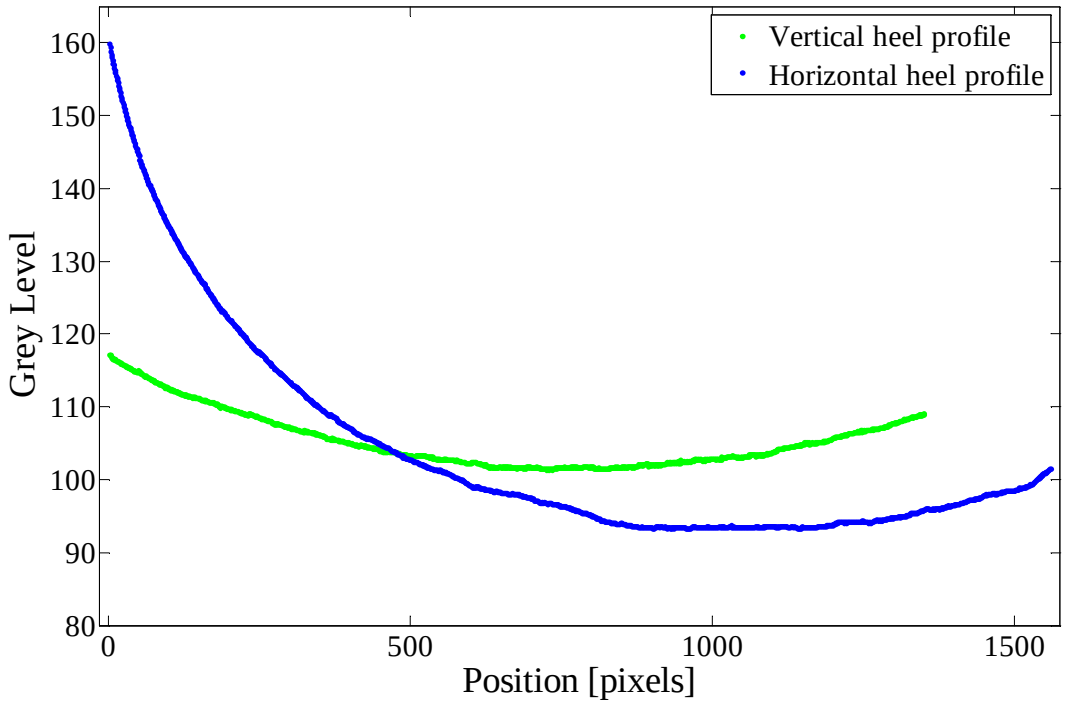

Figure 10.25: Horizontal (anode-cathode direction) and vertical profiles of the heel effect in an empty field X-ray.

This analysis of the heel effect was performed on the unattenuated X-ray beam. However, in clinical X-rays, the beam passes through objects such as a patient's body. This causes beam hardening which can reduce the magnitude of the heel effect so that the imbalance of X-rays is evened out. In order to get an indication of this, the heel effect was measured by filtration with a 2 mm thick piece of copper. The result is shown in Figure 10.26. As the image shows, the magnitude of the heel effect was approximately halved (57% of the non copper-filtered heel effect). This illustrated how the magnitude of the heel effect is reduced as a result of object attenuation.

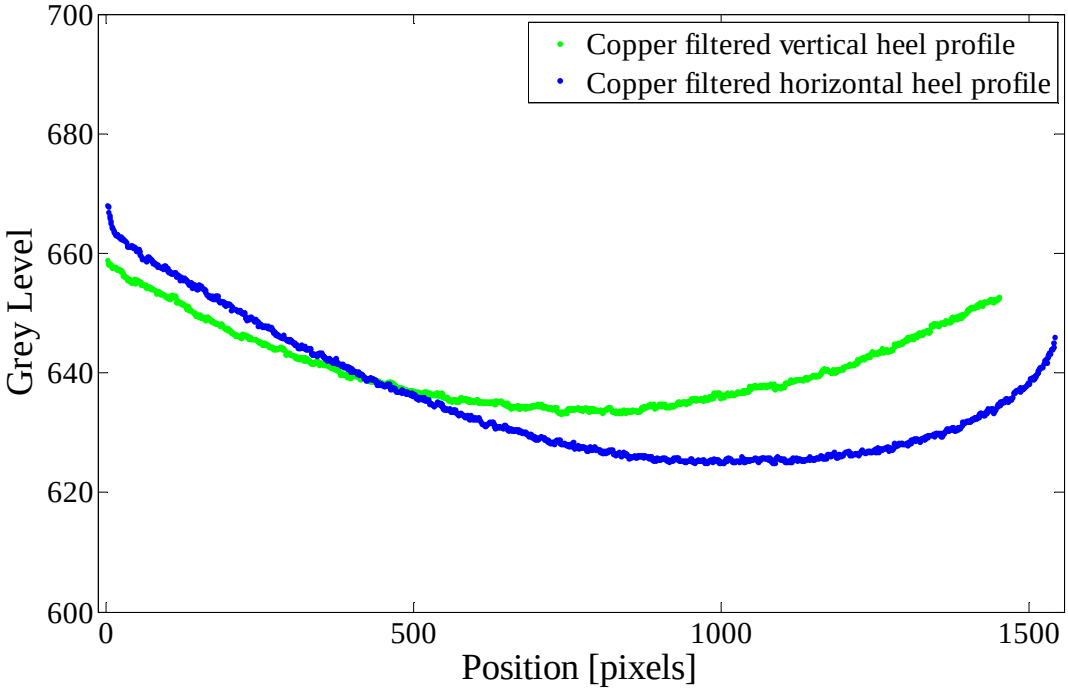

Figure 10.26: Horizontal (anode-cathode direction) and vertical profiles of a copper filtered heel effect.

In order to correct for the heel effect, a model of the background variation it produced had to be estimated. The first attempt at this was a Gaussian distribution as used by do Nascimento *et al.* [115]

$$ae^{-(((x-b)/c)^2)} + d \tag{10.14}$$

with $-\infty < a < 1000$, $1000 < b < 2000$, $500 < c < 9000$ and $0 < d < 2000$. Although a reasonable coefficient of determination ($R^2 = 0.95$) was obtained, the Gaussian was not a good model of the data, as shown in Figure 10.27. A reasonable fit was obtained in the central portion of the profile but became inaccurate towards the outer edges.

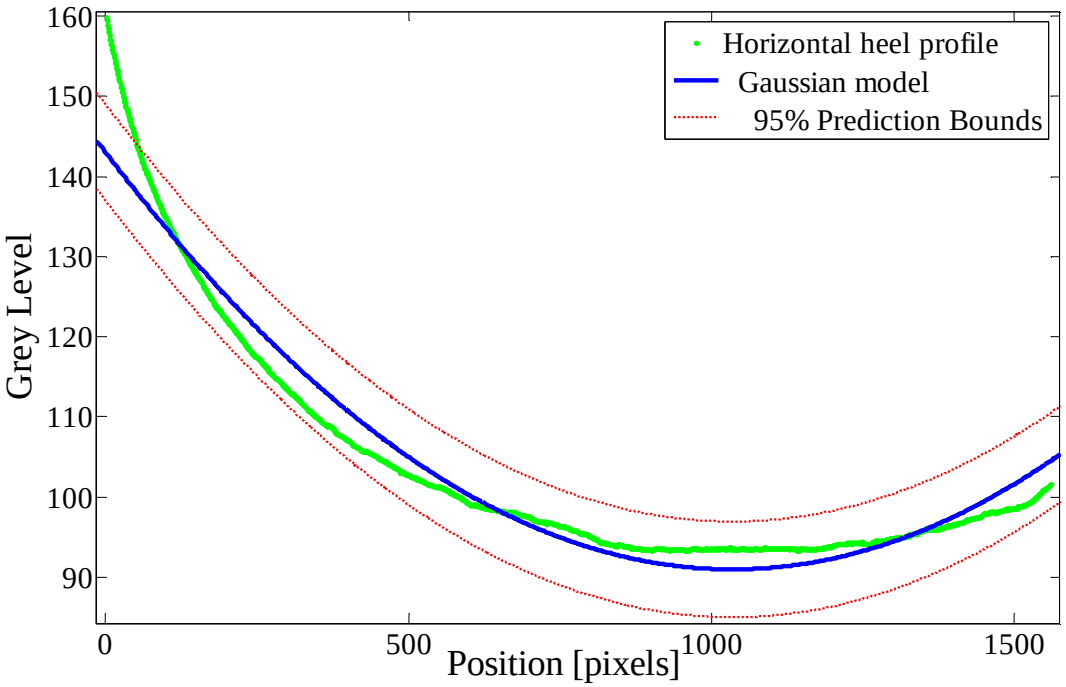

Figure 10.27: Gaussian model of an empty field profile showing 95% prediction bounds.

The next approach was to consider the Lambert-Beer Law ($I = I_0 e^{-\mu x}$) and the fact that the anode heel effect is caused by attenuation of the beam through the anode material. The background was therefore modelled using an exponential curve of the form

$$ae^{-bx} + c \tag{10.15}$$

where $a > 0$, $b > 0$ and $c > 0$. Again, a reasonable R^2 value of 0.98 was obtained, as shown in Figure 10.28. An exponential fit was a slight improvement on a Gaussian fit but still did not model the data ideally on the edges of the profile.

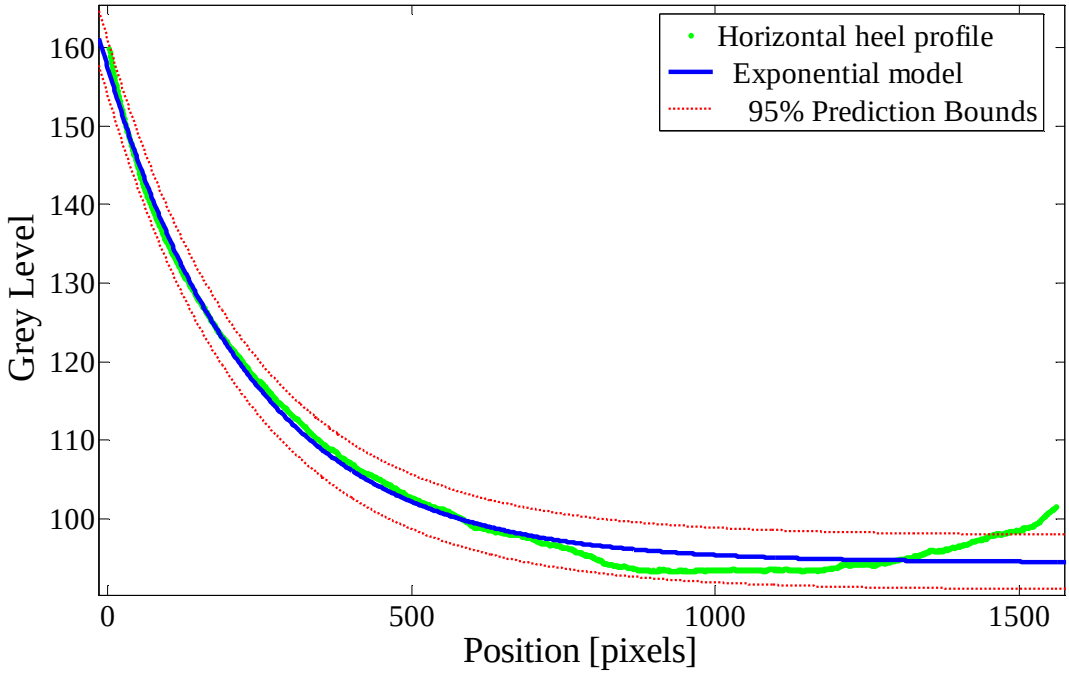

Figure 10.28: Graph showing an exponential model of the background profile with 95% prediction bounds.

The theoretical explanation of the heel effect only predicts a single exponential if the X-ray beam is monoenergetic. However, the X-ray beam is polyenergetic and the heel effect is therefore best modelled by a collection of exponential models, each modelling μ for a different energy. A simplification of this was used to fit the background profile with a double exponential of the form

$$ae^{bx} + ce^{dx} \tag{10.16}$$

where $a > 0$, $-1 < b < 0$, $c > 0$ and $0 < d < 1$. Fitting using this model provided an improved R^2 value of 0.99 and the resulting fit is shown in Figure 10.29. This gave a very good model of the heel effect in an empty field image.

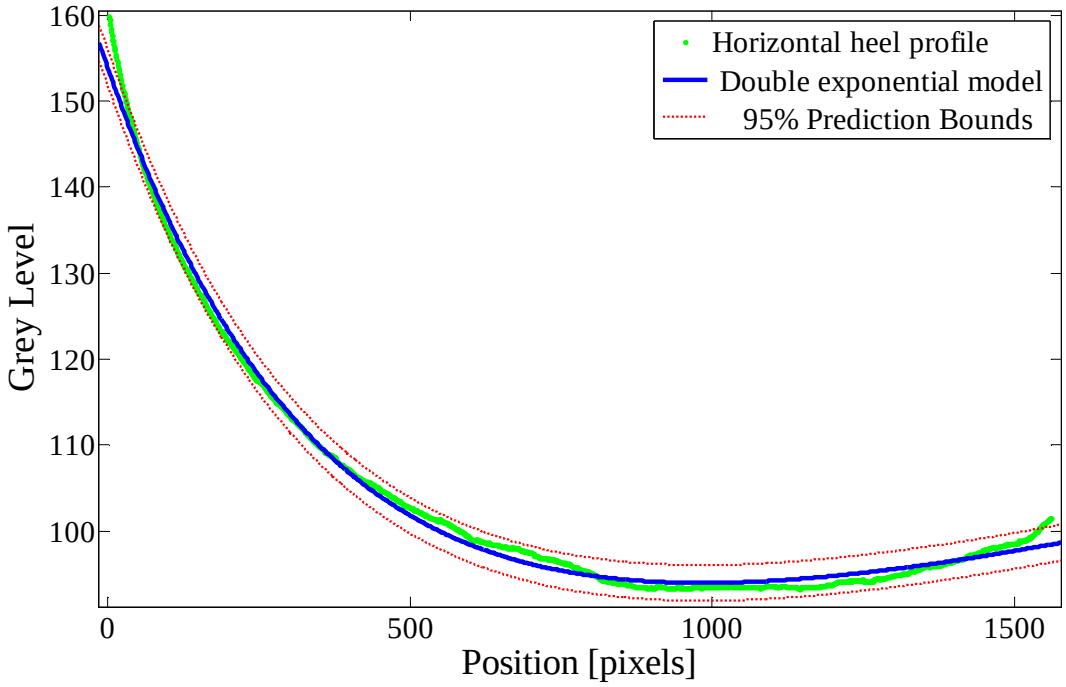

Figure 10.29: Graph showing a double exponential model of the background profile of an empty image with 95% prediction bounds.

10.6.3 Heel Effect Correction

Having developed an accurate model of the heel effect it was used to eliminate grey level variations in the image. This was tested by using an empty field image to 'flatten' the heel profile. For each pixel in a column, the magnitude of the fitted model in that column was subtracted from the original grey level value, essentially subtracting the heel effect. The resulting corrected image is shown in Figure 10.30. As can be seen, the profile of the corrected image was flat, showing only minimal changes in intensity throughout the image. Furthermore, this correction reduced the background of the image to zero, which agreed with what it should be theoretically if fully exposed.

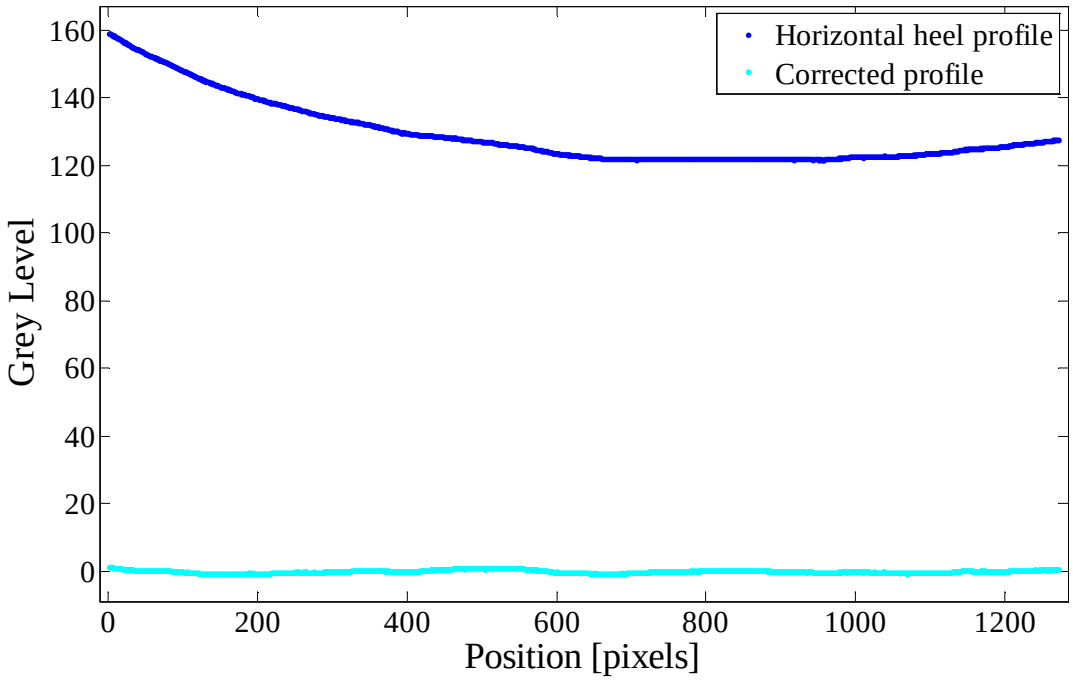

Figure 10.30: The uncorrected profile of the heel effect (blue) and the flattened profile after correction (cyan).

One approach to correcting for the heel effect would be to take an empty field correction X-ray at regular intervals. The exponential model of the heel effect image would be used to correct for all subsequent images taken using that equipment and would reduce differences due to the position of an object in the field of view. In order to investigate the extent that the heel effect varied over time, a set of empty field X-rays was taken at weekly intervals using the same X-ray apparatus. These are shown in Figure 10.31.

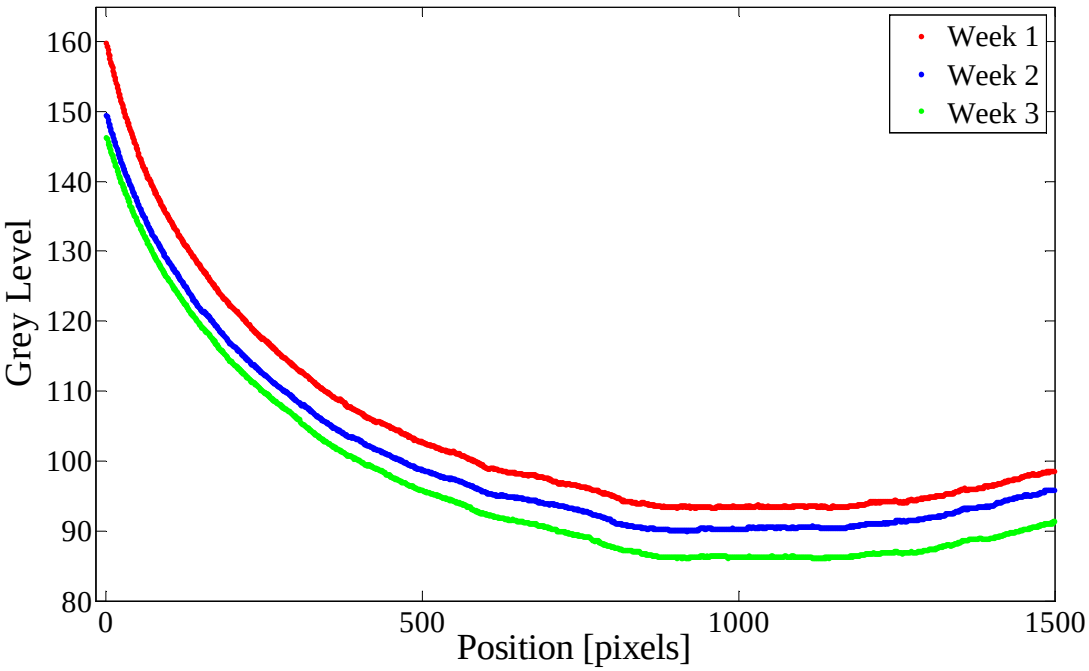

Figure 10.31: Weekly variation in heel effect magnitude.

As the figure shows, there was a slight variation between the profiles for different weeks. The maximum variation equated to 20% of the total magnitude of the heel effect. This is a fairly sizeable change and suggested that weekly, or more frequent, correction X-rays would be necessary if this approach was to be used to account for the heel effect in routine images.

Although it might be feasible in some situations to take regular correction X-rays at certain settings, it is not always possible to do this. This is especially true for X-rays taken at different locations that need to be consistently analysed. Ideally, a simple way for correcting for the heel effect using just the image itself would be useful. Since the margins of some X-ray images are fully exposed, it was decided to attempt correction for the heel effect using these. In the image of interest, the biggest fully exposed margin at the top or bottom of the image was cropped. This was then used to form a 1D heel effect profile which was modelled with a double exponential curve as previously discussed and used to correct the entire image. The same correction could be performed in the vertical direction.

In order to test the accuracy of this approach, an empty field X-ray was analysed with only the top portion (approximately 200 pixels x 1200 pixels) used to form the heel effect exponential model. This was then used to 'flatten' the entire image which is shown in Figure 10.32. As can be seen, the resulting 'flat' profile was very similar to that obtained when performing the full 1D heel effect correction. This demonstrated that this method could effectively and simply correct for the heel effect in most images taken using a range of exposure settings and in various situations. This eliminated the need for regular correction X-rays.

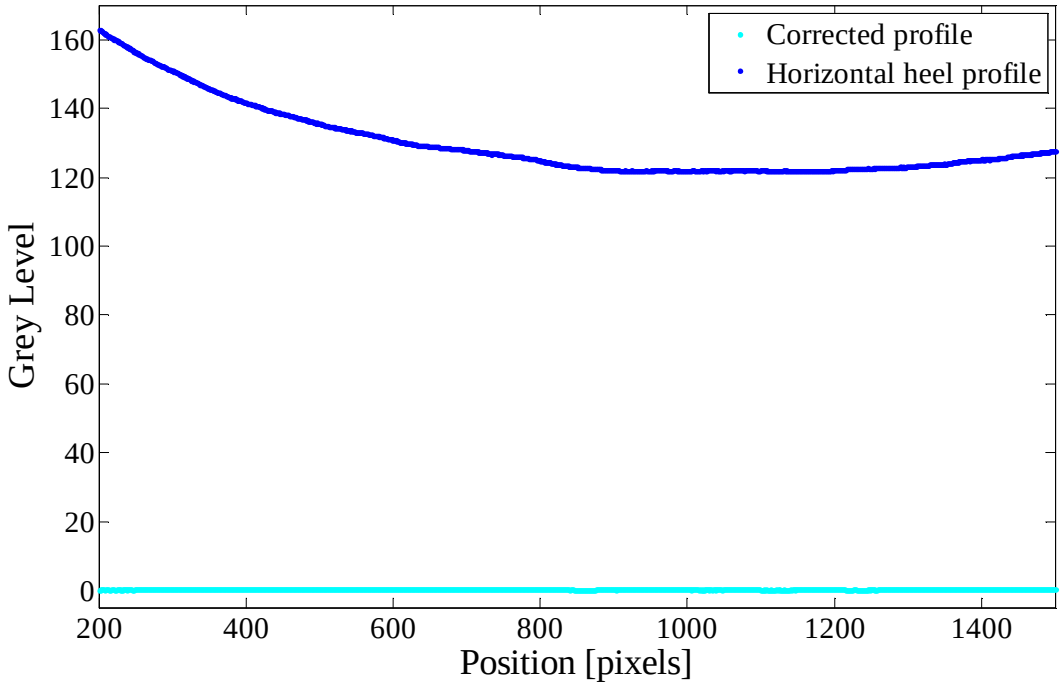

Figure 10.32: The uncorrected image profile and corrected profile using a margin of the image.

Although a simple technique had been developed to correct for the heel effect, it is important to note that the maximum variation due to the effect is approximately 7% of the total image range of 0 - 1023. When attenuated by an object, this reduces to just 4%. This suggested that for less precise measurements, heel correction may not be necessary. However, for equipment which introduces greater variations, or measurements requiring a high degree of precision, correction for the heel effect could be made.

10.6.4 Placement of the Wedge

Another way of reducing the impact of the heel effect is to ensure that the step wedge is always placed as close as possible to the area of interest in the image. This means that a similar amount of radiation reaches both the wedge and the area of interest, since they are not far enough apart in the axis of the heel effect for any fluctuations to take effect. To illustrate this, a series of experiments was performed using a radiographic knee phantom and the step wedge. The knee was consistently placed in the centre of the X-ray and a computerised procedure was implemented to detect three areas of interest, as follows:

1. On the knee phantom, the user selects two easily and consistently defineable anatomical landmarks – the tip of the tibial tuberosity and the point where the fibula meets the top of the tibia.

2. The location of these points are used to define two 30 x 30 pixel samples on the bony area of the knee. Since the landmarks are consistently chosen, the sample areas are also consistent in each image.

3. The mean grey level of each sample is found and the mean of the two sample means calculated.

4. This is repeated three times for each image and the mean of the three iterations is calculated.

5. The steps of the wedge are located, mean grey levels found and the grey level to Aluminium thickness calibration curve calculated.

6. The Aluminium-equivalent thickness of the total mean grey level is resolved for each image.

This procedure was followed for five images. In each image, the knee was placed in the centre of the X-ray. The wedge was positioned differently in each image: i) in the centre next to the phantom, ii) in the top left corner, iii) the top right corner, iv) the bottom left corner and v) the bottom right corner. Except for when the wedge was in the central position, it was subjected to different amounts of radiation in comparison to the knee phantom due to the heel effect. Examples of the wedge placement are shown in Figure 10.33.

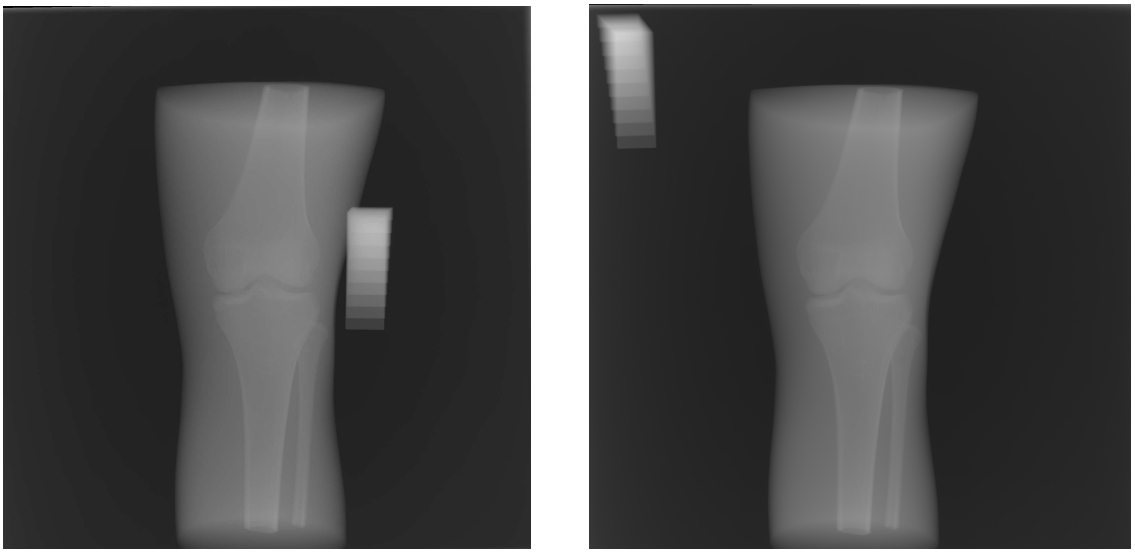

(a) (b)

Figure 10.33: X-rays of the knee with the wedge in the a) central position and b) top left corner.

The measurement procedure was also repeated three times for the knee and wedge in the centre of the image to determine the amount of fluctuation that was not due to placement effects. The images were then all corrected for the heel effect using the margin correction method described previously and Aluminium-equivalent thickness was recalculated. The results are given in Table 10.9.

Table 10.9: Position dependent differences in Aluminium-equivalent thickness.

Position	**Non heel corrected [mmAl]**		**Heel corrected [mmAl]**	
	AlEq	**Difference from Centre**	**AlEq**	**Difference from Centre**
Centre	19.5	0.0	19.3	0.0
Top Left	16.5	3.0	20.8	1.5
Top Right	18.0	1.5	17.5	1.8
Bottom Left	20.3	0.8	20.3	1.0
Bottom Right	15.1	4.4	18.8	0.6

The table shows the mean Aluminium-equivalent thickness for the ROI of the knee for each different wedge position. Despite the fact that a consistent ROI was chosen in each image, different Aluminium-equivalent values were calculated. This is due to the heel effect causing a different calibration graph to be calculated for each wedge position. The SD of

calculated Aluminium-equivalent thicknesses amongst the different test images decreased from 2.1 mmAl for non heel corrected images to 1.3 mmAl for heel corrected images. The maximum difference from the ROI calculated for the wedge in the central position decreased from 4.4 mmAl to 1.8 mmAl when heel correction was used. For repeated measurements of the wedge in the central position, a mean of 19.5 mmAl with a SD of just 0.1 mmAl was obtained. This showed that the deviations between measurements were due to different wedge positioning and not other errors.

This set of exposures showed that if no correction for the heel effect was to be made, it was essential to place the step wedge close to the area of interest to avoid differences in Aluminium calibration curve. If this was not possible, heel effect correction using a fully exposed margin of the image improved the consistency of results.

10.6.5 Discussion

This section addressed the heel effect in X-ray images. Dose and grey level measurements of the heel effect show that it is greatest in the anode-cathode direction and negligible in the perpendicular direction, as expected theoretically. This agrees with previous investigators modelling the effect, who find it essentially constant in the perpendicular axis [114]. Several different proposals for correcting for the effect have been put forward by investigators, although none of them was implemented with step wedge calibration. Behiels *et al.* suggested that the heel effect could be modelled in an exponential form in the direction of the anode-cathode axis and that a 1D model was sufficient for accurate correction [78, 114]. Do Nascimento *et al.* modelled the heel effect in digital mammograms [115]. They proposed a Gaussian distribution in the anode-cathode axis and a logarithmic distribution perpendicular to this. In this study it was found that a double exponential provided the best model, giving an improvement on both Gaussian and single exponential models. A method to correct for the heel effect using a model based on a fully exposed section of the image of interest was developed. Behiels *et al.* also use the background of X-rays to form the parameters of their heel effect correction, although, since they used hand radiographs with no fully exposed margins, this involved more complex searches for the background in X-rays. Despite the simplicity of the method used here, tests showed that this effectively reduced the heel effect in clinical images. Do Nascimento *et al.* and Behiels *et al.* both suggested that a 2D correction model was more thorough, but did note that the magnitude of the variation in the axis perpendicular to the anode-cathode axis was small enough to justify use of a 1D model, which was the approach taken here.

However, it is important to note that the magnitude of the heel effect is only 4% - 7% of the entire range of grey levels, which is consistent with the magnitude found by previous authors [105, 115]. This means that correction for the heel effect may not always be necessary, and that a fairly high level of precision can be maintained even without it. It has also been shown that a simple way to reduce the impact of the effect is to ensure the step wedge is placed as near as possible to the ROI in the X-ray, especially in the direction of the anode-cathode axis. This means that the same radiation reaches both the wedge and ROI, so they are less affected by the heel variations throughout the image.

The heel effect is often neglected when examining step wedge calibration. Few authors reporting results of step wedge calibration have mentioned its effect. Martin *et al.* referred to image inhomogeneities and they formed a pixel-by-pixel correction method based on a single correction image [88]. However, in this study, examination of the weekly variation in heel effect using the same equipment at the same settings showed that using a single correction graph to correct for heel effect may not be accurate. In cases when comparing X-rays taken at different sites, using different settings and on different equipment, it is the case that maintaining an accurate heel effect correction graph is impractical. Instead it has been found that the heel effect is simple to measure and a good correction can be made without the need for calibration images or complex models. If no correction is required, simple positioning when taking X-rays can be implemented to reduce the inaccuracies introduced by the heel effect.

10.7 SCATTER AND SOFT TISSUE THICKNESS

The ideal of including a step wedge in X-ray images is to obtain an Aluminium-equivalent thickness for an ROI and be able to compare it to X-rays taken at different times. It has already been discussed how the heel effect can change the effectiveness of comparative Aluminium thickness measurements in X-ray images. Two more factors also contribute to inaccuracy, the first is scatter. As discussed in Section 4.6, X-rays which fall on the imaging plate but are not directly incident from the X-ray tube can cause changes in the grey level and therefore Aluminium-equivalent thickness of an ROI. The second is soft tissue attenuation where an X-ray passing through different thicknesses of soft tissue will be attenuated differently and therefore give a different Aluminium-equivalent measurement depending on the amount of soft tissue it has passed through. Thus, the extent of the effect of both these factors needed to be analysed in the context of digital X-ray and possibilities for correcting for these factors were explored.

10.7.1 Materials and Methods

The X-ray phantoms used were described in Section 9.3. The first phantom was a tibia submerged in a Perspex, water-filled box. Different coverings of water modelled different soft tissue thicknesses. The second phantom was more uniform in design and consisted of a Perspex box with a bone-equivalent rod in the centre. Different layers of Perspex added above the box mimicked different thicknesses of soft tissue.

X-ray images were taken at both 63 kV, 1.8 mAs and 52 kV, 1.1 mAs with both types of phantom. Unless otherwise stated, the results reported in this section are for images of the Perspex phantom taken using 52 kV and 1.1 mAs. As discussed in Section 10.5.2, the Fuji system applies a logarithmic LUT to convert the stored light on the CR cassette to grey levels. The stored light is proportional to dose and it is therefore appropriate to perform analyses and corrections in terms of dose, as this gives a more direct reflection of the physical situation. For this reason, all grey levels measured from the X-rays were converted to dose using the equations in Section 10.5.2.

10.7.2 Analysing Scatter Contributions

To measure the scatter, all direct X-rays in a region must be blocked. This was achieved using 2 mm thick pieces of lead, which has been shown to completely block incident radiation at these X-ray energies [133]. The lead was positioned on a Perspex table placed above the X-ray cassette. A strip of lead was placed over half the step wedge and at various positions on the X-ray phantoms. Measurements of grey levels (or dose) under the lead are equivalent to measurements of the scatter contribution in that region, i.e. the grey level is due only to scattered X-rays and not to incident X-rays. Measurements of the grey level in adjacent areas is a measurement of the contribution from direct as well as scattered X-rays. In order to get a measurement due only to the direct X-rays, the contribution from scatter must be corrected for. The configuration used for making scatter measurements is shown in Figure 10.34.

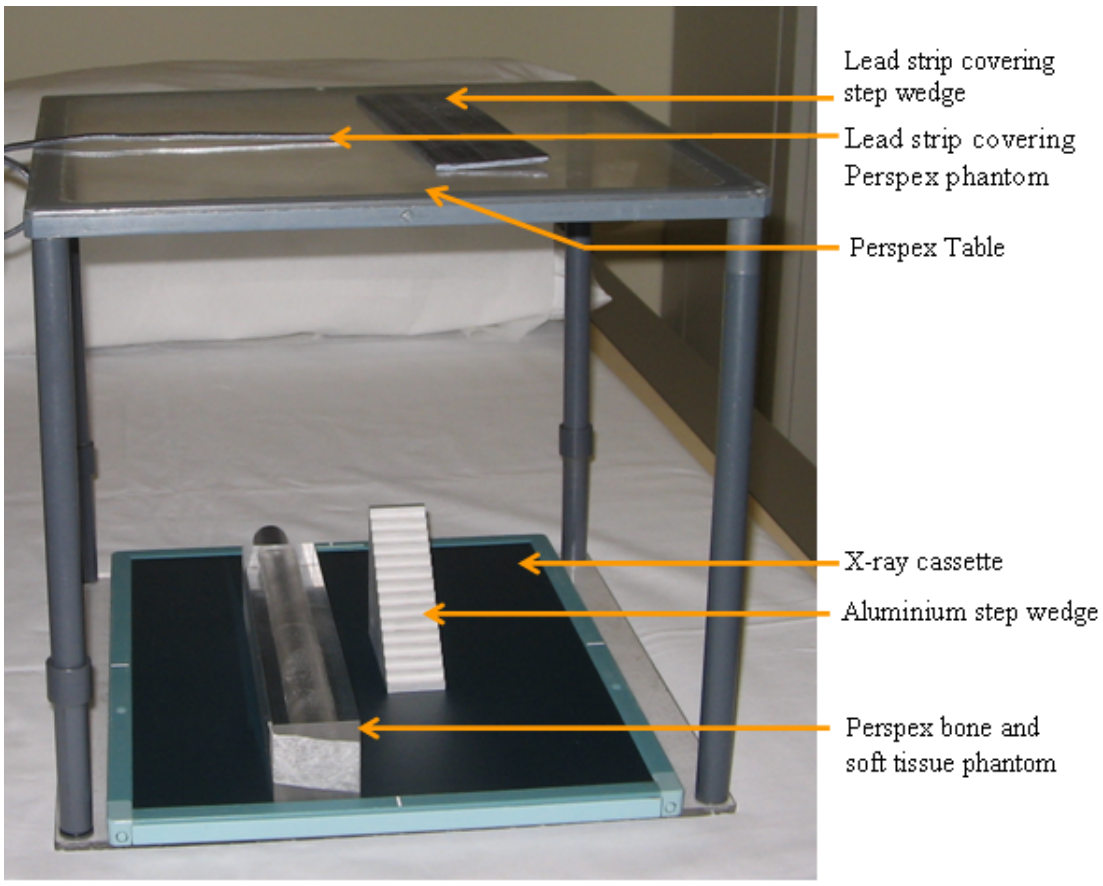

Figure 10.34: Photograph of the experimental set up showing the Perspex table and overlying lead strips used for scatter measurements.

The figure shows the placement of the pieces of lead above the bone phantom and the Aluminium step wedge. Figure 10.35 shows an X-ray image of this arrangement illustrating the regions in which measurements were made.

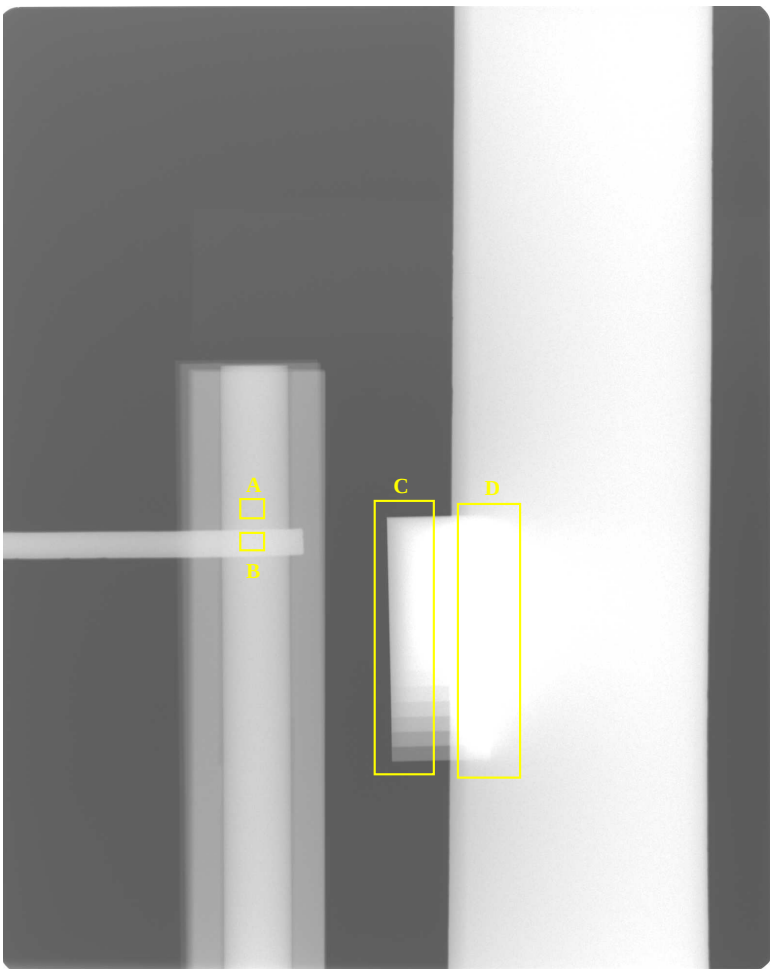

Figure 10.35: X-ray image showing the regions used for scatter measurements: A) bone ROI measuring scatter + primary dose, B) bone ROI under the lead measuring scatter dose only, C) Aluminium steps measuring scatter + primary dose and D) Aluminium steps under the lead measuring scatter dose only.

The quantity of scatter was measured as a percentage of the dose due to scatter compared to the total dose for the ROI. Several tests were performed using the tibia and Perspex phantoms. In each, the dose was measured in a consistent ROI over the bone or bone-equivalent material under the lead samples and compared to the dose of an adjacent, uncovered area. This was repeated for different coverings of water/Perspex to model increasing soft tissue thickness. All investigations showed the same trend with respect to soft tissue coverage. The results of an investigation using the Perspex phantom, which was repeated three times, are given in Table 10.10.

Table 10.10: Scatter dose as a percentage of total dose in three repeated measurements.

Perspex Covering Rod [mm]	**Scatter Dose as % of Total Dose**	
	Mean	**SD**
0	23	0.4
20	53	1.4
40	58	0.3
60	64	1.6
80	68	0.7
100	73	0.7
120	84	5.8

The results illustrate the increase in scatter contributions as the amount of soft tissue was increased. The low SD between the three measurements demonstrated high repeatability for the experiment.

To ascertain that the step wedge can be used as a consistent calibration method it was necessary to verify that the scatter contributions to the steps were consistent in different X-ray images, regardless of the other objects in the field of view. The results from a set of six X-ray images taken at 63 kV and 1.8 mAs are shown in Figure 10.36 and Table 10.11.

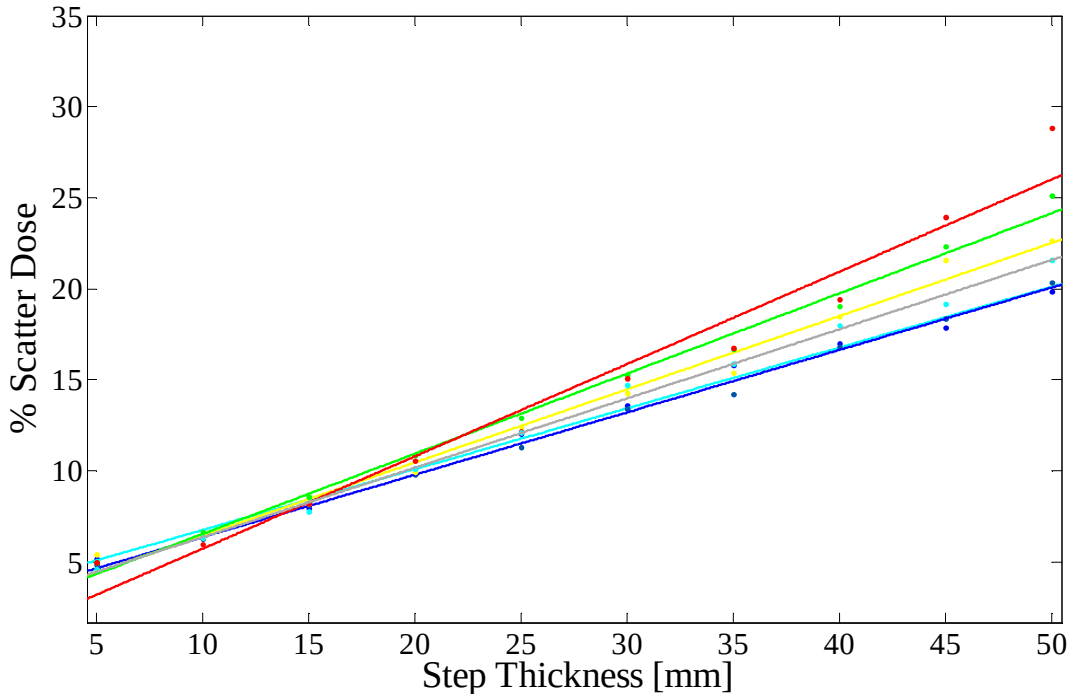

Figure 10.36: Graph showing the scatter dose as a percentage of the total dose for each step of the wedge in six consecutive exposures.

Table 10.11: The mean scatter dose as a percentage of total dose in six X-rays and the SD between measurements.

Step Thickness [mm]	**Scatter Dose as % Total Dose**	
	Mean	**SD**
5	5	0.6
10	6	0.2
15	8	0.3
20	11	1.0
25	13	1.5
30	15	2.0
35	17	3.2
40	19	4.0
45	22	4.6
50	24	4.7

The graph in Figure 10.36 shows the consistency of scatter measurements in all six X-ray images, with a maximum discrepancy between images of 5% of the total dose. It also illustrates the increasing contribution of scatter for increasing step thickness which can also be seen in Table 10.11. The small SD between measurements illustrated high repeatability for the experiment.

Even with no soft tissue present, the percentage of scatter contributing to the dose measured by the plate was more than 20%. This is a non-negligible amount. Furthermore, for different levels of soft tissue as well as different step thicknesses, it could be seen that scatter increased for increasing thickness. This meant that a simple scatter correction could not be made for all X-ray images but differed according to the thickness of soft tissue or Aluminium that the X-ray beam had passed through. However, despite this complication, these results also illustrated that scatter measured directly using lead strips was consistent in repeated exposures. This indicated that a set of correction X-ray images which measured the scatter directly could be used to correct subsequent X-ray images in which no direct scatter measurement was made.

10.7.3 Analysing Soft Tissue Contributions

For the same underlying bone or bone substance, a different Aluminium-equivalent thickness is obtained due to different amounts of overlying soft tissue. An investigation into the magnitude of this effect and the potential to correct for it was conducted. Although overlying soft tissue would reduce the dose incident on the X-ray cassette, it was possible that this was a negligible effect. In order to measure the magnitude of effect likely in a

clinical situation, the Perspex box phantom was used with several thickness of overlying Perspex. The contributions due to scatter were measured with overlying lead strips. A consistent ROI was analysed over the bone-equivalent rod in each image. The resulting dose was corrected for scatter and converted into grey level. The equivalent Aluminium thickness was found using the scatter corrected calibration graph from the step wedge. The resulting Aluminium-equivalent thickness for different layers of Perspex covering are given in Table 10.12.

Table 10.12: Calculated Aluminium-equivalent thickness of the ROI under different Perspex thicknesses.

Perspex Covering [mm]	**AlEq [mmAl]**
20	22
30	26
40	30
50	42
60	35
70	51
80	66
100	69

The results show that a difference of 47 mmAl, equivalent to twice the value of the rod alone, occurred when 100 mm of Perspex was added. Even for smaller amounts of soft tissue, large differences in the equivalent thickness were obtained.

The question as to how the thickness of soft tissue affects the dose incident on the plate was important. If this effect could be consistently measured in repeated exposures, then it could be corrected for. In order to measure this, three repeated exposures of different thicknesses of Perspex were taken. The scatter corrected dose under the bone-equivalent rod was measured in each case. The results are given in Table 10.13 and showed that the dose was consistently measured in repeated exposures, with a typical SD of 0.00 - 0.03 μGy.

Table 10.13: Consistency of dose measurements for different thicknesses of overlying Perspex.

Perspex Covering Rod [mm]	**Dose under Perspex [μGy]**	
	Mean	**SD**
0	1.17	0.02
20	0.74	0.03
40	0.45	0.01
60	0.26	0.00
80	0.16	0.00
100	0.11	0.00
120	0.05	0.02

Both these investigations showed, firstly, that the effect of different thicknesses of Perspex on the calculated Aluminium-equivalent thickness of the same ROI was not negligible. This indicated that the error that would be introduced when giving an Aluminium equivalent thickness that did not take into account overlying soft tissue would result in large disparities between areas that might have the same underlying bone density. Secondly, changes in dose introduced by different thicknesses of Perspex could be measured with a high degree of repeatability. This meant that a consistent relationship existed between added Perspex and added dose, which could be modelled and corrected for.

10.7.4 Correcting for Scatter and Soft Tissue Contributions

The results of the preceding experiments indicated that it was necessary to correct for both scatter and soft tissue contributions when making an Aluminium-equivalent thickness measurement of an ROI. They also indicated that the contributions of both these factors were consistent enough to be measured with correction graphs, rather than directly in each X-ray image. Therefore a set of correction X-rays was taken using the Perspex phantom and the Perspex table with overlying lead. X-rays were taken with the bone-equivalent rod only and then with increasing thicknesses of overlying Perspex (i.e. soft tissue equivalent material). Using these measurements, three correction graphs were developed.

Step Wedge Scatter Correction

From visual inspection of the measurements, the relationship between the dose incident on each step of the wedge and the corresponding percentage of scatter dose was plotted using a double exponential of the form $y = ae^{bx} + ce^{dx}$. A resulting goodness of fit of $R^2 = 0.99$ was obtained (with a = 1.77, b = -3.95, c = 0.27 and d = -0.35). This graph is shown in Figure 10.37.

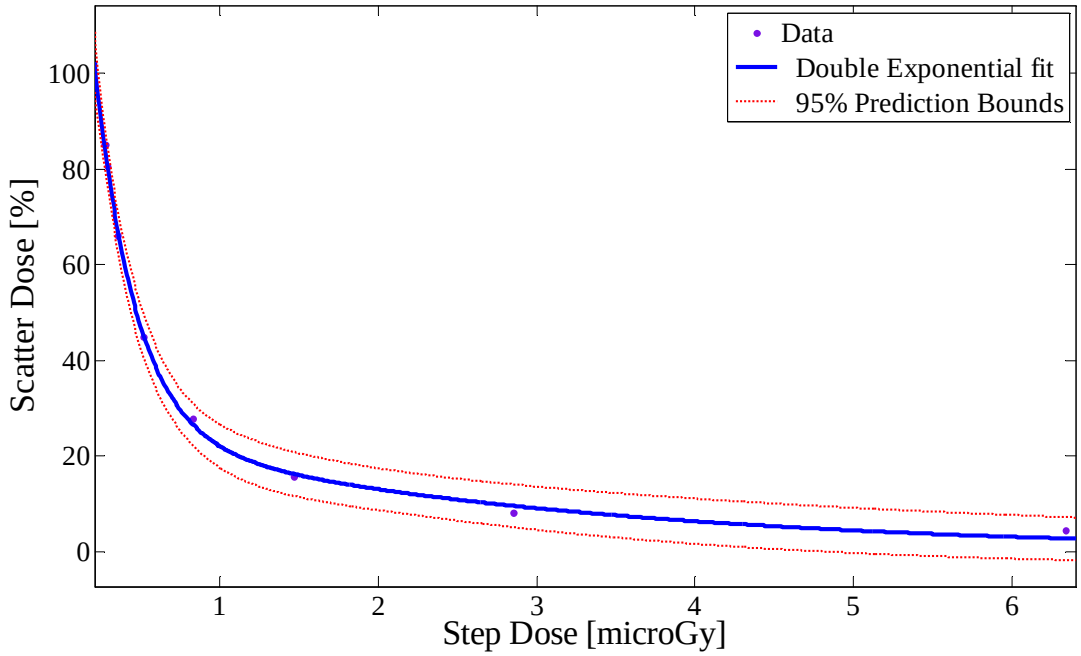

Figure 10.37: Modelling the step dose to percentage scatter dose relationship with a double exponential relationship.

The graph was used to obtain an estimation of the percentage of scatter contributing to each step of the wedge. The correction for added scatter dose was performed as follows

$$\begin{aligned} D_s &= D_{u_s} - D_{c_s} \\ &= (P_s + S_s) - S_s \\ &= P_s \end{aligned} \tag{10.17}$$

where D_s is scatter-free step dose, D_{u_s} is the uncovered step dose, D_{c_s} is the covered step dose, P_s is the primary step dose and S_s is the scatter step dose. This correction was performed for each step of the Aluminium wedge to provide scatter-free grey levels.

ROI Scatter Correction

Visual inspection of the measurements suggested that the relationship between the thickness of overlying Perspex and the percentage of scatter dose could be plotted using a straight line of the form $y = mx + c$. A resulting R^2 value of 0.97 (with $m = 0.29$ and $b = 46.87$) was achieved. The graph is shown in Figure 10.38.

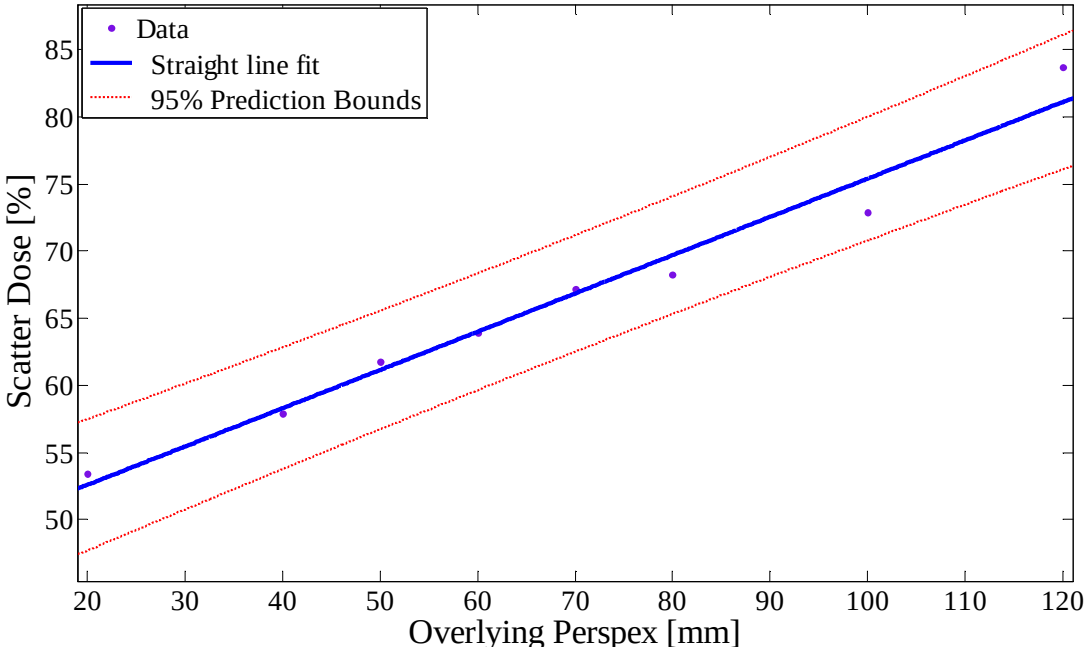

Figure 10.38: Modelling the percentage scatter dose to the thickness of overlying Perspex with a straight line relationship.

The graph was used to obtain an estimation of the percentage of dose contributed by scatter to the ROI for a given thickness of overlying Perspex. Correction was performed as

$$\begin{aligned} D_r &= D_{u_r} - D_{c_r} \\ &= (P_r + S_r) - S_r \\ &= P_r \end{aligned} \tag{10.18}$$

where D_r is the scatter-free ROI dose, D_{u_r} is the uncovered ROI dose, D_{c_r} is the covered ROI dose, P_r is the primary ROI dose and S_r is the scatter ROI dose. This correction was performed for the mean of the bone ROI to provide a mean scatter-free dose measurement.

Correction for Overlying Perspex

The relationship between the thickness of overlying Perspex and the added scatter-free dose in comparison to no overlying Perspex was modelled with an exponential of the form $y = ae^{-bx} + c$ using the data from Table 10.13. The resulting fit had an R^2 value of 0.99 (with a = -1.19, b = 0.02 and c = 1.19). The graph is shown in Figure 10.39.

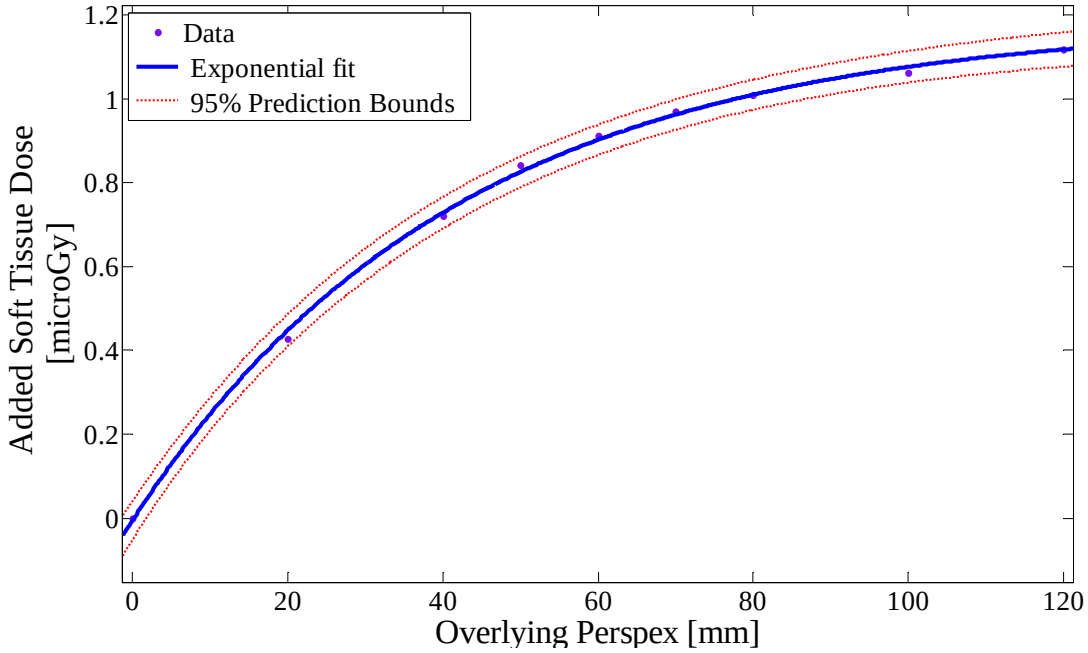

Figure 10.39: Modelling the relationship between overlying Perspex and added dose with an exponential relationship.

This graph was used to obtain an estimation of the dose reduction in the ROI due to the overlying Perspex. Correction for this dose was performed as

$$D_p = D - D_t \tag{10.19}$$

where D_p is the Perspex-free dose, D is the scatter-free dose and D_t is the dose due to overlying Perspex. This correction was performed on the mean of the scatter-free dose in the ROI and converted to a grey level representing the underlying bone in the ROI, free from the effects of overlying Perspex.

Correction for the Absence of the Measuring Equipment

A 2 mm thick Perspex table with lead strips was present when taking the scatter and soft tissue correction X-rays. However, this equipment was not present in normal X-rays and it was therefore necessary to account for its absence. The Perspex table was expected to attenuate the X-ray beam to a small extent. Absence of the lead strips meant that the areas underneath them that did not experience any direct radiation in the correction X-rays would now contribute to the scatter dose. Both of these factors were expected to result in an increase in scatter dose in the measurements made without the scatter equipment. Measurements of the same ROIs on the Perspex phantom with and without the scatter equipment indicated that an increase in dose of 15% occurred when the equipment was not present. Therefore, correction for the absence of the equipment in the ROI measurement was

$$D_t = D_{u_r} - 15\%(D_{u_r}) \tag{10.20}$$

where D_t is the equipment-free ROI dose and D_{u_r} is the uncovered ROI dose. Measurements on the steps of the wedge showed a varying difference due to the scatter equipment for each step. This was fitted with $y = a_1 e^{-((x-b_1)/c_1)^2} + a_2 e^{-((x-b2_1)/c_2)^2}$ with an R^2 value of 0.98 (and $a_1 = 12.90$, $b_1 = 29.10$, $c_1 = 6.61$, $a_2 = 9.47$, $b_2 = 15.63$ and $c_2 = 14.76$). The graph is shown in Figure 10.40.

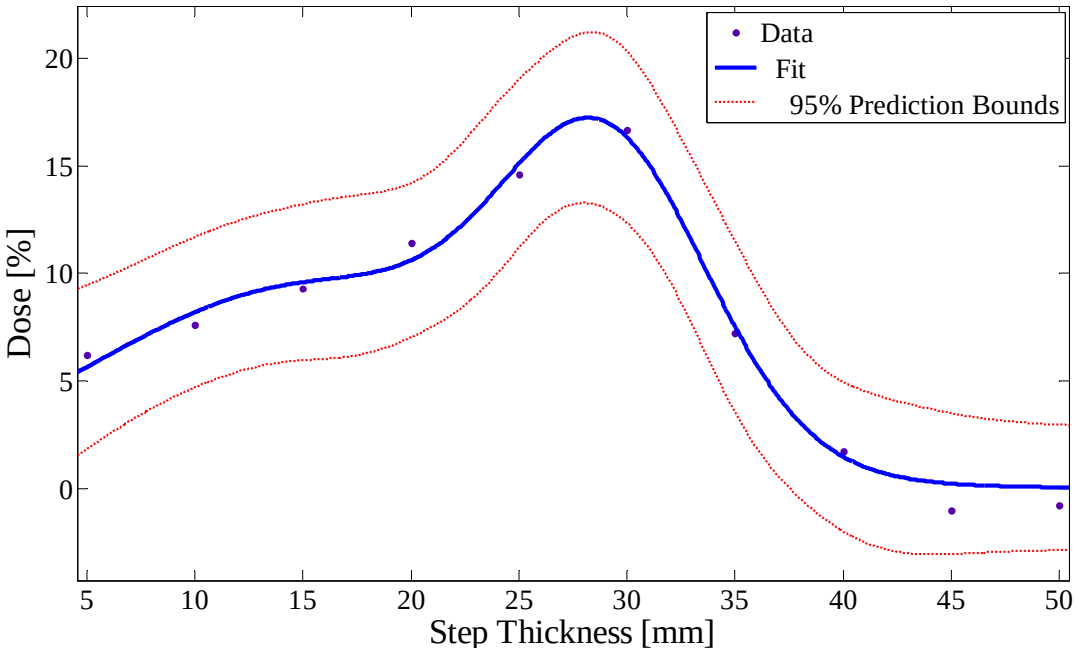

Figure 10.40: Percentage scatter due to the experimental equipment for different steps of the step wedge.

This graph was used to obtain an estimation of the extra dose present in the steps due to there being no table between the X-ray source and the plate. Correction for this dose was

$$D_{s_t} = D_{u_s} - Tx \tag{10.21}$$

where D_{s_t} is the equipment-free step dose, D_{u_s} is the uncovered step dose and T is the percentage dose due to the equipment for a step of thickness of x.

Correction Procedure

To test whether the calibration graphs could be used to correct for scatter and Perspex with no direct measurements, a second set of X-ray images was acquired with different thicknesses of overlying Perspex but with no table or lead in place. The final correction procedure used was as follows:

1. Measure the grey level of the ROI, i.e. over the bone and the steps of the wedge.
2. Convert all grey levels to dose.
3. Subtract 15% dose from the ROI to account for no scatter equipment being present, i.e. Equation (10.20).
4. Calculate the percentage dose added for each step of the wedge due to the absence of the scatter equipment and subtract this, i.e. Equation (10.21).
5. Correct each step of the wedge for scatter by finding the percentage scatter dose from the double exponential scatter graph and subtract this, i.e. Equation (10.17).
6. Correct the ROI for scatter by finding the percentage scatter dose for the overlying Perspex from the straight line graph, i.e. Equation (10.18).
7. Find the dose attenuated by the overlying Perspex using the exponential graph and add this to the ROI scatter-free dose, i.e. Equation (10.19).
8. Convert the final ROI dose and scatter-free steps doses to grey values.
9. Fit the exponential calibration graph to the step values.
10. Calculate the Aluminium-equivalent thickness of the ROI using the calibration graph, i.e. Equation (10.13).

This correction procedure was implemented in Matlab and carried out automatically. X-rays with 40, 60, 80 and 100 mm of overlying Perspex were taken to test the procedure. A comparison between the corrected and uncorrected Aluminium-equivalent thickness values for the same ROI of bone is given in Table 10.14.

Table 10.14: Comparison of Aluminium-equivalent thickness of the same ROI with and without correction for Perspex and scatter contributions.

Thickness [mm]	**AlEq [mmAl]**	
	Uncorrected	**Corrected**
40	18	15
60	22	15
80	26	14
100	30	14

The results showed that a consistent equivalent Aluminium thickness was achieved when using the Perspex and scatter correction method. The SD when uncorrected was 5.4 mmAl which improved to 0.5 mmAl when using correction. The results indicated that the technique and graphs derived from correction X-rays could be effectively used to correct for scatter and overlying Perspex contributions in images in which direct scatter measurements were not made. The resulting Aluminium-equivalent thickness was consistent for all thicknesses of overlying Perspex, deviating by only 1 mmAl. In comparison, the results where no correction was used had a maximum difference of 12 mmAl. The improvement when using Perspex and scatter correction is illustrated by these results.

10.7.5 Analysing the Effect of Other Overlying Materials

In many clinical situations X-rays are taken with other materials between the beam and the X-ray plate. The most common example of this is a cast around a fractured bone. The effect of the cast material on the above-mentioned relationships had to be investigated if these materials were also to be eliminated from the Aluminium-equivalent thickness calculation process.

Three types of cast material can be used in fracture treatment: polytape, fibreglass and plaster of Paris. To analyse the effect of each of these materials, a set of exposures identical to the correction X-rays described above was taken. In each set, one type of cast material was placed on top of the Perspex box or layers of Perspex. Measurements of the contributions of scatter and Perspex were then made to see how the overlying cast material affected these. A set of X-rays with different layers of Perspex and the different cast materials, but no direct scatter measurements, was then taken to test the correction methods.

The changes to the scatter correction graph for the step wedge were examined with polytape, plaster and fibreglass included in the calibration X-rays. Since the cast materials did not affect the wedge, no differences to the scatter correction graph for the step wedge occurred.

Small changes occurred in the graphs modelling the percentage scatter contribution for different overlying thicknesses of soft tissue. All graphs remained straight lines of the form $y = mx + c$. The resulting coefficients and R^2 values are given in Table 10.15.

Table 10.15: Straight line curve fitting values of scatter dose for different cast materials.

Overlying Material	**m**	**c**	**R^2**
None	0.29	46.87	0.97
Polytape	0.34	43.61	0.87
Plaster of Paris	0.42	41.96	0.91
Fibreglass	0.35	48.69	0.93

The table shows that different straight lines were needed to estimate the percentage scatter added by Perspex with each different type of cast material. Since the R^2 values were close to 1, a good fit of all these lines had been obtained.

Changes also occurred to the exponential fitting of the dose added by different thicknesses of Perspex. All graphs remained exponentials of the form $y = ae^{-bx} + c$. The resulting coefficient values and R^2 values are given in 10.16. The results show that different graphs of attenuated dose due to overlying Perspex resulted when different cast materials were used. An exponential graph provided an accurate model of this relationship for all the materials.

Table 10.16: Exponential curve fitting values of reduced Perspex dose for different cast materials.

Overlying Material	**a**	**b**	**c**	**R^2**
None	-1.19	0.02	1.19	0.99
Polytape	-0.76	0.03	0.76	0.99
Plaster of Paris	-0.53	0.02	0.54	0.99
Fibreglass	-0.62	0.08	0.62	0.99

To examine the effect of adding cast materials to the X-ray, the scatter dose as a percentage of total dose and the dose change due to different levels of Perspex were examined for each material. It was found that, for each different level of Perspex, the dose added by scatter was fairly consistent across all materials. However, the dose change due to Perspex was different for each material. This is shown in Table 10.17.

Table 10.17: Table showing the effect of overlying Perspex thickness for each cast material and the difference from the effect with no cast material.

Overlying Perspex [mm]	**Dose reduction due to overlying Perspex [μGy]**			
	No Cast Material	**PolyTape**	**Plaster of Paris**	**Fibreglass**
20	0.40	0.02	0.01	-0.01
40	0.69	0.27	0.18	0.33
60	0.90	0.46	0.31	0.51
80	1.03	0.59	0.42	0.52
100	1.08	0.67	0.49	0.38
Mean Difference from No Cast Material		**0.42**	**0.54**	**0.48**
SD of Difference		**0.03**	**0.09**	**0.14**

The table shows that the dose was reduced by different amounts for different Perspex thicknesses and for each different cast material. However, the difference between the dose reduction with and without cast material was consistent for each material at different Perspex thicknesses. The low SDs between measurements at different Perspex thicknesses for each cast material indicated that a consistent 'offset dose' was attenuated due to the addition of the cast material and that this was unique to each material.

A set of test X-rays for each cast material was taken. These consisted of different layers of overlying Perspex with the cast material on top and no measuring table or scatter measuring equipment. From the results of the calibration experiments, two approaches to correcting for the presence of cast material were attempted. The first used the individual correction graphs for scatter and Perspex contributions for each different cast material. The second was to correct all dose measurements by the 'offset dose' introduced by the addition of the cast material at the beginning of the correction procedure, i.e. to add this dose to the measured dose of the ROI. The normal correction procedure used when no cast material was present was then followed. The results of these two methods are shown in Table 10.18.

Table 10.18: Comparison of correction techniques for added cast materials using a) individual calibration graphs and b) offset dose correction.

(a)

Overlying Perspex [mm]	AlEq [mmAl]	Corrected AlEq of ROI [mmAl]		
	No Cast Material	PolyTape	Plaster of Paris	Fibreglass
40	15	16	18	16
60	15	15	18	16
80	14	17	19	17
100	14	16	18	17

(b)

Overlying Perspex [mm]	AlEq [mmAl]	Corrected AlEq of ROI [mmAl]		
	No Cast Material	PolyTape	Plaster of Paris	Fibreglass
40	15	14	14	14
60	15	14	13	14
80	14	14	14	14
100	14	13	13	13

The results show that correcting for an initial 'offset dose' provided the most accurate Aluminium-equivalent thickness meaurements when taking an overlying material into account during scatter and Perspex corrections. This was indicated by the low SD between the Aluminium-equivalent thickness measurements for different cast materials and Perspex thicknesses. Using the correction graphs, the SD between measurements was 1.1 mmAl and the equivalent thickness values showed a large variation. However, using the initial 'offset dose' correction, the values were much more consistent with a SD of 0.5 mmAl. Therefore, it was decided that in the final correction procedure to be used in clinical X-ray images, a standard offset dose would be subtracted depending on the cast material present, rather than modelling scatter and Perspex contributions with different graphs for each material.

10.7.6 Discussion

This investigation into the effect of scatter and soft tissue when calibrating X-ray images with an Aluminium step wedge illustrated several important points. An increase in overlying soft tissue would be expected to increase the apparent density measured in an ROI. However, few previous researchers have quantified this or described correction techniques. The correction experiments performed in this study showed the effect of overlying soft tissue, modelled with Perspex, in adding an erroneous value to the calculated Aluminium-equivalent thickness. Furthermore, they quantified the magnitude of this effect and showed that it was non-negligible. The tests also illustrated another important feature to consider when using step wedge calibration. This was the effect of scatter dose in changing the measured Aluminium thickness of an ROI. Again, this is not an issue that has been addressed by many researchers using Aluminium step wedges and no investigations into the magnitude of the effect were found in the literature. This investigation allowed measurement of the contribution due to scatter from the use of 2 mm lead strips blocking all direct radiation to the wedge. Ideally the scatter due only to the wedge could be measured. However, in this experimental set-up, scatter from the Perspex table on which the lead was placed contributed to both the uncovered and covered dose measurements. Measurements showed this effect to be of the order of 4%, which was considered acceptable. If it was considered necessary to eliminate this effect, an experimental set-up allowing placement of the lead directly on the wedge and phantom would be necessary.

The tests performed here showed that the magnitude of the scatter effect was non-negligible and that it increased with increasing overlying Perspex. Thus, correction for overlying Perspex (or soft tissue) and correction for scatter must be performed together. Finally, cast materials are commonplace, especially in fracture X-rays, where investigation of the density of the healing fracture site using step wedge calibration might be of particular use. Tests showed that different cast materials affected the resulting dose values differently and that the best method to correct for this was using the offset dose due to their presence in the X-ray.

To account for the presence of soft tissue, Haidekker *et al.* used a method of subtracting the dose measured in adjacent soft tissue from the bone dose, although this was not verified with any experiments [103]. However, the dose in an area adjacent to bone is not equivalent to the dose added by the soft tissue overlying the bone. Firstly, the beam traversing the bone goes through a smaller soft tissue thickness than that traversing soft tissue only. Secondly, due to the effects of the position of the limb, it is not necessarily accurate that the same amount of soft tissue is present on either side of the bone that is present superficial and deep to it. In this study, the modelling and application of correction graphs to correct for the scatter in both the step wedge and the ROI, as well as the effect of overlying Perspex, has

been performed. An accurate estimation of Perspex and scatter dose was made resulting in consistent Aluminium-equivalent thicknesses being calculated for the same ROI, despite the overlying Perspex or cast material. However, it must be noted that these experiments were performed in very consistent situations. Firstly, the same set of X-ray equipment was used. Different sets of equipment might produce different inhomogeneities. Secondly, the Perspex phantom was very uniform in shape. The irregularities introduced by anatomy and different quantities of fat and soft tissue seen in the clinical environment may introduce deviations from the correction graphs, as will the fact that Perspex is not an exact model of soft tissue. Thirdly, whilst the dimensions of the Perspex box might be a fairly good model for small anatomies such as the wrist, the correction graphs derived using it could not be applied to different parts of the body such as the hip or thigh. Despite shortcomings in using a Perspex and bone-equivalent model, it remains difficult to create correction graphs using clinical data. Although a design of apparatus to include direct scatter measurements in the clinical X-ray environment could be created, it is likely that these might occlude regions that are of interest to a clinician. Furthermore, it is difficult to add or subtract soft tissue to patients to obtain corrections, or to take measurements of the bone with no soft tissue added. For these reasons the calibration graphs obtained using the Perspex phantom were at least a close approximation to the true situation, and provided an improvement on using no correction at all.

In summary it has been shown that correction for soft tissue and scatter contributions to an ROI is a non-trivial and complex process that requires detailed investigation. In this study a simple method of obtaining corrections from a Perspex model to correct for scatter, soft tissue and other contributions to calculated Aluminium-equivalent thickness has been developed.

10.8 SOFT TISSUE AND BONE THICKNESS

As has been shown in the previous section, differing amounts of soft tissue overlying an ROI result in a different Aluminium-equivalent thickness being calculated. If comparisons are to be made between patients, or between different ROIs in the same patient, it is necessary to know how much soft tissue is covering the ROI and to account for this. Furthermore, if the density of bone is of interest, then the thickness of that bone must not affect the measurements. Two bones of the same density will give different Aluminium-equivalent thickness measurements if they are of different thicknesses, as the X-ray beam travelling through the thicker bone will have been attenuated by a greater quantity of material and therefore appear as a higher grey level. Thus, the thickness of the bone must also be taken into account when quoting Aluminium-equivalent thickness measurements for different ROIs and

different patients. This section discusses the measurement of soft tissue and bone thickness using X-ray images to provide this information.

In order to obtain a measure of the overlying soft tissue and the thickness of the bone, the data available in the normal clinical situation was considered. In X-ray studies of most parts of the body, two, orthogonal images (AP and lateral) are taken. It was therefore decided to use measurements from orthogonal views to correct for bone and soft tissue thickness. For example, if the AP image was of interest, then the lateral image could be used to measure the thickness of soft tissue or bone that the beam has travelled through, and vice versa.

10.8.1 Marking a Consistent ROI

If soft tissue and bone thickness information for the AP image was to be obtained from the lateral image, it was important to know that the measurement was being made at the same position in the bone in each view. For this purpose a computerised procedure was designed to consistently locate the ROI in each image.

Using the tibia as an example, the first step was to ensure that the tibia was aligned with the vertical and horizontal image axes. This was done by calculating the orientation of the long axis of the bone in the image and rotating it so that it was parallel to the image axes. The next step was to mark easily identifiable landmarks in each image. In the AP view, this was the tip of the tibial tuberosity and the distal point of the medial malleolus. This was repeated in the lateral view, marking the highest visible point on the proximal tibia (the tibial tuberosity) and the most distal point on the malleolus. The selected points on both images were displayed for visual confirmation by the user, as shown in Figure 10.41.

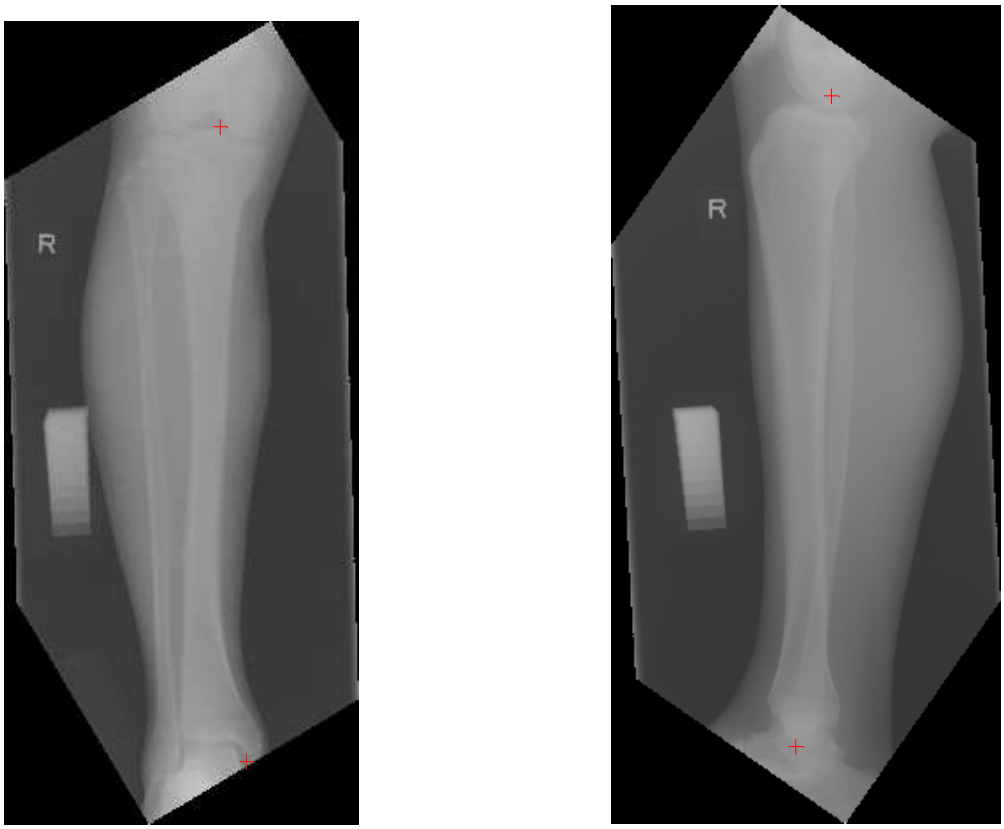

(a) (b)

Figure 10.41: The anatomical landmarks used in identifying the co-ordinate system for ROI selection in a) an AP X-ray and b) a lateral X-ray.

These two points provided the information to define a 2D co-ordinate system so that measurements made on the AP image could be repeated on the lateral image. This was achieved by creating a vertical axis running from the tip of the tibial tuberosity down to the height of the medial malleolus as shown in Figure 10.42. The horizontal axis was defined as perpendicular to this and the origin was the tip of the tibial tuberosity. Since there were only two images in two planes, a 3D co-ordinate system could not be defined. Whilst the z-axis measurements were consistent in each image, the x-axis measurements were made in the lateral image, and the y-axis measurements in the AP image, as there was not enough information to relate these axes between the two projections.

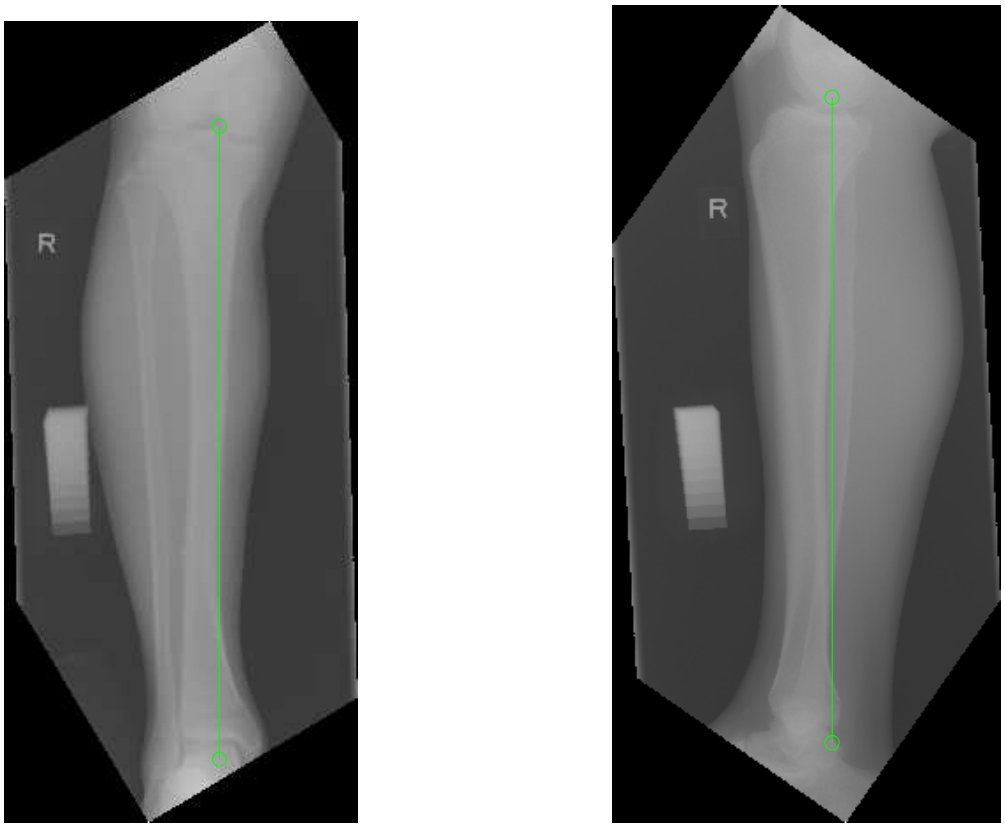

(a) (b)

Figure 10.42: The orientation of the vertical axes in a) the AP and b) the lateral image.

Having defined the axes in each image, the user was asked to mark the ROI in the AP image. The upper and lower borders of this AP ROI were displayed in the lateral image so that the user could select the same area in this view, as shown in Figure 10.43.

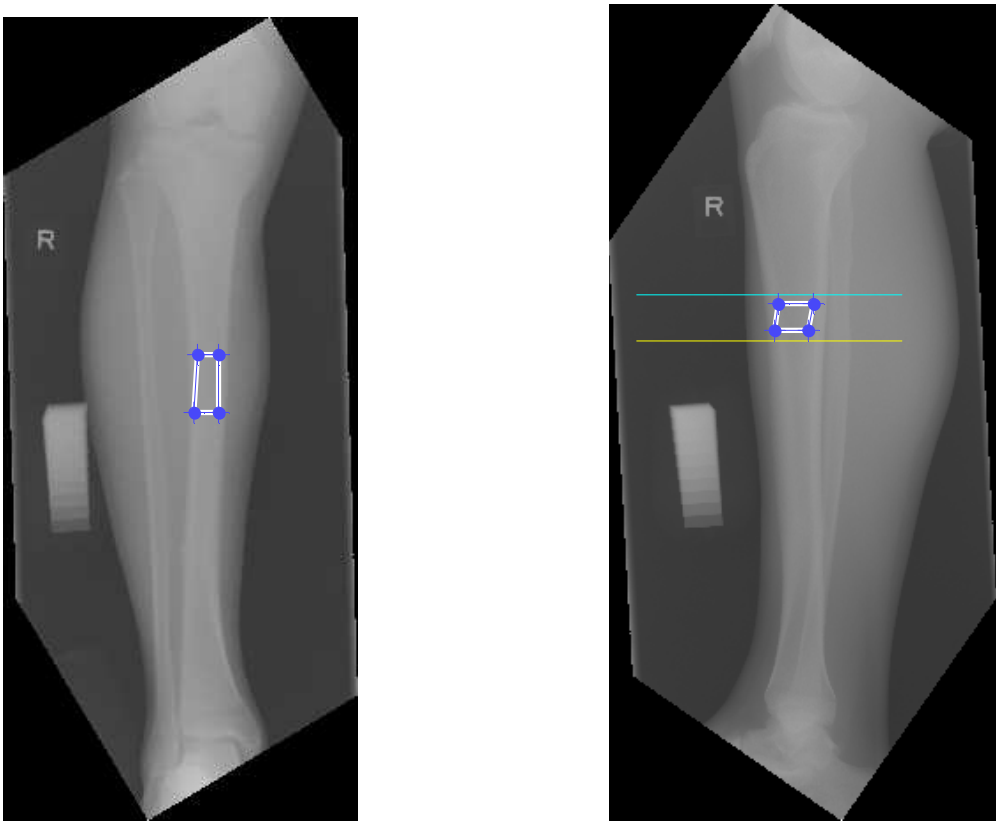

(a) (b)

Figure 10.43: a) ROI marked in the AP image (blue) and b) upper and lower guidance lines (cyan and yellow) and the ROI marked in the lateral image (blue).

10.8.2 Borders using Threshold Searching

The first method used to measure the bone boundaries was that used by Haidekker *et al.* [103] but modified for grey levels. A line across the image at the ROI was drawn which created a profile of the grey levels in this plane. A trace along the profile was made to calculate a threshold value as follows

$$T = Ma–(1–a)b \tag{10.22}$$

where T is the threshold, M is the maximum value in the profile, a is the sensitivity adjustment value ($0 < a < 1$) and b is the running average. At each point in the profile, if grey level was greater than the threshold, it was marked as a boundary. A trace was then made in the other direction to find further boundaries. This method worked to a certain extent. Although it could usually locate all the boundaries, the sensitivity value had to be manually adjusted to find the boundaries for the different areas of soft tissue, tibia and fibula. Furthermore, if the maximum value in the profile had been passed, it became impossible to find any further boundaries (as the threshold could no longer be exceeded). An example of boundaries found on an AP profile and X-ray are shown in Figure 10.44.

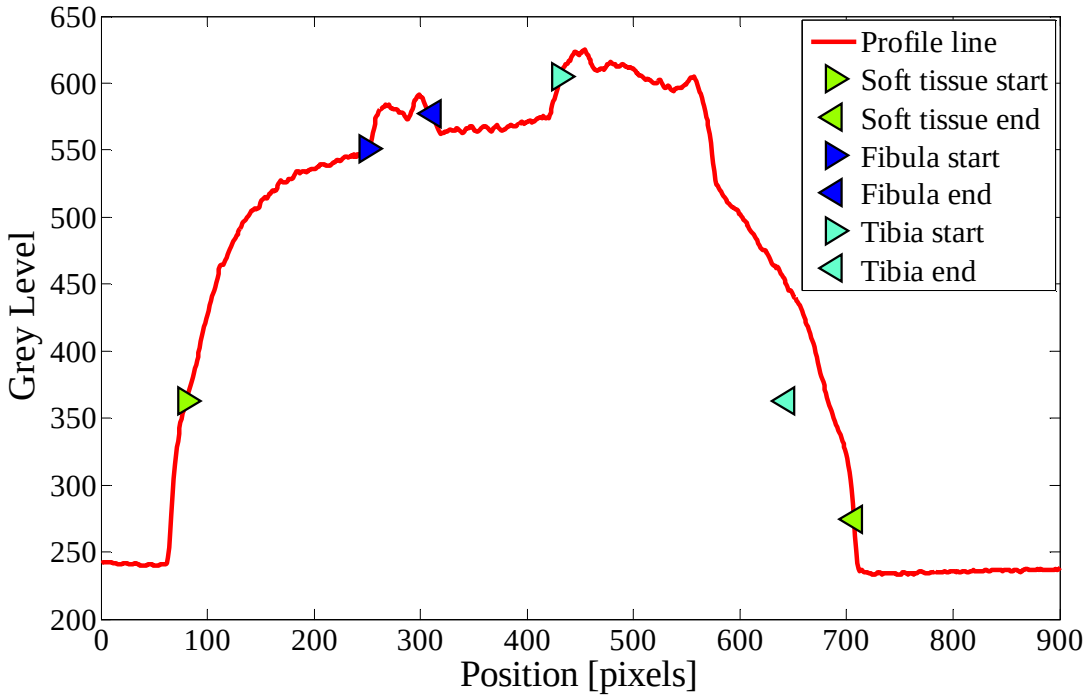

(a)

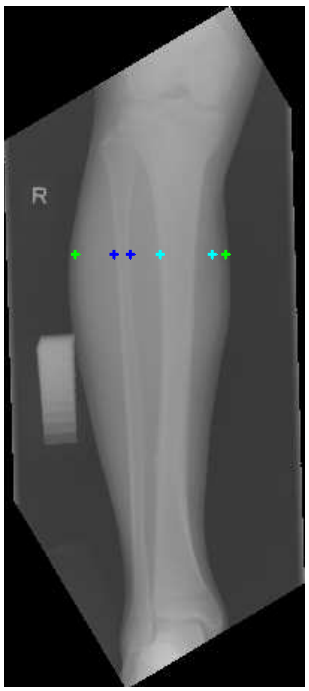

(b)

Figure 10.44: The selected borders on a) the profile across an ROI and b) the corresponding X-ray image.

The figure shows that, by visual inspection it can be said that the method identified the soft tissue and bone borders with reasonable accuracy. However, as in the case of the medial tibial border, errors sometimes occurred which would result in a miscalculation of the bone and soft tissue thickness. This, combined with the potential problems finding borders when maximum thresholds had been exceeded, meant that a more reliable method was needed to make soft tissue and bone thickness measurements.

10.8.3 Borders using Differentiation

Since differentiation is a measure of change, it was used as a way to find changes in the grey level profile of the regions of interest. A computerised procedure was designed where a profile line was drawn along the ROI. This was smoothed with a Gaussian filter to eliminate localised noise in the profile. The absolute value of the gradient (first derivative) of the profile was then calculated. A procedure traced through this profile and found peaks that were greater than m, a size threshold value, and further apart than p, a distance threshold value. If the correct number of peaks corresponding to the anatomical areas (e.g. six in this example) were found in the profile, the procedure stopped. Otherwise the p threshold was automatically adjusted and the procedure repeated up to five times until the correct number of peaks was found. After five iterations it was found that no useful information was added by changing the p value. Therefore if the correct peaks were not automatically selected, user interaction was required to identify the peaks.

This method gave good results by visual inspection and was fairly robust to profiles from different levels in either AP or lateral images. An example of the peaks found on an AP image is shown in Figure 10.45. The figure shows that the peaks located on the profile line were a good representation of the anatomy in the AP radiograph. However, as Figure 10.46 demonstrates, profiles can take on a wide variety of shapes. Different positions in the same image can generate a variety of profiles with different types and numbers of peaks. Due to this unpredictable variation, it was sometimes necessary to seek user interaction for the expected number of peaks. The program could then be tailored for various anatomical profiles.

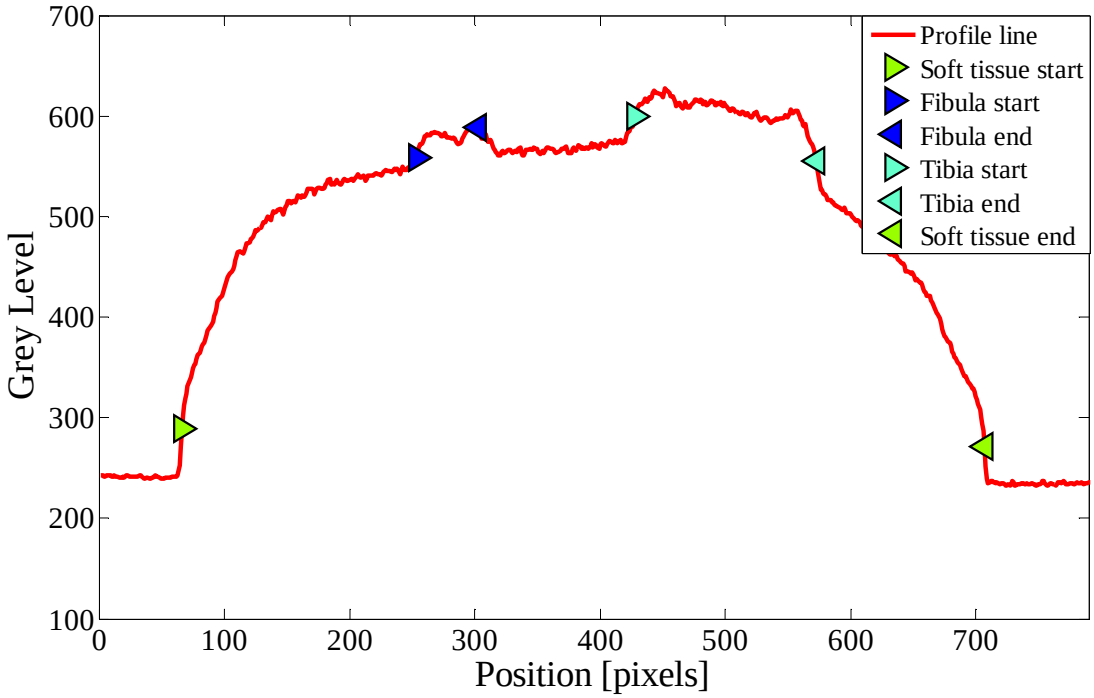

(a)

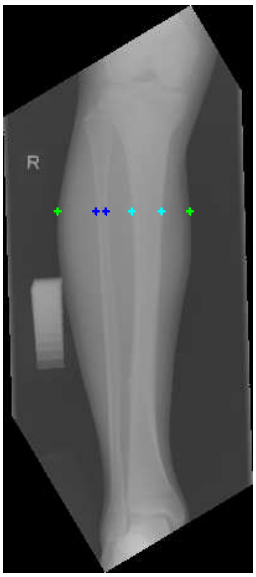

(b)

Figure 10.45: a) Peaks located on a profile of an AP image using differentiation and b) how these relate to the position of the boundaries on an X-ray image.

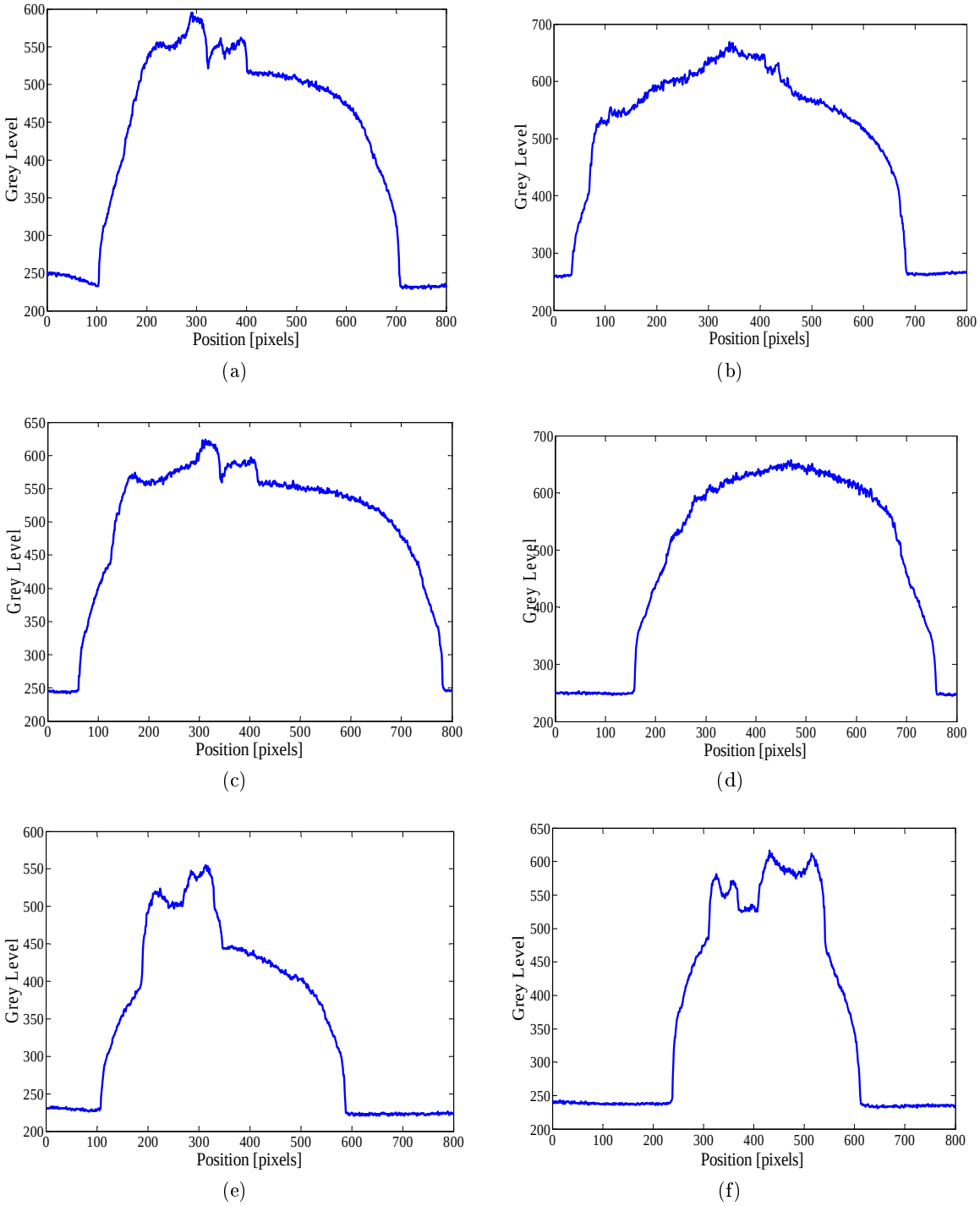

Figure 10.46: a) – f) Profile lines across AP and lateral X-ray images of a tibia, showing the variation in size, number and position of peaks.

10.8.4 Accounting for Bone Thickness

Regions in an X-ray image with the same mineral density will appear to have different equivalent Aluminium thicknesses if their geometry is not considered. A procedure was created which could accurately measure the thickness of bone that a beam had passed through by using the orthogonal image. In Section 10.7 correction for different thicknesses of overlying soft tissue was made. However, since the bone is the area of interest, it is inappropriate to make a 'correction' for bone thickness. Instead, it was decided that in order for Aluminium thickness measures to be comparable between different bones, they should be normalised for bone thickness using dimensions found from the orthogonal X-ray. In other words, the Aluminium-equivalent thickness measurement was divided by bone thickness and measured in mmAl/mm. This will be referred to as normalised Aluminium-equivalent thickness.

10.8.5 Discussion

This section described the measurement of the soft tissue and bone thickness of an ROI. These are important measurements to take into account when attempting to quantify bone using the step wedge. However, few authors discuss correction or measurement techniques for these factors. Section 10.7 discussed how differing amounts of overlying soft tissue in an ROI give different grey levels, even if the underlying bone is of the same density. Similarly, two bones of the same density but different thicknesses will have different grey levels. Both these situations would result in different estimations of equivalent Aluminium thickness using a calibration step wedge. Haidekker *et al.* used a thresholding method to find soft tissue and bone boundaries but investigation into their technique indicated that it required much user input and was not robust to different anatomies [103]. Furthermore, their calculations were made on the image of interest, which does not yield the same thicknesses as those the X-ray beam passed through. Although they used their measurements to correct for overlying soft tissue, they did not propose a method to take bone thickness into account. Symmons mentioned the importance of taking bone thickness into account and suggested measurement of this using orthogonal X-rays [108] and Martin *et al.* measured thickness directly on the imaged samples, although this would not be possible in the clinical setting [88]. Although neither of these investigators reported the effect of or correction for soft tissue, they suggested normalising for bone thickness by dividing the measured grey level by the sample thickness. This is the approach chosen here, thus making measurements between bones of different diameters comparable.

In this study it has been shown how anatomical landmarks on two orthogonal X-rays as taken in the clinical situation were used to define a unique co-ordinate system. This allowed identification of a consistent ROI in both AP and lateral views. Differentiation of the grey level profile line across this ROI in one image provided measurements of both the overlying soft tissue thickness and the thickness of the bone for the ROI of the orthogonal image. Although this method was simple, it was robust to noise and effective. If the anatomy was complicated, user interaction could ensure that useful measurements were always obtained. Analysing the orthogonal X-ray to determine the soft tissue and bone thickness that the beam had passed through is a simple way of obtaining attenuation data without requiring direct anatomical measurements to be made at the time of X-ray, although it does assume that little change in soft tissue thickness between the two images occurs. This is generally a good assumption, although in cases where a lot of soft tissue is involved, such as the thigh, the flattening and spreading effect of placing the soft tissue on the table may distort results. However, despite being impractical to make these measurements manually on a patient at the time of X-ray, it would not always be possible to get a good indication of soft tissue and bone thickness from the superficial anatomy. The method used here is simple and can be applied in the clinical setting to ensure that equivalent Aluminium thicknesses calculated using the step wedge can be normalised for bone thickness and corrected for overlying soft tissue using the method described in Section 10.7.

10.9 SUMMARY

This chapter has discussed the image processing tools developed to analyse digital X-ray images and provide measurements of equivalent Aluminium thickness in fracture healing. A program to automatically identify the steps of the wedge in a digital X-ray was developed. A thorough investigation into step wedge calibration was conducted and the appropriate calibration graph was chosen to provide an accurate model of the step thickness to grey level relationship. Experiments showed that using a wedge with fewer or thicker steps resulted in a decrease in calibration accuracy. A simple model to correct for the heel effect was developed and analysis of Fuji automatic processing and dose to grey level conversion was performed. Image processing techniques to automatically measure and correct for scatter and soft tissue and bone thickness from orthogonal X-rays were designed. The use of these tools to monitor changes in digital X-ray images is discussed in the following chapters.

Chapter 11

Pre-Clinical Density Evaluation

11.1 INTRODUCTION

The physical apparatus and image processing tools necessary for the use of digital X-ray imaging with step wedge calibration were discussed in Chapters 9 and 10. Preliminary investigations were conducted to ascertain the effectiveness of these devices and processes and these are described in this chapter. The use of the step wedge to monitor decalcification changes in animal bones and a comparison between the step wedge technique and pQCT to distinguish the density of different substances are discussed.

11.2 MATERIALS AND METHODS

Three investigations were carried out to test the step wedge. The first two involved the ability of calibrated digital X-ray images to monitor changes caused by decalcification. Although decalcification is not the inverse process of bone healing, it does provide a simple and controllable method of obtaining similar bone specimens of different densities. In their study on feline femora, Shah *et al.* described the benefits of using Ethylene Diaminatetra Acetic Acid (EDTA) to control the decalcification of bones without altering the structural properties [100]. Verdenius and Alma performed a thorough investigation of decalcification techniques [135]. They stressed that test samples should be of a consistent shape, of equal area and of equal density. Their results indicated that an increase in temperature and diffusion rate (i.e. by moving the sample) significantly decreased decalcification time. The lack of a technique to monitor calcification changes in small animal studies or in small areas of interest has been discussed in Section 4.5. Previous authors have shown how the inclusion of an Aluminium step wedge in X-rays can be used to provide this information [103]. In the

first two tests described here, the principles reported in these papers are used on samples of sheep femora and rat tibiae which were decalcified and X-rayed at various stages of decalcification.Preparation and decalcification of the rat tibiae were performed independently by a medical student, Graeme Hopper, who was investigating the action of ultrasonic decalcification. Preparation and decalcification of the sheep femora were performed with a colleague, Erin Ross, who was investigating the ability of 3D ultrasound imaging to monitor decalcification.The measurements obtained by post-processing step wedge data were compared to micron-level CT and ash weight results for the same samples.

The third test was a comparison between Peripheral Quantitative Computed Tomography (pQCT) densities and step wedge equivalent thicknesses. To provide a wider range of density samples than the decalcification tests in order to further test the performance of the step wedge, it was decided to use rods of materials with different densities. These samples were unsuitable for ash weight determination but comparison with an established imaging method of determining mineral density was desirable. For this reason it was decided to compare the Aluminium-equivalent thicknesses attained from digital X-ray images with the density values obtained using pQCT. pQCT is performed on the appendicular skeleton, usually the forearm. It determines the volumetric BMD in g/cm^3 inside an ROI using a pre-determined calibration standard. Due to the poor correlation between appendicular BMD and osteoporosis, pQCT has been an under utilised tool for monitoring bone density in comparison to DEXA. However, it has been demonstrated that it provides an accurate and precise measure of true volumetric mineral density [136]. In this experiment seven different materials of varying densities were X-rayed with the wedge to determine Aluminium-equivalent thickness and imaged using pQCT to provide a reference reading of volumetric density for comparison.

11.2.1 Samples

In the first test, the samples consisted of ten extricated sheep femora from five sheep. These were stripped of all soft tissue. The central point of each femur was found and a 20 mm section marked on either side. The sections from each right femur formed a group of ten test bones and the sections from each left femur formed a group of ten control bones. In the second test, 40 rat tibiae (including fibulae) were harvested and cleaned of all soft tissues. Their dimensions were measured using digital calipers. They were divided into four groups with ten tibiae in each group.

For the pQCT comparison, seven different materials with different diameters suitable for use in pQCT were chosen, as shown in Table 11.1.

Table 11.1: Materials and dimensions scanned using pQCT.

Material	**Diameter [mm]**
Acrylic Rod	10
Nylon 66 Rod	20
Delrin Rod	10
Biomechanical Sawbones tibia	32
HydroxyApatite Cylinder	59
Dried Human Femur	25
PVC Rod	25

11.2.2 Decalcification

Following both the results and protocols of Shah *et al.* and Verdenius and Alma, all the sheep femoral samples were fixed in a 10% buffered formalin solution for 12 hours to preserve the tissues [100, 135]. The test bones were then placed in individual sample pots containing 20 times their volume of 14% EDTA solution. These were placed in a shaker bath at 37°C to speed up the decalcification process. The control bones were placed in similar containers with 20 times their volume of distilled water. The solutions of both control and test bones were changed every 24 hours to maintain chemical concentration for decalcification.

Decalcification of the rat tibiae was achieved using ultrasonic agitation (sonification). This method has been described previously by different research groups [137, 138]. The theory behind sonification is that it increases the rate at which decalcification using EDTA occurs. Each tibia was placed in ten times the bone volume of 10% EDTA solution and placed in a sonification bath (Pulsatron KC, Guyson International Ltd, UK) filled with water. One group was a control group undergoing no sonification. The remaining three groups underwent 7, 14 and 21 hours of sonification respectively at 25 - 80kHz (baseline frequency of 38kHz) and 50°C.

11.2.3 pQCT

In the third test, pQCT measurements of the different materials were made. After performing the routine calibration procedure, each material was securely placed in the XCT 2000 Bone Scanner (Stratec Medzintechnik GmbH, Germany), as shown in Figure 11.1. Each sample was securely placed within the active area of the scanner. For the rods, a slice at 100 mm length was taken and the ROI automatically calculated to get a density reading in mg/cm^3. For anatomically shaped specimens, the same procedure was followed in an area of uniform diameter on the shaft of the bone. Readings were repeated three times for all materials and means were taken.

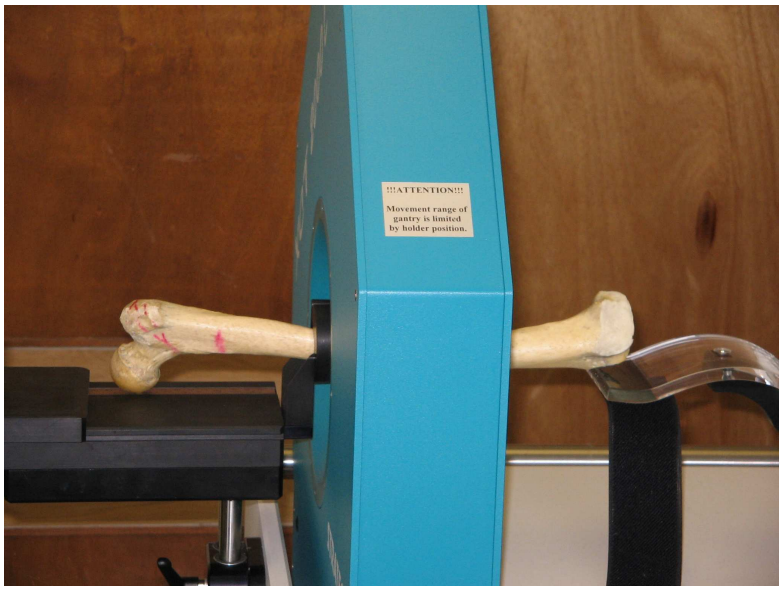

(a)

(b)

Figure 11.1: Images showing a) the human femur and b) Nylon rod in the pQCT scanner.

11.2.4 X-ray Protocol

All the sheep samples were X-rayed with the ten 5 mm step wedge at the beginning of the experiment and again when each sample was removed, which occurred at 24 – 72 hour intervals. The final bone was removed after 26 days of decalcification. The rat tibiae were X-rayed at the beginning and end of each sonification period with the ten 2 mm step wedge to aid calibration and look for small density changes. Both the tibiae and sheep samples were placed as close to the wedge as possible for each image.

The X-ray images of the animal samples and controls were taken using 60 kV and 2 mAs and the pQCT scanned materials were X-rayed at 63 kV and 2 mAs. All X-rays were taken using Fuji CR cassettes and processed on the 'Linearity' setting, as discussed in Section 10.5.1, with all automatic processing removed. The heel effect was analysed and the magnitude of the variation suggested that it was necessary to perform background correction based on using a fully exposed margin of each image, as described in Section 10.6.3. Automatic step detection and fitting of an exponential calibration graph were performed as described in Section 10.3.

For the decalcification tests, each bone sample was identified using thresholding. With this technique, a threshold level was selected through trial and error to produce a binary image with bone samples as white and the background as black. By identifying the location of white areas, the mean grey level of the pixels of each bone sample in the original X-ray image was calculated. The grey level calibration graph was used to provide an equivalent Aluminium thickness for each sample. All measurements of the sheep samples were related to the Aluminium-equivalent thickness of Control 1, the undecalcified control, to provide a percentage decalcification measure. For the rat tibiae, since the undecalcified group of bones was not X-rayed, mean values of the other groups before decalcification were used to provide '0 hours decalcification' X-ray measurements. The measurements were normalised for bone thickness using the measured dimensions of each bone. An overall mean for each group gave the final measurement of equivalent Aluminium thickness. The percentage decalcification for each bone was calculated using the undecalcified group as a reference.

For each pQCT sample material, three evenly sized ROIs were selected and the mean grey level of each was found. The mean of the three areas was calculated and used as the measurement of the grey level for that material. This was converted to an Aluminium-equivalent thickness measurement using the wedge calibration graph. Readings were also normalised for diameter to provide diameter independent measurements.

11.2.5 Comparative Measurements

As a reference comparison in the decalcification tests, the ash weight of the decalcified femoral and tibial samples was used. The procedure was based on modified methods from Li and Aspden [139, 140]. Each sample was weighed, volume measured and placed in a crucible. The samples were then dehydrated at 105°C for 48 hours and ashed in a furnace at 600°C for 24 hours. The remaining content was weighed to give the ash weight which is a measure of the mineral content. For the sheep femora, the ash weight of each test bone and two controls was found. The ash weight of each sample was related to the ash weight of Control 1 to give a measure of percentage decalcification that could be compared to X-ray and micron-level CT results. For the rat tibiae, five samples from each group were chosen randomly to be ash weighted. The percentage decalcification of each bone was calculated using the undecalcified bones as a reference.

In order to provide a comparison with a well regarded method for assessing bone mineral density in the femoral test, each sample was also imaged using a micron-level CT scanner (iCAT 125micron Cone Beam Scanner) after decalcification. Each sample provided 600 transverse slices. These were analysed using a thresholding technique which identified the area of the cross-sectional slice as well as the area of the calcified portion of cortical bone. The size of the IM canal was measured and subtracted to give the area of cortical bone. The area of the calcified section was calculated as a percentage of the entire area of bone to give a measurement of percentage calcification. This was then normalised to the percentage calcification of Control 1 to provide a measure of percentage decalcification that could be compared to X-ray and ash weight measurements.

11.3 RESULTS

11.3.1 Decalcification of Sheep Femora

A maximum decalcification of 64% measured by ash weight was achieved. The ash weight was used as the reference measure of the mineral content of the samples. This was compared to the micron-level CT measuring system. Both systems were compared to measures obtained using the digital X-ray images, with and without Aluminium step wedge calibration and with and without background heel correction. The measurements from X-ray using grey level, non heel corrected Aluminium-equivalent thickness and heel corrected Aluminium-equivalent thickness, as well as the micron-level CT results, were correlated with the ash weight results. The coefficient of determination (R^2) of a straight line modelling the result of plotting ash weight on the x-axis and the comparative measure on the y-axis was used as

a measure of the correlation coefficient, i.e a measure of the consistency of the relationship between the two methods. The results are given in Table 11.2 and Figure 11.2.

Table 11.2: Correlation between X-ray, micron-level CT and ash weight measures.

Method	**Correlation Coefficient R^2**
Micron-level CT	0.67
Grey level	0.77
Non heel corrected Aluminium-equivalent thickness	0.77
Heel corrected Aluminium-equivalent thickness	0.86

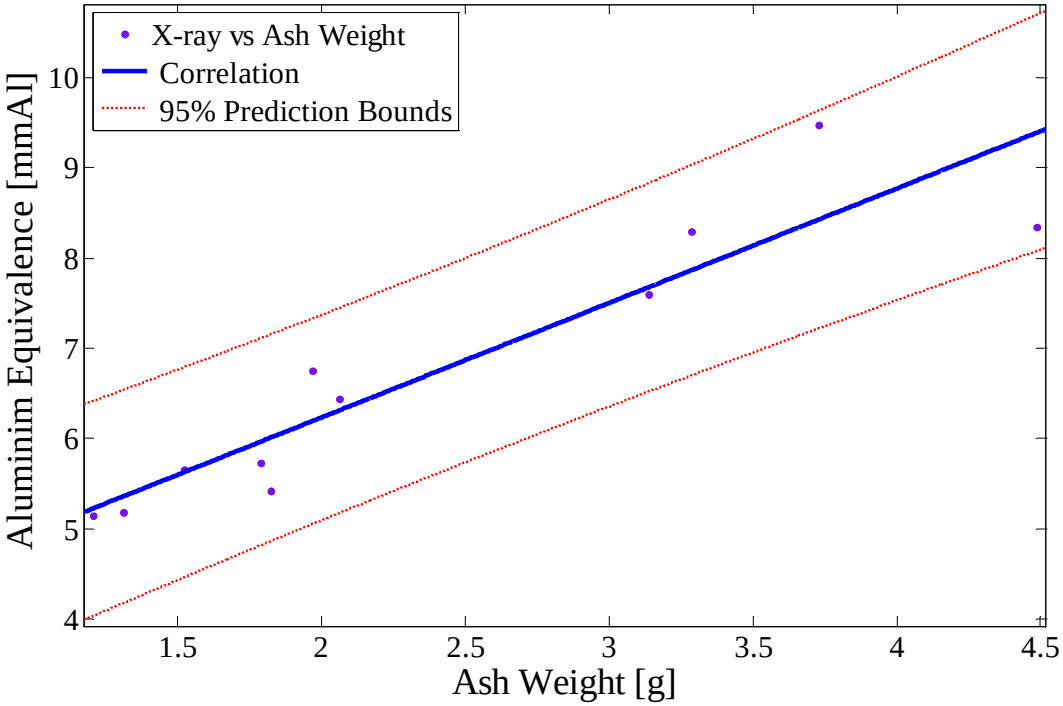

Figure 11.2: Correlation between ash weight and heel corrected X-ray Aluminium thickness where $R^2 = 0.86$.

The results show a good correlation between ash weight and heel corrected equivalent Aluminium thickness ($R^2 = 0.86$). This is an improvement on the correlation of micron-level CT with ash weight ($R^2 = 0.67$). Analyses show the correlation between X-ray grey level not calibrated using the step wedge and ash weight to be much lower ($R^2 = 0.77$) than that with the calibrated X-ray images. This is a similar result to that obtained if the heel effect correction is not used ($R^2 = 0.77$).

Ash weight, X-ray analysis and micron-level CT all provide measures of decalcification in different units. In order to compare the agreement of all three measurement techniques, the results were obtained as a percentage of the non-decalcified control sample. The resulting graph is shown in Figure 11.3.

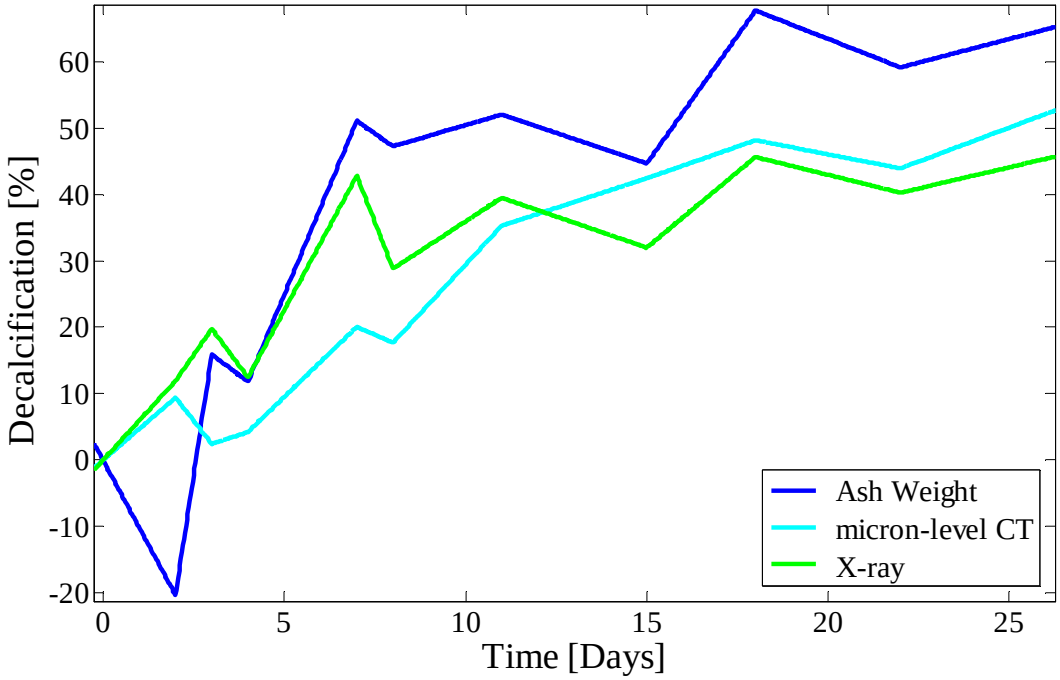

Figure 11.3: X-ray (green), micron-level CT (cyan) and ash weight (blue) measurements of percentage decalcification over time.

Although X-ray gives readings between 5% and 15% lower than ash weight for up to 50% decalcification, it follows an almost identical trend in measuring changes in calcium content. Micron-level CT also gives readings that are consistently lower than ash weight yet the relationship between the changes in decalcification is not as consistent. An uncharacteristic change in the calculated ash weight occurs for the day two sample. This could be due to incorrect sample weighing resulting in an incorrect ash weight value.

Statistical methods were employed to assess the agreement between heel corrected Aluminium-equivalent thickness measured on X-ray and ash weight density, both expressed as percentage decalcification relative to the non-decalcified sample [141]. The mean of the differences between measurements, the SD of the differences and the 95% limits of agreement were determined. The mean difference between X-ray and ash weight was found to be 6.8 $\pm$ 30%, although when the day two outlier was excluded, the limits of agreement improved to 10.8 $\pm$ 18%. The results for the full data set are shown in Figure 11.4.

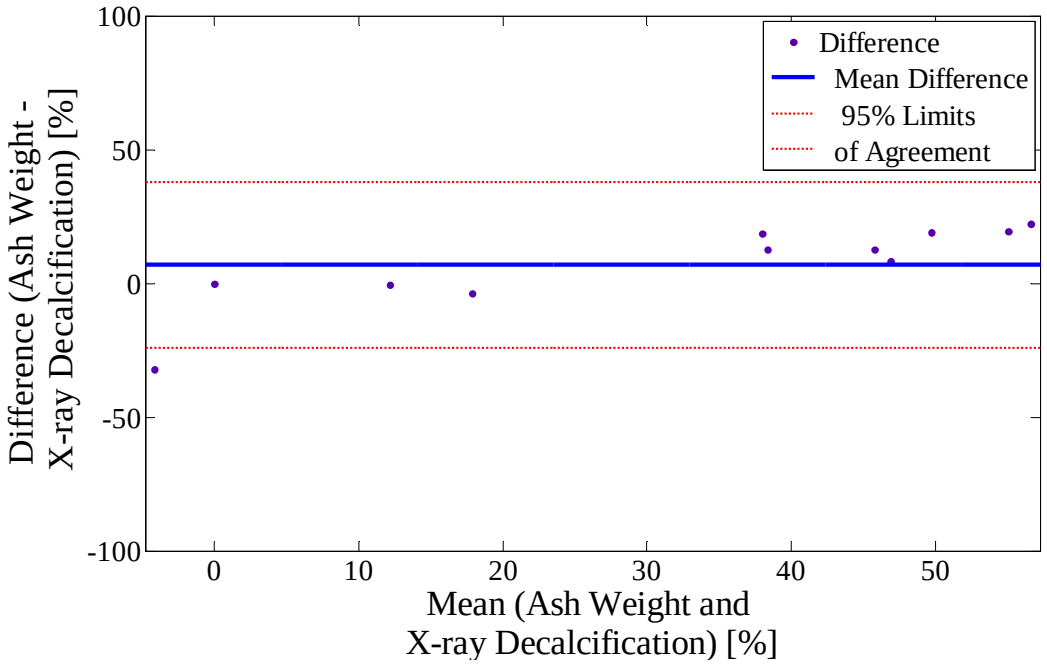

Figure 11.4: Bland Altman plot comparing agreement between ash weight and X-ray derived % decalcification. The mean difference and upper and lower 95% limits of agreement are also shown.

11.3.2 Decalcification of Rat Tibiae

According to ash weight measurement, a maximum decalcification of 80% was achieved in 21 hours. The results obtained using X-ray analysis, calibrated and uncalibrated and with and without heel effect correction were correlated with the ash weight measurements. The results are given in Table 11.3.

Table 11.3: Correlation of X-ray measurements with ash weight.

Method	**Correlation Coefficient R^2**
X-ray grey level	0.07
Non heel corrected Aluminium-equivalent thickness	0.98
Heel corrected Aluminium-equivalent thickness	0.98
Normalised Aluminium-equivalent thickness	0.99

Comparison of correlation results shows that using grey level alone results in a very low correlation ($R^2 = 0.07$). Calibrating using the step wedge results in a much improved correlation with ash weight ($R^2 = 0.98$ with and without heel correction). An excellent correlation is achieved between ash weight and Aluminium-equivalent thickness normalised for bone thickness ($R^2 = 0.99$), as shown in Figure 11.5.

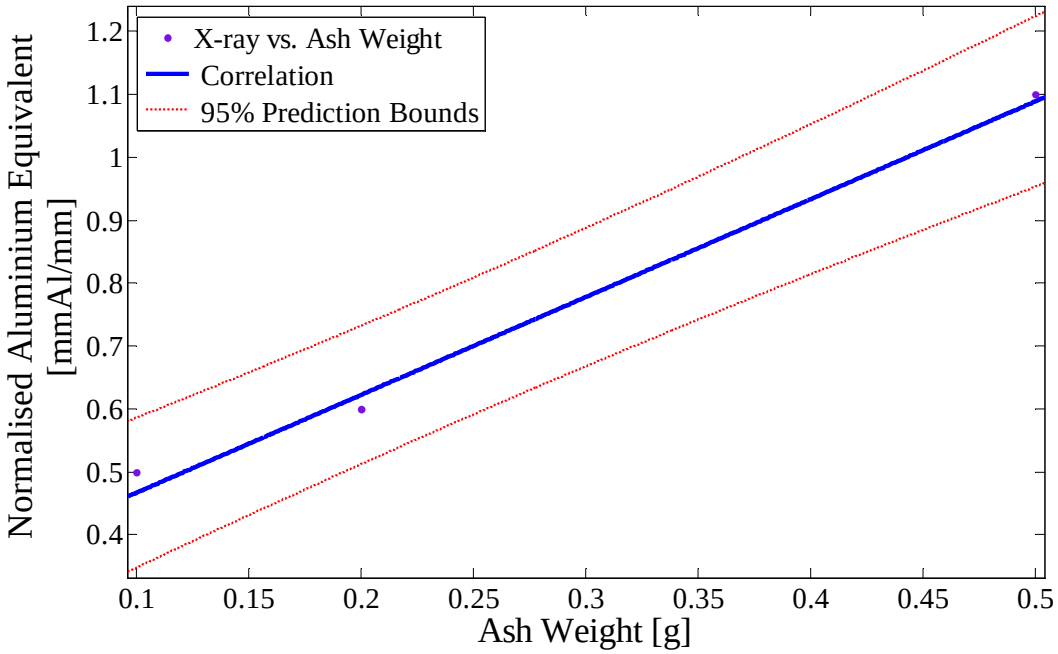

Figure 11.5: Graph showing the correlation between ash weight and normalised Aluminium-equivalent thickness.

Assessing decalcification using the different techniques resulted in measurements in different units. In order to compare the different techniques, all measurements were calculated as a percentage decalcification, with the undecalcified bone group representing zero decalcification. The results are shown in Figure 11.6. The graph shows how X-ray grey level alone is a poor measure of bone mineral content and has no similarity with the measurement provided by ash weight. Non heel corrected Aluminium-equivalent thickness is a slight improvement on this. However, the graph illustrates that normalised Aluminium-equivalent thickness follows the trend of the ash weight measurements very closely, although it gives readings of approximately 20% lower in value.

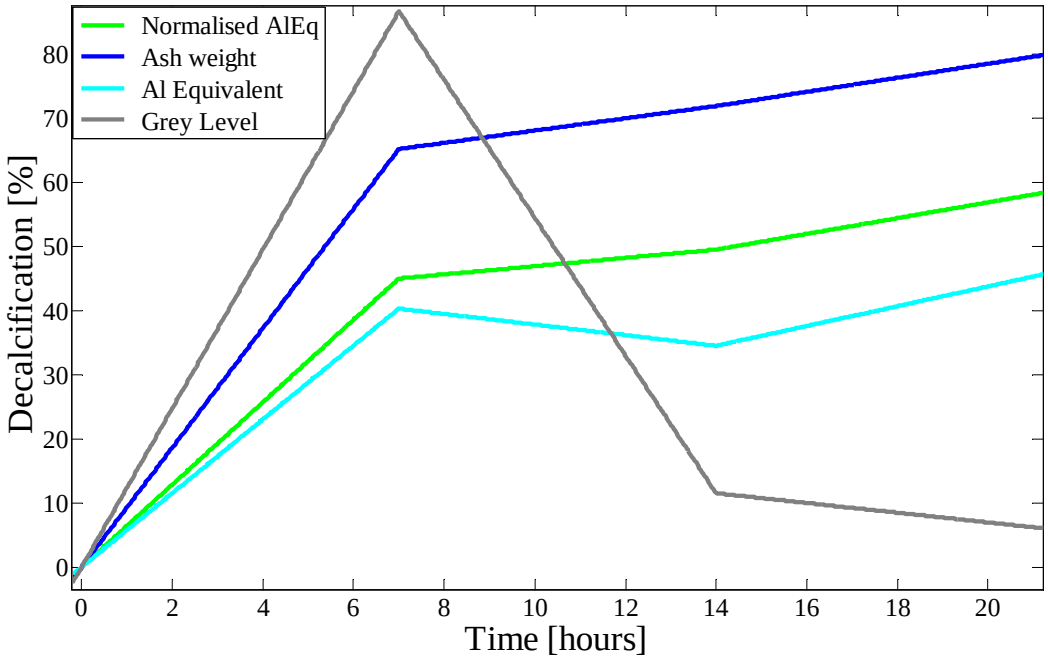

Figure 11.6: Agreement between ash weight, normalised Aluminium-equivalent thickness, non heel corrected Aluminium-equivalent thickness and grey level measurement of percentage decalcification.

Statistical methods were employed to assess the agreement between normalised Aluminium-equivalent thickness and ash weight densities, both expressed as percentage decalcification relative to the non-decalcified group. The mean of the differences between measurements, the SD of the differences and the 95% limits of agreement were determined. The mean difference between normalised Aluminium-equivalent thickness and ash weight was found to be $10.7 \pm 24\%$. The results are shown in Figure 11.7.

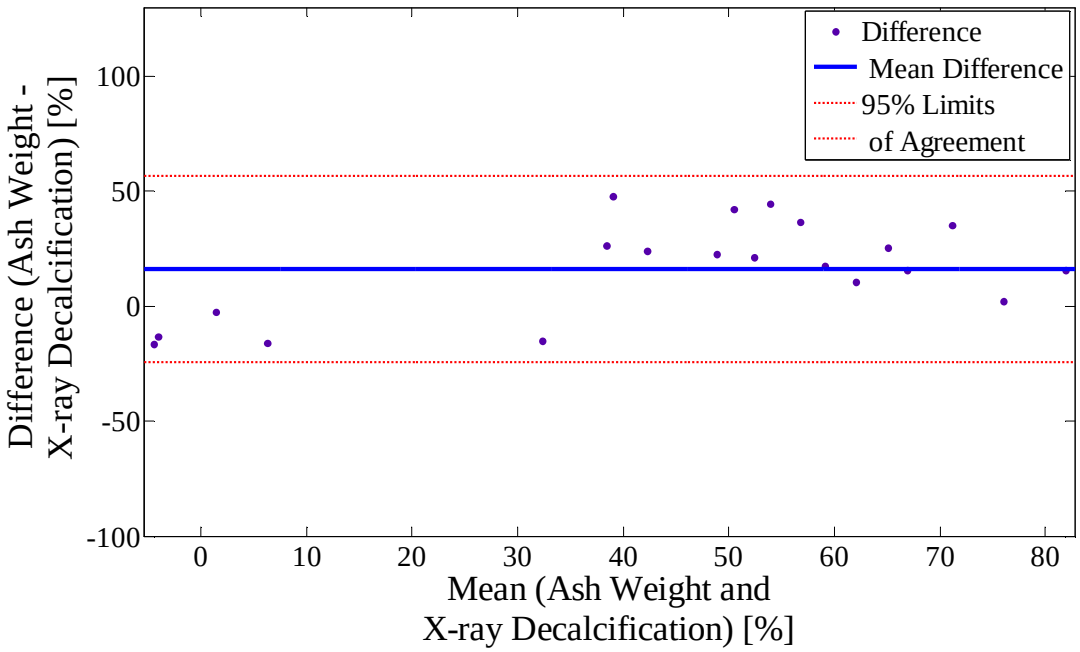

Figure 11.7: Bland Altman plot comparing agreement between ash weight and X-ray derived % decalcification. Also shown are mean and upper and lower 95% limits of agreement.

11.3.3 pQCT of Materials

pQCT was used as the reference measurement of material density. The results obtained using X-ray analysis, calibrated and uncalibrated and with and without normalisation for diameter were correlated with the pQCT measurements. The results are given in Table 11.4. The results show that the X-ray measurement technique, normalised for diameter, has an excellent correlation with pQCT measurements ($R^2 = 0.97$). Correlation with pQCT is reduced when material diameter is not taken into account or when the X-ray grey levels are not calibrated using the step wedge. Correlation graphs showing this are in Figure 11.8.

Table 11.4: Correlation of X-ray Aluminium-equivalent thickness with pQCT.

Measurement	**Correlation Coefficient R^2**
Aluminium-equivalent thickness	0.61
Grey level	0.64
Normalised Aluminium-equivalent thickness	0.97

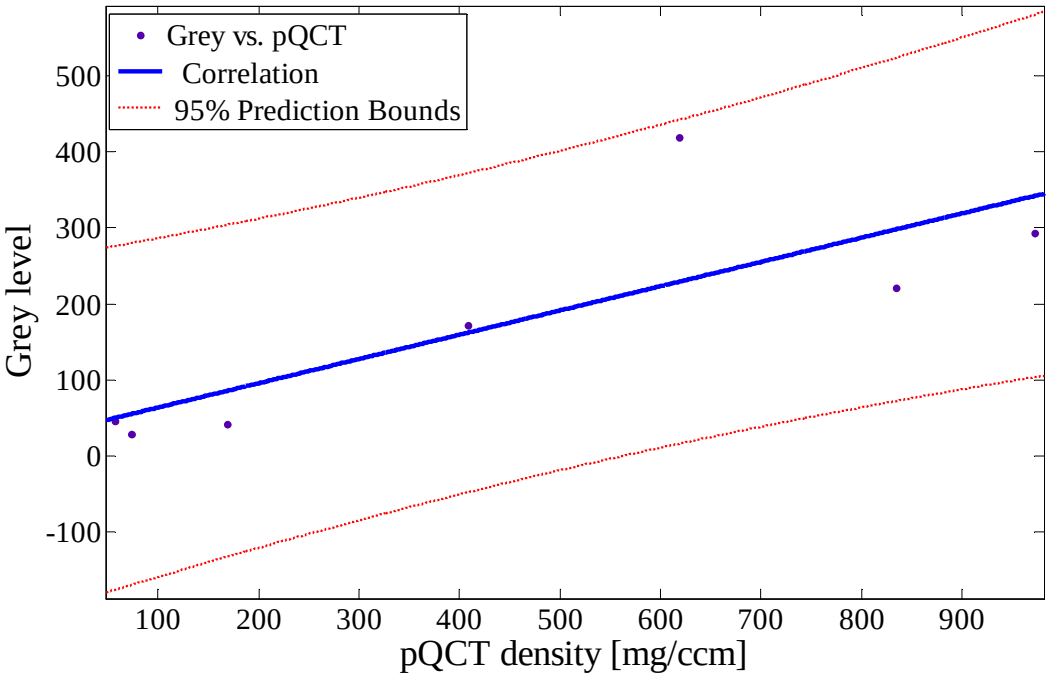

(a)

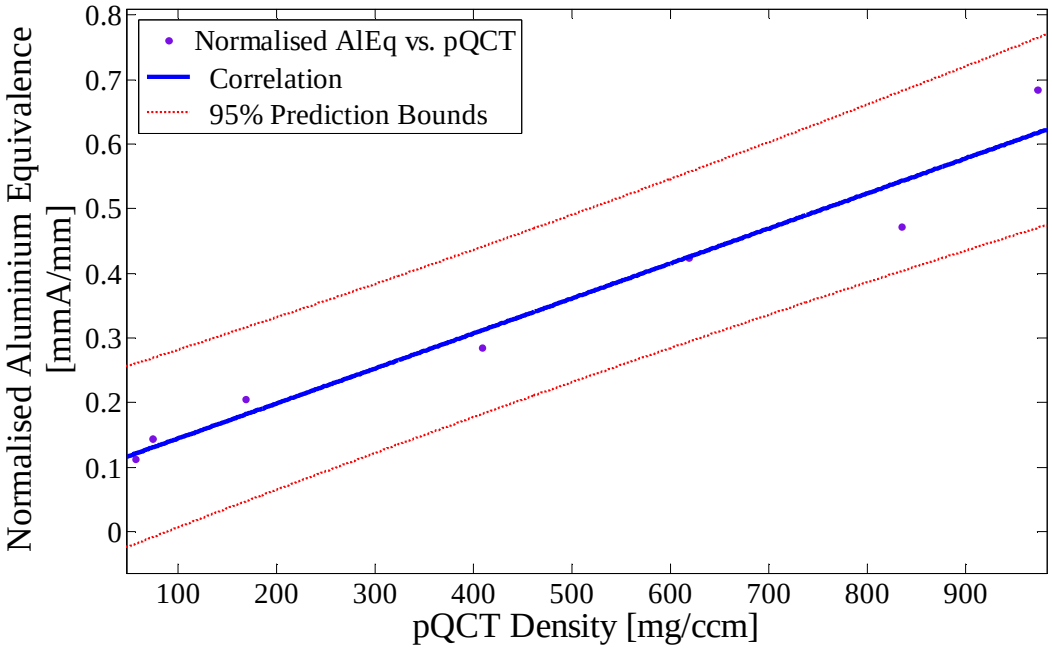

(b)

Figure 11.8: Correlation with ash weight showing 95% prediction bounds for a) grey level and b) normalised Aluminium-equivalent thickness.

The X-ray step wedge system provides measurements in mmAl/mm and the pQCT system provides measurements in mg/cm^3. In order to compare these two methods directly, all readings were obtained as a percentage of the PVC measurement, as this had the highest density. The results are shown Figure 11.9.

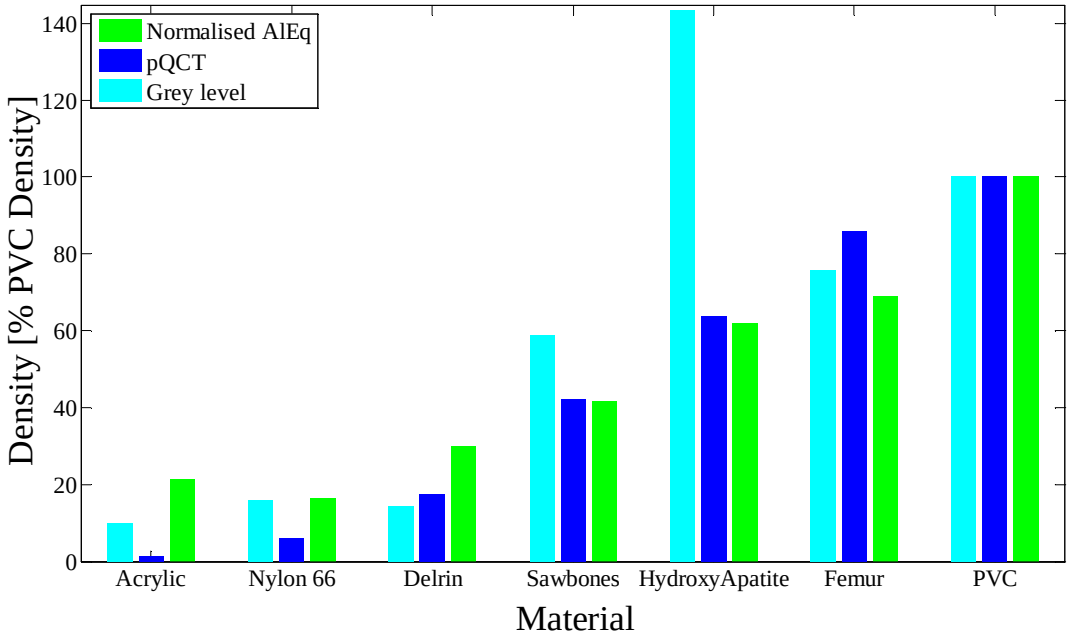

Figure 11.9: Bar graph showing a comparison of the density as calculated by grey level, normalised Aluminium-equivalent thickness and pQCT.

The graph shows that pQCT and normalised Aluminium-equivalent thickness provide fairly similar measurements, with a minimum difference of 0.3% occurring for Sawbones and a maximum difference of 20% occurring for Acrylic. The graph also illustrates the unreliability of using X-ray grey level alone, with a maximum difference of 80% occurring for HydroxyApatite.

Statistical methods were employed to assess the agreement between measurements made using normalised Aluminium-equivalent thickness from X-ray and pQCT, both expressed as percentage of the PVC measurement. The mean of the differences between measurements, the SD of the differences and the 95% limits of agreement were determined. The mean difference between normalised Aluminium-equivalent thickness and ash weight was found to be $2.6 \pm 21\%$. The results are shown in Figure 11.10.

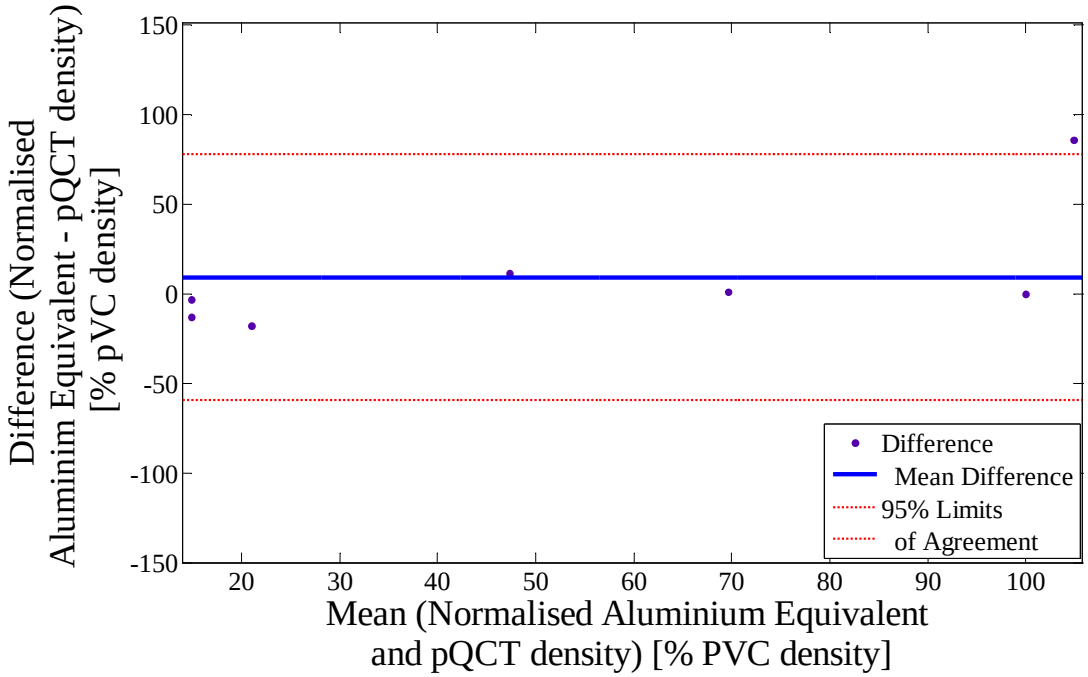

Figure 11.10: Bland Altman plot comparing agreement between X-ray normalised Aluminium-equivalent thickness and pQCT, indicating mean and upper and lower 95% limits of agreement.

11.4 DISCUSSION

Previous comparisons between X-ray derived Aluminium-equivalent thickness and a reference density technique are not well documented in the literature. To be able to use Aluminium-equivalent thickness in a similar way to, or in place of, density measurement techniques currently in clinical use, it is necessary to know the correlation and agreement between methods. Despite this, most previous investigators were prepared to use Aluminium-equivalent thickness alone as a comparative measurement between samples. In an early investigation, Rowland attempted to relate the Aluminium-equivalent thickness to the mass per unit area of calcium as an expression of bone mineral content [107]. He used his technique successfully to estimate mineral percentage in a variety of animal samples. However, he employed no reference technique to verify his results, although he stated that they related well to ash weights obtained by previous investigators on similar samples. A comparison between Aluminium-equivalent thickness and DEXA derived BMC was performed by Nackaerts *et al.* in dental radiographs [110]. They found a correlation of 0.89 between the two measures and that this reduced to just 0.65 when grey level was used with-

out calibration. They also found that 80% of the variation in calcium content as measured by DEXA could be explained by the calibrated step wedge measurements.

11.4.1 Decalcification

In the first two investigations, decalcification was used as a technique to produce samples of a variety of bone mineral contents that could be analysed using digital X-rays. In the study of Shah *et al.*, it took 12.5 days to reach 100% decalcification of their 6 cm feline samples [100]. In this study, in the same conditions using sections of sheep femora of a third that length, only 64% decalcification had been reached in more than twice this time. Verdenius and Alma noted that as decalcification progresses it slows down since the size of the reaction surface decreases [135]. However, the reason for only reaching partial decalcification in this study was unclear. Reaching full decalcification would have allowed a wider variety of densities to be analysed using X-ray. A possible explanation is that leaving the central bone marrow portion in the bone may have reduced the flow of EDTA into the bone surface thus reducing the surface area available for chemical decalcification. In the decalcification of rat tibiae using sonification, a better value of 80% was achieved, indicating the effectiveness of ultrasonic agitation to increase the chemical decalcification reaction with movement and heat.

In both groups, correlation results between Aluminium-equivalent thickness and ash weight were good which illustrated the possibility of using this method as a simple way to track density changes in bone samples. When X-ray measurements were corrected for background heel effect, calibrated using a step wedge and normalised for bone thickness they resulted in information which could be compared to the reference ash weight measurements. As in the study of Nackaerts *et al.*, the results also illustrated that the use of grey level alone to provide an indication of mineral content was an unreliable method with a much reduced correlation with ash weight. Furthermore, results from the scanned sheep femora indicated that calibrated X-ray results were better correlated with ash weight than the micron-level CT results.

Investigation into the comparability between ash weight and the X-ray measurements yielded interesting results. Plotting the trend of decalcification over time with the different measurement techniques showed that calibrated X-ray measurements tracked the loss of mineral content well. However, there was a consistent 'offset' whereby the X-ray measurements were 10% - 20% lower than ash weight. Nackaerts *et al.* [110] also found a 20% difference between measurements made with a step wedge and those made with DEXA. In this study, this difference might be due to the fact that X-ray takes into account the non-mineral constituents of bone when assessing density whereas ash weight is purely

a measure of the mineral content. Thus a constant over evaluation of bone density, and hence under evaluation of percentage decalcification, results when using X-ray analysis. This reasoning appears to be confirmed by the fact that the percentage difference between X-ray analysis and ash weight analysis increased as the bone mineral density decreased. This is because the non-mineral constituents contributed a larger proportion to the X-ray calculated density. Another important feature was also visible on these graphs when plotting X-ray grey level, as opposed to carefully calibrated X-ray measures. Decalcification appeared to occur almost randomly over time which was in contrast to both the expected results and those measured using ash weight. This further illustrated the unreliability of using X-ray grey level alone as a measure of mineral content, even in digital X-ray images.

The assessment of the agreement between ash weight and X-ray measurement was performed using a Bland Altman analysis. The results confirmed what was seen in the plots of decalcification over time, i.e that although the methods agree fairly well, there was an offset between them. In both the rat and sheep experiments, the agreement was found to be approximately $10 \pm 20\%$. As explained previously, this offset between the two techniques might be due to the measurement of non-mineral content in X-ray images. However, the results still illustrated the feasibility of using calibrated digital X-ray measurements to monitor mineral changes.

11.4.2 pQCT

This investigation provided interesting results on the ability of calibrated X-ray image analysis to provide comparable results to an existing validated image-based method of measuring density, i.e. pQCT. The results relating pQCT measurements with X-ray measurements corrected for object thickness showed an excellent correlation of 0.97. Furthermore, results comparing uncalibrated grey level measurements and Aluminium measurements not corrected for material diameter showed that the correlation was reduced by 30%. This provided a clear indication that, firstly, X-ray grey levels alone, even on digital X-ray images, do not provide sufficient information on material density. Secondly, these results show that not taking the thickness of an object into account can have detrimental effects on measurements, even those calibrated with a step wedge, especially when the objects being measured have widely varying diameters. Both these results can be translated into the clinical situation and point to the need for a standard calibration tool to enhance the information from digital X-ray images, as well as the need to take anatomy into account when analysing measurements.

The results from each measurement technique were expressed as a percentage of the highest density material (PVC) for comparison. A bar graph comparing the results showed that normalised Aluminium-equivalent thickness and pQCT have comparable results for each material, and when compared to grey level, reinforced the need for calibration and diameter correction. However, a discrepancy of up to 20% between calibrated X-ray and pQCT results still occurred. It is noted that the discrepancies occurred for the thinner rods and femur, and not the thick HydroxyApatite and biomechanical Sawbones. Therefore, some discrepancy might have been due to the ROI measurement on the X-ray images, since the beam was not passing through a uniform area of thickness in each material (due to its curved profile), an ROI measurement which took into account anything except the very centre of the object could have introduced an error. Since the measurements were made manually and not with a computer routine, this was a difficult aspect to control. However, despite these issues, the results were still encouraging. More precise comparisons between the X-ray technique and other imaging techniques using a wider variety of densities and multiple measurements is necessary to validate whether X-ray measurements using a step wedge can ever be directly comparable to density measurements using other imaging techniques.

The Bland Altman comparison of the agreement between pQCT and normalised Aluminium-equivalent thickness showed that a good agreement (i.e. $2.6 \pm 20\%$) was achieved, although the limits of agreement were too high to say that X-ray measurements can be used in place of pQCT measurements without further investigation into the relationship between the two measures. From the correlation results it is more reliable to say that the X-ray technique is useful in providing comparative measurements rather than quantitative values for density.

All three investigations showed that the results of comparing the assessment of bone mineral content using X-ray versus ash weight and pQCT were encouraging and good correlation was observed. This indicates that step wedge based X-ray measurements can be used as reliably as validated density measurements to compare changes in the same sample or patient. However, agreement results indicate that Aluminium-equivalent thickness cannot be used as a replacement for either ash weight or pQCT density measures and that further validation tests are needed to investigate the relationship between Aluminium-equivalent thickness and a validated measurement of density. Rather, the results show that X-ray should be used as a tool to monitor changes in decalcification or mineralisation.

11.5 SUMMARY

This chapter described three different investigations performed to ascertain the efficacy of the step wedge in aiding the monitoring of fracture healing. The apparatus and X-ray analysis techniques described in Chapters 9 and 10 were applied to models representing different physical densities. Animal models decalcified using EDTA were used to compare X-ray derived Aluminium-equivalent thickness from the step wedge calibration technique with the density achieved using ash weight. Results showed a good correlation with ash weight, although agreement tended to have a 10% – 20% offset, possibly due to the X-ray technique measuring both mineral and non-mineral constituents of the bones. In the comparison between various materials measured using X-ray Aluminium calibration compared to pQCT, results were also encouraging. Again, a good correlation between the two methods was found, although there was some discrepancy between the quantitative values of each. These three studies using the step wedge in digital X-rays, indicated its potential to monitor changes in density, if not to provide quantitative density measurements that are comparable with existing standards.

Chapter 12

Calibration to Monitor Fracture Healing

12.1 INTRODUCTION

This chapter presents results of the step wedge calibration of radial fracture X-ray images used to provide Aluminium-equivalent thickness information. Investigations into the step wedge as described in Chapters 10 and 11 have shown that, with thorough application of correction techniques, the calibration graph of Aluminium step thickness to grey level could be used to provide a measurement of Aluminium-equivalent thickness and was useful in tracking changes in this measurement over time. In order to test whether these concepts extended to the clinical situation, where the X-ray environment was less controllable and different patient factors could complicate the analysis, it was decided to test the use of the wedge on a series of fracture patients throughout the course of their healing.

12.2 MATERIALS AND METHODS

12.2.1 Patients

The patient group selected for this study was radial fracture patients which was chosen due to the high prevalence of these fractures seen in the RIE, as well as the fact that most of these are treated conservatively. Patients were selected over a period of six months. A total of 20 patients were identified for participation in the study. However, due to missed appointments and X-rays, incorrect X-ray procedure and subsequent surgical treatment, only four female patients, aged 67 – 89 years (median 82.5 years) were followed until the end of their treatment. Table 12.1 shows the details of the patients.

Table 12.1: Details of patients included in the radial fracture study.

Number	First Follow -Up (Days after Fracture)	Second Follow-Up (Days after Fracture)
8	15	43
9	9	37
10	15	43
11	18	46

12.2.2 X-ray Procedure

Permission to include the wedge in patient X-rays was obtained from the Lothian Research Board (See Appendix F). Due to the screening process, the first X-ray of patients in which the wedge was included was on their third visit to the hospital, i.e. after their initial Accident and Emergency visit and first fracture clinic follow-up. The wedge was included in as many subsequent X-rays as was possible until the end of their healing, which was judged to be at eight weeks. Wedge placement was as close to the fracture site as possible, directly on the X-ray bed, although occasionally the wedge was erroneously placed on padding by the radiography nurses. All X-rays were taken on Fuji CR cassettes and processed on the 'Linearity' setting.

12.2.3 X-ray Analysis

Two methods of analysing the radial fractures were attempted and compared. In the first method, an ROI including the fracture was measured. The first process in this method was registration of the images. For each patient's images, anatomical landmarks were chosen to provide registration for the AP and lateral images taken at different times. In the AP view the landmarks were the medial and lateral ends of the distal end of the radius. In the lateral view the landmarks were the anterior and posterior tips of the distal end of the radius, as shown in Figure 12.1. Landmarks were marked in all the AP and lateral images. An ROI was then defined in the first AP X-ray and, using the positions of the anatomical landmarks, the same ROI was marked in all subsequent images. An example of two corresponding AP ROIs is shown in Figure 12.2.

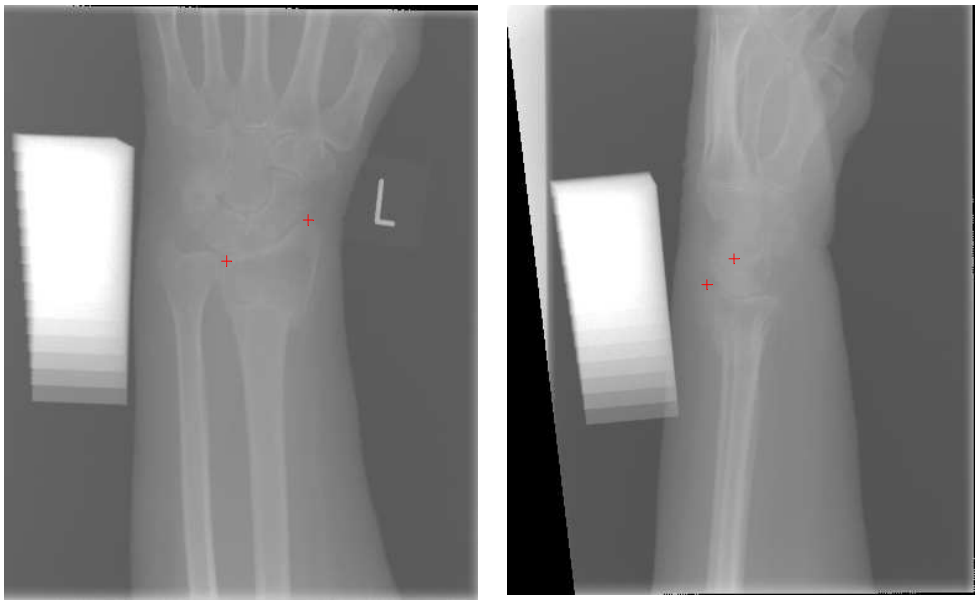

(a) (b)

Figure 12.1: X-rays showing the anatomical landmarks used for image registration in a) the AP and b) the lateral X-rays.

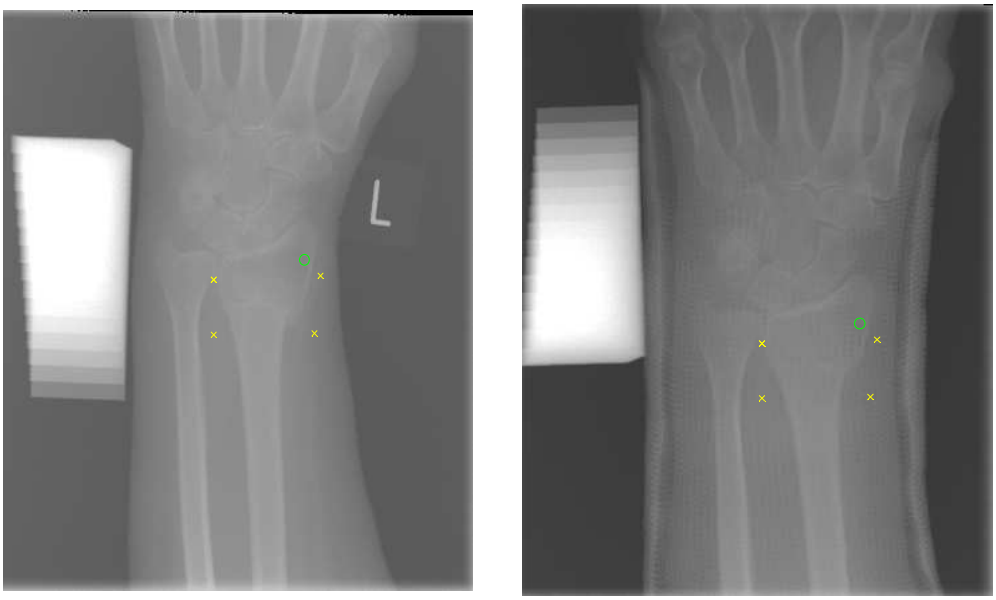

(a) (b)

Figure 12.2: X-rays showing the ROI in the same patient marked in a) the first and b) the second AP X-ray, taken 28 days later.

Using these ROIs, the soft tissue and bone thickness for each region were found using the procedure described in Section 10.8. The average grey level in each ROI was calculated using a thresholding method which selected only the bony areas. This was converted to dose and corrected for overlying soft tissue and scatter as described in Section 10.7. After some experimentation, it was found that the best method to correct for varying imaging settings and overlying cast materials was by measuring the step grey level and a region of soft tissue between the radius and ulna that was affected by the same overlying cast effects as the bone ROI. Differences in the step doses in each image were corrected for and the dose of the soft tissue region was used to correct the ROI for overlying cast material. The final, corrected dose was converted to a grey level and an equivalent Aluminium measurement using the corrected calibration graph. This was then normalised for bone thickness obtained from the lateral X-ray.

The second method analysed the fracture using an image profile line manually drawn across the fracture site. The first part of the analysis, involving anatomical landmark selection, was performed as above. A profile line across the fracture site was then drawn in the first AP image and from the anatomical landmark information, copied to all subsequent images. Two methods of obtaining the Aluminium-equivalent thickness within the fracture were attempted. The first was calculating the mean density of the single profile line and the second was obtaining the mean Aluminium-equivalent thickness of a group of 50 profile lines on either side of the central fracture. It was found that the narrow width of a single profile line did not adequately take into account the entire fracture, so the group of 50 profile lines was chosen. Figure 12.3 illustrates the profile lines in X-ray images. The mean grey level of the 50 profile lines was calculated and corrected for scatter, soft tissue and overlying materials as in the first method and was also normalised for bone thickness.

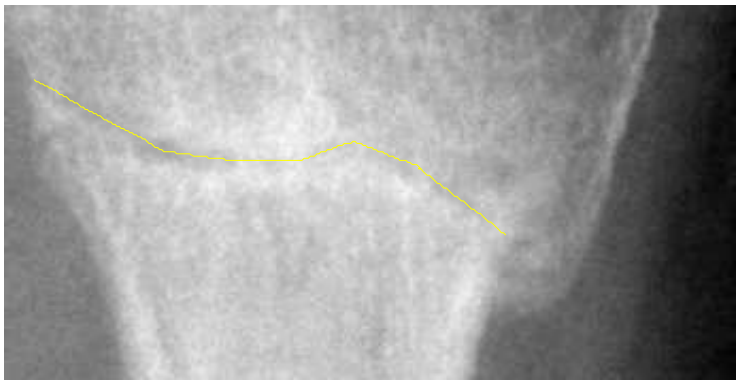

(a)

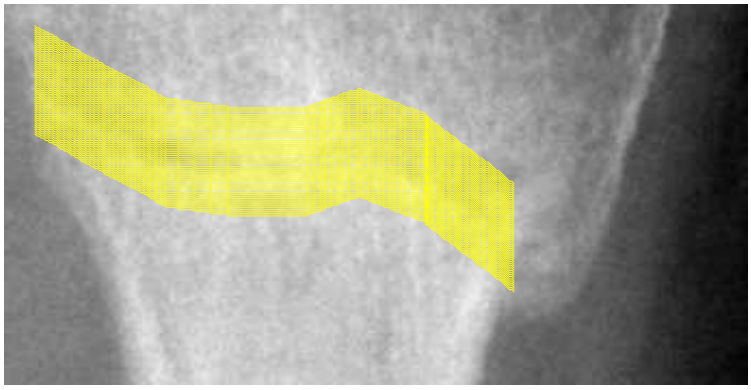

(b)

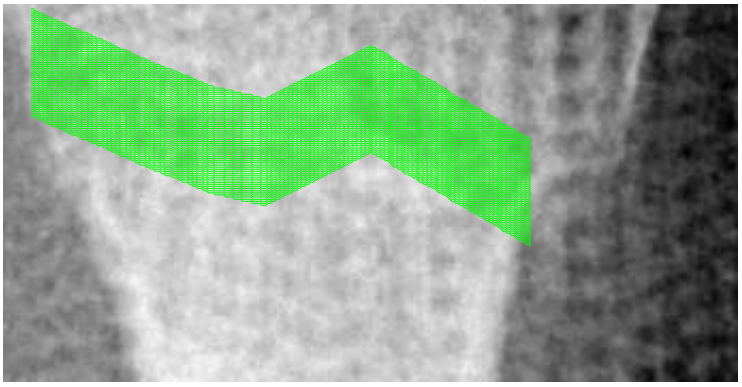

(c)

Figure 12.3: a) A single profile line in the fracture gap, b) a set of 50 profile lines on the first AP image and c) corresponding set of 50 profile lines in the second AP image, taken 28 days later.

12.3 RESULTS

The analyses were performed for each set of patient images and the results are given in Table 12.2. The results showed that the first method gave smaller changes in Aluminium-equivalent thickness during the course of fracture healing than the second method. However, the second method illustrated a decrease in Aluminium-equivalent thickness in the second follow-up image of patient 8. Both methods recorded only small increases in Aluminium-equivalent thickness during healing. The changes in Aluminium-equivalent thickness between early and late healing measured using the second method are shown in Figure 12.4 below.

Table 12.2: Measurements showing the differences between the first and second follow-up X-rays measured as normalised Aluminium-equivalent thickness using both methods.

Patient ID	**Change in Normalised AlEq [mmAl/mm]**	
	Method 1 ROI	**Method 2 Profile Lines**
8	0.00	-0.20
9	0.07	0.11
10	0.01	0.03
11	0.01	0.01

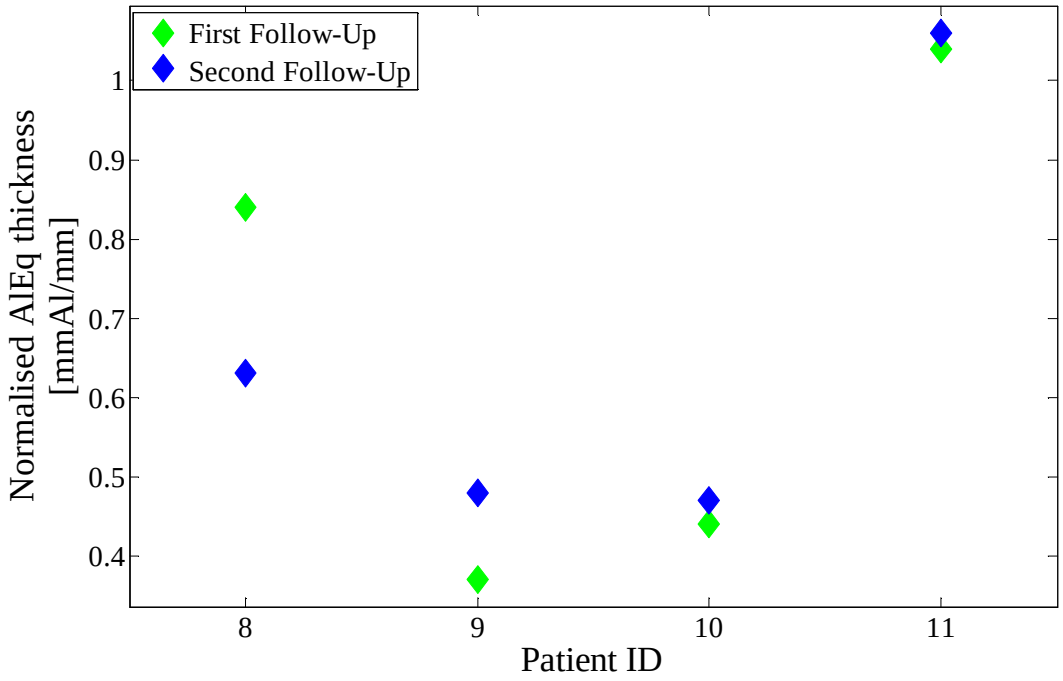

Figure 12.4: Changes in normalised Aluminium-equivalent thickness between the first and second X-rays for the second analysis method.

12.4 DISCUSSION

This pilot study on radial fractures aimed to show whether a step wedge was useful in allowing comparisons of Aluminium thickness to be made within a fracture site using digital X-rays. Two different methods of analysing the X-rays were used. The first method found the equivalent Aluminium thickness of a user selected ROI in each X-ray image. The same ROI was chosen in subsequent images with the use of anatomical landmark registration. This method worked in that it illustrated a small increase over the course of fracture healing. However, this method took into account a large area surrounding the fracture. It is therefore likely that measurements of increased Aluminium-equivalent thickness at the fracture site were offset by measurements of decreased Aluminium-equivalent thickness in surrounding areas due to disuse osteoporosis. This resulted in a reduced indication of healing at the fracture site which would be improved by using a smaller ROI selection. However, there might be potential to extend this ROI method to other areas such as the monitoring of osteoporosis.

The second method used a smaller, more focused set of profile lines around the fracture site to obtain a mean Aluminium-equivalent thickness of the fracture line and surrounding healing areas. The results showed that this provided larger measurements of the healing differences between early and late follow-ups and it was considered that this was due to the fact that it primarily measured increased bone density in and around the fracture gap whilst omitting surrounding areas that may have undergone osteoporotic changes. However, the measured changes were still small.

Comparison of the normalised measurements between the patients showed very different densities in both early and late X-rays. It was unclear whether this was due to the fact that the patients really had widely varying bone densities, or whether some anomalies were added due to the use of different X-ray equipment and wedge positioning. Unfortunately a direct density comparison with a technique like DEXA was not possible with these patients, but further investigation into the relationship between step wedge derived density measurements and those from previously validated sources in patients would be useful.

12.5 SUMMARY

This chapter described a pilot study of the use of the Aluminium step wedge in patient X-rays. The wedge was included in early and late X-rays of four radial fracture patients and used to provide Aluminium thickness information during healing. The results from this study and the previous chapters are used to draw conclusions and make recommendations in the following section.

Part IV

Conclusions and Recommendations

Chapter 13

Conclusions

In this chapter the results from the apparatus design, image processing development and pre-clinical and clinical studies are used to draw conclusions pertaining to the hypothesis of this thesis that *"Image processing of digital X-ray images can be optimised to aid the management of fracture patients."* These conclusions are grouped according to the research questions posed about the two main aspects of the thesis: monitoring fracture stiffness and monitoring fracture density using digital X-ray images.

13.1 FEASIBILITY OF MONITORING STIFFNESS

In this section, the results are used to form conclusions about mechanical stiffness measurement based on the secondary research questions and to answer the major research question for this section, "*Can the stiffness of a fracture be monitored using analysis of digital X-rays of loaded and unloaded fractures?"*

13.1.1 Applied Load During X-ray

In Chapter 5 a discussion of the design of the apparatus to apply load during X-ray was given. A frame to apply four point bending to IM nailed tibial fractures and a set of apparatus to apply tensile axial loading to conservatively treated humeral fractures were developed. Chapter 7 described the testing of this apparatus in the X-ray environment. In Chapter 8 the equipment was used in a clinical setting to monitor patients. The observations from these tests indicated that both sets of apparatus were effective in the X-ray environment. The tibial bending frame could apply a load to tibial fractures without a radiographer being exposed to extra radiation. The frame was easy to manoeuvre in and

out of X-ray and the loading tests were quickly and efficiently carried out. Similarly, in the case of the humeral equipment, the testing introduced very little extra time to the X-ray procedure and did not disrupt the normal radiography environment.

A suitable method to apply load in X-ray for both bending and tensile stiffness measurements has been developed.

13.1.2 Comparing Loaded and Unloaded X-rays

In Chapter 6 the image processing of loaded and unloaded X-rays was described. Chapter 8 described how the software was successfully used to obtain measurements from all the patients in the tibial and humeral fracture studies. The results of these tests showed that the cross-correlation technique was effective in aligning the loaded and unloaded X-rays and making angular and offset measurements from these. The repeatability and accuracy of the program were acceptable. It is possible that a more precise way of verifying the results of the program would yield better accuracy. The program was robust to different types of images and could be applied successfully to both test and patient images.

An effective method of measuring displacement between loaded and unloaded X-rays has been developed.

13.1.3 Movement at the Fracture Site

Chapter 7 described tests applying load to anatomical fracture models. Application of bending and tensile forces to fracture patients was described in Chapter 8. The results from these tests showed that the angular and lateral displacements that occurred in IM nailed tibial fractures were very small and were at the level of accuracy of the measuring system. The results from humeral tests showed that more measureable displacements occurred, although these were not restricted to axial displacement and included angular and lateral offsets.

It is therefore concluded that, in this small cohort of patients, very small angular and displacement movements occurred in loaded IM nailed tibial fractures while more measurable changes occurred in conservatively treated humeral fractures.

13.1.4 Meaningful Stiffness Measurements

In Chapter 8 the angular and displacement measurements and the magnitude of the applied forces were used to calculate the stiffness of patient fractures. A wide range of stiffness values was measured, showing no consistency between patients. The unpredictability and lack of pattern in these results indicated that true stiffness measurements could not be calculated from the small displacements measured at the fracture site in IM patients. Although humeral results were more encouraging, the small patient cohort meant that no conclusion as to the effectiveness of stiffness measurements could be made.

Displacements in IM nailed tibial patients were too small to provide meaningful stiffness measurements. Measurement of axial stiffness were encouraging but require further investigation.

13.1.5 Indication of Healing

The stiffness measurements made on tibial patients presented in Chapter 8 did not show a pattern of increased stiffness in either loading direction, using either angular or displacement measurements. The expected increase in stiffness as healing progressed was possibly occluded by the IM nail and could not be measured by the frame and X-ray measurement system. Again, although axial measurements showed an increase in stiffness with healing, the small cohort of humeral patients limited the conclusions that could be drawn about axial loading.

Stiffness measurements could not be related to stage of healing in IM nailed tibial patients. Further investigation into the healing information from axial stiffness is required.

13.1.6 Stiffness Monitoring

These conclusions provide the information necessary to answer the major research question for this section. Although the apparatus and image analysis technique developed were effective, the results from the patients in the tibial study indicated that true four point bending was not occurring at the fracture site and that displacement measurements were too small to provide meaningful stiffness values that could be related to healing. Humeral results were more encouraging showing an increase in axial stiffness during healing but the small patient numbers limited the conclusions that could be drawn.

It is therefore concluded that IM nailed tibial fracture stiffness could not be measured using the system for loaded and unloaded X-ray images reported in this thesis. Results using axial humeral stiffness were encouraging but inconclusive.

13.2 FEASIBILITY OF MONITORING DENSITY

In this section conclusions regarding the use of an Aluminium step wedge in digital X-ray are made in order to answer the secondary research questions for this investigation. These conclusions are used to answer the major research question, *"Can an Aluminium step wedge included in digital X-rays be used to assess the bone and callus density in fracture patients?"*

13.2.1 Optimal Step Wedge Design

Chapter 9 described the design and comparison of various step wedge formats. In Chapter 10 experiments compared the accuracy of calibration graphs in wedges with different numbers and sizes of steps. It was found that a thickness of 50 mmAl could be detected on X-ray images. Thicker steps and having fewer than ten steps reduced calibration accuracy. It was also shown that using wider steps with a higher thickness range than that needed for calibration provided shielding from scatter.

The optimal design of step wedge was a 15, 5 mm step Aluminium wedge with a width of 25 mm.

13.2.2 Calibration Technique for Digital X-rays

In Chapter 10 the use of different calibration graphs based on techniques used with conventional X-ray and in conventional optical density analyses was discussed. An updated method utilising the grey level output of digital radiography and modern computing capabilities was developed.

An exponential relationship of the form $G = ae^{-bx} + c$ between Aluminium step thickness and grey level provided the best calibration technique for step wedges in digital X-ray images.

13.2.3 Reducing Background Inhomogeneities

Chapter 4 described the anode heel effect and its effect on X-ray quality. The magnitude of this effect was explored in Chapter 9. A double exponential model was successfully used to correct empty field images of the inhomogeneities due to the heel effect. A simple technique to apply this to whole images where only a fully exposed margin was visible was also developed and used successfully in the pre-clinical studies described in Chapter 11. It was also found that the detrimental effect of the heel effect on Aluminium-thickness calibration could be reduced by placing the step wedge as close as possible to the ROI.

The loss of accuracy due to the heel effect could be reduced by careful wedge placement and could be corrected, if necessary, using a double exponential model of the form $ae^{bx} + ce^{dx}$ fitted to a fully exposed margin of the X-ray image.

13.2.4 Accounting for Other Effects

The effect on density measurement of overlying soft tissue and scatter was studied in Chapter 10. A set of calibration graphs to correct for overlying soft tissue and scatter was developed and tested successfully on phantoms. A method to measure soft tissue and bone thickness automatically using X-ray profiles was also developed. In order to take into account the thickness of bone, normalisation of Aluminium-equivalent thickness measurements was suggested. These procedures were successfully used in the patient study on radial fractures.

Bone thickness, overlying soft tissue and scatter could be measured and corrected for in digital X-ray measurements.

13.2.5 Comparison to Validated Measurements

Chapter 11 described the comparison of Aluminium-equivalent thickness results using the step wedge to ash weight and pQCT results. A good correlation between methods was found, although the agreement was not as good. These results showed that step wedge based measurements could be used as effectively as ash weight or pQCT to compare density changes in the same sample or patient. However, further validation tests are needed to assess the ability of Aluminium-equivalent thickness to replace these techniques.

Aluminium-equivalent thickness measurements using digital X-ray were correlated to ash weight and pQCT density measurements.

13.2.6 Aluminium-equivalent Thickness and Healing

Chapter 12 gave the results of Aluminium-equivalent thickness measurements in radial fracture patients over the course of their healing. Although the patient cohort was too small to be statistically relevant and only small changes in Aluminium-equivalent thickness were measured, the results showed that the measurements increased over time for most of the patients, which was in agreement with the clinically expected progression of healing.

Aluminium-equivalent thickness measurements tracked density increases during healing.

13.2.7 Step Wedge Calibration to Monitor Healing

These conclusions provide the information necessary to answer the major research question for this section. A comprehensive method of using an Aluminium step wedge in digital X-rays has been developed. Tests comparing this to validated density measurements showed the ability to measure within-sample changes. The results from the patient study showed that the calibrated X-ray measurements tracked small Aluminium-equivalent thickness increases during healing.

It is therefore concluded that an Aluminium step wedge in digital X-rays has potential for monitoring the healing of fractures.

13.3 DIGITAL X-RAY TO MONITOR FRACTURES

To make an overall conclusion about the hypothesis of this study, both aspects of monitoring fracture healing are considered. In the case of mechanical stiffness measurements, optimisation of the image processing of digital X-ray images with applied mechanical force did not result in a useful measure of fracture stiffness that could be used to accurately monitor fracture healing in tibial patients. The results in humeral patients were more promising, although a larger patient group is required to give more conclusive results.

In the case of Aluminium-equivalent thickness measurements using a step wedge, optimisation of digital X-ray image processing provided measurements that could be used to track healing changes and therefore might allow accurate monitoring of fracture healing.

Chapter 14

Recommendations for Future Work

On the basis of the conclusions, the following recommendations for each section of the thesis are made.

14.1 MECHANICAL STIFFNESS

14.1.1 Validate the Accuracy of Cross-Correlation

Although validation of the measurements made using the cross-correlation procedure was attempted in this study, it was difficult to be certain that the manual measurements of displacement used to compare the program's results with were the true measurements of displacement. To be certain of the effectiveness of the cross-correlation procedure, it is recommended that further tests comparing measurements made using the procedure to known angular, lateral and axial offsets in anatomical fracture models are made.

14.1.2 Investigate Movement at the Fracture Site

In the case of bending stiffness measurements, previous authors have reported the measurement of angular displacements. Although no previous researchers have applied tensile loads to humeral fractures, tests indicated that an axial displacement should occur. However, in patient tests, X-ray images at the fracture site showed that lateral displacement took place at the tibial fracture site and lateral, axial and angular displacement at the humeral fracture site. To be certain of which mechanical stiffness is being measured using both this technique and existing techniques, further investigations should be performed into the response of fractures to different loads.

14.1.3 Bending Tests of Conservatively Treated Tibial Fractures

Results from bending tests on IM nailed tibial fractures showed that very little displacement occurred at the fracture site, probably due to the placement of the nail. However, there is potential for the method to provide measurements in conservatively treated fractures. A possible modification of a patient's cast to include straps that could be attached to the frame might provide the means of making these measurements without cast removal. Bending tests applying the frame to these patients should be performed to check the feasibility of this method.

14.1.4 Further Tests on Humeral Fractures

Due to the small number of humeral shaft fracture patients, only one full and one partial case study could be made for this project. However, the potential of the method to provide at least a qualitative analysis of response of the fracture to load was shown. Bigger displacements that could be more reliably measured than those occurring in the tibial fractures were seen. The patients in this study were already five weeks from initial fracture when first tested, so it is likely that callus was already reducing the movement at the fracture site. Further studies on a larger number of conservatively treated fracture patients, earlier in their course of healing, should be performed to clarify whether there is potential in using this method to quantify fracture healing.

14.2 ALUMINIUM-EQUIVALENT MEASUREMENTS

14.2.1 Validated Density Measures

In the validation tests, a good correlation between Aluminium-equivalent thickness and ash weight and pQCT measurements was found. However, the agreement between the methods was not as good. Some of this can be explained by the inclusion of non-mineral constituents in X-ray measurements, or the method of relating the different measurements from each technique by normalising all measurements to one sample. A more precise validation of the accuracy of the X-ray technique compared to these methods should be performed. Specifically, comparisons should be made to create a relationship between measurements in mmAl and g/cm^3 to ascertain whether the step wedge technique can give standard density measurements.

14.2.2 Larger Patient Study

The step wedge technique was successfully used to track density changes in a small patient study. However, a study on a larger group of patients with more frequent X-ray measurements should be performed to provide a more statistically significant evaluation of the efficacy of this method.

14.2.3 DEXA Comparison

Although it has been shown that changes in density can be tracked using the step wedge, it would be useful to compare the results to those using the clinical standard in measuring density, i.e. DEXA. This could show the potential for step wedge calibration to give an indication of osteoporosis. Patients receiving step wedge measurements should also undergo regular DEXA scans so that the relationship between the two can be explored.

14.2.4 Correlate to Stiffness

In order to make the step wedge technique a useful indicator of healing progression, it would be useful to know how measurements made using calibration compare to other measurements of healing. Stiffness tests should be performed on patients undergoing step wedge measurements and the correlation between the two measurements should be investigated.

14.2.5 Assess the Predictive Value

For the step wedge to be clinically useful in fracture healing it should be possible to identify fractures that may go on to delayed or non-union so that a preventative response can be made. Analyses of Aluminium-equivalent thickness measurements on fracture patients should be made to investigate the relationship between early measurements and rate of healing.

Appendix A

Tibial Bending Frame Plans

This appendix gives the plans for the tibial bending frame showing the frame set up for AP and lateral X-rays.

A.1 FRAME IN POSITION FOR AP X-RAY

The drawings in Figures A.1, A.2 and A.3 show the front, top and side views of the frame configured for taking an AP X-ray, i.e. applying a lateral load. The X-ray plate is shown as a shaded rectangle.

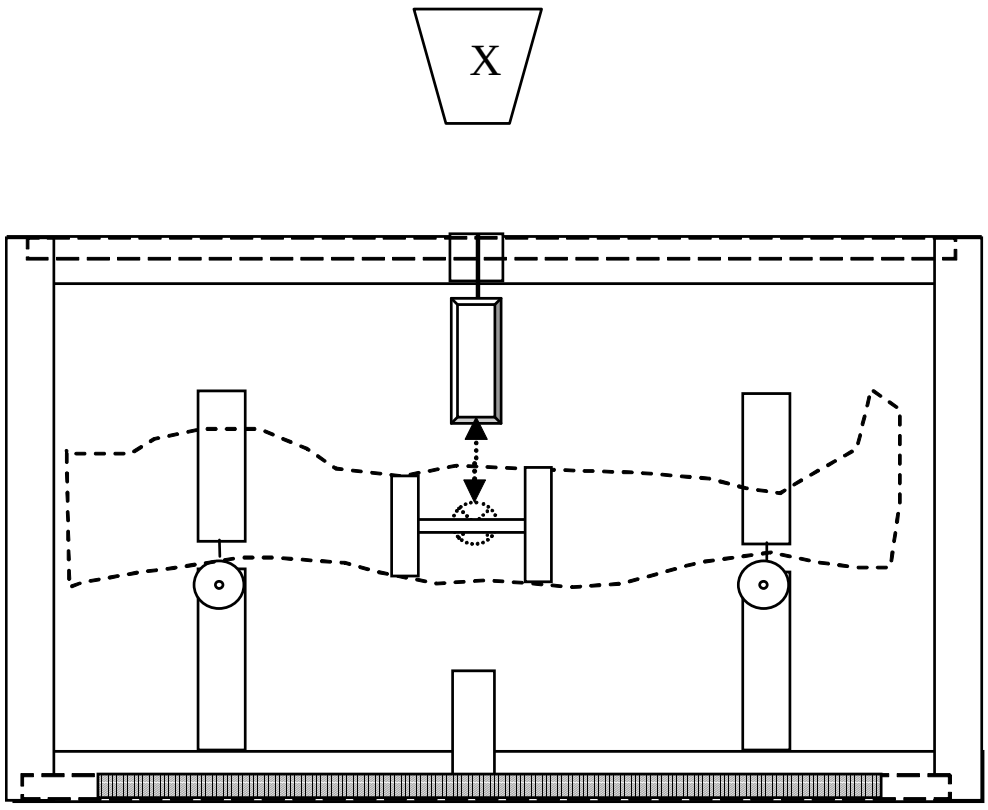

Figure A.1: Front view of the frame set up for taking an AP radiograph.

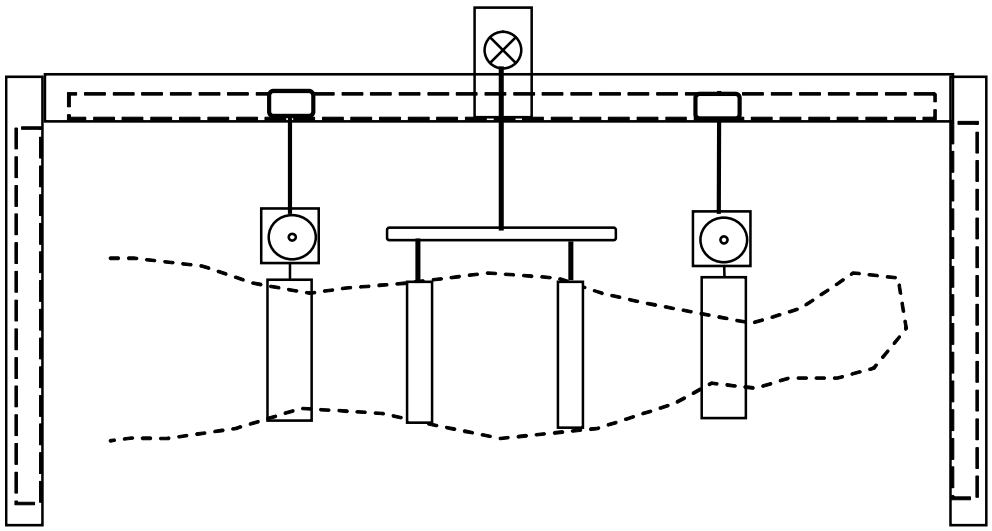

Figure A.2: Top view of the frame set up for taking an AP radiograph (X-ray plate not shown).

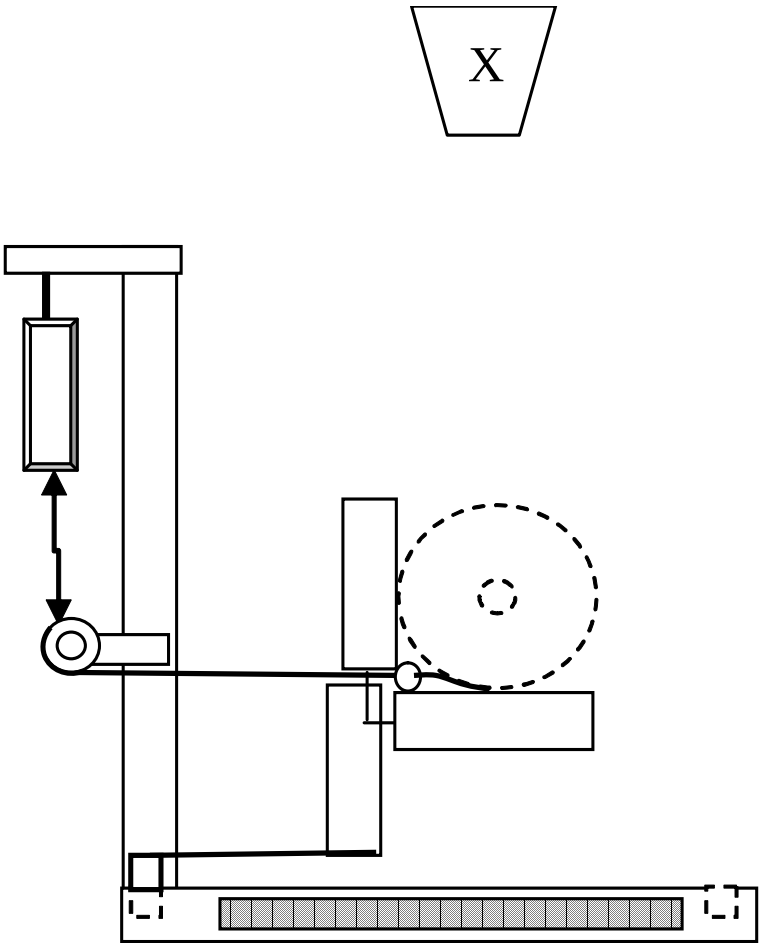

Figure A.3: Side view of the frame set up for taking an AP radiograph.

A.2 FRAME IN POSITION FOR LATERAL X-RAY

The drawings in Figures A.4, A.5 and A.6 show the front, top and side views of the frame configured for taking a lateral X-ray, i.e. applying an AP load. The X-ray plate is shown as a shaded rectangle.

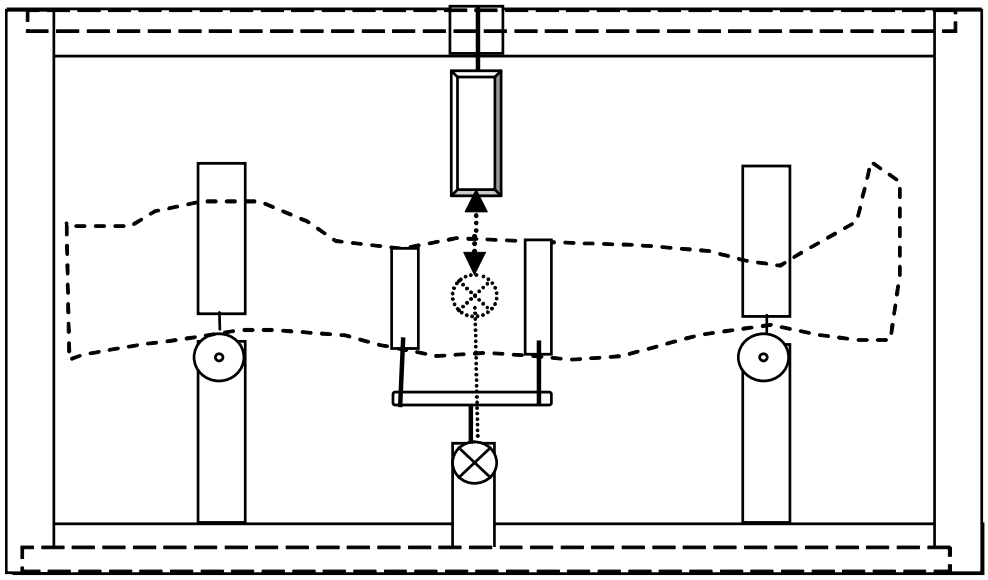

Figure A.4: Front view of the frame set up for taking a lateral radiograph (X-ray plate not shown).

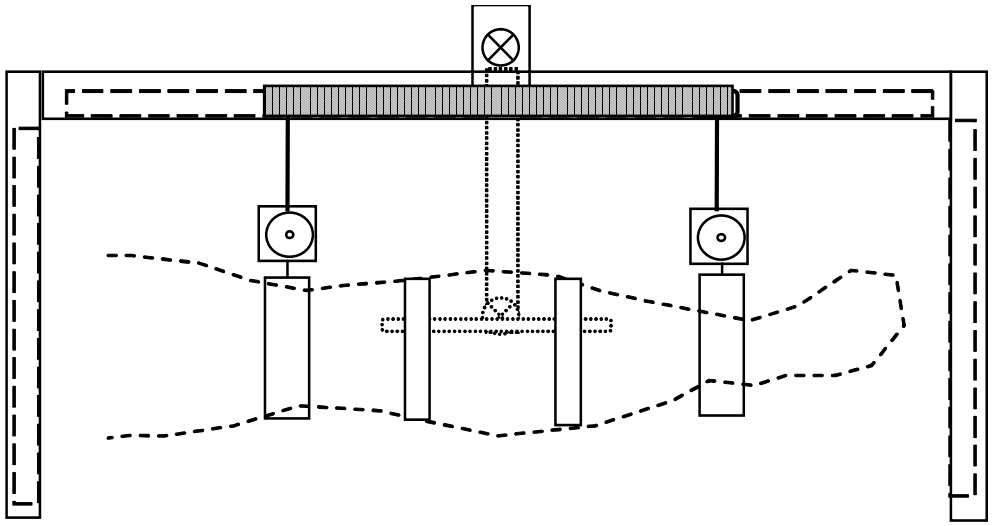

Figure A.5: Top view of the frame set up to take a lateral radiograph.

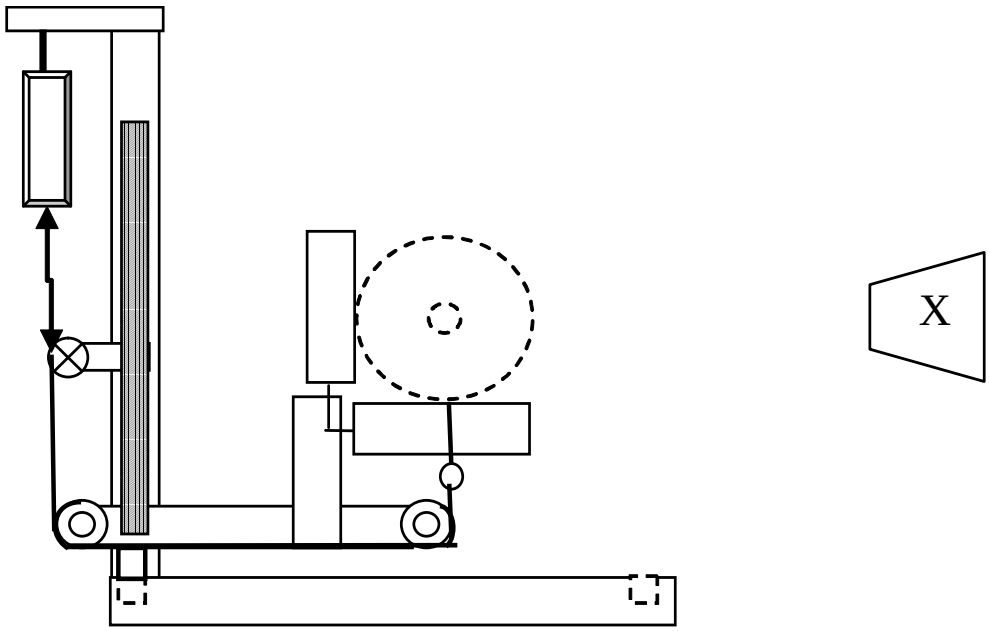

Figure A.6: Side view of the frame set up to take a lateral radiograph.

Appendix B

Four Point Bending Calculations

This appendix gives the full bending moment and force calculations for symmetrical and asymmetrical four point bending.

B.1 SYMMETRICAL FOUR POINT BENDING

In the usual four point bending situation, the inner and outer fulcra are symmetrically and evenly spaced from the central point of the beam which is shown in Figure B.1.

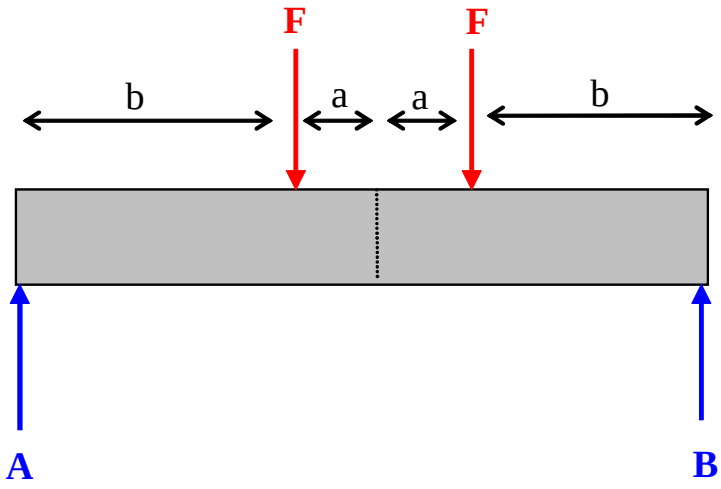

Figure B.1: Typical, symmetrical four point bending set up.

In this situation, calculation of the bending moment diagram starts with the assumption that the set up is in equilibrium. Therefore, the sum of the moments at any point is zero

$$\sum M = 0 \tag{B.1}$$

where M is the bending moment. Allowing upwards forces to be negative, and downwards forces to be positive, the reaction forces, A and B, at the supported ends can be calculated

$$\begin{aligned} \sum_A M &= 0 \\ &= Fb + F(b+2a) - B(2b+2a) \\ B &= F \end{aligned} \tag{B.2}$$

where F is the force at one fulcra, B is a reaction force and a and b are as illustrated in Figure B.1. Similarly, by putting

$$\sum_B M = 0 \tag{B.3}$$

It can be seen that

$$A = F \tag{B.4}$$

where A is the reaction force at the opposite end to B. All the forces in the systems are now known, so the shear force diagram can be drawn, as shown in Figure B.2 (a). From this, the bending moment diagram can be derived by allowing the forces at each point along the beam in the shear force diagram to be the gradients of the bending moment diagram. The bending moment diagram is shown in Figure B.2 (b) and illustrates how the bending moment between the two inner fulcra is constant at $-Fb$ Nm [142, 143].

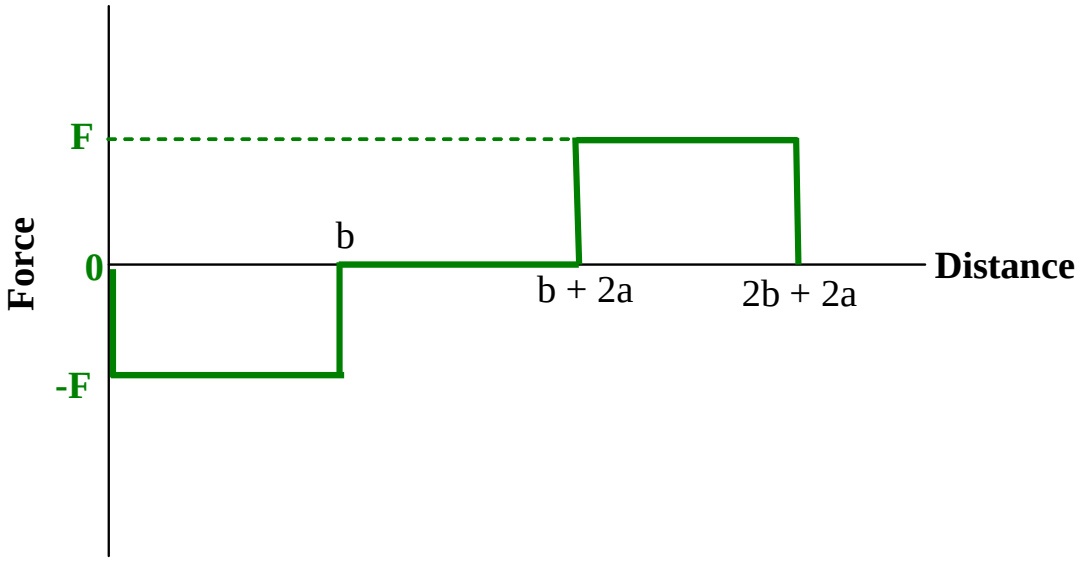

(a)

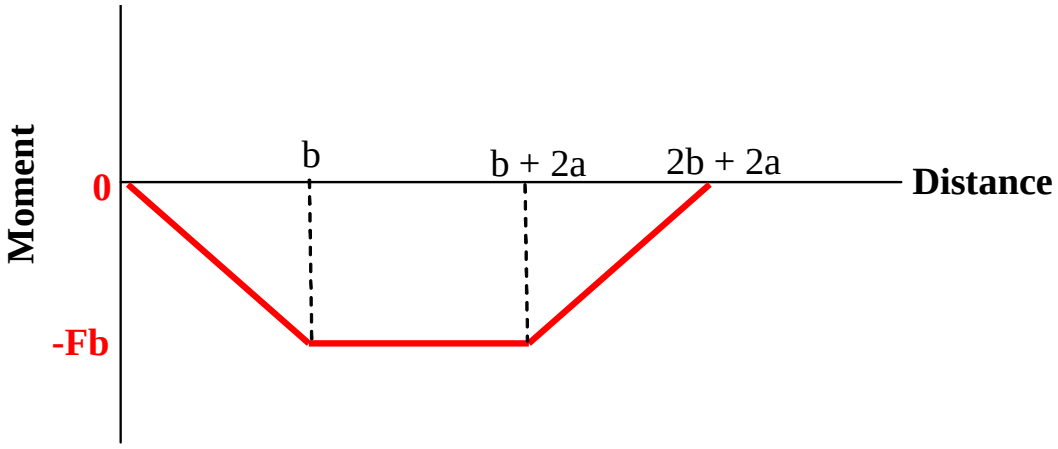

(b)

Figure B.2: a) Shear force and b) bending moment diagrams for symmetrical four point bending.

B.2 ASYMMETRICAL FOUR POINT BENDING

In some cases the distances between the fulcra are not balanced, resulting in four point bending being applied in an asymmetrical way. In this case calculation of the forces and moments becomes more complicated. An example of this type of set up is shown in Figure B.3.

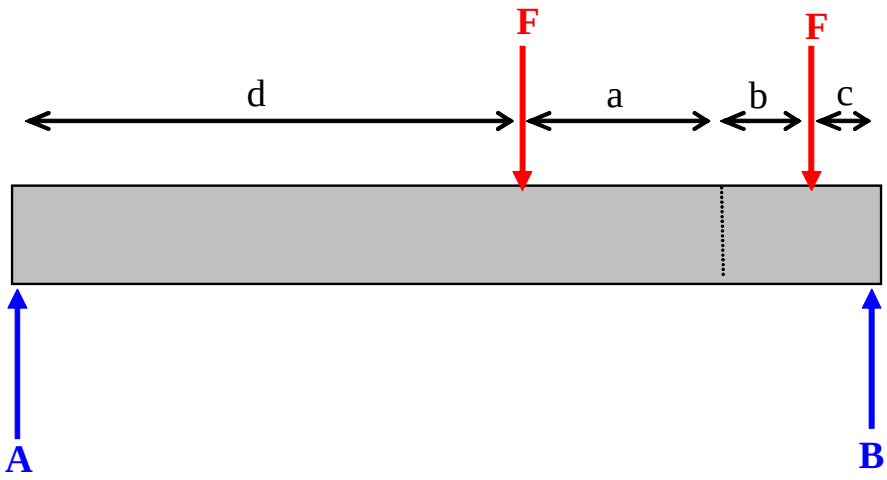

Figure B.3: Asymmetrical four point bending set up.

Again, the reaction forces, A and B, are calculated using the fact that the sum of moments at any point is zero

$$\begin{aligned} \sum_{A} M &= 0 \\ &= Fd + F(a+b+d) - B(a+b+c+d) \\ B &= \frac{F(2d+a+b)}{(a+b+c+d)} \end{aligned} \tag{B.5}$$

$$\begin{aligned} \sum_{B} M &= 0 \\ &= Fc + F(a+b+c) - A(a+b+c+d) \\ A &= \frac{F(a+b+2c)}{(a+b+c+d)} \end{aligned} \tag{B.6}$$

where a, b, c and d are as illustrated in Figure B.3. In this situation it is important to note that A is not equal to B, and neither is equal to the applied force F. In this case, the shear force and bending moment diagrams are as shown in Figure B.4 .

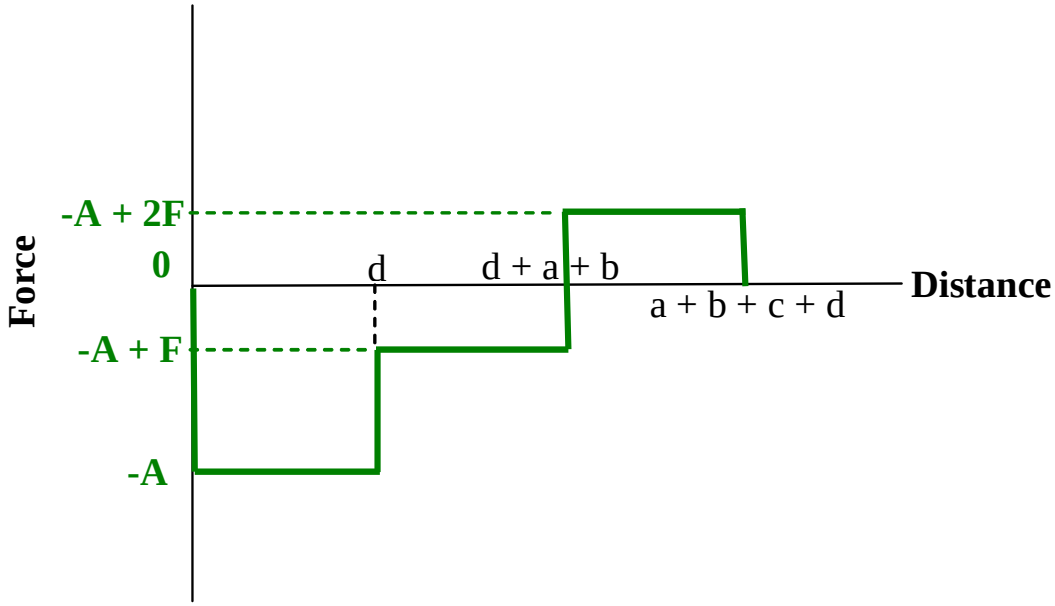

(a)

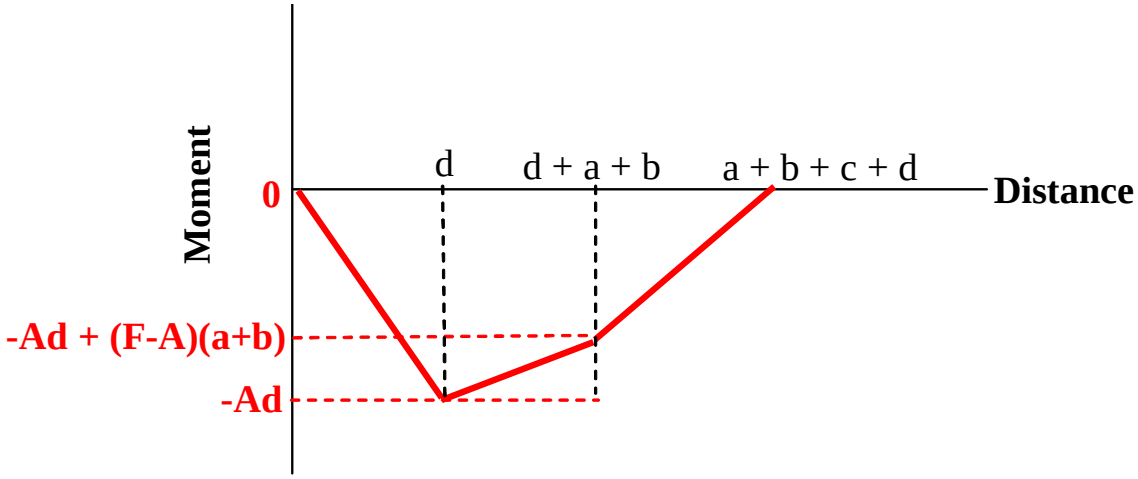

(b)

Figure B.4: a) Shear force and b) bending moment diagrams for asymmetrical four point bending.

As Figure B.4 (b) shows, the bending moment between the two points of force application is no longer constant. However, if the distances a, b, c and d are known, as well as the forces applied, these can be used to calculate the exact bending moment any point of interest (e.g. the fracture site). For instance, the values for a typical situation where a total of 100 N is applied across both fulcra, the following calculations could be performed

Let $F = 50$ N, $a = 0.05$ m, $b = 0.03$ m, $c = 0.04$ m and $d = 0.06$ m.

$$\begin{aligned} A &= F(a+b+2c)/(a+b+c+d) \\ &= 50(0.05+0.03+2(0.04))/(0.05+0.03+0.04+0.06) \\ A &= 44.44N \end{aligned}$$

From the bending moment diagram, at a distance d from A, the bending moment is

$$\begin{aligned} M_d &= -Ad \\ &= (-44.44)(0.06) \\ &= 2.67Nm \end{aligned} \tag{B.7}$$

where M_d is the moment at distance d. At the fracture site, the bending moment is

$$\begin{aligned} M_f &= M_d + M_a \\ &= 2.67 + (-A+F)a \\ &= 2.67 + (5.56)0.05 \\ &= 2.95Nm \end{aligned} \tag{B.8}$$

where M_f is the moment at the fracture site and M_a is the moment at distance a. These calculations show that the bending moment at the fracture site can be calculated for any four point bending set up if all the information about distances and force is known.

Appendix C

Humeral Force Calculations

This appendix explains how the forces acting in the axial loading set up in the humerus are calculated and what effect changing angles and distances might have on the final force estimation.

C.1 FORCE CALCULATION

Figure C.1 shows a lateral view of the forces associated with the humeral axial set up. In the diagram, forces which are potentially at an angle (F_B and F_T) have been resolved into their vertical and horizontal components. The forces and distances are

- F_T: The upwards reaction force of the force plate.
- W: The weight of the arm and forearm.
- F_A: The downwards force of the applied weights.
- F_B: The upwards reaction force of the arm to the applied weight.
- s: The distance from the force plate to the centre of mass of the arm system.
- p: The distance from the force plate to the point of force application.
- m: The distance from the force plate to the elbow.

Some forces and distances in the system are known

- F_{T_Y}: This is the vertical force measured by the force plate.
- F_A: This is the known weight applied to the band around the arm.

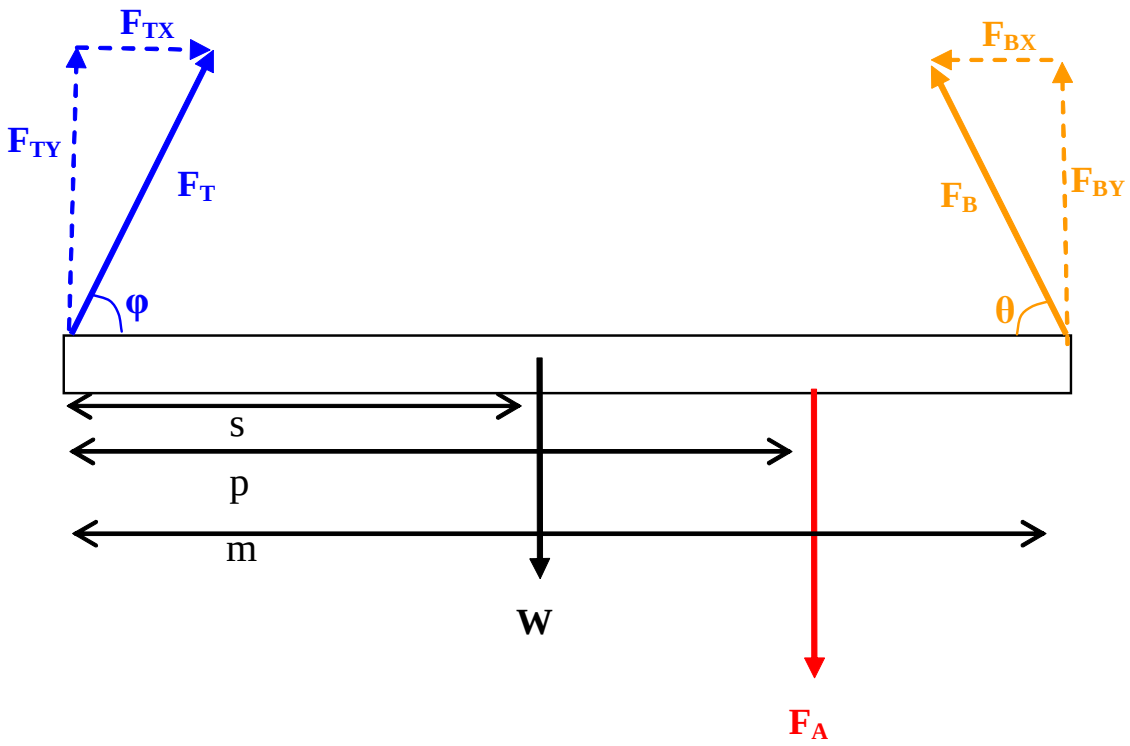

Figure C.1: Free body diagram of the forces acting on the arm and forearm during axial loading.

The force of interest is F_B, the reaction force through the arm. This is not necessarily vertical, so the angle θ is necessary to calculate the force through the arm. Since the system is in static equilibrium, the sum of the forces in the x and y directions is zero.

$$\begin{aligned} \sum_x F &= 0 \\ F_{B_X} - F_{T_X} &= 0 \\ F_{B_X} &= F_{T_X} \end{aligned} \tag{C.1}$$

and

$$\begin{aligned}
\sum_{y} F &= 0 \\
0 &= F_{B_Y} - F_A - W + F_{T_Y} \\
F_{B_Y} &= F_A + W - F_{T_Y} \qquad \text{(C.2)}
\end{aligned}$$

The system is also in rotational equilibrium, so the sum of the torques at any given point is zero.

$$\begin{aligned}
\sum_{hand} \tau &= 0 \\
0 &= F_T(0) - W(s) - F_A(p) + F_B(m \sin\theta) \\
0 &= -Ws - F_A p + \frac{F_{B_Y} m \sin\theta}{\sin\theta} \\
0 &= -Ws - F_A p + F_{B_Y} m \qquad \text{(C.3)}
\end{aligned}$$

substituting from Equation (C.2)

$$\begin{aligned}
0 &= -Ws - F_A p + (F_A + W - F_{T_Y})m \\
0 &= -Ws - F_A p + F_A m + Wm - F_{T_Y} m \\
W &= \frac{-F_A p + F_A m - F_{T_Y} m}{s - m} \qquad \text{(C.4)}
\end{aligned}$$

substituting Equation (C.4) into Equation (C.2)

$$F_{B_Y} = F_A - F_{T_Y} + \frac{(-F_A p + F_A m - F_{T_Y} m)}{s - m} \qquad \text{(C.5)}$$

Since $F_{B_Y} = F_B \sin\theta$,

$$F_B = (F_A - F_{T_Y} + \frac{-F_A p + F_A m - F_{T_Y} m}{(s - m)}) \frac{1}{\sin\theta} \qquad \text{(C.6)}$$

This is the equation necessary to calculate the force, F_B, through the fractured humerus.

C.1.1 Effect of Humeral Angle

Equation (C.6) shows how the force through the humeral fracture could be calculated with knowledge of the angle θ and the distances s, m and p . However, these measurements could not be made using an AP radiograph. To assess whether this calculation was necessary and what the effect of assuming θ to be 90 degrees was, a simulation of what might occur clinically was made with F_A= 100 N, F_{T_Y} = 4 N, s = 0.15 m, m = 0.3 m, p = 0.2 m and θ at various values. For θ= 90 degrees, F_B was 37.3 N. For θ between 80 and 90 degrees, a maximum error in estimating F_B of only 0.6 N (2%) was made. These calculations showed that if care is taken in minimising the angle of the humerus to the horizontal, then the assumption that θ = 90 degrees introduces negligible errors to the calculation of F_B.

C.2 SIMPLIFIED FORCE CALCULATION

The distances necessary for a full calculation of F_B could not be measured using an AP radiograph. However, the previous section has shown that an acceptably small error was introduced when assuming that the forces in this plane acted vertically. A further assumption was made that the vertical force through the humerus was equal to the applied force, F_A, minus the change in force measured at the force plate during loading. In the unloaded situation

$$F_{B_{Y0}} = W - F_{T_{Y0}} \tag{C.7}$$

and in the loaded situation

$$F_{B_{YL}} = W - F_{T_{YL}} + F_A \tag{C.8}$$

where $F_{B_{Y0}}$ is the vertical force through the humerus and $F_{T_{Y0}}$ is the force measured on the force plate with no load applied. $F_{B_{YL}}$ is the vertical force through the humerus and $F_{T_{YL}}$ is the force measured on the force plate with load F_A applied. The change in vertical force through the humerus due to loading is

$$\begin{aligned} F_{B_Y} &= F_{B_{YL}} - F_{B_{Y0}} \\ &= F_A - (F_{T_{YL}} - F_{T_{Y0}}) \end{aligned} \tag{C.9}$$

Using this, the system shown in Figure C.2 was used to make calculations of the force through, and stiffness of, a humeral fracture using the measurements from the AP radiograph. $\triangle L$ is the change in distance between the fracture ends with loading.

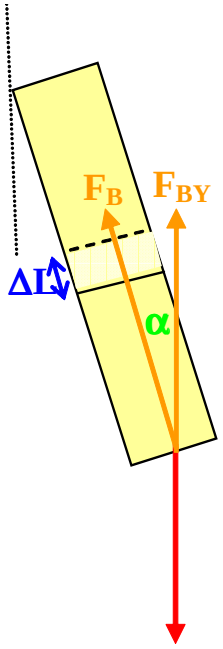

Figure C.2: Simplified free body diagram of the humeral fracture force system in the AP view.

The following calculation for the force through the humerus can be made

$$F_B = \frac{F_{B_Y}}{\cos\alpha} \tag{C.10}$$

where α is the angle of the humerus to the vertical when viewed in the AP direction. Since it was likely that α would be small in the radiographic set up, a simulation of the errors introduced by assuming the effect of α to be negligible was made using F_A =25 N, $F_{T_{Y0}}$ = 5.7 N, $F_{T_{YL}}$ =16.8 N and α varying from 0 degrees to 10 degrees. For α = 0 degrees, F_B was calculated to be 14 N and a maximum error in estimating F_B of only 0.2 N (2%) was made when $\alpha = 10$ degrees. This showed that, although α could be measured directly from the radiographs, its effect on calculations of F_B were negligibly small.

C.2.1 Stiffness

The stiffness, S_H, was calculated as the force through the fracture divided by the displacement at the fracture site due to loading, and was measured in N/mm

$$\begin{aligned} S_H &= \frac{F_A - (F_{T_{YL}} - F_{T_{Y0}})}{\triangle L} \\ &= \frac{F_{B_Y}}{\triangle L} \end{aligned} \tag{C.11}$$

Thus, with several simplifying assumptions, force and stiffness calculations could be made for the humeral system which would allow stiffness comparisons to be made between loaded and unloaded X-rays.

Appendix D

Offset Co-ordinate Axes Transformation

This appendix explains how the co-ordinates of the bone 'corners' of a fractured tibia were transformed from the Matlab image co-ordinate system to a co-ordinate system with its origin at one of the bone corners and its axes parallel to the angle of the fracture.

D.1 EXISTING AND REQUIRED CO-ORDINATES

Figure D.1 shows the existing Matlab image co-ordinate system (x, y) and the required co-ordinate system (x', y'). The Matlab co-ordinate system is parallel to the borders of the image. However, in order to measure an offset between the two bone segments, a co-ordinate system parallel to the fracture was required. Figure D.2 shows the positions of the bone corners.

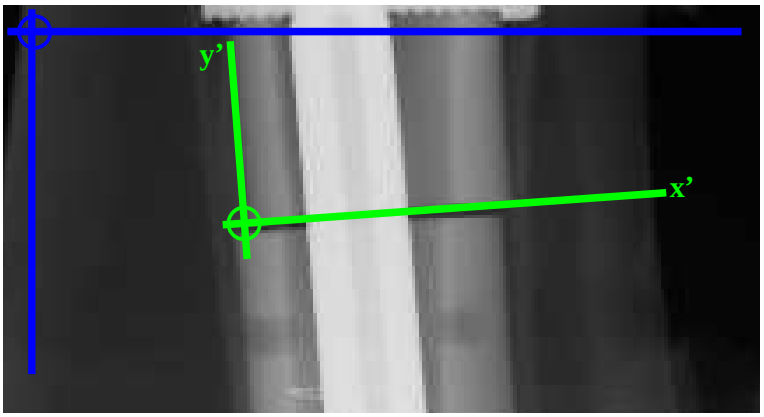

Figure D.1: Matlab image co-ordinate system (blue) and required co-ordinate system (green).

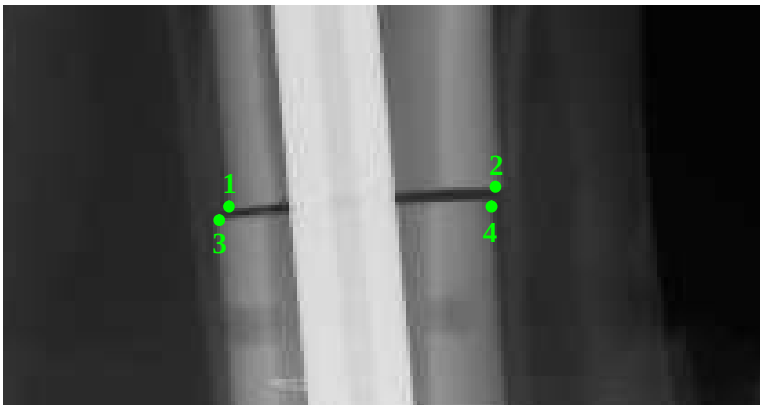

Figure D.2: Bone corners $1, 2, 3$ and 4.

In the Matlab co-ordinate system, let the co-ordinates of these points be

$$\begin{array}{ll} 1 & (a, b) \\ 2 & (c, d) \\ 3 & (e, f) \\ 4 & (g, h) \end{array}$$

In the new co-ordinate system, let them be

$$\begin{aligned} 1' &\quad (a', b') \\ 2' &\quad (c', d') \\ 3' &\quad (e', f') \\ 4' &\quad (g', h') \end{aligned}$$

The new origin of the (x', y') co-ordinate system will be at point $1'(a', b')$ and will be known as the bone co-ordinate system.

D.2 TRANSFORMING CO-ORDINATE SYSTEMS

To obtain the transformation from the Matlab image co-ordinate system to the new co-ordinate system, the following calculations were made:

Calculating 1'

Since 1' is the origin,

$$a' = 0 \tag{D.1}$$

and

$$b' = 0 \tag{D.2}$$

Calculating 2'

Since 2' lies on the x' axis,

$$d' = 0 \tag{D.3}$$

c' is the distance between 1 and 2 so

$$\begin{aligned} c' &= \sqrt{(c-a)^2 + (d-b)^2} \\ c' &= D_{12} \end{aligned} \tag{D.4}$$

Calculating 3'

The Figure D.3 shows the relative positions of 1' and 3'.

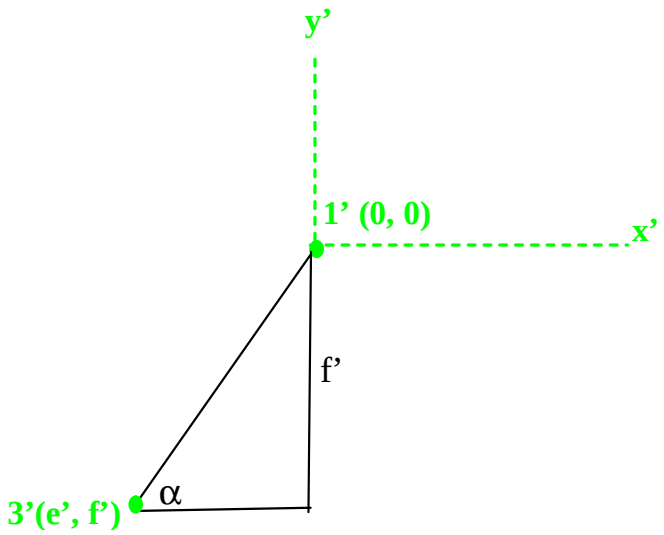

Figure D.3: 1' and 3' in the bone co-ordinate system.

As the figure shows, e' is the horizontal edge of the triangle and f' is the vertical edge. D_{13} is the distance between 1' and 3' so

$$D_{13} = \sqrt{(f-b)^2 + (e-a)^2}$$

and m_{13} is the gradient of the hypotenuse so

$$m_{13} = \frac{f-b}{e-a}$$

and

$$m_{34} = \frac{h-f}{g-e}$$

and

$$\alpha = \arctan(\frac{m_{13} - m_{34}}{1 + m_{13}m_{34}})$$

therefore

$$e' = D_{13}\cos\alpha \quad \text{(D.5)}$$

$$f' = D_{13}\sin\alpha \quad \text{(D.6)}$$

Calculating 4'

Figure D.4 shows the relative positions of 1' and 4'.

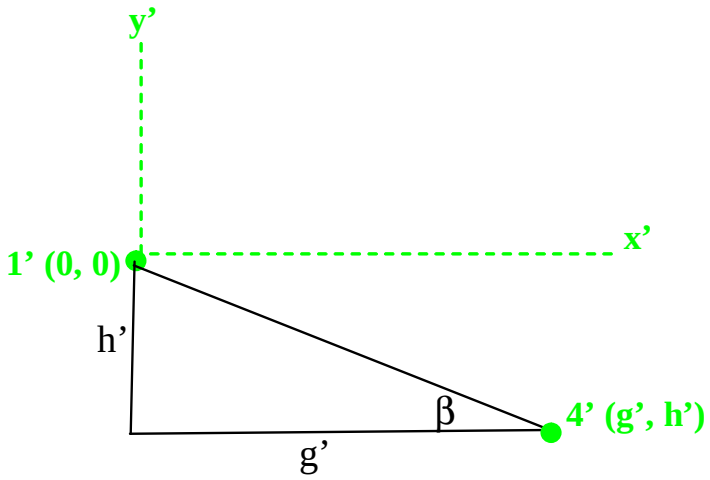

Figure D.4: Corners 1' and 4' in the bone co-ordinate system.

As the figure shows, g' is the horizontal edge of the triangle and h' is the vertical edge. D_{14} is the distance between 1' and 4' so

$$D_{14} = \sqrt{(h-b)^2 + (g-a)^2}$$

and m_{14} is the gradient of the hypotenuse so

$$m_{14} = \frac{h-b}{f-a}$$

and

$$\beta = \arctan(\frac{m_{14} - m_{34}}{1 + m_{14}m_{34}})$$

so

$$g' = D_{14}\cos\beta \quad \text{(D.7)}$$

$$h' = D_{14}\sin\beta \quad \text{(D.8)}$$

D.3 CALCULATING OFFSETS

From these calculations, the co-ordinates of each point could be transformed to the new bone co-ordinate system so the offset induced in the bone due to the application of force could be calculated as the horizontal displacement in the bone co-ordinate system, i.e. the x'-displacement.

Appendix E

Image Padding for Cross-Correlation

This appendix explains how the unloaded and loaded images were aligned using the cross-correlation information. The procedure used to attain images of the same size and aligned co-ordinate systems was to pad the loaded and unloaded X-ray images with zeroes.

E.1 PADDING FOR THE PROXIMAL SEGMENT

The cross-correlation procedure began with the loaded and unloaded images that had been cropped to identical sizes, let these be A and B. The proximal fracture segment in the loaded image was then selected (let this be b) and cross-correlation was performed with this image and the unloaded image. A, B and b are represented in Figure E.1.

This gave the two pieces of information necessary to align the proximal segments of the loaded and unloaded images:

1. The position of the peak of the cross-correlation matrix gave the x and y distances of the top left corner of b from the top left corner of A: (x_1, y_1).
2. The cropping rectangle gave the position of the top left corner of b from the top left corner of B: (x_2, y_2).

From this

$$H_1 = x_2 - x_1 \tag{E.1}$$

and

$$V_1 = y_2 - y_1 \tag{E.2}$$

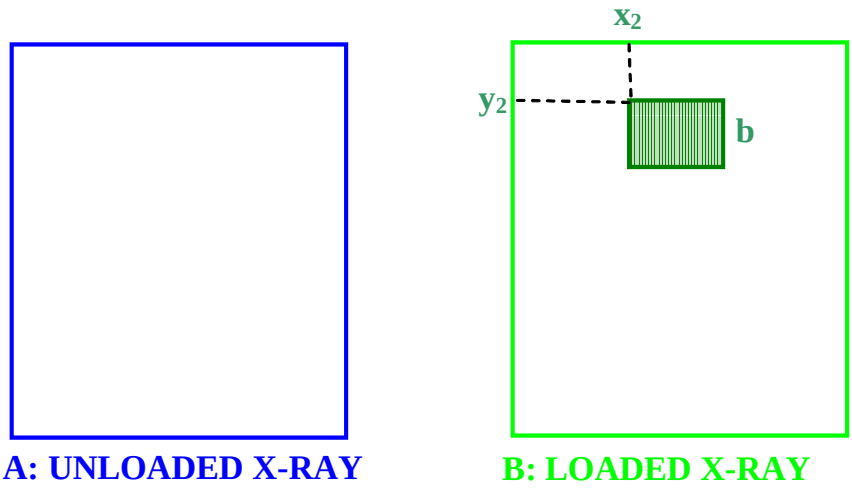

Figure E.1: Representation of the unloaded and loaded X-ray images, A and B, and the cropped proximal segment, b.

where H_1 is the horizontal offset and V_1 is the vertical offset between the proximal fracture segments of A and B. Images A and B were then padded with H_1 zeros on the horizontal border and V_1 zeros on the vertical border to attain two padded images, C and D that were the same size and were aligned according to their proximal segments. This was done differently depending on whether H_1 and V_1 were positive or negative:

- If $H_1 > 0$ and $V_1 > 0$ then pad A at the top and left edges and B at the lower and right edges.
- If $H_1 < 0$ and $V_1 < 0$ then pad A at the lower and right edges and B at the top and left edges.
- If $H_1 < 0$and $V_1 > 0$ then pad A at the top and right edges and B at the lower and left edges.
- If $H_1 > 0$ and $V_1 < 0$ then pad A at the lower and left edges and B at the top and right edges.

An example of where the padding would occur in the case of $H_1 > 0$ and $V_1 > 0$ is shown in Figure E.2.

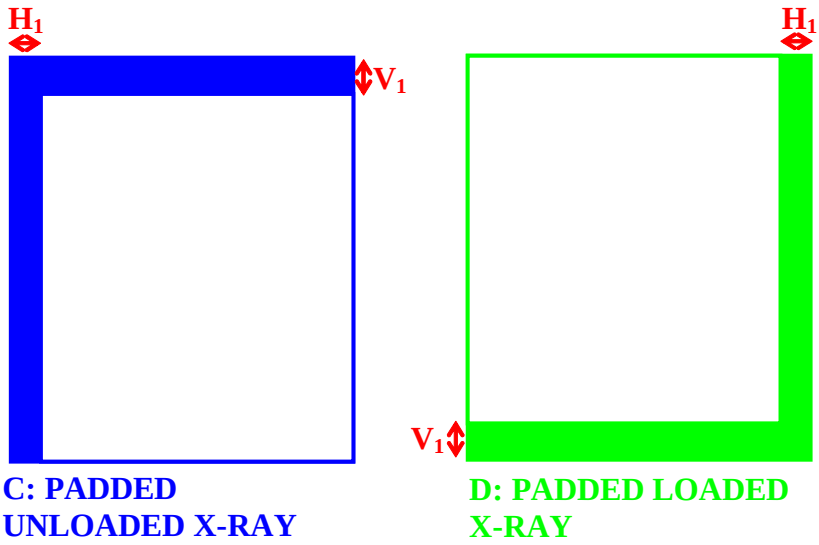

Figure E.2: Zero padding (in solid colour) of A and B to create C and D with proximal segments aligned.

E.2 PADDING FOR THE DISTAL SEGMENT

The distal segment, d, was then cropped from the padded image D and cross-correlation was performed with C. As in the case of the proximal segment, the cross-correlation matrix and cropping rectangle provided the information necessary to pad the two images C and D with zeros so that they were the same size and aligned at the distal segment.

Appendix F

Details of Ethical Approval

F.1 ETHICAL APPROVAL FOR TIBIAL AND HUMERAL STUDIES

Ethical approval was sought and received from the Lothian Local Research Ethics Committee (LREC) before commencing the tibial or humeral fracture stiffness trials. Details of the agreement are shown in Figure F.1.

F.2 ETHICAL APPROVAL FOR RADIAL STUDY

Permission to include the Aluminium step wedge in patient X-rays was sought from the South East Scotland Research Ethic Service. Permission requiring no ethical review was granted. A copy of the agreement is in Figure F.2.

Lothian NHS Board 5 DEC 2007

Deaconess House
148 Pleasance
Edinburgh
EH8 9RS
Telephone 0131 536 9000
Fax 0131 536 9009
www.nhslothian.scot.nhs.uk

NHS Lothian

30 November 2007

Professor AHRW Simpson
Professor of Orthopaedics & Trauma Department of Orthopaedic Surgery
University of Edinburgh
Department of Orthopaedic Surgery & Trauma, Musculoskeletal Tissue Eng
Chancellor's Building
EDINBURGH EH16 4SB

Dear Professor Simpson

Full title of study: **X-ray Evaluation of the Stiffness of Bone Callus as a Measure of Fracture Healing**
REC reference number: **07/S1103/38**

Thank you for your letter of 15 November 2007, responding to the Committee's request for further information on the above research and submitting revised documentation.

The further information was considered on behalf of the Committee by the Chair, Dr Christine West.

Confirmation of ethical opinion
On behalf of the Committee, I am pleased to confirm a favourable ethical opinion for the above research on the basis described in the application form, protocol and supporting documentation as revised.

Ethical review of research sites
The favourable opinion applies to the research sites listed on the attached form.

Conditions of approval
The favourable opinion is given provided that you comply with the conditions set out in the attached document. You are advised to study the conditions carefully.

Approved documents
The final list of documents reviewed and approved by the Committee is as follows:

Document	*Version*	*Date*
Application	AB/1111260/1	20 August 2007
Investigator CV	1 - for Dr Thomas Joseph MacGillivray	20 August 2007
Investigator CV	1 - for Sarah Dawson	20 August 2007
Investigator CV	1 - for Professor A H R W Simpson	20 August 2007
Protocol	1	20 August 2007
Covering Letter	1 - with original submission	20 August 2007
Covering Letter	2 - with changes	15 November 2007
Letter from Sponsor	ACCORD	11 July 2007
Compensation Arrangements	from AON Commercial Insurance	28 July 2006
GP/Consultant Information Sheets	1.0	20 August 2007
Participant Information Sheet	1.1	15 November 2007
Participant Consent Form	1.0	20 August 2007
Honorary contract for Sarah Dawson		20 July 2007

R&D approval

All researchers and research collaborators who will be participating in the research at NHS sites should apply for R&D approval from the relevant care organisation, if they have not yet done so. R&D approval is required, whether or not the study is exempt from SSA. You should advise researchers and local collaborators accordingly.

Guidance on applying for R&D approval is available from http://www.rdforum.nhs.uk/rdform.htm.

Statement of compliance

The Committee is constituted in accordance with the Governance Arrangements for Research Ethics Committees (July 2001) and complies fully with the Standard Operating Procedures for Research Ethics Committees in the UK.

After ethical review

Now that you have completed the application process please visit the National Research Ethics Website > After Review

Here you will find links to the following

a) Providing feedback. You are invited to give your view of the service that you have received from the National Research Ethics Service on the application procedure. If you wish to make your views known please use the feedback form available on the website.
b) Progress Reports. Please refer to the attached Standard conditions of approval by Research Ethics Committees.
c) Safety Reports. Please refer to the attached Standard conditions of approval by Research Ethics Committees.
d) Amendments. Please refer to the attached Standard conditions of approval by Research Ethics Committees.
e) End of Study/Project. Please refer to the attached Standard conditions of approval by Research Ethics Committees.

We would also like to inform you that we consult regularly with stakeholders to improve our service. If you would like to join our Reference Group please email referencegroup@nationalres.org.uk .

REC Reference Number	07/S1103/3	Please quote this number on all correspondence

With the Committee's best wishes for the success of this project

Yours sincerely

pp **Chair**
Lothian Local Research Ethics Committee 03
Email: elizabeth.harden@lhb.scot.nhs.uk

Enclosures: *Standard approval conditions*
Site approval form

Copy to: Ms Marise Bucukoglu
R&D office for NHS Lothian

Figure F.1: LREC Ethics approval form for humeral and tibial stiffness trial.

South East Scotland Research Ethics Service

Deaconess House
148 Pleasance
Edinburgh
EH8 9RS
Tel: 0131 536 9067
Fax: 0131 536 9346

NHS Lothian

Name: Sarah Dawson
Address: Edinburgh Orthopaedic Engineering Collaboration
Room FU 413
Chancellor's Building
49 Little France Crescent
Edinburgh
EH16 4SB

Date: 23/02/2009
Your Ref:
Our Ref: NR/0209AB12
Enquiries to: Alex Bailey
Extension:
Direct Line: 0131 536 9050
Email: alex.bailey@nhslothian.scot.nhs.uk

Dear Sarah,

Full title of project: Density Evaluation of Fracture Healing

You have sought advice from the South East Scotland Research Ethics Service on the above project. This has been considered by the Scientific Officer and you are advised that, based on the submitted documentation (DENSITY EVALUATION OF FRACTURE HEALING.DOC), it does not need NHS ethical review under the terms of the Governance Arrangements for Research Ethics Committees in the UK. The advice is based on the following:

- *The project is an audit using only data obtained as part of usual care but note the requirement for Caldicott Guardian approval to permit sharing or publication of patient-identifiable information.*

If this project is being conducted within NHS Lothian you should inform the relevant local Quality Improvement Team(s).

Please note that this advice is issued on behalf of the Research Ethics Service and does not constitute a favourable opinion or an endorsement from a Research Ethics Committee. It may be provided to journal editors, conference organisers or others who require evidence of consideration of the need for ethical review prior to publication or presentation of your results. If you wish you may still decide to apply to a REC, but note that a retrospective ethical opinion cannot be given.

You should retain a copy of this letter with your project file as evidence that you have sought advice from the South East Scotland Research Ethics Service.

Yours sincerely,

Alex Bailey
Scientific Officer
South East Scotland Research Ethics Service

Enclosure: NRES leaflet - "Defining Research"

1

Figure F.2: Form confirming permission to conduct radial fracture step wedge trial.

References

[1] Edinburgh Orthopaedic Trauma Unit. Scottish orthopaedic research trust into trauma. *Edinburgh Orthopaedic Trauma Unit [online], UK*, [last accessed 14 June 2009]:Available at http://www.trauma.co.uk/unit/sortit.asp, 2007.

[2] Blokhuis TJ, den Boer FC, Bramer JAM, van Lingen A, Roos JC, Bakker FC, Patka P, and Haarman HJTM. Evaluation of strength of healing fractures with dual energy xray absorptiometry. *Clinical Orthopaedics and Related Research*, 380:260–268, 2000.

[3] Markel MD and Chao EYS. Noninvasive monitoring techniques for quantitative description of callus mineral content and mechanical properties. *Clinical Orthopaedics and Related Research*, 293:37–45, 1993.

[4] McRae R and Esser M. *Practical Fracture Treatment*. Elsevier Churchill Livingstone, UK, 2008.

[5] Van de Graaff KM. *Human Anatomy*. McGraw Hill, New York, 2002.

[6] Chakkalakal DA, Lippiello L, Wilson RF, Shindell R, and Connolly JF. Mineral and matrix contributions to rigidity in fracture healing. *Journal of Biomechanics*, 23(5):425–434, 1990.

[7] Hamblen DL and Simpson AHRW. *Adams's Outline of Fractures*. Churchill Livingstone Elsevier, UK, 2007.

[8] Perren SM. Physical and biological aspects of fracture healing with special reference to internal fixation. *Clinical Orthopaedics and Related Research*, 138:175–196, 1979.

[9] Wade RH, Moorcroft CI, and Thomas PBM. Fracture stiffness as a guide to the management of tibial fractures. *Journal of Bone and Joint Surgery, British*, 83-B(4):533–535, 2001.

[10] Evans M, Kenwright J, and Cunningham JL. Design and performance of a fracture monitoring transducer. *Journal of Biomedical Engineering*, 10:64–69, 1988.

[11] Webb J, Herling G, Gardner T, Kenwright J, and Simpson AHRW. Manual assessment of fracture stiffness. *Injury*, 27(5):319–320, 1996.

[12] Eastaugh-Waring SJ, Hardy JRW, and Cunningham JL. Fracture stiffness measurement using the orthometer: reproducibility and sources of error. *Clinical Biomechanics*, 15:140–142, 2000.

[13] Blokhuis TJ, de Bruine JHD, Bramer JAM, den Boer FC, Bakker FC, Patka P, Haarman HJTM, and Manoliu RA. The reliability of plain radiography in experimental fracture healing. *Skeletal Radiology*, 30:151–156, 2001.

[14] Sarmiento A, Schaeffer JF, Beckerman L, Latta LL, and Enis JE. Fracture healing in rat femora as affected by functional weight bearing. *Journal of Bone and Joint Surgery, British*, 59-A(3):369–375, 1977.

[15] Tiedeman JJ, Lippiello L, Connolly JF, and Strates BS. Quantitative roentgenographic densitometry for assessing fracture healing. *Clinical Orthopaedics and Related Research*, 253:279–286, 1990.

[16] Nicholls PJ, Berg E, Bliven FE, and Kling JM. X-ray diagnosis of healing fractures in rabbits. *Clinical Orthopaedics and Related Research*, 142:234–236, 1979.

[17] Panjabi MM, Walter SD, Karuda WM, White AA, and Lawson JP. Correlations of radiographic analysis of healing fractures with strength: A statistical analysis of experimental osteotomies. *Journal of Orthopaedic Research*, 3:212–218, 1985.

[18] Hammer RRR, Hammerby S, and Lindholm B. Accuracy of radiologic assessment of tibial shaft fracture union in humans. *Clinical Orthopaedics and Related Research*, 199:233–238, 1985.

[19] Page CM. Correspondence: Delay in the union of fractures. *British Medical Journal of Biomechanics*, 28:305, 1942.

[20] Marsh DM. Concepts of fracture union, delayed union and nonunion. *Clinical Orthopaedics and Related Research*, 355S:S22–S30, 1998.

[21] Ogrodnik PJ, Moorcroft CI, and Thomas PBM. A fracture movement monitoring system to aid in the assessment of fracture healing in humans. *Proceedings Institution of Mechanical Engineers*, 215(H):405–414, 2001.

[22] Wade R and Richardson J. Outcome in fracture healing a review. *Injury*, 32:109–114, 2001.

[23] Chehade MJ, Pohl AP, Pearcy MJ, and Nawan N. Clinical implication of stiffness and strength in fracture healing. *Journal of Bone and Joint Surgery, British*, 79-B(1):9–12, 1997.

[24] Shah KM, Nicol AC, and Hamblen DL. Fracture stiffness measurement in tibial shaft fractures: a non-invasive method. *Clinical Biomechanics*, 10(8):395–400, 1995.

[25] Shefelbine SJ, Simon U, Claes L, Gold A, Gabet Y, Bab I, Muller R, and Augat P. Prediction of fracture callus mechanical properties using micro-ct images and voxel-based finite element analysis. *Bone*, 36:480–488, 2005.

[26] Eyres KS, Bell MJ, and Kanis JA. Methods of assessing new bone formation during limb lengthening. *Journal of Bone and Joint Surgery, British*, 75-B(3):358–364, 1993.

[27] Tselentakis G, Owen PJ, Richardson JB, Kuiper JH, Haddaway MJ, Dwyer JSM, and Evans GA. Fracture stiffnes in callotasis determined by dual-energy x-ray absorptiometry scanning. *Journal of Pediatric Orthopaedics*, Part B, 10:248–254, 2001.

[28] Kolbeck S, Bail H, Weiler A, Windhagen H, Haas N, and Raschke M. Digital radiography a predictor of regenerate bone stiffness in distraction osteogenesis. *Clinical Orthopaedics and Related Research*, 366:221–28, 1999.

[29] Derbyshire ND and Simpson AH. A role for ultrasound in limb lengthening. *British Journal of Radiology*, 65(775):576–80, 1992.

[30] Guglielmi G, Gluer CC, Majumdar S, Blunt BA, and Genant. Current methods and advances in bone densitometry. *European Radiology*, 5:129–139, 1995.

[31] Beck T. Measuring the structural strength of bones with dual-energy x-ray absorptiometry: principles, technical limitations, and future possibilities. *Osteoporosis International*, 14 (Suppl 5):S81–S88, 2003.

[32] Faulkner KG, Gluer CC, Majumdar S, Lang P, Engelke K, and Genant HK. Noninvasive measurements of bone mass, structure and strength: Current methods and experimental techniques. *American Journal of Roentgenology*, 157:1229–1237, 1991.

[33] Harp JH, Aronson J, and Hollis M. Noninvasive determination of bone stiffness for distraction osteogenesis by quantitative computed tomography scans. *Clinical Orthopaedics and Related Research*, 301:42–48, 1994.

[34] Lynch JA, Grigoryan M, Fierlinger A, Guermazi A, Zaim S, MacLEan DB, and Genant HK. Measurement of changes in trabecular bone at fracture sites using x-ray ct and automated image registration and processing. *Journal of Orthopaedic Research*, 22:362–367, 2004.

[35] Roberts SG and Steele CR. Efficacy of monitoring long-bone fracture healing by measurement of either bone stiffness or resonant frequency: Numerical simulation. *Journal of Orthopaedic Research*, 18:691–697, 2000.

[36] Bauer JS, Kohlmann S, Exkstein F, Mueller D, Lochmuller EM, and Link TM. Structural analysis of trabecular bone of the proximal femur using multislice computed tomography: A comparison with dual x-ray absorptiometry for predicting biomechanical strength in vitro. *Calcified Tissue International*, 78:78–89, 2006.

[37] Sano H, Uhthoff HK, Backman DS, and Yeadon A. Correlation of radiographic measurements with biomechanical test results. *Clinical Orthopaedics and Related Research*, 368:271–278, 1999.

[38] Moorcroft CI, Ogrodnik PJ, Thomas PBM, and Wade RH. Mechanical properties of callus in human tibial fractures: a preliminary investigation. *Clinical Biomechanics*, 16:776–782, 2001.

[39] Bedford AM and Liechti KM. *Mechanics of Materials*. Prentice Hall, 2000.

[40] Hall IH. *Deformation of Solids*. Thomas Nelson and Sons Ltd., London, 1968.

[41] Cordey J. Introduction: Basic concepts and definitions in mechanics. *Injury*, 31:S–B1–S–B13, 2000.

[42] Hulse R and Cain J. *Structural Mechanics*. MacMillan, UK, 1991.

[43] Reilly DT and Burstein AH. The mechanical properties of cortical bone. *Journal of Bone and Joint Surgery*, 56:1001–1022, 1974.

[44] Currey JD. The mechanical properties of bone. *Clinical Orthopaedics and Related Research*, 73:209–31, 1970.

[45] Carter DR and Spengler DM. Mechanical properties and composition of cortical bone. *Clinical Orthopaedics and Related Research*, 135:192–217, 1978.

[46] Keller TS, Mao Z, and Spengler DM. Young's modulus, bending strength, and tissue physical properties of human compact bone. *Journal of Orthopaedic Research*, 8(4):592–603, 1990.

[47] Minns RJ, Campbell J, and Bremble GR. The bending stiffness of the human tibia. *Calcified Tissue Research*, 17:165–168, 1975.

[48] Hoffmeister BK, Smith SR, Handley SM, and Rho JY. Anisotropy of young's modulus of human tibial cortical bone. *Medical and Biological Engineering and Computing*, 38(3):333–8, 2000.

[49] Leuven KU. Biomechanics in dentistry. *ICB Dent [online], Belgium*, [last accessed 14 June 2009]:Available at http://www.feppd.org/ICB–Dent/campus/biomechanics in dentistry/ldv data/mech/basic bone.htm, 31 January 2005.

[50] Instron. Tensile testing. *Instron [online], UK*, [last accessed 14 June 2009]:Available at http:///www.instron.co.uk/wa/applications/test types/tension/default.aspx, 2009.

[51] Boresi AP, Schmidt RJ, and Sidebottom OM. *Advanced mechanics of materials*. John Wiley and Sons , New York, 1993.

[52] Beardmore R. Shear force and bending moment diagrams. *RoyMech [online], UK*, [last accessed 14 June 2009]:Available at http://www.roymech.co.uk/Useful Tables/Beams/Shear Bending.html, 15 February 2008.

[53] Clyne B. Bending and torsion of beams. *University of Cambridge [online], UK*, [last accessed 14 June 2009]:Available at http:///www.doitpoms.ac.uk/tlplib/beam bending/index.php, April 2008.

[54] Richardson JB, Kenwright J, and Cunningham JL. Fracture stiffness measurement in the assessment and management of tibial fractures. *Clinical Biomechanics*, 7:75–79, 1992.

[55] Richardson JB, Cunningham JL, Goodship AE, O'Connor BT, and Kenwright J. Measuring stiffness can define healing of tibial fractures. *Journal of Bone and Joint Surgery, British*, 76-B(3):389–394, 1994.

[56] Dwyer JSM, Owen PJ, Evans GA, Kuiper JH, and Richardson JB. Stiffness measurements to assess healing during leg lengthening. *The Journal of Bone and Joint Surgery*, 78-B:286–9, 1996.

[57] Floerkemeier T, Hurschler C, Witte F, Wellmann M, Thorey F, Vogt U, and Windhagen H. Comparison of various types of stiffness as predictors of the load-bearing capacity of callus tissue. *Journal of Bone and Joint Surgery, British*, 87-B:1694–9, 2005.

[58] Hammer R, Edholm P, and Lindholm B. Stability of union after tibial shaft fracture: Analysis by a non-invasive technique. *Journal of Bone and Joint Surgery, British*, 66-B(4):529–534, 1984.

[59] Hammer RRR. Strength of union in human tibial shaft fractures: A prospective study of 104 cases. *Clinical Orthopaedics and Related Research*, 199:226–232, 1985.

[60] Edholm P, Hammer R, Hammerby S, and Lindholm B. The stability of union in tibial shaft fractures: Its measurement by a non-invasive method. *Arch Orthop Trauma Surg*, 102:242–247, 1984.

[61] Ding M, Dalstra M, Danielsen CC, Kabel J, Hvid I, and Linde F. Age variations in the properties of human tibial trabecular bone. *Journal of Bone and Joint Surgery*, 79-B (6):995–1002, 1997.

[62] Choi K, Kuhn JL, Ciarelli MJ, and Goldstein SA. The elastic moduli of human subchondral , trabecular and cortical bone tissue and the size-dependency of cortical bone modulus. *Journal of Biomechanics*, 23(11):1103–1113, 1990.

[63] Aarnes GT, Steen H, Leif PK, Festa E, and Ludvigsen P. Optimum loading mode for axial stiffness testing in limb lengthening. *Journal of Orthoapedic Research*, March:348–354, 2006.

[64] Schmickal T, von Recum J, and Wentzensen A. Stiffness measurement of the neocallus with the fraktometer fm 100. *Archives of Orthopedic Trauma Surgery*, 125:653–659, 2005.

[65] Aarnes GT, Steen H, Ludvigsen P, Waanders NA, Huiskes R, and Goldstein SA. In vivo assessment of regenerate axial stiffness in distraction osteogenesis. *Journal of Orthopaedic Research*, 23:494–498, 2005.

[66] Kristiansen B and Borgwardt A. Fracture healing monitored with strain gauges. *Acta Orthopaedica Scandinavica*, 63(6):612–614, 1992.

[67] Hente R, Cordey J, and Perren SM. In vivo measurement of bending stiffness in fracture healing. *Biomedical Engineering OnLine*, 2:8, 2003.

[68] Stoffel K, Cunneen S, Morgan R, Nicholls R, and Stachowisk G. Comparative stability of perpendicular versus parallel double-locking plating systems in osteoporotic comminuted distal humerus fractures. *Journal of Orthopaedic Research*, June:778–784, 2008.

[69] Ahmad M, Nanda R, Bajwa AS, Candal-Couto J, Green S, and Hui AC. Biomechanical testing of the locking compression plate: When does the distance between bone and implant significantly reduce construct stability? *Injury*, 38:358–364, 2007.

[70] Schwartz A, Oka R, Odell T, and Mahar A. Biomechanical comparison of two different periarticular plating systems for stabilization of complex distal humerus fractures. *Clinical Biomechanics*, 21:950–955, 2006.

[71] Beaupre GS, Hayes WC, Jofe MH, and White AA III. Monitoring fracture site properties with external fixation. *Journal of Biomechanical Engineering*, 105:120–126, 1983.

[72] Simpson AHRW, Gardner RN, Evans M, and Kenwright J. Stiffness, strength and healing assessment in different bone fractures-a simple mathematical model. *Injury*, 31:777–781, 2000.

[73] Carter MD, Gilbert JA, and Dahners LE. An evaluation of the bending stiffness of various tibial fixation methods. *Clinical Orthopaedics and Related Research*, 224(November):289–293, 1987.

[74] Beltrame F, Cancedda R, Canesi B, Crovace A, Mastrogiacomo M, Quarto R, Scaglione S, Valastro C, and Viti F. A simple non invasive computerized method for the assessment of bone repair within osteoconductive porous bioceramic grafts. *Biotechnology and Bioengineering*, 92(2):189–198, 2005.

[75] Rontgen WC. On a new kind of ray. *Nature*, 53:274–276, 1896.

[76] Seibert JA. X-ray imaging physics for nuclear medicine technologists. part 1: Basic principles of x-ray production. *Journal of Nuclear Medicine Technology*, 32(3):139–147, 2004.

[77] Seibert JA and Boone JM. X-ray imaging physics for nuclear medicine technologists. part 2 x-ray interactions and image formation. *Journal of Nuclear Medicine Technology*, 33(1):3–18, 2005.

[78] Behiels G, Maes F, Vandermeulen D, and Suetens P. Retrospective heel effect correction in conventional radiography. *Proceedings of the IEEE Workshop on Mathematical Methods in Biomedical Image Analysis*, page 87, 2001.

[79] Hendee WR and Ritenour HE. *Medical Imaging Physics*. John Wiley and sons Inc., New York, 2002.

[80] Curry TS, Dowdey JE, and Murry RC. *Christensen's Physics of Diagnostic Radiology*. Lea and Febiger, London, 1990.

[81] Fung KKL and Gilboy WB. Anode heel effect on patient dose in lumbar spine radiography. *The British Journal of Radiology*, 73:531–536, 2000.

[82] Allisy-Roberts PJ and Williams JR. *Farr's Physics for Medical Imaging*. Saunders Ltd,. UK, 2007.

[83] Boone JM and Seibert JA (b). Monte carlo simulation of the scattered radiation distribution in diagnostic radiology. *Medical Physics*, 15(5):713–720, 1988.

[84] Bansal GJ. Digital radiography. a comparison with modern conventional imaging. *Postgraduate Medical Journal*, 82:425–428, 2006.

[85] Kato H, Miyahara J, and Takano M. New computed radiography using scanning laser stimulated luminescence. *Neurosurgical Review*, 8:53–62, 1985.

[86] Rowlands JA. The physics of computed radiography. *Physics in Medicine and Biology*, 47:R123–R166, 2002.

[87] Nomoto R, Mishima A, Kobayashi K, McCabe JF, Darvell BW, Watts DC, Momoi Y, and Hirano S. Quantitative determination of radio-opacaity: Equivalence of digital and film x-ray systems. *Dental Materials*, 24:141–147, 2008.

[88] Martin RB, Papamichos T, and Dannucci GA. Linear calibration of radiographic mineral density using video-digitizing methods. *Calcified Tissue International*, 47:82–91, 1990.

[89] Carvalho-Junior JR, Correr-Sobrinho L, Correr AB, Sinhoreti MAC, Consani S, and Sousa-Neto MD. Radiopacity of root filling materials using digital radiography. *International Endodontic Jourrnal*, 40:514–520, 2007.

[90] Workman A and Cowen AR. Signal, noise and snr transfer properties of computed radiography. *Physics in Medicine and Biology*, 38:1789–1808, 1993.

[91] Gu S, Rasimick BJ, Deutsch AS, and Musikant BL. Radiopacity of dental materials using a digital x-ray system. *Dental Materials*, 22:765–770, 2006.

[92] DICOM. Digital imaging in communications and medicine standard. *National Electrical Manufacturers Association [online]*, [Last accessed 15 June 2008]:Available at ftp://medical.nema.org/medical/dicom/2008/, 2008.

[93] Aro H, Eerola E, and Aho AJ. Determination of callus quantity in 4-week old fractures of the rat tibia. *Journal of Orthopaedic Research*, 3:101–108, 1985.

[94] Spencer RF. The effect of head injury on fracture healing. *Journal of Bone and Joint Surgery*, 69:525–528, 1987.

[95] Oni OOA, Dunning J, Mobbs RJ, and Gregg PJ. Clinical factors and the size of the external callus in tibial shaft fractures. *Clinical Orthopaedics and Related Research*, 273:278–283, 1991.

[96] Powell ES, Lawford PV, Duckworth T, and Black MM. Is callus calcium content an indicator of the mechanical strength of healing fractures? an experimental study in rat metatarsals. *Journal of Biomedical Engineering*, 11:271–281, 1989.

[97] Carter DR and Hayes WC. Bone compressive strength: the influence of density and strain rate. *Science*, 194(4270):1174–6, 1978.

[98] Vose GP. Determination of organin-inorganic ratio in osseous tissue by x-ray absorption. *Analytical Chemistry*, 30:1819–1821, 1958.

[99] Vose GP and Kubala AL. Bone strength-its relationship to x-ray determined ash content. *Human Biology*, 31(3):261–270, 1959.

[100] Shah KM, Goh JCH, Karunanithy R, Low SL, Das De S, and Bose K (b). Effect of decalcifcation on bone mineral content and bending strength of feline femur. *Calcified Tissue International*, 56:78–82, 1995.

[101] de Josselin de Jong E, van der Linden AHIM, and ten Bosch JJ. Longitudinal microradiography: a non-destructive automated quantitative method to follow mineral changes in mineralised tissue slices. *Physics in Medicine and Biology*, 32(10):1209–1220, 1987.

[102] Trouerbach WT, Steen WHA, Zwamborn AW, and Schouen HJA. A study of the radiographic aluminium equivalent values of the mandible. *Oral Surgery*, 58:610–616, 1984.

[103] Haidekker MA, Stevens HY, and Frangos JA. Computerized methods for x-ray based small bone densitometry. *Computer Methods and Programs in Biomedicine*, 73:35–42, 2004.

[104] Colbert C, Spruit JJ, and Davila LR. Biophysical properties of bone: Determining mineral concentration from the x-ray image. *Transactions New York Academy of Sciences*, 30:271–290, 1967.

[105] de Josselin de Jong E and ten Bosch JJ. Error analysis of the microradiographic determination of mineral content in mineralised tissue slices. *Physics in medicine and Biology*, 30(10):1067–1075, 1985.

[106] Watts DC and McCabe JF. Aluminium radiopacity standards for dentistry: an international survey. *Journal of Dentistry*, 27:73–78, 1999.

[107] Rowland RE, Jowsey J, and Marshall JH. Microscopic metabolism of calcium in bone: Iii. microradiographic measurements of mineral density. *Radiation Research*, 10(2):234–242, 1959.

[108] Symmons R. Digital photodensitometry: a reliable and accessible method for measuring bone density. *Journal of Archaeological Science*, 31:781–789, 2004.

[109] Abdel-Wahed N, Abdel-Wahab, SA Elabedeen, AZ Gadallah, SM Sollouma NH, and Kadah YM. Computer assisted radiographic characterization of alloimplant materials used as bone substitutes in dentistry. *Proceedings SPIE Medical Imaging*, February 2003, San Diego, 2003.

[110] Nackaerts O, Jacobs R, Horner K, Zhao F, Lindh C, Karayianni K, van der Stelt P, Pavitt S, and Devlin H. Bone density measurements in intra-oral radiographs. *Clinical Oral Investigations*, 11:225–229, 2007.

[111] Escarpinati MC, da Costa Vieira MA, and Schiabel H. Computer technique for digital radiographic images correction based on the digitizer characteristic curve. *Journal of Digital Imaging*, 15 (Suppl. 1):228–230, 2002.

[112] ISO 4049:2000. Dentistry-polymer-based filling, restorative and luting materials. *British Standard EN ISO 4049*, 2000.

[113] ISO 9917 1:2007. Dentistry-water-based cements-part 1 : Powder/liquid acid-base cements. *British Standard EN ISO 9917-1*, 2007.

[114] Behiels G, Maes F, Vendermeulen D, and Suetens P. Retrospective correction of the heel effect in hand radiographs. *Medical Image Analysis*, 6:183–190, 2002.

[115] do Nascimento MZ, Frere AF, and Germano F. An automatic correction method for the heel effect in digitized mammography images. *Journal of Digital Imaging*, 177-87:21(2), 2008.

[116] Boone JM and Seibert JA. An analytical model of the scattered radiation distribution in diagnostic radiology. *Medical Physics*, 15(5):721–725, 1988.

[117] Gardner TN and Evans M Kenwright J (b). A biomechanical study on five unilateral external fracture fixations devices. *Clinical Biomechanics*, 12(21):87–96, 1997.

[118] Gardner TN, Evans M, and Kenwright J. The influence of external fixators on fracture motion during simulated walking. *Medical Engineering and Physics*, 18(4):305–313, 1996.

[119] Gardner TN, Mishra S, and Marks L. The role of osteogenic index, octahedral shear stress and dilatational stress in the ossification of a fracture callus. *Medical Engineering and Physics*, 26:493–501, 2004.

[120] Lowet G, Davuan X, and van der Perre G. Study of the vibrational behaviour of a healing tibia using finite element modelling. *Journal of Biomechanics*, 29(8):1003–10, 1996.

[121] Beilin V, Ito K, and Pande GN. The effect of roughness on biophysical stimuli of the bone-cartilage interface. *Journal of Biomechanics*, 36(9):1381–5, 2003.

[122] Ifeachor EC and Jervis BW. *Digital Signal Processing: A practical approach*. Addison-Wesley Publishing Company, Wokingham, 1993.

[123] Carne EB. *Telecommunications Topics: Applications of Functions and Probabilities to Electronic Communications*. Prentice Hall, New Jersey, 1998.

[124] Grant PM, Cowan CN, Mulgrew B, and Dripps JH. *Analogue and Digital Signal Processing and Coding*. Chartwell-Bratt, Sweden, 1989.

[125] Chehade MJ, Solomon LB, Callary SA, Benveniste SH, Pohl AP, and Howie DW. Differentially loaded radiostereometric analysis to monitor fracture stiffness: a feasibility study. *Clinical Orthopaedics and Related Research*, 467(7):1839–47, 2009.

[126] Downing MR, Ashcroft PB, Johnstone AJ, Bach O, Mackenzie S, and Ashcroft GP. Assessment of inducible fracture micromotion in distal radial fractures using radiostereometry. *Journal of Orthopaedic Trauma*, 22(8 Suppl):S96–105, 2008.

[127] Han SM, Benaroya H, and Wei T. Dynamics of transversely vibrating beams using four engineering theories. *Journal of Sound and Vibration*, 225(5):935–988, 1999.

[128] Canny J. A computational approach to edge detection. *IEEE transactions on Pattern Analysis and Machine Intelligence*, PAMI-8 (6):679–698, 1986.

[129] Hall R and Flatow J. Canny edge detection. *Rice University Connexions [online], Texas*, [last accessed on 22 June 2009]:Available at http://cnx.org/content/m13218/latest/, 15 December2005.

[130] MacQueen J. Some methods for classification and analysis of multivariate observations. *Proceedings of the Fifth Berkeley Symposium on Mathematical Statistics and Probability*, 1:281–297, 1967.

[131] Duda RO and Hart PE. Use of the hough transformation to detect lines and curves in pictures. *Comm. ACM*, 15:11–15, 1972.

[132] Hough PVC. Machine analysis of bubble chamber pictures. *Proc Int Conf High Energy Accelerators and Instrumentation, CERN*, pages 554–6, 1959.

[133] Simpkin DJ. Transmission data for shielding diagnostic x-ray facilities. *Health Physics*, 68:704–9, 1995.

[134] Fuji. Imaging and information. *FujiFilm (Japan)*, Chapter 3:Auto Density Control, 2004.

[135] Verdenius HHW and Alma L. A quantitative study on decalcification methods in histology. *Journal of Clinical Pathology*, 11:229–236, 1958.

[136] Grampp S, Adams JE, Barkmann R, Bernecker PM, and Diacinti D. *Radiology of Osteoporosis*. Springer 2008, 2008.

[137] Thorpe EJ, Bellomy BB, and Sellers RF. Ultrasonic decalcification of bone-an experimental and clinical study. *Journal of Bone and Joint Surgery, American*, 45(6):1257–9, 1963.

[138] Milan L and Trachtenburg MC. Ultrasonic decalcification of bone. *American Journal of Surgical Pathology*, 5(6):573–580, 1981.

[139] Li B and Apsden RM (a). Composition and mechanical properties of cancellous bone from the femoral head of patients with osteoporosis or osteoarthritis. *Journal of Bone and Mineral Research*, 12(4):641–51, 1997.

[140] Li B and Aspden RM (b). Material properties of bone from the femoral neck and calcar femorale of patients with osteoporosis or osteoarthritis. *Osteoporosis International*, 7(5):450–6, 1997.

[141] Bland JM and Altman DG. Statistical methods for assessing agreement between two methods of clinical measurement. *Lancet*, 1:307–310, 1986.

[142] Hodgkinson JM. *Mechanical Testing of Advanced Fibre Composites*. Woodhead publishing, 2000.

[143] Liu AF. *Mechanics and Mechanisms of Fracture*. ASM International, 2005.

Publications and Conference Proceedings

The following abstracts and papers have been accepted at conference proceedings:

1. **Dawson SP, MacGillivray TJ, Muir AY, Simpson AHRW** (2008) "Quantitative Density Information with Computed Radiography", *Bi-Annual Meeting of the British Orthopaedic Research Society (BORS) and the British Research Society (BRS)*, Manchester, June 2008. To be published in the Journal of Bone and Joint Surgery (Br).

2. **Dawson SP, MacGillivray TJ, Muir AY, Simpson AHRW**, (2008) "Density Calibration in Computed Radiography", *Bi-Annual Meeting of the European Orthopaedic Research Society (EORS)*, Madrid, April 2008. To be published in the Journal of Bone and Joint Surgery (Br), Vol 91-B, Numm Supp_III, 2009. See enclosed abstract.

3. **Dawson SP, Ross E, MacGillivray TJ, Muir AY, Simpson AHRW**, (2009) "The Use of Digital X-ray to Monitor Decalcification in Sheep Femora", *Triennial World Congress in Medical Physics and Biomedical Engineering, Munich, September 2009.* To be published in the Proceedings Series of the International Organisation for Medical Physics and International Federation for Medical and Biological Engineering. See enclosed abstract.